An investigation into the behaviour, kinetics & mechanisms involved in the precipitation of a moderately soluble system

by

Emily Ann Musil
Bachelor of Science in Chemical Engineering

A dissertation submitted for the degree of Master of Science in Chemical Engineering

Crystallization & Precipitation Research Unit, Department of Chemical Engineering
Faculty of Engineering and the Built Environment
University of Cape Town

September 2011

Declaration

I know the meaning of plagiarism and declare that all work in this dissertation, save for which is properly acknowledged, is my own.

Emily Musil
September 2011

Abstract

Reliable kinetic data are of fundamental importance for the successful modelling and scale-up of precipitation processes and in controlling these processes such that a desired output is achieved. For crystallization processes, where information is readily available, many techniques exist for the determination of the kinetics. However, the same cannot be said of precipitation processes where little is known and only a few techniques exist.

This dissertation consists of three interrelated sections dealing with: (i) Development of a suitable seed preparation technique, (ii) Determination of growth and aggregation kinetics and (iii) Determination of the induction period. Calcium oxalate was chosen as the model system for the present work as it is a moderately soluble system with K_{sp} (37°C) = 2.47×10^{-9} $(mol.dm^{-3})^2$. All experiments were carried out in a batch reactor where particle size distributions (PSD) were measured using a Coulter Multisizer III.

In the first section of the dissertation, seeds were produced for use in the kinetic experiments. A number of operating parameters were investigated, namely supersaturation, mixing rate, reactant addition rate and addition method. From PSD and SEM results it was found that all of the factors significantly influenced both the size and morphology of the seeds, with a higher mixing rate and the double-jet reactant addition method yielding the best control of the PSD.

The second part of the dissertation involved extracting growth and aggregation kinetics from the experimental PSDs. The kinetics were investigated over a supersaturation range of S_i = 2.3 - 5.8. An expression for the crystal growth rate as a function of supersaturation was found to be: $G = 1.4\times10^{-8}(S-1)^2$ $m.s^{-1}$. The aggregation rate was found to be in the range of $\beta_0 = 1.3\times10^{-16}$ - 3.2×10^{-12} $m^3.s^{-1}$. The kinetics agreed with those found in literature. SEM images confirmed both growth and aggregation within the system.

The final section of the dissertation dealt with the determination of the induction period from conductivity measurements. The induction period was found to decrease with an increase in the initial supersaturation following a power law fit: $t_{ind} = 2464S_i^{-2.6}$. Within the supersaturation range investigated (S_i = 2.1 - 9.7), the calcium oxalate system exhibited a shift in nucleation from the heterogeneous to the homogeneous mechanism.

Finally, from an analysis of the combined results, it was concluded that the current experimental method for determining the precipitation kinetics may be suitable for use with a more insoluble system as long as $S_i \leq 6$.

Acknowledgements

Firstly, I would like to express my sincerest gratitude to my supervisor, Professor Alison Lewis, for her assistance and guidance in the development of this project. Her theoretical and technical knowledge in the field of Chemical Engineering and specifically in Crystallization and Precipitation has been very helpful over the past two years.

I would also like to acknowledge the following people who have been of great help to me in completing different aspects of this work:

Christine Olsen - for always being friendly and willing to help with administrative issues surrounding my work.

Tracy-Ann Craig and Sinethemba Nkukwana - for their technical assistance in the CPU labs. Thank you for helping me to source equipment, set-up my reactor and for teaching me how to use different analytical equipment.

Marcos Rodriquez-Pascual - for his time and assistance in not only filming the “dye visualization experiments” but also for conducting the image processing using MATLAB.

Miranda Waldron of the Electron Microscope Unit (University of Cape Town) - for her assistance with the SEM and for helping me to produce wonderful images of my samples.

Theresa Feltes - for running the XRD scans of all my samples.

UCT PGFO, CSIR & UCT Chemical Engineering department - for providing both personal and project funding.

Table of Contents

Declaration i
Abstract ii
Acknowledgements iii
List of Figures viii
List of Tables xii
Glossary xiii
Nomenclature xiii
Chapter 1 INTRODUCTION 1
1.1 Background to Dissertation 1
1.2 Scope and Context of the Work 1
1.3 Summary of Dissertation Structure 2
Chapter 2 THEORY AND LITERATURE REVIEW 3
2.1 Precipitation Thermodynamics and Kinetics 3
2.1.1 Supersaturation and Solubility 3
2.1.2 Nucleation 6
2.1.2.1 Induction Time 9
2.1.3 Particle Growth 11
2.1.3.1 Diffusion-Controlled Growth 11
2.1.3.2 Surface-Integration Controlled Growth 12
2.1.4 Aggregation and Other Secondary Processes 14
2.1.4.1 Aggregation 14
2.1.4.2 Ageing 17
2.2 Particle Characteristics, Morphology and Behaviour 18
2.2.1 Introduction 18
2.2.2 Crystal Systems 18
2.2.3 Crystal Habit 19
2.2.4 Polymorphism 19
2.2.5 Dendrites 20
2.2.6 Composite Crystals and Twinning 20
2.3 Batch Precipitation and Mixing 21
2.3.1 Overview 21
2.3.2 Mixing Strategies 22
2.3.3 Mixing Times and Scales 24
2.3.3.1 Macromixing 24
2.3.3.2 Mesomixing 24
2.3.3.3 Micromixing 25
2.3.3.4 Reynolds Number 25
2.4 Particle Size Analysis Techniques 26
2.4.1 Overview of Existing Techniques 26
2.4.2 Laser Light Scattering (Fraunhofer) Technique 26
2.4.3 Electrical Sensing Zone Technique – The Coulter Principle 27
2.5 Seeds and Seeding 29

2.5.1 Overview ... 29
2.5.2 Previous Seed Preparation Techniques for Moderately Soluble Systems ... 29
2.5.3 Considerations for Developing a Suitable Seed Preparation Technique ... 30
2.6 Thermodynamic Modelling: OLI Stream Analyser ... 31
2.6.1 Background ... 31
2.6.2 Application of OLI ... 32
2.7 Kinetic Modelling for Precipitation Systems – The Population Balance ... 32
2.7.1 Equations for Nucleation, Growth and Aggregation ... 32
2.7.2 The Moment Form ... 33
2.7.3 Analytical and Numerical Solutions ... 34
2.7.4 Analysis of the Discretized Population Balance (DPB) ... 34
2.7.5 Mixed-Suspension-Mixed-Product-Removal (MSMPR) Modelling ... 34
2.8 Methods for Determining Precipitation Kinetics ... 35
2.8.1 Methods for Determining the Nucleation Rate ... 36
2.8.2 Determining the Induction Time for Precipitating Systems ... 40
2.8.3 Methods for Determining the Growth and/or Aggregation Rates ... 43
2.9 Model System – Calcium Oxalate Monohydrate ... 48
2.9.1 Choice of a Moderately Soluble System ... 48
2.9.2 General Information and Significance ... 48
2.9.3 Physical and Chemical Properties ... 48
2.9.3.1 Behaviour and Solubility ... 48
2.9.3.2 Morphology and Polymorphism ... 49
2.9.4 Kinetics and Mechanisms ... 52
2.9.4.1 Nucleation Kinetics ... 52
2.9.4.2 Growth Kinetics ... 53
2.9.4.3 Aggregation Kinetics ... 55
2.9.4.4 Breakage Kinetics ... 57
2.10 Overall Objectives and Key Questions ... 57
Chapter 3 PREPARATION OF SEEDS FOR A MODERATELY SOLUBLE SYSTEM ... 58
3.1 Introduction ... 58
3.2 Materials and Methods ... 58
3.2.1 Seed Preparation Guidelines ... 58
3.2.2 Reagents ... 59
3.2.3 Experimental Set-Up and Operating Conditions ... 59
3.2.4 Reactant Addition Methods ... 60
3.2.4.1 Single-Jet Method ... 60
3.2.4.2 Double-Jet Method ... 60
3.2.5 Filtering and Storage ... 60
3.2.6 Particle Size and Morphology Analysis ... 61
3.2.6.1 Beckman Coulter Multisizer III – Coulter Counter ... 61
3.2.6.2 Scanning Electron Microscopy (SEM) ... 61
3.2.6.3 X-Ray Diffraction (XRD) ... 61
3.2.7 Dye Visualization Experiments ... 61

3.3 Results 62
3.3.1 Mixing in the Batch Reactor 62
3.3.1.1 Mixing Times and Scales 62
3.3.1.2 Dye Visualization Experiments 64
3.3.2 Seed Particle Size Distributions 66
3.3.3 Morphology Charts 70
3.3.4 Polymorphism in the Seed Samples 71
3.3.5 Summary Table 73
3.4 Discussion 75
3.4.1 Factors Effecting Particle Size and Morphology 75
3.4.1.1 Supersaturation 75
3.4.1.2 Agitation Rate 77
3.4.1.3 Addition Rate 77
3.4.1.4 Addition Method 78
3.4.2 Choice of Seeds for the Kinetic Experiments 78
3.5 Preliminary Conclusions 79
Chapter 4 DETERMINATION OF THE GROWTH & AGGREGATION KINETICS 80
4.1 Introduction 80
4.2 Materials and Methods 80
4.2.1 Reagents 80
4.2.2 Experimental Set-Up and Procedure 80
4.2.3 Preventing Nucleation in the Kinetic Experiments 82
4.2.4 Sampling and PSD Measurements 83
4.2.5 Repeatability and Error Analysis 83
4.2.6 Filtering and Storage 83
4.2.7 Other Analyses 83
4.2.7.1 Scanning Electron Microscopy 83
4.2.7.2 X-Ray Diffraction 83
4.2.8 Calculation of G and β_0 84
4.3 Results 84
4.3.1 Nucleation in the Experiments 84
4.3.2 Evolution of the Zeroth and Third Moments 85
4.3.3 Morphology and Size of Particles 88
4.3.4 Growth and Aggregation Kinetics 90
4.4 Discussion 94
4.4.1 Effect of Supersaturation and Seed Concentration on Growth and Aggregation 94
4.4.2 Growth Kinetics 95
4.4.3 Aggregation Kinetics 96
4.4.4 Influence of Particle Size and Morphology on the Kinetics 96
4.4.5 Applicability of Bramley *et al.*'s (1996) Method to Precipitation Systems 97
4.5 Preliminary Conclusions 97
Chapter 5 DETERMINATION OF THE INDUCTION PERIOD 99
5.1 Introduction 99
5.2 Materials and Methods 99

5.2.1 Reagents 99
5.2.2 Experimental Set-Up and Procedure 99
5.2.3 Determining the Induction Period from the Conductivity Profiles 100
5.3 Results 101
5.4 Discussion 106
5.5 Preliminary Conclusions 107
Chapter 6 FINAL CONCLUSIONS & RECOMMENDATIONS 108
References 111
Appendix A: PSD and SEM Results from Seed Experiments ..... A
A.1 Seed Experiments with S_i = 10 ..... A
A1.1 Single-Jet Method ..... A
A1.2 Double-Jet Method C
A.2 Seed Experiments with S_i = 17 ..... F
A2.1 Single-Jet Method ..... F
A2.2 Double-Jet Method I
A.3 Seed Experiments with S_i = 30 ..... K
A3.1 Single-Jet Method ..... K
A3.2 Double-Jet Method ..... N
A.4 Purchased COM sample ..... Q
Appendix B: Results from Kinetic Experiments ..... R
B.1 Evolution of m_0 and m_3 ..... R
B.2 SEM Photographs ..... W
B.3 Growth Kinetics Results ..... Y
B.4 Aggregation Kinetics Results ..... AA
Appendix C: Raw Data & Sample Calculations ..... DD
C.1 Chapter 3 ..... DD
C.2 Chapter 4 ..... RR
C.3 Chapter 5 ..... ZZ
Appendix D: Ethics Form ..... BBB

List of Figures

Figure 1: Solubility-supersolubility diagram (adapted from Jones, 2002)..... 3
Figure 2: The role of supersaturation in precipitation processes (Sohnel & Garside, 1992)..... 4
Figure 3: Kinetic processes involved in precipitation (Sohnel & Garside, 1992)..... 6
Figure 4: Mechanisms responsible for nucleus formation (Randolph & Larson, 1988) 7
Figure 5: Empirical dependence of induction period of $Ni(NH_4)_2(SO_4)_2.6H_2O$ at 25°C on relative supersaturation in logarithmic coordinates (Sohnel & Mullin, 1979, cited in Myerson, 2002)..... 10
Figure 6: Induction period as a function of initial supersaturation for a number of precipitating systems at 25°C (Sohnel & Mullin, 1978)..... 11
Figure 7: Crystal growth by the rough growth mechanism (Giulietti *et al.*, 2001)..... 12
Figure 8: Crystal growth by the birth and spread mechanism (Giulietti *et al.*, 2001)..... 13
Figure 9: Crystal growth by screw dislocations (Giulietti *et al.*, 2001) 13
Figure 10: Comparison of the three surface growth mechanisms (Lewis & van Rosmalen, 2010) 14
Figure 11: The effect of shear rate on the collision and aggregation rate constants (adapted from Mumtaz *et al.*, 1997)..... 16
Figure 12: Illustration of the seven crystal systems 19
Figure 13: An example of dendritic growth (Mullin, 2001) 20
Figure 14: (left) Parallel growth on a crystal of potash alum, (middle) interpenetrant twin of two cubes, and, (right) partial interpenetrant twin (Mullin, 2001) 21
Figure 15: Typical flow pattern in a baffled tank with a (left) propeller or axial flow turbine and (right) turbine positioned on center (Perry *et al.*, 1997)..... 22
Figure 16: Possible reactant addition methods (Mullin, 2001)..... 23
Figure 17: Illustration of laser diffraction (Malvern Instruments Ltd., 2011) 26
Figure 18: Malvern Mastersizer 2000 (Malvern Instruments Ltd., 2011)..... 26
Figure 19: Schematic of the workings of a Coulter Counter (Beckman Coulter Inc., 2011)..... 27
Figure 20: Beckman Coulter Multisizer III (Beckman Coulter Inc., 2011)..... 28
Figure 21: Population balance for an MSMPR crystallizer (Giulietti *et al.*, 2001)..... 35
Figure 22: Schematic representation of the method applied to measure nucleation rates (Roelands *et al.*, 2004)..... 38
Figure 23: (left) Conductivity profiles for various reagent concentrations, and, (right) Enlarged conductivity-time curve for $[CaCl_2] = [Na_2CO_3] = 0.0025$ M (Chien *et al.*, 1999)..... 42
Figure 24: Plot of induction time versus supersaturation developed from the data of Chien *et al.* (1999) 42
Figure 25: Typical PSDs at the beginning and completion of a batch precipitation experiment by (a) number and (b) volume (Bramley *et al.*, 1996) 47
Figure 26: SEM photograph of COM (Houcine *et al.*, 1997)..... 50
Figure 27: SEM photograph of COD crystals – mag. 1040x (Bretherton & Rodgers, 1998)..... 50
Figure 28: SEM photograph of COT (Houcine *et al.*, 1997) 50
Figure 29: SEM images of calcium oxalate crystals – (a) calcium oxalate agglomerate, (b) Intergrowth of particles, (c) Agglomeration and disruption effects, and, (d) Twinned particle (Zauner & Jones, 2000)..... 51
Figure 30: Different forms of calcium oxalate viewed under an optical microscope: A – monoclinic prismatic COM, B – weddellite COD, C –COT needles, D & E – COM twins, F to H – COM dendrites, I to M – atypical forms, N to P – COM agglomerates (Thongboonkerd *et al.*, 2006) 51
Figure 31: Precipitation boundary (24hr) for calcium oxalate at 25°C. P = plates, D = dendrites, and, A = agglomerates (Mullin, 2001) 52

Figure 32: The dependence of growth rate on supersaturation for all experiments (Bramley *et al.*, 1997)..... 54
Figure 33: Growth rate of calcium oxalate versus supersaturation (Zauner & Jones, 2000)..... 54
Figure 34: The dependence of the aggregation rate constant on supersaturation (Bramley *et al.*, 1997)..... 55
Figure 35: Agglomeration rate of calcium oxalate versus energy dissipation (Zauner & Jones, 2000) 56
Figure 36: Correlation between the aggregation rate constant to the instantaneous growth rates, average particle diameter and stirrer speed (Liew *et al.*, 2003) 56
Figure 37: Reactor set-up for seed preparation experiments..... 59
Figure 38: Reynolds number versus impeller speed 62
Figure 39: Macro, meso and micro mixing times in the batch reactor with V = 1L versus impeller speed..... 62
Figure 40: Macro mixing time as a function of reactor volume..... 63
Figure 41: Meso mixing time as a function of reactor volume 63
Figure 42: Impeller power (left) and average energy dissipation rate (right) versus impeller speed .. 64
Figure 43: Mixing image before (left) and after (right) additional image processing 65
Figure 44: Images highlighting the addition of reagents and their dispersion into the bulk solution... 66
Figure 45: Single-jet, N = 300rpm & slow addition seed PSDs at varying S_i 67
Figure 46: Single-jet, N = 900rpm & slow addition seed PSDs at varying S_i 67
Figure 47: Single-jet, N = 300rpm & fast addition seed PSDs at varying S_i..... 67
Figure 48: Single-jet, N = 900rpm & fast addition seed PSDs at varying S_i..... 68
Figure 49: Double-jet, N = 300rpm & slow addition seed PSDs at varying S_i..... 68
Figure 50: Double-jet, N = 900rpm & slow addition seed PSDs at varying S_i..... 69
Figure 51: Double-jet, N = 300rpm & fast addition seed PSDs at varying S_i 69
Figure 52: Double-jet, N = 900rpm & fast addition seed PSDs at varying S_i 69
Figure 53: 3D chart showing the morphologies of calcium oxalate at various conditions for the single-jet addition method..... 70
Figure 54: 3D chart showing the morphologies of calcium oxalate at various conditions for the double-jet addition method..... 71
Figure 55: Flat needle-like COT plate found in seed sample B2.1.1 (approximately 60µm in length) 72
Figure 56: Dendritic COD crystal found in seed sample B3.1.2 (approximately 40µm in diameter)... 72
Figure 57: XRD spectrum for pure COM from seed sample A1.1.1..... 72
Figure 58: XRD spectrum showing peaks for COM, COD & COT from seed sample B2.2.2..... 73
Figure 59: Comparison of initial supersaturation levels used by Bramley *et al.* (1997) and used in this work..... 81
Figure 60: Evolution of m_0 and m_3 for the case when nucleation occurred in the experiments 84
Figure 61: Number (left) and volume (right) size distributions for the case when nucleation occurred in the experiments..... 85
Figure 62: Evolution of m_0 and m_3 for S_i = 5.8 & C_{seeds} = 0.15g.dm^{-3} 86
Figure 63: Number (left) and volume (right) size distributions for S_i = 5.8 & C_{seeds} = 0.15g.dm^{-3} 86
Figure 64: Number (left) and volume (right) size distributions for S_i = 2.3 & C_{seeds} = 0.15g.dm^{-3} confirming equilibration of the system..... 87
Figure 65: Evolution of m_0 and m_3 for S_i = 3.3 & C_{seeds} = 0.03g.dm^{-3} 87
Figure 66: Number (left) and volume (right) size distributions for S_i = 3.3 & C_{seeds} = 0.03g.dm^{-3} 88
Figure 67: Change in mean particle size, $d_{1,0}$ (right) & $d_{4,3}$ (left), with time for the various kinetic experiments..... 88

Figure 68: SEM images of purchased $CaC_2O_4.H_2O$ seed material 89
Figure 69: SEM images of A3.2.1 seed material 89
Figure 70: SEM images from kinetic experiment with S_i = 3.3 & C_{seeds} = 0.03g.dm^{-3} 89
Figure 71: XRD spectrum showing fit to major COM peaks for kinetic experiment with S_i = 5.8 & C_{seeds} = 0.15g.dm^{-3} 90
Figure 72: Summary of all determined growth rates at various initial supersaturations 91
Figure 73: Overall growth rate plot to determine the growth rate constant 91
Figure 74: Average aggregation rate constant profiles for different combinations of initial supersaturation and seed concentration 92
Figure 75: Aggregation rate constants versus supersaturation for various combinations of initial supersaturation and seed concentration 93
Figure 76: Comparison of the growth and aggregation rates for two different seed samples with S_i = 3.3 & C_{seeds} = 0.03g.dm^{-3} 93
Figure 77: Typical conductivity profile for the induction time experiments where S_i = 6.5 100
Figure 78: Zoomed-in conductivity profile clearly showing the induction period and onset of precipitation 101
Figure 79: Conductivity profiles for varying initial supersaturation levels 101
Figure 80: Power law fit of induction time versus initial supersaturation for COM 102
Figure 81: Plot of $log(t_{ind})$ versus $log(\sigma)$ 103
Figure 82: Plot of $\log(t_{ind})$ versus $log(S_i)^{-2}$ 103
Figure 83: Comparison of induction times for various compounds 104
Figure 84: Zoomed-in plot of induction time versus supersaturation for various compounds (see legend in Figure 83) 104
Figure 85: Fit of all induction time data to a power law trendline 105
Figure 86: Number and volume distributions for seed sample A1.1.1 ..... A
Figure 87: SEM images for seed sample A1.1.1 ..... A
Figure 88: Number and volume distributions for seed sample A1.2.1 ..... A
Figure 89: SEM images for seed sample A1.2.1 ..... B
Figure 90: Number and volume distributions for seed sample A1.1.2 ..... B
Figure 91: SEM images for seed sample A1.1.2 ..... B
Figure 92: Number and volume distributions for seed sample A1.2.2 C
Figure 93: SEM images for seed sample A1.2.2 C
Figure 94: Number and volume distributions for seed sample B1.1.1 C
Figure 95: SEM images for seed sample B1.1.1 ..... D
Figure 96: Number and volume distributions for seed sample B1.2.1 ..... D
Figure 97: SEM images for seed sample B1.2.1 ..... D
Figure 98: Number and volume distributions for seed sample B1.1.2 ..... E
Figure 99: SEM images for seed sample B1.1.2 ..... E
Figure 100: Number and volume distributions for seed sample B1.2.2 ..... E
Figure 101: SEM images for seed sample B1.2.2 ..... F
Figure 102: Number and volume distributions for seed sample A2.1.1 ..... F
Figure 103: SEM images for seed sample A2.1.1 ..... F
Figure 104: Number and volume distributions for seed sample A2.2.1 ..... G
Figure 105: SEM images for seed sample A2.2.1 ..... G
Figure 106: Number and volume distributions for seed sample A2.1.2 ..... G
Figure 107: SEM images for seed sample A2.1.2 ..... H
Figure 108: Number and volume distributions for seed sample A2.2.2 ..... H

Figure 109: SEM images for seed sample A2.2.2 ..... H
Figure 110: Number and volume distributions for seed sample B2.1.1 I
Figure 111: SEM images for seed sample B2.1.1 I
Figure 112: Number and volume distributions for seed sample B2.2.1 I
Figure 113: SEM images for seed sample B2.2.1 ..... J
Figure 114: Number and volume distributions for seed sample B2.1.2 ..... J
Figure 115: SEM images for seed sample B2.1.2 ..... J
Figure 116: Number and volume distributions for seed sample B2.2.2 ..... K
Figure 117: SEM images for seed sample B2.2.2 ..... K
Figure 118: Number and volume distributions for seed sample A3.1.1 ..... K
Figure 119: SEM images for seed sample A3.1.1 L
Figure 120: Number and volume distributions for seed sample A3.2.1 L
Figure 121: SEM images for seed sample A3.2.1 L
Figure 122: Number and volume distributions for seed sample A3.1.2 ..... M
Figure 123: SEM images for seed sample A3.1.2 ..... M
Figure 124: Number and volume distributions for seed sample A3.2.2 ..... M
Figure 125: SEM images for seed sample A3.2.2 ..... N
Figure 126: Number and volume distributions for seed sample B3.1.1 ..... N
Figure 127: SEM images for seed sample B3.1.1 ..... N
Figure 128: Number and volume distributions for seed sample B3.2.1 ..... O
Figure 129: SEM images for seed sample B3.2.1 ..... O
Figure 130: Number and volume distributions for seed sample B3.1.2 ..... O
Figure 131: SEM images for seed sample B3.1.2 ..... P
Figure 132: Number and volume distributions for seed sample B3.2.2 ..... P
Figure 133: SEM images for seed sample B3.2.2 ..... P
Figure 134: Number and volume distributions for purchased COM sample ..... Q
Figure 135: SEM images for purchased COM sample ..... Q
Figure 136: Evolution of m_0 and m_3 for S_i = 4.6 & C_{seeds} = 0.15g.dm^{-3} ..... R
Figure 137: Number (left) and volume (right) size distributions for S_i = 4.6 & C_{seeds} = 0.15g.dm^{-3} ..... R
Figure 138: Evolution of m_0 and m_3 for S_i = 3.3 & C_{seeds} = 0.15g.dm^{-3} ..... S
Figure 139: Number (left) and volume (right) size distributions for S_i = 3.3 & C_{seeds} = 0.15g.dm^{-3} ..... S
Figure 140: Evolution of m_0 and m_3 for S_i = 2.3 & C_{seeds} = 0.15g.dm^{-3} ..... T
Figure 141: Number (left) and volume (right) size distributions for S_i = 2.3 & C_{seeds} = 0.15g.dm^{-3} ..... T
Figure 142: Evolution of m_0 and m_3 for S_i = 2.3 & C_{seeds} = 0.03g.dm^{-3} ..... U
Figure 143: Number (left) and volume (right) size distributions for S_i = 2.3 & C_{seeds} = 0.03g.dm^{-3} ..... U
Figure 144: Evolution of m_0 and m_3 for S_i = 3.3, C_{seeds} = 0.03g.dm^{-3} & seed sample A3.2.1 V
Figure 145: Number (left) and volume (right) size distributions for S_i = 3.3, C_{seeds} = 0.03g.dm^{-3} & seed sample A3.2.1 V
Figure 146: SEM images from kinetic experiment with S_i = 5.8 & C_{seeds} = 0.15g.dm^{-3} ..... W
Figure 147: SEM images from kinetic experiment with S_i = 4.6 & C_{seeds} = 0.15g.dm^{-3} ..... W
Figure 148: SEM images from kinetic experiment with S_i = 3.3 & C_{seeds} = 0.15g.dm^{-3} ..... W
Figure 149: SEM images from kinetic experiment with S_i = 2.3 & C_{seeds} = 0.15g.dm^{-3} X
Figure 150: SEM images from kinetic experiment with S_i = 2.3 & C_{seeds} = 0.03g.dm^{-3} X
Figure 151: SEM images from kinetic experiment with S_i = 3.3, C_{seeds} = 0.03g.dm^{-3} & A3.2.1 seeds X
Figure 152: Growth results for kinetic experiment: S_i = 5.8 & C_{seeds} = 0.15g.dm^{-3} ..... Y
Figure 153: Growth results for kinetic experiment: S_i = 4.6 & C_{seeds} = 0.15g.dm^{-3} ..... Y
Figure 154: Growth results for kinetic experiment: S_i = 3.3 & C_{seeds} = 0.15g.dm^{-3} ..... Y

Figure 155: Growth results for kinetic experiment: S_i = 3.3 & C_{seeds} = 0.03g.dm^{-3} ..... Z
Figure 156: Growth results for kinetic experiment: S_i = 2.3 & C_{seeds} = 0.15g.dm^{-3} ..... Z
Figure 157: Growth results for kinetic experiment: S_i = 2.3 & C_{seeds} = 0.03g.dm^{-3} ..... Z
Figure 158: Growth results for kinetic experiment: S_i = 3.3 & C_{seeds} = 0.03g.dm^{-3} using seed sample A3.2.1 .....AA
Figure 159: Aggregation results for kinetic experiment: S_i = 5.8 & C_{seeds} = 0.15g.dm^{-3} .....AA
Figure 160: Aggregation results for kinetic experiment: S_i = 4.6 & C_{seeds} = 0.15g.dm^{-3} .....AA
Figure 161: Aggregation results for kinetic experiment: S_i = 3.3 & C_{seeds} = 0.15g.dm^{-3} .....BB
Figure 162: Aggregation results for kinetic experiment: S_i = 3.3 & C_{seeds} = 0.03g.dm^{-3} .....BB
Figure 163: Aggregation results for kinetic experiment: S_i = 2.3 & C_{seeds} = 0.15g.dm^{-3} .....BB
Figure 164: Aggregation results for kinetic experiment: S_i = 2.3 & C_{seeds} = 0.03g.dm^{-3} CC
Figure 165: Aggregation results for kinetic experiment: S_i = 3.3 & C_{seeds} = 0.03g.dm^{-3} using seed sample A3.2.1..... CC

List of Tables

Table 1: Common aggregation kernels used in the modeling of precipitation processes (Bramley *et al.*, 1996)..... 16
Table 2: The seven crystal systems and their properties (Mullin, 2001) 18
Table 3: Mixing stages in precipitation (Myerson, 2002) 24
Table 4: Analysis of the Malvern Mastersizer for particle size analysis (Lewis & van Rosmalen, 2010, and, Malvern Instruments Ltd., 2011) 27
Table 5: Analysis of the Coulter Counter for particle size analysis (Lewis & van Rosmalen, 2010, and, Beckman Coulter Inc., 2011)..... 28
Table 6: Solubility products for calcium oxalate hydrates at T = 25 and 37°C 49
Table 7: Operating variables for seed experiments 59
Table 8: Mixing times and variables for N = 300 & 900 rpm at the start of a seed experiment i.e. V = 0.5L..... 64
Table 9: Summary of seed preparation findings 74
Table 10: Supersaturation levels investigated by Bramley *et al.* (1997) and the current work 81
Table 11: Properties of the two seed concentrations used in the kinetic experiments 82
Table 12: Summary of results from induction time experiments..... 102
Table 13: Solubility products for three precipitation systems calculated using OLI Stream Analyser (OLI Systems, 2008) 105
Table 14: Comparison of supersaturations for different precipitation systems @ 25°C..... 105
Table 15: Raw data from seed experiment A1.2.1 ..... DD
Table 16: Sample calculations for seed experiment A1.2.1 .....KK
Table 17: Raw data from kinetic experiments with S_i =3.3, C_{seeds} = 0.03g.dm^{-3} & A3.2.1..... RR
Table 18: Results from sample calculations for kinetic experiments with S_i =3.3, C_{seeds} = 0.03g.dm^{-3} & A3.2.1 XX
Table 19: Sample calculations showing results for the determination of G .....YY
Table 20: Sample calculations showing results for the determination of S.....YY
Table 21: Sample calculations showing results for the determination of β_0 ..... ZZ
Table 22: Raw conductivity-time data from an induction time experiment with S_i = 6.5 ..... AAA

Glossary

BCF	Burton-Cabrera-Frank Model
CDJP	Controlled Double-Jet Precipitation
CFD	Computational Fluid Dynamics
CNT	Classical Nucleation Theory
COD	Calcium Oxalate Dihydrate
COM	Calcium Oxalate Monohydrate
COT	Calcium Oxalate Trihydrate
CSD	Crystal Size Distribution
CSTR	Continuous Stirred Tank Reactor
DPB	Discretized Population Balance
DTB	Draft Tube Baffled Reactor
HEN	Heterogeneous Nucleation
HKF	Helgeson-Kirkham-Flowers Model
HON	Homogeneous Nucleation
IAP	Ionic Activity Product
MSMPR	Mixed-Suspension-Mixed-Product-Removal Crystallizer
PBE	Population Balance Equation
PFC	Poiseuille Flow Crystallizer
PSD	Particle Size Distribution
SEM	Scanning Electron Microscopy/Microscope
SSE	Sum-of-Square Errors
ST	Scaling Tendency
XRD	X-Ray Diffraction

Nomenclature

Symbol	Definition	Units
a	activity	[-]
a	constant	[-]
A	surface area of a particle	[m^2]
A	kinetic parameter	[$m^{-3}.s^{-1}$]
A	ratio of the activity coefficients (= γ/γ^*)	[-]
a^*	activity of a saturated solution	[-]
A'	kinetic parameter	[$m^{-3}.s^{-1}$]
a_A	equilibrium activity of component A	[-]
a_B	equilibrium activity of component B	[-]
a_{eq}	equilibrium activity	[-]
a_{H_2O}	activity of water	[-]
$A_{HON,D}$	kinetic parameter for volume-diffusion control HON	[$m^{-3}.s^{-1}$]
$A_{HON,I}$	kinetic parameter for interface-transfer control HON	[$m^{-3}.s^{-1}$]

a_j	activity of species j	[-]
A_T	total area of particles	[$m^2.m^{-3}$]
B	thermodynamic parameter	[-]
B_u	source function	[$\#.m^{-3}.s^{-1}$]
C	concentration	[$mol.dm^{-3}$]
c	solution concentration	[$mol.dm^{-3}$]
c^*	equilibrium concentration	[$mol.m^{-3}$]
C^*	equilibrium concentration of nuclei	[$\#.m^{-3}$]
C^*	saturation concentration	[$mol.dm^{-3}$]
Δc	concentration driving force	[$mol.dm^{-3}$]
C_A	concentration of reactant A	[$mol.m^{-3}$]
C_A	equilibrium concentration of component A	[$mol.dm^{-3}$]
C_B	concentration of reactant B	[$mol.m^{-3}$]
C_B	equilibrium concentration of component B	[$mol.dm^{-3}$]
$C_{Ca^{2+}}$	concentration of calcium ions	[$mol.dm^{-3}$]
C_{int}	solid-liquid interface concentration	[$mol.m^{-3}$]
c_0	bulk concentration	[m^{-3}]
C_0	concentration of nucleation sites	[$\#.m^{-3}$]
$C_{Ox^{2-}}$	concentration of oxalate ions	[$mol.dm^{-3}$]
C_{pi}^0	standard heat capacity	[$kJ.kg^{-1}.K^{-1}$]
C_s	concentration of the solid phase	[$mol.m^{-3}$]
C_{seeds}	seed concentration	[$g.dm^{-3}$]
D	diffusion coefficient	[$m^2.s^{-1}$]
$d_{1,0}$	number mean particle size	[µm]
$d_{4,3}$	volume mean particle size	[µm]
D_{lin}	rate of linear dissolution	[$m.s^{-1}$]
D_{meso}	turbulent diffusivity	[$m^2.s^{-1}$]
d_{stir}	impeller diameter	[m]
E	activation energy	[$J.mol^{-1}$]
f^*	attachment frequency	[s^{-1}]
f_s	surface shape factor	[-]
f_v	volume shape factor	[-]
g	kinetic order of the growth rate	[-]
g	gravitational acceleration	[$m.s^{-2}$]
G	growth rate	[$m.s^{-1}$]
$\Delta G_{i,T,P}^0$	standard Gibbs free energy	[$J.mol^{-1}$]
h	step height or height of a growth unit	[m]
H_i^0	standard enthalpy	[J]
I	ionic strength	[$mol.dm^{-3}$]
J	nucleation rate	[$m^{-3}.s^{-1}$]
J_{2D}	2D nucleation rate	[$m^{-3}.s^{-1}$]
k	Boltzmann constant	[$J.K^{-1}$]

K	constant	[-]
K	mass transfer coefficient	[m.s^{-1}]
k_a	area shape factor	[-]
k_d	mass transfer coefficient	[m.s^{-1}]
k_g	growth rate constant	[m.s^{-1}]
$K_{i,T,P}$	equilibrium constant of reaction i at temperature T and pressure P	[-]
k_L	length shape factor	[-]
k_N	nucleation rate parameter	[#.m^{-3}.s^{-1}]
k_r	growth rate parameter	[m.s^{-1}]
K_{sp}	solubility product	[mol.dm^{-3}]^2
k_v	volume shape factor	[-]
L	characteristic dimension	[m]
$\bar{L}_i$	arithmetic average of the upper and lower sizes of interval i	[m]
L_T	total length of particles	[m.m^{-3}]
M	molecular weight of substance	[kg.kmol^{-1}]
m	stoichiometric coefficient in Equation (2)	[-]
m_j	moments of the distribution	[-]
M_s	molar mass of the solid phase	[kg.mol^{-1}]
n	stoichiometric coefficient in Equation (2)	[-]
n	kinetic order of nucleation	[-]
n	number density distribution	[#.m^{-4}]
N	impeller speed	[s^{-1}]
N	particle number concentration	[#.m^{-3}]
N	total number of nuclei generated by nucleation	[#]
Δn	number of moles of substance deposited per unit volume	[kmol.m^{-3}]
$\dot{N}_1$	rate of change of crystal number in first size interval	[#.s^{-1}]
n^*	critical nucleus size	[#]
n_0	population density of nuclei	[#.m^{-4}]
N_P	power number	[-]
N_q	flow number	[-]
N_T	total number of particles	[#.m^{-3}]
P	power	[W]
P	pressure	[atm]
P_s	solubility product	[mol^2.m^{-6}]
Q	volumetric flow rate	[m^3.s^{-1}]
q_c	pumping capacity of the impeller	[m^3.s^{-1}]
R	universal gas constant	[J.mol^{-1}.K^{-1}]
r	ratio = $\sqrt[3]{2}$ in DPB	[-]
r	crystal growth kinetic order	[-]
r_{agg}	rate of aggregation	[m^3.s^{-1}]

Re	Reynolds number	[-]
r_N	nucleation rate	[#.m^{-3}.s^{-1}]
S	supersaturation ratio	[-]
S_c	concentration-based supersaturation ratio	[-]
S_i	initial supersaturation	[-]
S_i^0	standard entropy	[J.K^{-1}]
T	temperature	[K] or [°C]
t	time	[s]
t_c	circulation time	[s]
$T_{Ca^{2+}}$	total calcium ion concentration	[kmol.m^{-3}]
$T^0_{Ca^{2+}}$	total initial calcium ion concentration	[kmol.m^{-3}]
t_g	time for nucleus to grow to a detectable size	[s]
t_i	injection time	[s]
t_{ind}	induction time	[s]
t_{macro}	macro mixing time	[s]
t_{meso}	meso mixing time	[s]
t_{micro}	micro mixing time	[s]
t_n	time to achieve a quasi-steady-state distribution of molecular clusters	[s]
$T_{Ox^{2-}}$	total oxalate ion concentration	[kmol.m^{-3}]
$T^0_{Ox^{2-}}$	total initial oxalate ion concentration	[kmol.m^{-3}]
t_r	relaxation time	[s]
t_{res}	residence time	[s]
t_v	time interval between instant of supersaturation creation and crystal formation observable to the naked eye	[s]
u	feed flow velocity	[m.s^{-1}]
V	volume of the reactor/liquid volume	[m^3]
V_i^0	standard molecular volume	[m^3.mol^{-1}]
v_{step}	step velocity	[m.s^{-1}]
V_T	total volume of particles	[m^3.m^{-3}]
V_{tube}	volume of the nucleation tube	[m^3]
W^*	nucleation work	[J]
W_0	initial seed concentration	[kg.m^{-3}]
W_t	solids concentration	[kg.m^{-3}]
x	film thickness	[m]
z	Zeldovich factor	[-]
z_i	charge on component i	[-]

Greek Symbol	**Definition**	**Units**
α^+	ionic charge for component A	[-]
α_v	detectable volume/mass fraction of new crystalline phase in solution	[-]

$\beta(L,\lambda)$	aggregation rate constant/aggregation kernel	[$m^3.s^{-1}$]
β^-	ionic charge for component B	[-]
β_{aggl}	aggregation rate constant	[$m^3.s^{-1}$]
β_{coll}	collision rate constant	[$m^3.s^{-1}$]
β_{disr}	disruption kernel	[$m.s^{-1}$]
β_0	size-independent aggregation kernel	[$m^3.s^{-1}$]
γ	interfacial energy	[$J.m^{-2}$]
γ	shear rate	[s^{-1}]
$\gamma^{\pm}$	stoichiometric mean activity coefficient	[-]
$\gamma_{Ca^{2+}}$	calcium ion activity coefficient	[-]
γ_{ef}	effective interfacial energy	[$J.m^{-2}$]
$\gamma_{Ox^{2-}}$	oxalate ion activity coefficient	[-]
$\delta(L)$	Dirac delta function	[-]
ε	local energy dissipation rate	[$m^2.s^{-3}$]
$\bar{\varepsilon}$	average energy dissipation rate	[$m^2.s^{-3}$]
λ	characteristic dimension	[m]
Λ	macroscale turbulence	[m]
μ	chemical potential	[J]
μ	dynamic viscosity	[$kg.m^{-1}.s^{-1}$]
$\Delta\mu$	change in chemical potential	[J]
μ_c	chemical potential of a molecule in crystal phase	[J]
μ_0	standard potential	[J]
μ_s	chemical potential of a molecule in solution	[J]
ν	kinematic viscosity	[$m^2.s^{-1}$]
ν	number of ions in a formula unit of a salt	[-]
$\nu_{i,j}$	stoichiometric coefficient of species j in reaction i	[-]
v_0	molecular volume	[m^3]
ρ	density	[$kg.m^{-3}$]
ρ_c	density of the solid phase	[$kg.m^{-3}$]
σ	relative supersaturation	[-]
τ	residence time	[s]
ϕ_s	surface shape factor	[-]
ϕ_v	volumetric shape factor	[-]
ψ	crystal size distribution density function	[$\#.m^{-4}$]
ψ	collision efficiency	[-]

Chapter 1

INTRODUCTION

1.1 Background to Dissertation

Precipitation is a widely used industrial process utilized in the manufacture of photographic chemicals, pharmaceuticals, paints and pigments, polymers, plastics and the production of ultrafine powders (Mullin, 2001). Precipitation may be defined as a process which embodies fast crystallization (Sohnel & Garside, 1992) and can be identified by the following features (Giulietti *et al.*, 2001):

(i) Formation of a slightly soluble compound.
(ii) Generation of supersaturation by chemical reaction.
(iii) Fast processing.
(iv) Production of small particles.

Precipitation processes take place rapidly as a consequence of the high supersaturations involved. The supersaturation necessary for precipitation to occur is quite frequently obtained by way of a chemical reaction thus precipitation is commonly referred to as reactive crystallization. Sparingly soluble substances can easily exhibit high levels of supersaturation due to their low solubility products and thus precipitation is an active process for these substances (Jones, 2002). Nucleation is a significant mechanism in precipitation processes as it occurs at high supersaturations. The characteristically high nucleation rates in precipitation processes result in the production of a large number of particles which limits the average size to which individual particles can grow (Sohnel & Garside, 1992). Thus growth is generally not a key mechanism in processes containing insoluble compounds. Because of the high nucleation rates the particle concentration is usually very high, typically 10^{11}-10^{16} particles.cm^{-3}, and the particle size is usually relatively small i.e. 0.10-10μm (Sohnel & Garside, 1992). Furthermore, secondary processes such as ripening, ageing, agglomeration, coagulation and breakage may occur due to the sufficiently small size of the precipitated particles. These secondary processes can change the particle morphology and particle size distribution (PSD) quite considerably. Thus it is important to gain a sound fundamental understanding of precipitation systems so that new processes can be designed and optimized and the nature of a desired product can be controlled.

1.2 Scope and Context of the Work

For industrial precipitation processes, the properties of the individual particles (e.g. size, shape and microstructure) and the bulk properties (e.g. chemical composition, PSD, specific surface area and density) are important aspects of the production process (Ntuli & Lewis, 2009). These parameters are determined by the overall precipitation kinetics which are governed by the relative rates and mechanisms of the kinetic processes of nucleation, growth, aggregation and breakage (Sohnel & Garside, 1992). Thus, in order to control the particle properties one needs to identify the kinetic mechanisms active during the precipitation process.

Numerous methods can be found in the literature for measuring and predicting the rates of nucleation, crystal growth and, to a lesser extent, secondary processes such as aggregation and breakage. These techniques are generally specific to the chemistry and operating conditions of the system and thus cannot be directly used for any process. As of yet, there has not been much work conducted on developing generic models. Also, in the modelling of crystallization processes, it is possible to make the assumption of perfect mixing which simplifies the problem considerably. It is also possible to confine the mechanisms to nucleation and growth only. However, neither of these assumptions is valid in precipitation problems, which makes them highly non-linear and more difficult to solve.

Thus, the scope of the current work involves investigating the behaviour and kinetic mechanisms involved in the precipitation of a moderately soluble system at different operational conditions. The active mechanisms will be determined from PSDs and SEM photographs. The experimental kinetic method of Bramley *et al.* (1996) will be used to determine the growth and aggregation kinetics of a moderately soluble system. The kinetics will be determined from the measurement of experimental PSDs and the extraction of the rate constants from the calculated moments. The induction period will be determined from solution conductivity profiles. The final aspect of the dissertation will be to determine whether the method of Bramley *et al.* (1996) can be utilized for more insoluble systems by using the results from the experimental and modelling work.

1.3 Summary of Dissertation Structure

The dissertation begins with a comprehensive literature review detailing the thermodynamics and kinetics of precipitation processes and the different mechanisms involved. Also included in the literature review are sections on: mixing strategies, mixing times and scales, seeding, particle size analysis techniques and thermodynamic and kinetic modelling. Various methods found in literature for determining the induction time, nucleation, growth and aggregation kinetics are also reviewed. The chosen moderately soluble system is reviewed with information regarding the physical and chemical properties as well as the kinetics and mechanisms involved in the precipitation of the compound. The literature review chapter is concluded with a statement of the objectives and formulation of the key questions.

After the literature review three chapters follow i.e. (i) Preparation of seeds for a moderately soluble system, (ii) Determination of the growth and aggregation kinetics and (iii) Determination of the induction time, which encompass the main body of work. Each of these chapters includes materials and methods, results, discussion and preliminary conclusions sections. The main body of the dissertation ends with a final conclusions and recommendations chapter where the conclusions from the previous three chapters are tied together. The appendices, which can be found at the end of the dissertation, include additional results from Chapters 3 & 4, raw data, sample calculations and the faculty ethics form.

Chapter 2

THEORY AND LITERATURE REVIEW

2.1 Precipitation Thermodynamics and Kinetics

2.1.1 Supersaturation and Solubility

Solubility may be defined as the amount of solute required to make a saturated solution at a given condition (Myerson, 2002). Precipitation from solution occurs when the solute concentration in a solvent exceeds its solubility yielding a so-called supersaturated solution. Supersaturation may also be created when a very insoluble product is produced from the reaction between two or more soluble reactants. An equilibrium phase diagram or solubility-supersolubility plot (Figure 1 below) shows the solubility line and different regions of saturation. In the undersaturated or stable region all particles present will dissolve and no precipitation will occur. The metastable region is a supersaturated zone in which spontaneous crystallization is improbable (Mullin, 2001). However, particle growth is possible if a seed were to be placed within the "metastable" solution. The width of the metastable region depends on the degree of agitation, concentration of crystalline solids in suspension, and the degree to which other solutes are present in solution (Randolph & Larson, 1988). In the labile or unstable region spontaneous nucleation is probable, but not inevitable.

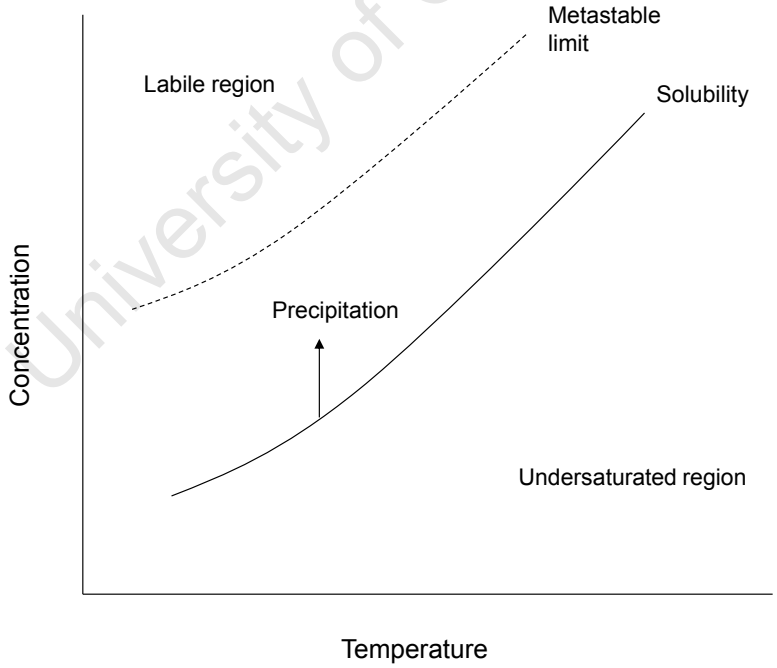

Figure 1: Solubility-supersolubility diagram (adapted from Jones, 2002)

The solubility diagram is significant in the present work as it allows for the determination of the operating region of the chosen system. This is very important in a system where nucleation must be hindered i.e. in order to hinder nucleation in the process the system must be within the metastable region and reasonably close to the solubility line. If the system is too close to the metastable limit i.e.

labile region the chance of spontaneous nucleation is much higher. Seed crystals may however still grow within the metastable region.

Solubilities of sparingly soluble substances are usually represented as solubility products from which the concentrations of the individual species in a saturated solution can be determined. The thermodynamic solubility product of a compound dissociating in solution according to

$$A_mB_n(s) \leftrightarrow mA^{\alpha+} + nB^{\beta-} \quad \ldots (1)$$

is defined by the following equation

$$K_{sp} = a_A^m \cdot a_B^n = \gamma^{\pm(m+n)} C_A^m \cdot C_B^n \quad \ldots (2)$$

where a_A is the equilibrium activity of component A

a_B is the equilibrium activity of component B

$\gamma^{\pm}$ is the activity coefficient

C_A is the equilibrium concentration of component A [mol.dm^{-3}]

C_B is the equilibrium concentration of component B [mol.dm^{-3}]

m & n are stoichiometric coefficients

α^+ & β^- are the ionic charges for components A and B respectively

Supersaturation is the key variable in any precipitation process with the level of supersaturation in the precipitating solution governing the rates of the different processes (Sohnel & Garside, 1992). Figure 2 highlights how supersaturation and the precipitation process are linked.

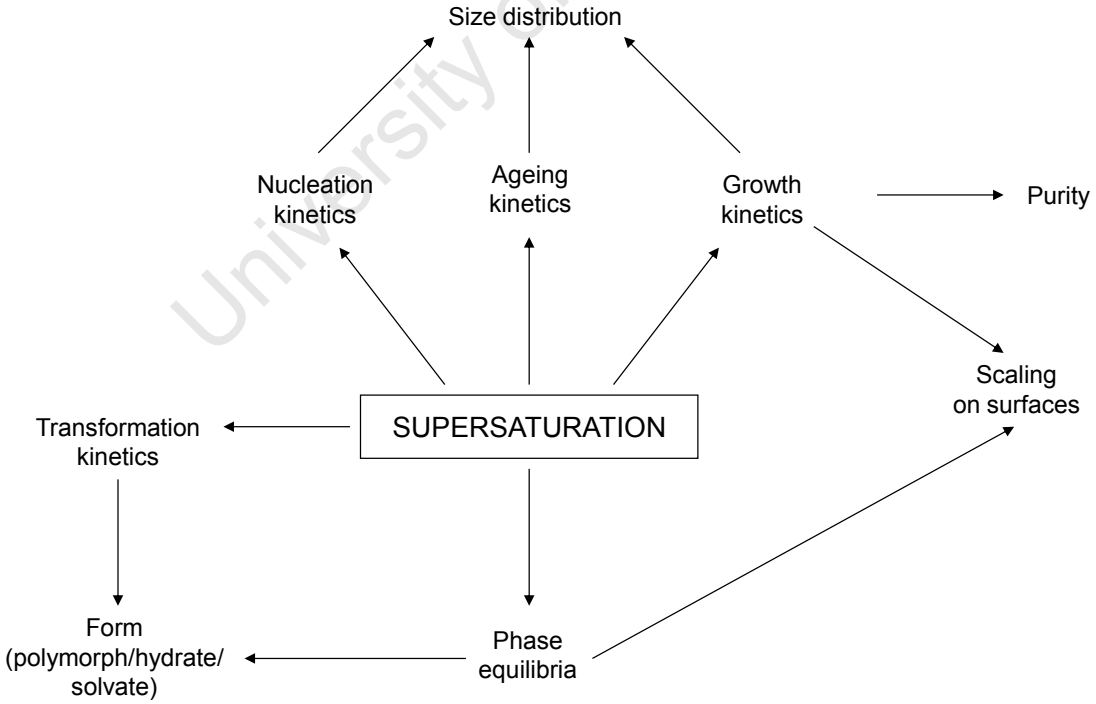

Figure 2: The role of supersaturation in precipitation processes (Sohnel & Garside, 1992)

According to Myerson (2002), there are four main ways to create supersaturation. These include:

i. Temperature change
ii. Evaporation of solvent

iii. Chemical reaction
iv. Changing the solvent composition

In the present work chemical reaction will be the method of creating supersaturation.

The driving force for a crystallization process is the difference in Gibbs free energy between the actual condition of the system and the equilibrium condition (Roelands *et al.*, 2006). For a one-component crystal in liquid solution under isothermal and isobaric conditions, the thermodynamic driving force for precipitation i.e. supersaturation, $\Delta\mu$, is given by

$$\Delta\mu = \mu_s - \mu_c \quad \ldots (3)$$

where μ_s and μ_c are the chemical potentials of a molecule in solution and in the bulk of the crystal phase, respectively (Roelands *et al.*, 2006). Physically, the supersaturation is the gain in free energy per molecule (or atom) associated with the passage of the phase from the minimum with higher Gibbs free energy to the minimum with lower Gibbs free energy (Kashchiev, 2000). When $\Delta\mu > 0$, the system is supersaturated and nucleation and growth are possible. The chemical potential, μ, is defined in terms of the standard potential, μ_0, and the activity, a, by

$$\mu = \mu_0 + RTlna \quad \ldots (4)$$

where R is the universal gas constant and T is the absolute temperature. The fundamental dimensionless driving force for crystallization may therefore be expressed as (Mullin, 2001)

$$\frac{\Delta\mu}{RT} = ln\left({}^{a}/_{a^*}\right) = ln(S) \quad \ldots (5)$$

where a^* is the activity of a saturated solution and S is the fundamental supersaturation, i.e.

$$S = exp\left({}^{\Delta\mu}/_{RT}\right) \quad \ldots (6)$$

For practical purposes supersaturations are generally expressed directly in terms of solution concentrations. The most common expressions of supersaturation are the concentration driving force, Δc, the supersaturation ratio, S_c, and the relative supersaturation, σ (Mullin, 2001). These quantities may be expressed as follows

$$\Delta c = c - c^* \quad \ldots (7)$$

$$S_c = \frac{c}{c^*} \quad \ldots (8)$$

$$\sigma = \frac{\Delta c}{c^*} = S_c - 1 \quad \ldots (9)$$

where c is the solution concentration and c^* is the equilibrium saturation at a given temperature. The relationship between the concentration-based supersaturation and the fundamental (activity-based) supersaturation is as follows

$$S = S_c A \quad \ldots (10)$$

where $A = {}^{\gamma}/_{\gamma^*}$ is the ratio of the activity coefficients. According to Mullin (2001), supersaturations in aqueous solutions of sparingly soluble electrolytes are best expressed in terms of the solubility product

$$S = \left({}^{IAP}/_{K_{sp}}\right)^{\frac{1}{\nu}} \quad \ldots (11)$$

where IAP is the ionic activity product of the lattice ions in solution, K_{sp} is the activity solubility product of the salt (i.e. the value of IAP at equilibrium) and ν is the number of ions in a formula unit of the salt. Using the notation from Equation (1), Equation (11) can be further expanded to

$$S = \left(\frac{a_A^m \cdot a_B^n}{K_{sp}}\right)^{\frac{1}{(m+n)}} = \gamma^{\pm}\left(\frac{C_A^m \cdot C_B^n}{K_{sp}}\right)^{\frac{1}{(m+n)}} \quad \ldots (12)$$

For ideal solutions the activity coefficient can be assumed to be equal to unity whereas for other situations it must be calculated using the appropriate equations e.g. Bromley's method. The ionic strength of a solution, required in the calculation of the activity coefficient, can be determined from

$$I = 0.5 \sum_i C_i z_i^2 \quad \ldots (13)$$

where z is the charge on component i.

Precipitation consists of many individual steps and kinetic processes that are illustrated in Figure 3 below. There are three processes by which precipitation of both soluble and sparingly soluble substances generally occurs. These are:

i. Particle nucleation
ii. Particle growth
iii. Secondary changes (e.g. agglomeration, ageing and recrystallization)

Both nucleation and growth consume supersaturation and therefore conditions favouring rapid nucleation quickly deplete supersaturation thus resulting in negligible growth (Ntuli & Lewis, 2009). Furthermore, growth will be favoured by conditions that suppress nucleation.

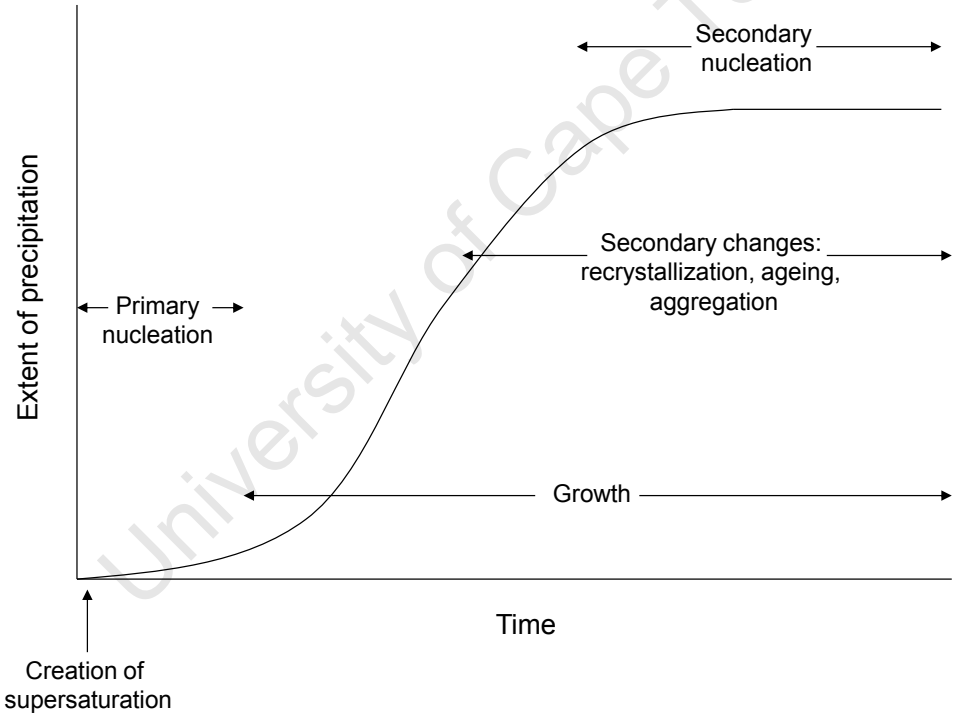

Figure 3: Kinetic processes involved in precipitation (Sohnel & Garside, 1992)

A discussion of the above processes, including the mechanisms and kinetics, is presented within the following sections of the report.

2.1.2 Nucleation

Kaschiev (2000) defined nucleation as: *"The process of random generation of those nanoscopically small formations of the new phase that have the ability for irreversible overgrowth to macroscopic sizes"*. In more general terms, nucleation is the formation of new nuclei that will grow to form the solid

phase and can occur by way of primary or secondary mechanisms. Primary nucleation is characterized as the spontaneous production of nuclei. Secondary nucleation, however, requires the presence of a metastable solution plus some source of “shock” or “seed” for nuclei to form. There are two types of primary nucleation: homogeneous nucleation (HON) and heterogeneous nucleation (HEN). In homogeneous nucleation a new solid phase is spontaneously formed without there being contact with another phase or molecular species. In heterogeneous nucleation the formation of a new solid phase is brought about by the presence of a foreign solid phase such as dust or apparatus surfaces e.g. the reactor walls or impeller. The rate of heterogeneous nucleation depends on both the supersaturation and on the availability of active nucleation sites. In secondary nucleation the formation of solid particles are initiated by the presence of solid material of the same precipitating substance. These parent crystals have a catalyzing effect and therefore result in nucleation at a lower supersaturation than for spontaneous nucleation (Myerson, 2002). Secondary nucleation occurs by way of a number of crystal surface phenomena which are a function of the agitation of the growing particles. Figure 4 shows the various forms of nucleation.

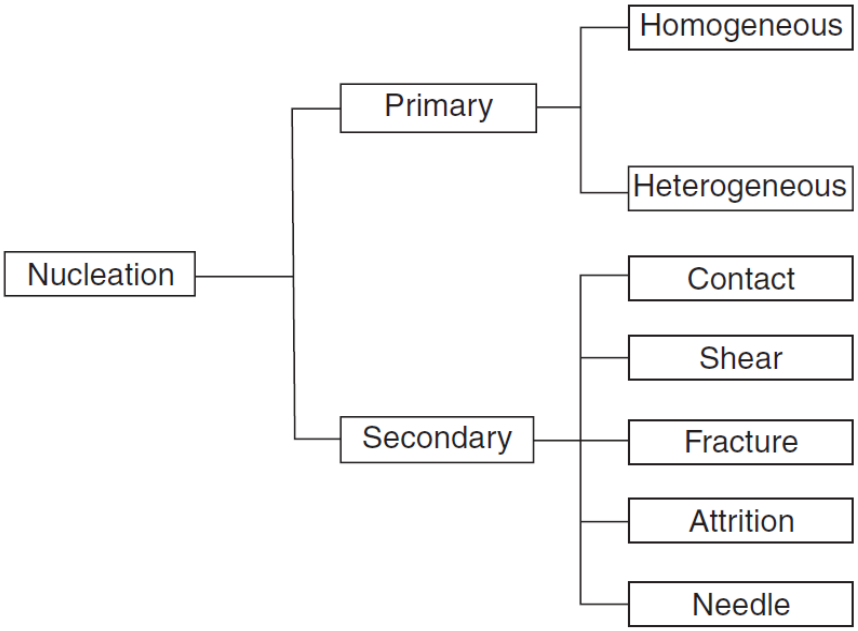

Figure 4: Mechanisms responsible for nucleus formation (Randolph & Larson, 1988)

According to Randolph & Larson (1988), the critical nucleus size, n^*, is such that to grow clusters of crystals with a size smaller than n^* requires an increase in free energy, while growth clusters larger than n^* will result in a decrease in free energy. It is presumed that in supersaturated solutions, solute clusters are constantly forming and dispersing but only those exceeding size n^* result in viable nuclei and thus contribute to the nucleation process (Randolph & Larson, 1988). Both the activation energy and n^* decrease as the supersaturation increases. This thus increases the probability that a nucleus will be formed. For a spherical nucleus, the critical nucleus size and the nucleation work, W^*, can be derived from the condition, $\frac{dW}{dn} = 0$ for $n = n^*$ (Roelands *et al.*, 2006). The critical nucleus size can be determined from the Gibbs-Thompson equation and the nucleation work can be determined as follows

$$n^* = \frac{32\pi v_0^2 \gamma^3}{3(kT)^3 (lnS)^3} \quad \text{... (14)}$$

$$W^* = \frac{16\pi v_0^2 \gamma^3}{3(kT)^2(lnS)^2} = \frac{1}{2} n^* kTln(S) \quad \text{... (15)}$$

where v_0 is the molecular volume [m^3] and γ is the interfacial energy [$J.m^{-2}$]. The nucleation rate, $J(t)$, can be derived for three states, namely, the equilibrium, stationary and non-stationary states. For the equilibrium state: $J(t) = 0$, for the stationary state: $J(t)$ is constant, and for the non-stationary state: $J(t)$ changes with time. According to the Classical Nucleation Theory (CNT) the stationary nucleation rate, J [$m^{-3}.s^{-1}$], is the frequency of the appearance of a stable cluster per unit volume at time t (Kashchiev, 2000) and can be represented by

$$J = zf^*C^* \quad \text{… (16)}$$

where z is the Zeldovich factor, f^* is the attachment frequency [s^{-1}], and C^* is the equilibrium concentration of nuclei [m^{-3}], which can be represented by

$$C^* = C_0 exp\left(-\frac{W^*}{kT}\right) \quad \text{… (17)}$$

where C_0 is the concentration of nucleation sites. The stationary nucleation rate, applicable to any type of nucleation, can finally be represented by

$$J = A' exp\left(-\frac{W^*}{kT}\right) \quad \text{... (18)}$$

where $A' = zf^*C_0$ [$m^{-3}.s^{-1}$ or $m^{-2}.s^{-1}$] is an essentially kinetic quantity accounting for the concrete kinetic and spatial peculiarities in each specific nucleation case (Kashchiev, 2000). According to Kashchiev (2000), the pre-exponential factor is usually in the range of A' = 10^{13} to 10^{41} $m^{-3}.s^{-1}$ or 10^8 to 10^{31} $m^{-2}.s^{-1}$, where the smaller values are indicative of the presence of active centres, seeds etc. in the system and/or a lower frequency of monomer attachment to the nuclei.

For the particular case of classical HON or 3D HEN in vapours or solutions with $S \geq 1$, the stationary nucleation rate can be described by CNT as

$$J = ASexp\left({}^{-B}/_{(lnS)^2}\right) \quad \text{… (19)}$$

where the dimensionless thermodynamic parameter, B, is characterized by

$$B = \frac{16\pi v_0^2 \gamma_{ef}^3}{3(kT)^3} \quad \text{… (20)}$$

$\gamma_{ef} = \gamma$ for HON and $\gamma_{ef} < \gamma$ for 3D HEN in the volume of the solution or on the surface of a foreign substrate. Equation (19) indicates that three main parameters govern the nucleation rate: (i) degree of supersaturation, (ii) temperature, and, (iii) interfacial tension (Mullin, 2001). The kinetic parameter, A [$m^{-3}.s^{-1}$], for homogenous nucleation can be estimated for either volume-diffusion or interface-transfer control as follows

$$A_{HON,D} = \left(\frac{kT}{v_0^2 \gamma}\right)^{\frac{1}{2}} Dc_0 ln(S) \quad \text{… (21)}$$

$$A_{HON,I} = \left(\frac{4\pi}{3v_0}\right)^{\frac{1}{3}} \left(\frac{\gamma}{kT}\right)^{\frac{1}{2}} Dc_0 \quad \text{… (22)}$$

where D is the diffusion coefficient [$m^{-2}.s^{-1}$] and c_0 is the bulk concentration [m^{-3}]. As for A', the smaller values of A are indicative of the presence of foreign particles in the system i.e. heterogeneous nucleation while the higher values are typical of homogeneous nucleation (Mangere *et al.*, 2009). Typically, A_{HON} ~ 10^{35} $m^{-3}.s^{-1}$ while A_{HEN} ~ 10^{15}-10^{25} $m^{-3}.s^{-1}$ (Kashchiev & van Rosmalen, 2003). Equation (19) is based on the assumption of spherical particles, thus for other particle shapes the nucleation rate can be determined from

$$J = ASexp\left(\frac{-4f_s^3 v_0^2 \gamma_{ef}^3}{27 f_v^2 (kT)^3 (lnS)^2}\right) \quad \text{... (23)}$$

where f_s and f_v are the surface and volume shape factors respectively (Kuldipkumar *et al.*, 2007).

2.1.2.1 Induction Time

The time elapsed from the creation of the initial supersaturation (by mixing two reacting solutions) to the detection of the first crystals formed in the solution is termed the induction period, t_{ind} (Jones, 2002). The induction time is a measure of the ability of the system to remain in metastable equilibrium (Kashchiev, 2000) and is an experimentally measurable quantity. According to Roelands *et al.* (2006), the accuracy of the induction period depends not only on the nucleation rate but also on the growth rate of the crystals, on the applied observation technique, and its detection limit. Thus, because different experimental techniques detect the first nuclei with a resolution specific to that technique, t_{ind} may not have the same value (Kashchiev, 2000). Myerson (2002) stated that with an increasing agitation rate at constant supersaturation, t_{ind} decreases up to a certain critical agitation rate, beyond which it remains unchanged. Thus, it is important to establish this critical agitation rate for a specific supersaturation so that the determined induction time is accurate. Also, in the case of very fast chemical reactions, high reactant concentrations, and/or a diffusion-controlled precipitation reaction the induction period becomes too short to be measured accurately. Therefore, if the induction period is shorter than the mixing period, mixing becomes a process-controlling factor.

The induction period may be assumed to consist of a number of parts i.e.

$$t_{ind} = t_r + t_n + t_g \quad \text{... (24)}$$

where t_r represents the relaxation time, t_n is the time required for the system to achieve a quasi-steady-state distribution of molecular clusters, and, t_g is the time required for the nucleus to grow to a detectable size (Mullin, 2001). However it is difficult to determine or even predict these separate quantities, thus the induction time is usually evaluated as a whole.

The induction period has been used experimentally to determine the nucleation rate using the following simple relationship

$$J = \frac{K}{t_{ind}} \quad \text{... (25)}$$

where K is a constant. Over limited ranges of supersaturation, the nucleation rate can be expressed as

$$J = k_N S^n \quad \text{... (26)}$$

where k_N is the nucleation rate constant and n is the kinetic order of nucleation (Myerson, 2002). By combining Equations (25) and (26), an expression for the induction time in terms of supersaturation can be obtained as follows

$$t_{ind} = \left(\frac{K}{k_N}\right) S^{-n} \quad \text{... (27)}$$

Equation (27) has been used to characterize the mechanism of nucleation i.e. homogeneous or heterogeneous. Many other equations exist for relating the induction time to both the nucleation and/or growth rates. One of these equations is for situations where it is assumed that the system is brought out of metastable equilibrium at the same moment when the first nucleus appears, and is represented by

$$t_{ind} = {}^{1}/_{JV} \quad \text{... (28)}$$

where V is the liquid volume. This is termed the "mononuclear" mechanism. For systems where metastability is lost as a result of the progressive appearance of many nuclei and their growth to macroscopically large sizes or "polynuclear" mechanism, the induction time is expressed as

$$t_{ind} = \left(\frac{3\alpha_v}{\pi G^3 J}\right)^{1/4} \quad \text{... (29)}$$

where α_v is the detectable volume or mass fraction of the new crystalline phase formed in solution (Kashchiev & van Rosmalen, 2003). Although it may be easier to indirectly calculate the nucleation rate from induction time measurements, it is generally more accurate to determine the nucleation rate directly from counting techniques.

According to Myerson (2002) certain precipitating systems exhibit different slopes when the empirical dependence of $logt_{ind}$ versus $logS$ is plotted. Figure 5 below shows three distinctive regions:

i. Region I – At low supersaturations, heterogeneous nucleation is the dominant mechanism.
ii. Region III – At high supersaturations, homogeneous nucleation is the dominant mechanism.
iii. Region II – An intermediate region in which both heterogeneous and homogeneous nucleation mechanisms may coexist.

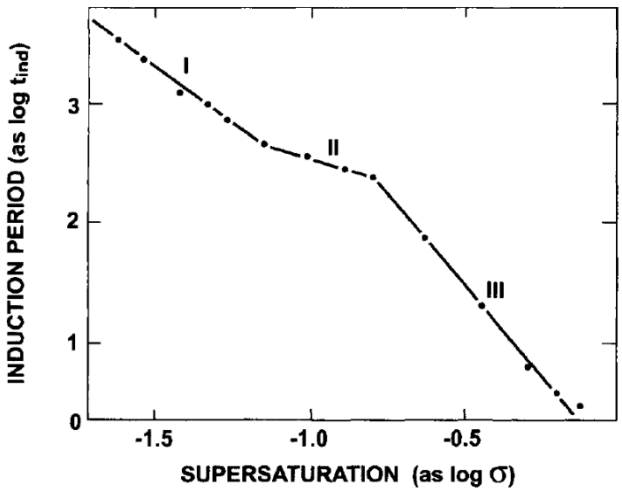

Figure 5: Empirical dependence of induction period of $Ni(NH_4)_2(SO_4)_2.6H_2O$ at 25°C on relative supersaturation in logarithmic coordinates (Sohnel & Mullin, 1979, cited in Myerson, 2002)

Mullin (2001) stated that the induction period can be considered to be inversely proportional to the nucleation rate

$$t_{ind} \propto J^{-1} \quad \text{... (30)}$$

Using this assumption, the classical nucleation relationship (Equation 19) may be re-written as

$$logt_{ind} \propto \left[\frac{\gamma^3}{T^3(logS)^2}\right] \quad \text{... (31)}$$

It can be inferred from Equation (31) that an increase in the supersaturation will result in a decrease in the induction time. Equation (31) suggests that, at a specific temperature, a plot of $logt_{ind}$ versus $(logS)^{-2}$ will yield a straight line (Mullin, 2001). The slope of the line would allow for the calculation of the interfacial tension however this is only viable for the case of true homogeneous nucleation. Figure 6 below shows an example of this relationship where the change in slope of the $CaCO_3$ line indicates a transition from homogeneous to heterogeneous nucleation (inferred by a change in the surface tension).

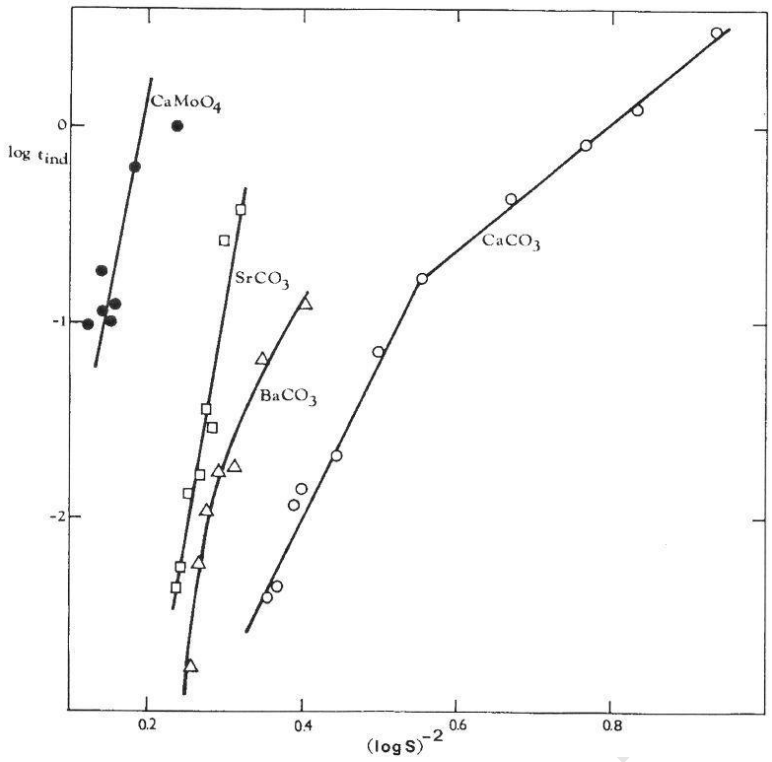

Figure 6: Induction period as a function of initial supersaturation for a number of precipitating systems at 25°C (Sohnel & Mullin, 1978)

2.1.3 Particle Growth

Particle growth from solution is characterized by the transportation of the solute to the particle surface and then the orientation of the solute into the crystal lattice. Two successive steps are required:

i. Diffusion, and,
ii. Surface reaction or particle integration

It is possible for either diffusion, surface reaction or a combination of the two to be the rate limiting step in the process. However, according to Collier & Hounslow (1999), if the crystals are sparingly soluble, quite small, or are in a well-mixed suspension, the diffusion of material to the surface will be rapid, and the surface reaction is likely to be the rate limiting step.

2.1.3.1 Diffusion-Controlled Growth

Diffusion-controlled growth is when the growth rate is limited by the rate of diffusion through a laminar layer of solution. This mechanism is generally significant in systems in which there is no agitation. The growth rate can thus be represented by a simple mass transfer equation

$$\frac{dM}{dt} = \left(\frac{D}{x}\right) A(C - C^*) \quad \text{... (32)}$$

where D is the diffusion coefficient, x is the film thickness, A is the surface area of the particle, and $(C - C^*)$ is the difference between the actual concentration and the saturation concentration (Randolph & Larson, 1988). As x is generally not known, a mass transfer coefficient, K, can be substituted in place of it, yielding

$$\frac{dM}{dt} = KA(C - C^*) \quad \text{... (33)}$$

Also, particles are generally sized on the basis of diameter rather than mass therefore Equation (33) can be recast in the following form as

$$\frac{dL}{dt} = \left(\frac{Kk_a}{3k_v\rho}\right)(C - C^*) \quad \text{... (34)}$$

where the growth rate is given a characteristic dimension, L, k_v and k_a are the volume and area shape factors respectively, and ρ is the density [kg.m^{-3}] (Randolph & Larson, 1988). When growth is diffusion controlled, it will increase as the velocity of the supersaturated solution is increased relative to the crystal surface. As the velocity is increased further, a point will be reached where an increase in the velocity no longer increases the growth rate. This point represents that the growth is now surface-integration controlled.

2.1.3.2 Surface-Integration Controlled Growth

The rate of growth of this mechanism is governed by the supersaturation and the mechanism of solute integration with the crystal surface. The most common expression relating the growth rate to the supersaturation is the following empirical equation

$$G = k_g\sigma^g \quad \text{... (35)}$$

where G is the linear crystal growth rate [m.s^{-1}], k_g is the growth rate constant, and g is the kinetic order of growth. A number of possible surface growth mechanisms have been postulated with the most commonly controlling mechanisms being:

i. Rough growth
ii. Birth and Spread growth (2D nucleation model)
iii. Spiral growth (Burton-Cabrera-Frank (BCF) model)

The rough growth mechanism generally occurs at high supersaturations where the growth units attach at any point on the crystal surface e.g. terraces, steps or kinks and as a result the crystal surface becomes rough (see Figure 7) (Giulietti *et al.*, 2001). Due to the high supersaturation the rough growth mechanism is linear in nature and can be represented by the following equation

$$G = k_g\sigma \quad \text{... (36)}$$

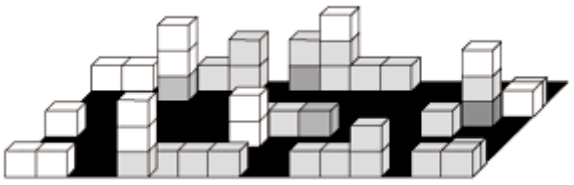

Figure 7: Crystal growth by the rough growth mechanism (Giulietti *et al.*, 2001)

At medium supersaturations, growth generally occurs by way of two-dimensional (2D) nucleation on the crystal surface. This 2D nucleation generates the necessary kinks for further growth to be achieved (see Figure 8). When the growth rate of the 2D nuclei is high in comparison to the nucleation rate, a smooth surface is produced. However, at higher supersaturations, the nucleation rate dominates resulting in a rough surface (Giulietti *et al.*, 2001).

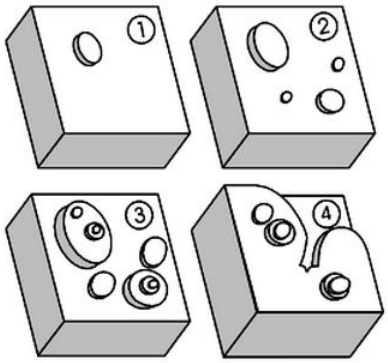

Figure 8: Crystal growth by the birth and spread mechanism (Giulietti *et al.*, 2001)

The 2D nucleation model can be represented by the following equation

$$G = \left(\frac{1}{3}\pi v_{step}^2 J_{2D}\right)^{\frac{1}{3}} h \quad \text{... (37)}$$

where v_{step}^2 is the step velocity, J_{2D} is the 2D nucleation rate, and, h is the step height or height of a growth unit. Thus, the birth and spread growth mechanism can be approximated by an exponential equation

$$G = k_g (S-1)^{\frac{2}{3}} S^{\frac{1}{3}} e^{-\frac{J_{2D}}{3lnS}} \quad \text{... (38)}$$

which can be further simplified to

$$G = k_g \sigma^{\frac{5}{6}} e^{-\frac{J_{2D}}{3\sigma}} \quad \text{... (39)}$$

At low supersaturations, growth units are only incorporated at kinks on the crystal surface resulting in spiral growth. This happens by way of the generation of a defect on the surface which proceeds in layer upon layer growth such that a spiral dislocation is formed (see Figure 9). The spiral is self-propagating and thus never dies. As a result, the crystal surface is smooth at an atomic level (Giulietti *et al.*, 2001). The BCF relationship may be represented as

$$G = A\sigma^2 \tanh\left({}^{B}/_{\sigma}\right) \quad \text{... (40)}$$

where A and B are temperature-dependent constants. At low supersaturations the BCF model is parabolic in nature and can be represented by

$$G = k_g \sigma^2 \quad \text{... (41)}$$

At high supersaturations, however, the BCF model approximates a linear growth law (Equation 36).

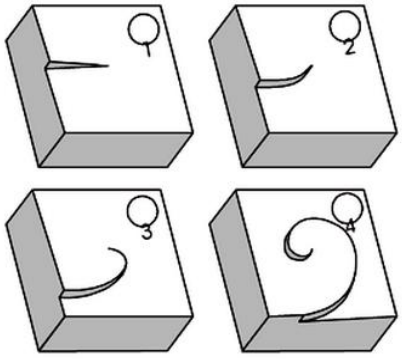

Figure 9: Crystal growth by screw dislocations (Giulietti *et al.*, 2001)

The three most common surface growth mechanisms are represented in Figure 10 below.

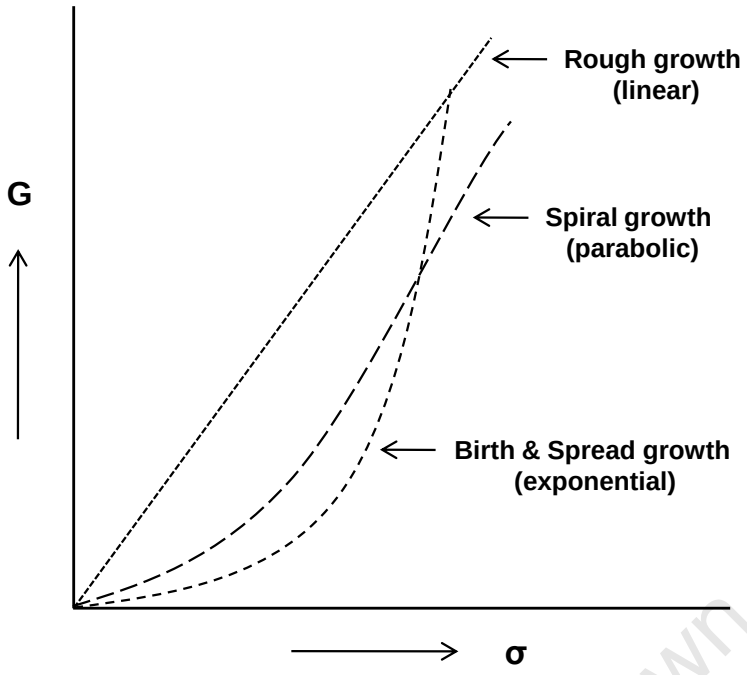

Figure 10: Comparison of the three surface growth mechanisms (Lewis & van Rosmalen, 2010)

The active growth mechanism can be found by the experimental determination of the growth kinetics and microscopic evaluation of the crystals. The most commonly found mechanism is that of spiral growth (Giulietti *et al.*, 2001). Andreassen & Hounslow (2004) stated that the growth rate of sparingly soluble salts is often found to be surface reaction controlled, quite often following the parabolic relationship of Equation (41). For precipitation from solution, the McCabe ΔL law suggests that the linear rate of particle growth is size-independent (Bramley *et al.*, 1996). McCabe's ΔL law states that all particles of the same substance growing under the same conditions should grow at the same rate (Sohnel & Garside, 1992). This is based on the assumption that the particles are growing from a pure binary mixture under conditions where the system is not influenced by outside factors thus the growth rate is a function of supersaturation only. This however has been found to not always be true. According to Giulietti *et al.* (2001) the rough regime should be avoided as far as possible as it results in excessive secondary nucleation. The small crystals formed by secondary nucleation have varying degrees of mechanical stress and have lower rates of growth than larger crystals. However, these crystals tend to "heal" as they grow which results in their growth behavior becoming similar to that of larger crystals. Giulietti *et al.* (2001) stated that this behavior highlights two crystal growth phenomena:

(i) Growth rate dispersion – different individual crystals have varying rates of growth.

(ii) Size-dependent growth – smaller crystals grow slower than large ones.

2.1.4 Aggregation and Other Secondary Processes

2.1.4.1 Aggregation

An agglomerate is generally characterized as the formation of a mass by the cementation of individual particles as a result of the chemical forces between the particles. On the contrary, an aggregate is a mass formed of mixtures of particulate and agglomerate particles which have a binding force intermediate between agglomerates and flocculates (Randolph & Larson, 1988). In an

agitated solution, particles are drawn together by van der Waals forces which cause them to form aggregates. In supersaturated solutions new crystal bonds are formed between particles which cause them to be cemented together as agglomerates. These two terms (aggregate & agglomerate) however are generally used interchangeably and have come to exhibit a similar definition i.e. the joining of two particles via a crystal bridge to form a single larger particle.

The rate of agglomeration is dependent on a number of parameters (Giulietti *et al.*, 2001):

(i) Mixing (energy dissipation) – a higher energy dissipation rate generally yields a higher agglomeration rate due to the increase in particle collisions, however there exists a maximum value after which the agglomeration rate decreases (see below).

(ii) Supersaturation – a high supersaturation decreases the time needed for the binding of particles, thus aiding agglomeration.

(iii) Solids concentration – this also increases the collision frequency thus increasing the rate of agglomeration.

(iv) pH – this has a very strong effect on the surface potential. Every compound has a value for the pH where the particle surface is electrically neutral (the isoelectric point). At this pH, the agglomeration rate is the highest due to there being no particle-particle repulsion.

(v) Ionic strength – a high ionic strength depresses the laminar double layer of the particles, thus stimulating the agglomeration process.

Deviating opinions about the basic principles of the aggregation process have been found in recent literature on the effect of growth rate and stirrer speed on aggregation in precipitation processes. Two particles will join together due to the ortho-kinetic collision frequency between them however the success of the aggregation event is dependent on the growth-controlled cementation (Andreassen & Hounslow, 2004). High shear rates within the solution will break-up particles and thus the growth of a sufficiently strong bridge is required at the time of contact of the two particles. According to Andreassen & Hounslow (2004), differing opinions are with regards to whether the disintegration of an aggregate of two barely attached particles should be considered as an unsuccessful aggregation event or as a breakage event. If disintegration of the particle is considered to be a breakage event then this should result in higher aggregation rates to produce a PSD that is consistent with that of the unsuccessful aggregation event (Andreassen & Hounslow, 2004).

In a multiparticulate system, the rate, $r_{agg}(L,\lambda)$, at which particles of size $[L, L+dL]$ aggregate with particles of size $[\lambda, \lambda+d\lambda]$ is proportional to the product of the number of particles in these respective size ranges (Bramley *et al.*, 1996). A rate constant, $\beta(L,\lambda)$, also termed the aggregation kernel can be used to characterize the rate of aggregation as follows

$$r_{agg}(L,\lambda) = \beta(L,\lambda) dN_L dN_\lambda \quad \text{... (42)}$$

The aggregation kernel is a measure of the frequency with which a particle of size L aggregates with a particle of size λ (Bramley *et al.*, 1996). Equation (42) is built on the assumption that all particle collisions are binary and this suggests that the particle concentrations of the system are sufficiently low. The aggregation kernel, however, is more commonly viewed as follows

$$\beta(L,\lambda) = \beta_0 \times f(L,\lambda) \quad \text{... (43)}$$

where β_0 is dependent on the operating conditions (e.g. local fluid velocity field and chemical environment) and independent of the size of the particles (Bramley *et al.*, 1996). $f(L,\lambda)$ is a function of particle size and can suggest the mechanism thought to have caused aggregation. A number of kernels commonly used to model aggregation are reflected in Table 1.

Table 1: Common aggregation kernels used in the modeling of precipitation processes (Bramley *et al.*, 1996)

Mechanism	Kernel $\boldsymbol{\beta(L,\lambda)}$
Size-independent	β_0
Brownian motion (Smoluchowski, 1917)	$\beta_0(L+\lambda)(L^{-1}+\lambda^{-1})$
Gravitational settling (Berry, 1967)	$\beta_0(L+\lambda)^2\lvert L-\lambda\rvert$
Shear (Smoluchowski, 1917 and Low, 1975)	$\beta_0(L+\lambda)^3$
Particle inertia (Drake, 1972)	$\beta_0(L+\lambda)^2\lvert L^2-\lambda^2\rvert$
Thompson kernel (empirical) (Thompson, 1968)	$\beta_0\frac{(L^3-\lambda^3)^2}{(L^3+\lambda^3)}$

It is suggested that the aggregation rate tends to zero at very low and very high agitation rates with a maximum value in between (Mumtaz *et al.*, 1997). Low aggregation rates are a result of very few collisions between the suspended particles occurring at low agitation rates. However, at high agitation rates, there are many collisions. The majority of these collisions do not produce aggregation events due to the new aggregates being split-up by the large hydrodynamic forces before a stable particle has time to develop. Between these extremes, there are a reasonable number of collisions, some of which are successful, giving a moderate aggregation rate. According to Mumtaz *et al.* (1997), the aggregation rate constant, β_{aggl}, is a function of the collision rate constant, β_{coll}, which is characterized by the following equation

$$\beta_{aggl} = \psi(\gamma,\sigma)\beta_{coll}(\gamma) \quad \text{... (44)}$$

where ψ is the overall efficiency of the collisions, and γ is the shear rate [s^{-1}]. Figure 11 illustrates the concept discussed above.

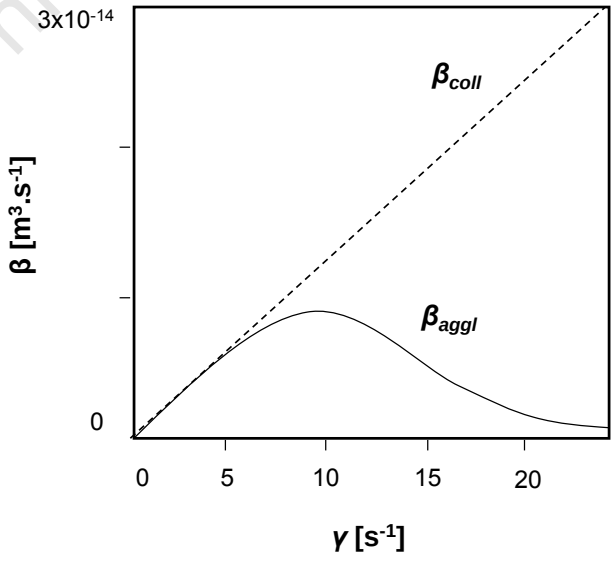

Figure 11: The effect of shear rate on the collision and aggregation rate constants (adapted from Mumtaz *et al.*, 1997)

Andreassen & Hounslow (2004) found in their work that the aggregation process was characterized by a size-independent kernel and a rate constant that was dependent on the solution supersaturation, was directly proportional to the instantaneous growth rate and decreased with increasing stirrer speed. A size independent aggregation rate constant was also found by Bramley *et al.* (1996) and Collier & Hounslow (1999). According to Zauner & Jones (2000) both aggregation inefficiency and particle disruption increase with particle size. These dispersive processes can counteract the positive effect of aggregation thereby imposing agglomerate particle size limitations which may give rise to apparent size independence (Zauner & Jones, 2000). Hounslow *et al.* (2001) stated that although it is possible to analyse aggregation rates using a size-independent kernel, as size ratios do not seem to be very important, the average particle size has an influence on the value of the deduced kernel. This influence comes from the collision efficiency in forming aggregates (Hounslow *et al.*, 2001).

Another secondary precipitation process is breakage. The breakage rate is generally independent of the supersaturation. This means that breakage effects should be more noticeable at long times, once aggregation has stopped due to the supersaturation being exhausted (Collier & Hounslow, 1999).

2.1.4.2 Ageing

The thermodynamic stability of a solid compound arises from the ordered arrangement of its molecules in a crystal lattice in an infinite medium (Giulietti *et al.*, 2001). According to Giulietti *et al.* (2001), the average stability for particles of a finite size is dependent on the particle volume and surface contributions. Thus, due to surfaces having low stability, the smaller the particle the lower the stability and therefore the higher the particles' solubility. Ageing is an important effect for particles less than 1μm in size (Giulietti *et al.*, 2001). In the late stages of batch precipitation, when supersaturation is low, an ageing process known as 'Ostwald ripening' generally occurs. The process of 'Ostwald ripening' occurs when smaller solid particles, dispersed in their own saturated solution, exhibit a tendency to dissolve back into solution and for the solute to be subsequently deposited onto the larger particles (Mullin, 2001). As a result of this process, the smaller particles disappear and the larger particles become bigger resulting in a mono-disperse particle size distribution. The reason for ripening behavior is the propensity of the solid phase to adjust itself to achieve a minimum total surface free energy (Mullin, 2001). Ripening is largely dependent on the particle size and solubility of the system, thus small crystals of a moderately soluble system will age much faster than those of an insoluble substance if kept in solutions with the same supersaturation.

The dissolution of crystals may be surface disintegration controlled where the rate of linear dissolution, D_{lin}, may be expressed as

$$D_{lin} = \frac{2}{\rho} K(C^* - C) \quad \ldots (45)$$

This expression, however, is only applicable to very slightly soluble compounds, for very low ΔC and for very small crystals (Lewis & van Rosmalen, 2010).

Another important ageing process is that of phase transformation. This occurs by way of the first-precipitation of a metastable phase followed by a phase transformation to the final product. The metastable phase may be either an amorphous precipitate, a polymorph of the final material, a hydrated species, or some system-contaminated substance (Mullin, 2001).

Ageing can take days or even months however it generally helps to improve product quality as it results in larger crystal sizes and improved product crystallinity (Giulietti *et al.*, 2001).

2.2 Particle Characteristics, Morphology and Behaviour

2.2.1 Introduction

The morphological development of a precipitate is a complex combination of a variety of processes, including nucleation, growth, habit modification, phase transformation, ripening, agglomeration, etc. (Mullin, 2001). These processes are usually governed by the level of supersaturation and active impurities within the crystallizing system. Orientation (crystalline) and aggregation (non-crystalline) are both influenced by supersaturation and temperature however the type of species is also important.

The following sub-sections will cover a brief discussion of the common crystal systems as well as a number of processes which change the typical crystal structures.

2.2.2 Crystal Systems

In terms of crystal symmetry there exist 32 classes which can be grouped into seven crystal systems as follows:

Table 2: The seven crystal systems and their properties (Mullin, 2001)

System	Other names	Angles between axes	Length of axes
Regular	Cubic, Octahedral, Isometric, Tesseral	$\alpha = \beta = \gamma = 90°$	$x = y = z$
Tetragonal	Pyramidal, Quadratic	$\alpha = \beta = \gamma = 90°$	$x = y \neq z$
Orthorhombic	Rhombic, Prismatic, Isoclinic, Trimetric	$\alpha = \beta = \gamma = 90°$	$x \neq y \neq z$
Monoclinic	Monosymmetric, Clinorhombic, Oblique	$\alpha = \beta = 90° \neq \gamma$	$x \neq y \neq z$
Triclinic	Anorthic, Asymmetric	$\alpha \neq \beta \neq \gamma \neq 90°$	$x \neq y \neq z$
Trigonal	Rhombohedral	$\alpha = \beta = \gamma \neq 90°$	$x = y = z$
Hexagonal	None	z is perpendicular to the x, y and u axes, which are inclined at 60°	$x = y = u \neq z$

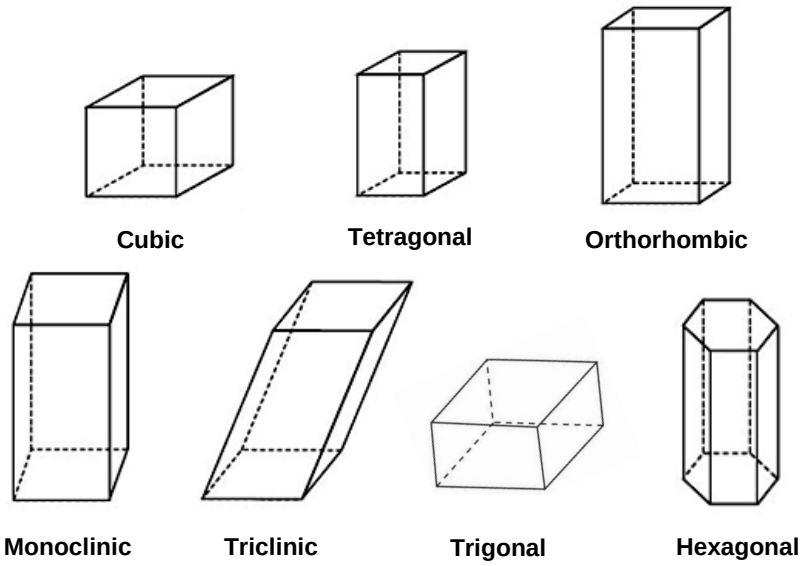

Figure 12: Illustration of the seven crystal systems

2.2.3 Crystal Habit

Even though crystals may be classified according to the seven crystal systems, the relative sizes of the faces of a particular crystal can vary quite considerably, termed 'a modification of habit' (Mullin, 2001). Reasons for this variation can be due to crystals growing more rapidly, or being stunted, in a particular direction. An elongated growth of the prismatic habit yields a needle-shaped crystal while stunted growth yields a flat plate-like crystal (Mullin, 2001). According to Mullin (2001), perfect geometric symmetry is rarely observed in crystals thus almost all crystals that are manufactured or occur naturally are distorted to some degree.

A number of factors can be used to alter and control the relative growths of the faces of a crystal. Rapid crystallization e.g. sudden cooling or seeding of a supersaturated solution may produce needle crystals (Mullin, 2001). If impurities exist in the solution, crystal growth may be stunted in certain directions. Mullin (2001) stated that the degree of supersaturation and the agitation of a system are properties that can significantly influence the crystal habit.

2.2.4 Polymorphism

Polymorphism is the capability of a substance to crystallize into different, but chemically identical, crystalline forms (Mullin, 2001). This is a result of the substance having more than one possible arrangement of solutes in a crystalline lattice. According to Giulietti *et al.* (2001) polymorphs behave differently with regards to solubility, and nucleation and growth rates. An example of a common polymorph is calcium carbonate which precipitates as either: aragonite, vaterite or calcite. Apart from these precipitates exhibiting different morphologies and behaviours, they all have the same chemical formula viz. $CaCO_3$. Ionic salts generally display 'pseudo polymorphism' which is the occurrence of varying amounts of hydration water within the precipitated salts (Giulietti *et al.*, 2001).

The Ostwald rule of stages states that the first phase to precipitate is generally the most soluble, due to the fact that polymorphs with higher solubilities precipitate faster. Thus, this first phase will re-

dissolve while new phases of decreasing solubility are formed. Finally, the only polymorph left is that with the lowest solubility. All precursors are metastable phases and the final polymorph is the only thermodynamically stable phase (Giulietti *et al.*, 2001).

2.2.5 Dendrites

Dendrites generally occur by way of rapid crystallization from supercooled melts, supersaturated solutions and vapours. The 'tree-like' formations occur because the main crystal stem grows rapidly and at a later stage primary branches grow at a slower rate perpendicular to the stem (Mullin, 2001). Smaller secondary branches may also grow slowly out from the primary branches. The branching will eventually cease and the dendritic pattern will be filled in with other crystalline material.

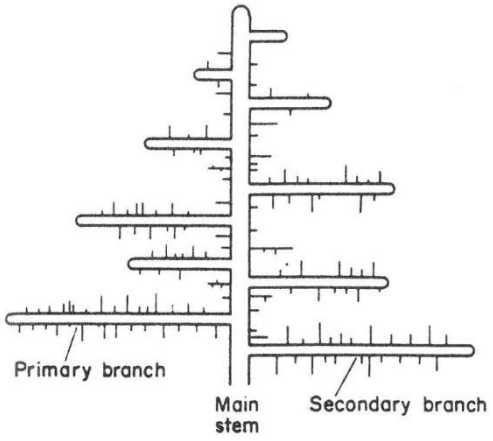

Figure 13: An example of dendritic growth (Mullin, 2001)

Dendrites usually form in the early stages of crystallization because at later stages a more normal uniform growth occurs and the dendritic pattern ceases to exist (Mullin, 2001). Agitation tends to suppress dendritic growth.

2.2.6 Composite Crystals and Twinning

Composite crystals may occur in simple symmetrical forms or in random clusters (Mullin, 2001). Some precipitated particles are often confused with a true agglomerate. These crystals are formed when crystalline out-growths originate from different surfaces of an original heteronucleus (Mullin, 2001). Further growth leads to the development of a particle that appears deceptively like an agglomerate.

Parallel growth occurs when individual forms of the same substance grow on top of one another resulting in all the corresponding faces and edges of the crystals being parallel.

Another example of a composite crystal is a twin or macle. Twinning occurs when two intergrown crystals, similar in form, are joined symmetrically about an axis or a plane (Mullin, 2001). Twins may show an interpenetration (giving the appearance of one individual having passed completely through the other) or a partial interpenetration (Mullin, 2001). Mimetic twinning is when a twin may present the outward appearance of a form that possesses a high degree of symmetry than that of the individuals. Twinning is most frequently encountered in the orthorhombic and monoclinic crystal systems.

Figure 14: (left) Parallel growth on a crystal of potash alum, (middle) interpenetrant twin of two cubes, and, (right) partial interpenetrant twin (Mullin, 2001)

According to Mullin (2001), parallel growth and twinning usually occur due to:

(i) Poor agitation
(ii) The presence of impurities in the crystallizing solution
(iii) Seeding at high degrees of supersaturation
(iv) The presence of too many seed crystals (leading to conditions of overcrowding in the crystallizer)

2.3 Batch Precipitation and Mixing

2.3.1 Overview

The hydrodynamics of a precipitation system play a very important role, as they (Lewis & van Rosmalen, 2010):

(i) Mix reactants
(ii) Keep solids in suspension
(iii) Promote contact among particles

Batch precipitation is usually carried out by adding one reactant solution to a process vessel in which a second reactant solution has already been added. Precipitation processes involve the creation of highly supersaturated solutions and thus it is difficult to obtain uniform conditions throughout a reaction vessel (Mullin, 2001). This means that the level of the supersaturation ratio may vary strongly with the location in the vessel as well as with time (Roelands *et al.*, 2006). The method of mixing the reactants is thus very important in order to prevent zones of excessively high supersaturation (Mullin, 2001). Also, due to the high supersaturations involved, the characteristic reaction time for precipitation is generally of the same order of magnitude as the mixing time (Giulietti *et al.*, 2001). Thus, the mixing determines the course of supersaturation which in turn influences the (Lewis & van Rosmalen, 2010):

(i) PSD (via the local supersaturation and nucleation)
(ii) Crystal habit
(iii) Polymorphic modification
(iv) Crystallinity
(v) Degree of agglomeration
(vi) Purity

The feed rate of reactant solutions may be important, especially in the case when seeds are added prior to precipitation (Sohnel & Garside, 1992). If the feed rate is maintained at a level that creates a supersaturation lower than the critical value for nucleation, the existing supersaturation will be

preferentially released onto the seed particles. If the initial PSD of the seeds is narrow, the product PSD will also be narrow. If, however, the feed rate is higher than the critical value, new nuclei are formed and a polydisperse size distribution results (Sohnel & Garside, 1992). The sequence in which reactants are mixed together is also a significant parameter and often results in a completely different precipitated product. If large crystals with high crystallinity and purity are desired, precipitation should be performed at a low supersaturation (Giulietti *et al.*, 2001). According to Giulietti *et al.* (2001), reactants should be added at points of high mixing intensity and as far away from one another as is possible. This will promote good dispersion of the reactant solutions throughout the reactor vessel. If, however, fine particles with a narrow size distribution are desired, intense mixing should be utilized to ensure rapid contact between the reactant solutions (Giulietti *et al.*, 2001).

2.3.2 Mixing Strategies

Mixing occurs through the bulk flow of the liquid, and, on a microscopic scale, by the motion of the turbulent eddies created by the impeller (Sinnott *et al.*, 1999). Bulk flow is the principal mixing mechanism required for the blending of miscible liquids and for solids suspension (Sinnott *et al.*, 1999). Turbulent mixing is important in operations involving mass and heat transfer; which can be considered as shear controlled processes. According to Sinnott *et al.* (1999) Rushton turbines are radial-flow devices which are suitable for processes controlled by turbulent mixing. The propeller and pitched-blade turbines, however, are axial-flow devices which are suitable for bulk fluid mixing. A reactor vessel is generally equipped with four baffles. The baffles help to improve the top-to-bottom mixing, prevent mixing-ineffective swirling motion and reduce problems with vortex formation (Perry *et al.*, 1997). Figure 15 below shows the typical flow patterns of different impellers.

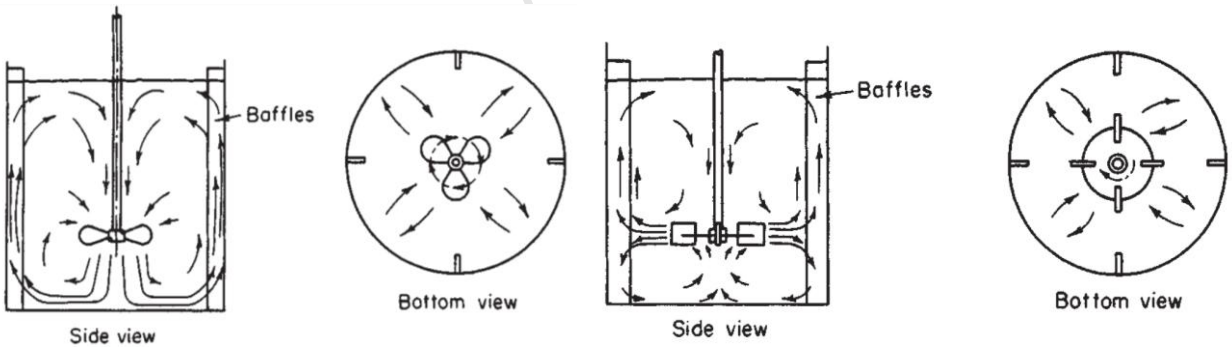

Figure 15: Typical flow pattern in a baffled tank with a (left) propeller or axial flow turbine and (right) turbine positioned on center (Perry *et al.*, 1997)

The position of reactant addition points generally has a significant influence on the quality of the precipitated product (Mullin, 2001). Many configurations exist within literature, with four possibilities illustrated below.

The 'single-jet' mode (a) of reactant addition is when a reactant A is fed on or near the surface of a reactant B which is already within the reaction vessel. Another possibility exists where reactant A is fed into the agitated zone near the impeller blade (b). The second addition method usually results in larger precipitated particles as the better mixing reduces the levels of local supersaturation which in turn minimizes the rate of nucleation (Mullin, 2001).

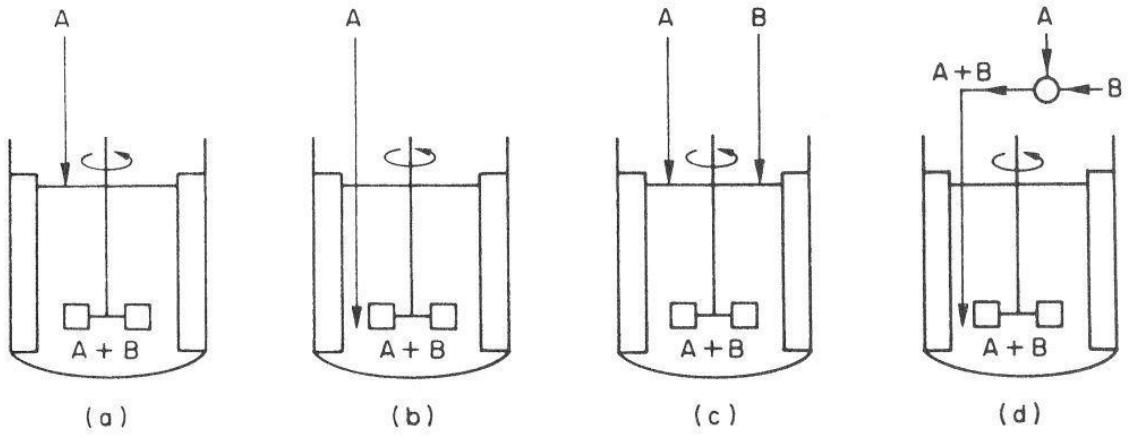

Figure 16: Possible reactant addition methods (Mullin, 2001)

Another alternative is that of the 'double-jet' mode of reactant addition. In this mode both reactants, A and B, are simultaneously added into the reaction vessel. Various possibilities exist for the exact point of introduction of the two solutions. For example, the reactants could be fed at the surface (c), or at the impeller tip. The two reactant streams could also be premixed and then fed to the reactor vessel as a single stream (d).

In precipitation processes, reactant streams are often premixed as this yields a certain amount of control over the initial supersaturation level (Mullin, 2001). Impinging jets and other in-line mixers (e.g. T-mixer, Y-mixer, Hartridge-Roughton mixer, vortex mixer, ball mixer etc.) are generally used because they have been found to achieve complete mixing within a few milliseconds (Mullin, 2001). Benet *et al.* (2002) investigated the operation of a number of mixing devices e.g. sliding-surface mixing device, vortex reactor and impinging jets mixing device, as these new technologies were found to exhibit a better control of the precipitation process over a simple stirred-tank reactor set-up. Benet *et al.* (2002) discussed that the stirred-tank reactor is not well adapted to control precipitation processes because of the complexity of its internal hydrodynamics. Thus, scaling-up a stirred-tank reactor is difficult as relatively small changes in the internal geometry of the reactor can lead to large variations in the mean crystal size (Benet *et al.*, 2002). Benet *et al.* (2002) concluded that the sliding-surface mixing device, vortex reactor and impinging jets mixing device all exhibited a better control of the precipitation process over the standard stirred-tank reactor. They also found that these new devices ensured a better precipitate quality, reproducibility and a better stability in a continuous mode of operation.

Stavek *et al.* (1992) developed a method known as controlled double-jet precipitation (CDJP) for the preparation of sparingly-soluble salts. From their work on silver halide precipitation, Stavek *et al.* (1992) found that the nucleation of unstable nuclei or primary particles continuously occurred near the reactant jets while monodisperse microcrystals continuously formed and grew within the bulk of the crystallizer. These two processes were found to occur simultaneously. Thus, the monodisperse particles were produced from the controlled Ostwald ripening or agglomeration of the unstable nuclei and thus growth of a constant number of stable particles (Stavek *et al.*, 1992).

2.3.3 Mixing Times and Scales

For a better understanding of a precipitation process the description of mixing is needed in time and length scales (ranging from the reactor size to the molecular diameter) (Lewis & van Rosmalen, 2010). Mixing can be described by an Eulerian approach i.e. compartment models such as computational fluid dynamics (CFD) and by a Lagrangian approach i.e. macro-, meso- and micro mixing. Only the latter approach will be further discussed in this dissertation.

A short description of the three types of mixing is shown in Table 3 below with a more detailed discussion in the following sub-sections.

Table 3: Mixing stages in precipitation (Myerson, 2002)

	Macromixing	**Mesomixing**	**Micromixing**
Scale	whole precipitator	diameter of the feed pipe	molecular
Phenomena	bulk fluid movement and blending determine environment conditions	coarse scale turbulent exchange between the fresh feed and its surroundings; inertial-convective disintegration of large eddies	viscous-convective deformation of fluid elements followed by molecular diffusion

2.3.3.1 Macromixing

Macromixing can be described as the bulk dispersion of a liquid throughout the reaction volume occurring at a scale equivalent to the size of the reactor. For a well-baffled tank and fully developed turbulence, the macromixing time, t_{macro} [s], is between three and five times the circulation time, t_c [s], yielding

$$t_{macro} = 4t_c \quad \text{... (46)}$$

For a reaction vessel using an impeller with four pitched blades the circulation time can be expressed as follows (Lewis & van Rosmalen, 2010)

$$t_c = \frac{V}{q_c} \quad \text{... (47)}$$

where V is the volume of the reactor vessel [m^3] and q_c is the pumping capacity of the impeller [$m^3.s^{-1}$], which can be expressed by

$$q_C = N_q N d_{stir}^3 \quad \text{... (48)}$$

where N_q is the flow number (taken as 0.73 for a pitched blade turbine (Nienow, 1997)), N is the impeller speed [s^{-1}] and d_{stir} is the impeller diameter [m].

2.3.3.2 Mesomixing

Mesomixing is the convective exchange of fluids at the reactor inlets and occurs at a scale comparable to the size of the reagent feed pipe (Lewis & van Rosmalen, 2010). The mesomixing time, t_{meso}, can be expressed as follows

$$t_{meso} = \frac{Q}{uD_{meso}} \quad \text{... (49)}$$

where Q is the volumetric reactant flow rate [$m^3.s^{-1}$], u is the feed flow velocity [$m.s^{-1}$], and, D_{meso} is the turbulent diffusivity [$m^2.s^{-1}$]. The mesomixing time, representing the turbulent disintegration of the feed, can be expressed as (Torbacke & Rasmuson, 2001)

$$t_{meso} = a\left(\frac{\Lambda^2}{\varepsilon}\right)^{\frac{1}{3}} \quad \text{... (50)}$$

where a is a constant (given as 2 (Baldyga *et al.*, 1997)), Λ is the macroscale turbulence [m], and, ε is the local energy dissipation rate [$m^2.s^{-3}$]. The macroscale turbulence can be estimated by

$$\Lambda = \sqrt{\frac{Q}{\pi u}} \quad \text{... (51)}$$

The local energy dissipation rate can be expressed as

$$\varepsilon = a\frac{N_p N^3 d_{stir}^5}{V} \quad \text{... (52)}$$

where N_p is the power number (taken as 1.5 for a pitched blade impeller (Uhl & Gray, 1966, cited in Lewis & van Rosmalen, 2010), and

$$N_p = \frac{Pg}{\rho N^3 d_{stir}^5} \quad \text{... (53)}$$

where P is the power [W], g is the gravitational acceleration [$m.s^{-2}$], and ρ is the liquid density [$kg.m^{-3}$].

2.3.3.3 Micromixing

Micromixing describes the segregation state of a fluid element in terms of its volume and homogeneity. Micromixing takes place by (Lewis & van Rosmalen, 2010):

(i) Molecular diffusion
(ii) Laminar deformation of striations below the Kolmogorov scale (smallest turbulent eddy)
(iii) Mutual engulfment of regions having different compositions

Because micromixing occurs at the molecular scale, it directly influences the chemical reaction, nucleation, and, crystal growth (Myerson, 2002). The characteristic time for micromixing, t_{micro}, can be expressed by (Lewis & van Rosmalen, 2010)

$$t_{micro} = 12\left(\frac{\nu}{\bar{\varepsilon}}\right)^{0.5} \quad \text{... (54)}$$

where ν is the kinematic viscosity [$m^2.s^{-1}$], and $\bar{\varepsilon}$ is the average energy dissipation rate, estimated by

$$\bar{\varepsilon} = 0.25 N^3 d_{stir}^2 \quad \text{... (55)}$$

2.3.3.4 Reynolds Number

The Reynolds number for a stirred tank may be expressed as follows (Sinnott *et al.*, 1999)

$$Re = \frac{\rho N d_{stir}^2}{\mu} \quad \text{... (56)}$$

where μ is the dynamic viscosity [$kg.m^{-1}.s^{-1}$]. A wide transition region between laminar and turbulent flow exists over the range of $10 < Re < 10^4$ while a system is said to be fully turbulent for $Re > 10^4$ (Perry *et al.*, 1997).

2.4 Particle Size Analysis Techniques

2.4.1 Overview of Existing Techniques

A large number of methods are available for the measurement of particle size, including sieving, microscopy, sedimentation, electrical sensing zone (Coulter), laser light scattering (Fraunhofer), permeametry and gas adsorption (Mullin, 2001). These techniques are able to measure a particles size over specific ranges of application and with varying degrees of resolution. All particle size measurements are conducted by indirect methods where a certain property of the solid particle, which can be related to size, is measured (Mullin, 2001). The 'equivalent diameter' (the diameter of a sphere that behaves in the same way as the given particle) is generally the most common expression used with regards to particle size. Two of the more common particle size analysis techniques will be discussed in further detail below.

2.4.2 Laser Light Scattering (Fraunhofer) Technique

The technique of laser diffraction is based on the principle that particles passing through a laser beam will scatter light at an angle that is directly related to their size (Malvern Instruments Ltd., 2011). Generally, the method involves the forward scattering of laser light through a dilute (< 1 vol%) suspension of crystals retained in a small agitated cell (Mullin, 2001). The primary measurement that occurs within a laser diffraction instrument is the capture of the light scattering data from the particles being tested. The resulting diffraction pattern is detected and translated, by means of the instrument software, into a PSD (Mullin, 2001). A typical laser diffraction instrument contains a laser, a sample presentation system, and a series of detectors (see Figure 17).

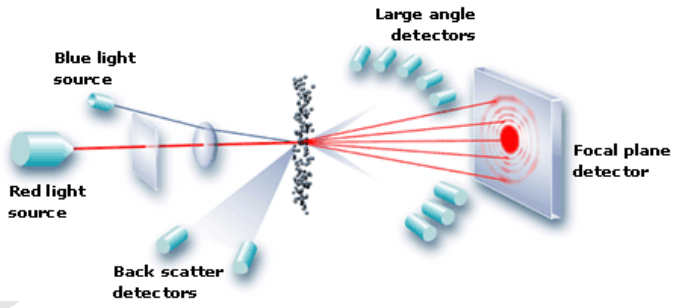

Figure 17: Illustration of laser diffraction (Malvern Instruments Ltd., 2011)

An example of a laser diffraction instrument is that of the Malvern Mastersizer 2000 illustrated in Figure 18 below.

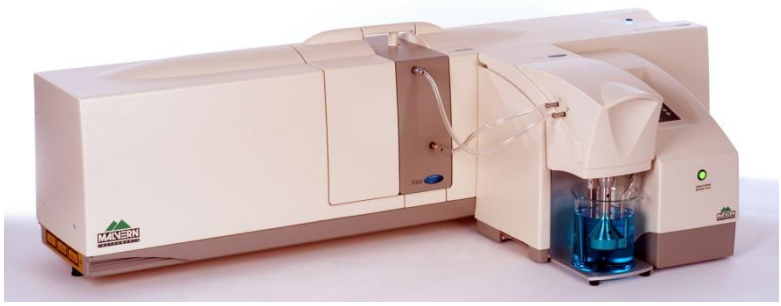

Figure 18: Malvern Mastersizer 2000 (Malvern Instruments Ltd., 2011)

A summary of the features and drawbacks to using a laser diffraction technique (Malvern Masterziser) are shown in Table 4 below:

Table 4: Analysis of the Malvern Mastersizer for particle size analysis (Lewis & van Rosmalen, 2010 & Malvern Instruments Ltd., 2011)

Measured variable	Projected area-based volume distribution
Size range	0.02 - 2000µm
Type of sample	Suspensions, emulsions and dry powders
Mode of operation	On-line
Solid concentration	< 1 vol.%
Accuracy	±1%
Resolution	High sensitivity to over-sized material
Robustness	+/-
Drawbacks	• Particle size is determined assuming the equivalent sphere approximation i.e. inaccuracies if particles not spherical. • Very dilute samples cannot be measured easily. • Yields inaccurate results for porous particles.

2.4.3 Electrical Sensing Zone Technique – The Coulter Principle

The Coulter principle works by measuring the changes in electrical conductance as particles or cells, suspended in a conductive fluid, pass through a small orifice. The Coulter principle is illustrated in Figure 19 below.

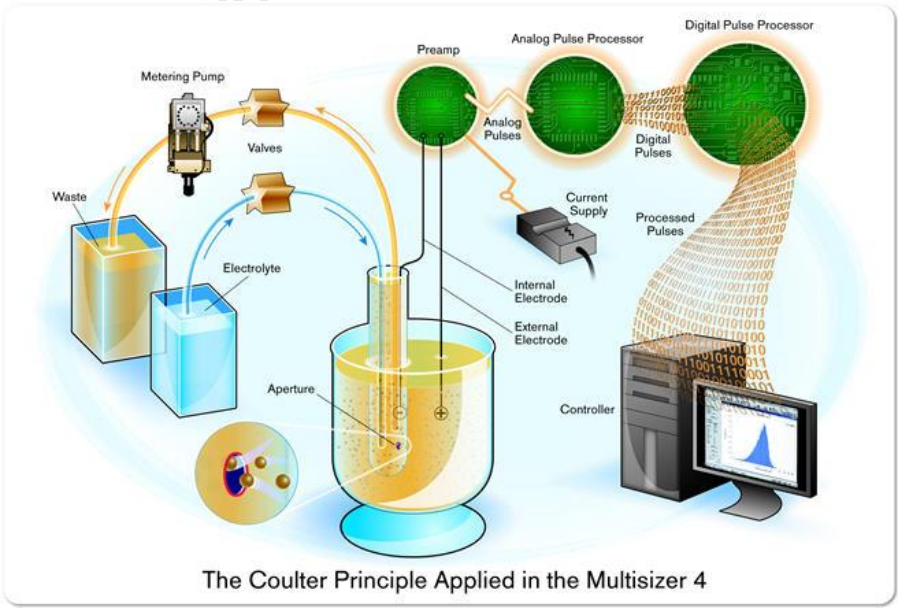

Figure 19: Schematic of the workings of a Coulter Counter (Beckman Coulter Inc., 2011)

In a Coulter Counter, a tube with a small aperture is placed in a beaker that contains particles suspended in a low concentration electrolyte. Two electrodes exist within the beaker, one within and one outside the aperture tube. When an electric field is applied to the electrolyte a current path is produced. The impedance between the two electrodes is measured with the aperture creating a "sensing zone". Particles are counted by passing them through the aperture which in turn displaces a volume of electrolyte equivalent to the immersed volume of the particle. This results in a change in the impedance across the aperture (which can be measured as a voltage or a current pulse). The pulse height is proportional to the particle volume. Thus, the number of particles and volume of each individual particle can be measured by an instrument using the Coulter principle e.g. the Beckman Coulter Multisizer III (see Figure 20).

Figure 20: Beckman Coulter Multisizer III (Beckman Coulter Inc., 2011)

A summary of the features and drawbacks to using a Coulter Counter for particle size analysis are highlighted in Table 5 below:

Table 5: Analysis of the Coulter Counter for particle size analysis (Lewis & van Rosmalen, 2010 & Beckman Coulter Inc., 2011)

Measured variable	Volume-based number size distribution
Size range	0.4 - 1600µm
Aperture sizes	20 - 200µm (each aperture can measure particles with a size range of 2 to 80% of its nominal diameter)
Counting and sizing rates	Up to 10 000 particles per second
Accuracy of size measurements	Better than 1%
Mode of operation	Off-line
Solid concentration	< 0.01 - 0.1vol.% (dilution in electrolyte)
Resolution	High (over a limited size range)
Robustness	Scaling; Electrical disturbances (especially at the lower size ranges)
Drawbacks	• Ability of the technology is limited to particles that can be suspended in an electrolyte solution. • High dilution ratios are needed (especially if suspension

	is highly concentrated). • Over-sizing at the top distribution, and low counting efficiency for small particles. • Limited size range - for wider size ranges, two or more apertures have to be used and the results overlapped to provide a complete PSD.

2.5 Seeds and Seeding

2.5.1 Overview

In batch crystallization, one of the main challenges is to control the supersaturation and nucleation in the initial stages of the process (Myerson, 2002). High supersaturation and excessive nucleation generally occur as there is only a small amount of crystal suspension present onto which solute can crystallize. An appropriate method for initiating a crystallization process (under reproducible operating conditions) is the addition of seeds to the reaction vessel. The use of seeds helps to minimize and control the process of primary nucleation (Mersmann, 2001).

The time of addition of the seeds and the location of the seed feed are important operating parameters (Mersmann, 2001). In the metastable zone of a crystallization system, crystal growth can occur but the supersaturation is too low for spontaneous nucleation (see Figure 1). Thus, if the supersaturation can be controlled within the metastable zone after seeding, only growth on the seed particles will occur (Myerson, 2002). If, however, the solution is undersaturated the seeds may dissolve back into solution. Another important factor is the seed mass per unit volume and the seed size and size distribution (Mersmann, 2001). These factors must be determined such that spontaneous nucleation is avoided. According to Mersmann *et al.* (2001), in order to obtain a large seed surface area, a small mass of small-sized seed particles is more beneficial than a large mass of coarse seeds. Fine seed particles, however, dissolve more readily than coarse crystals. For fine seed particles, there is always a tendency towards aggregation, resulting in a change in the specific surface area. In addition to other parameters, the efficiency of the seeding depends on the growth ability of the seed crystals (Mersmann, 2001). It has been found that the milling of crystals for the production of seed particles can either increase or decrease the growth rates of the seeds at a given supersaturation. The origin, purity, and, morphology of the seeds are also important parameters. According to Mersmann *et al.* (2001), the preparation of a pure seed with a rough surface (in the molecular sense) and a minimum amount of lattice deformation are prerequisites for increasing the selectivity of a crystallization process.

2.5.2 Previous Seed Preparation Techniques for Moderately Soluble Systems

According to Mersmann *et al.* (2001), the reproducibility of a seed sample is very difficult especially when no variation in the product from run to run is desired. A number of seed preparation techniques for more insoluble systems can be found in literature however these are specific to the precipitation process and system under investigation.

Andreassen (2001) investigated the production of vaterite seed particles using various operating conditions and reactor set-ups. For the instant addition of reactant solutions to a magnetically stirred beaker (method A), Andreassen (2001) found that the seeds produced were unsuitable as they were aggregated, possessed a low seed concentration, and were thus difficult to reproduce. For method B, which involved premixing the reactant solutions with a T-mixer and subsequent addition to a stirred-tank reactor, Andreassen (2001) found that the T-mixer did not yield the intended mixing. However, it was found that this method could produce suitable seeds at specific combinations of the operating parameters. Method C involved simultaneously pouring the reactant solutions into a stirred vessel. Andreassen (2001) stated that this very simple approach yielded the best and most robust results once the parameters had been appropriately set. This method utilized a high agitation rate (1500rpm) and the seeds were found to be stable for up to 20 hours with regards to number and form (i.e. pure vaterite).

Collier & Hounslow (1999) prepared calcite seed particles by nucleation from a supersaturated solution of calcium carbonate. The seed particles had to be prepared at the start of each experiment as they were found to undergo aging with time. The final mode size of the seeds was between 3 and 4μm.

Ryall *et al.* (1981) utilized a seed preparation technique for the production of calcium oxalate monohydrate (COM) seed particles. In this method, COM was wet ground in a mortar and pestle to disrupt the larger lumps. The seeds (1g) were then suspended in 1L of a 0.15kmol.m^{-3} saline solution. The seed suspension was stored at room temperature, stirred by a magnetic stirrer and left to equilibrate for two weeks (Ryall *et al.*, 1981). The number mean size for the final seed crystals was $\bar{d}_{1,0}$ = 4.15μm. The technique of Ryall *et al.* (1981) has also been successfully utilized by Bramley *et al.* (1996) and Bramley *et al*. (1997).

2.5.3 Considerations for Developing a Suitable Seed Preparation Technique

When determining the significant parameters in the preparation of a suitable seed sample the following points should be taken into consideration:

i. Initial solution supersaturation - If the initial supersaturation is too high, homogeneous nucleation consumes the majority of the supersaturation and hardly any growth (or aggregation) occurs. This results in a high number of extremely small seed particles (see point (v)). On the other hand, if the initial supersaturation is too low a relatively long induction time may occur. Also with respect to yield, a suitable supersaturation is required such that enough seed material is produced per experiment otherwise a large number of repeat runs are required.

ii. Addition of reactants - The mother liquor of the seed sample should be depleted with respect to both the reactant ions. This means that the reactants should be fed in stoichiometric amounts when preparing the seeds (Andreassen & Hounslow, 2004).

iii. Mixing in the reactor - Mixing is very important as it affects the precipitation process i.e. size and morphology of the seeds. Therefore the correct type of mixing or mixer must be determined dependent on the solubility of the substance, initial solution supersaturation and reactor set-up.

iv. Stability of seed sample - If suspended seeds are to be produced, the particles must not transform within a certain time interval within the reactor i.e. the morphology, polymorphism, number and volume must remain constant.

v. Particle size analysis - The seeds must be within the size range of the particle size analyser of choice i.e. the Malvern Mastersizer can measure particles over a wide range ~ 0.02 to 2000μm whereas the Coulter Counter requires the correct aperture to be selected which corresponds to a specific size range e.g. 100μm aperture → 2 to 60μm range. Thus, identifying the most suitable particle size analysis equipment is another factor which needs to be considered.

vi. Concentration of seed sample - The particle size analyzer of choice must be able to measure the particles without having to add too much sample (i.e. sample volume constraints in a reactor). Smaller sample dispersion units are available for the Malvern Mastersizer but for very dilute samples the Coulter Counter may be used. Very concentrated samples will have to be diluted in most circumstances.

vii. Characteristics of seed sample - The seed population must be relatively monodisperse. The seeds must be well-grown and possibly not agglomerated as it is best to have a blank surface for the particles to grow upon. Also, agglomeration decreases the surface area of the seed sample. Increasing the seed surface area reduces the chance of nucleation in a seeded system thus agglomerated seeds are not so desirable.

viii. Reproducibility - The seed preparation technique must be such that the seeds are reproducible with respect to both number and volume distributions across different runs of an experiment or sample.

2.6 Thermodynamic Modelling: OLI Stream Analyser

2.6.1 Background

OLI Stream Analyser, developed by OLI Systems Inc. (2008), is a thermodynamic modeling tool that can be used to investigate the phase behavior of various solutions. According to Liu & Papangelakis (2005), in order to describe aqueous and solid-aqueous equilibria of electrolyte solutions, OLI Stream Analyser employs the following conceptual mathematical framework: the equilibrium constant of any general reaction i at temperature T and pressure P is

$$K_{i,T,P} = \prod_j a_j^{\nu_{i,j}} \quad \ldots (57)$$

where a_j is the activity of species j and $\nu_{i,j}$ is the stoichiometric coefficient of species j in reaction i, positive for products and negative for reactants. The equilibrium constant, $K_{i,T,P}$, can then be calculated from the standard Gibbs free energy of reaction i as follows (Liu & Papangelakis, 2005)

$$\Delta G^0_{i,T,P} = -RTlnK_{i,T,P} \quad \ldots (58)$$

The OLI software uses the revised Helgeson-Kirkham-Flowers (HKF) model for the calculation of standard thermodynamic properties of aqueous species and the frameworks of Bromley, Zemaitis, Pitzer, Debye-Huckel, and others for the excess terms. The HKF model is represented by the following fundamental equations:

$$H^0_i = H^R_i + f_{H_i}(a_1, \ldots, a_4, c_1, c_2, \omega) \quad \ldots (59)$$

$$G^0_i = G^R_i - S^R_i(T - T^R) + f_{G_i}(a_1, \ldots, a_4, c_1, c_2, \omega) \quad \ldots (60)$$

$$S_i^0 = S_i^R + f_{S_i}(a_1, \dots, a_4, c_1, c_2, \omega) \quad \dots (61)$$

$$C_{p_i}^0 = C_{p_i}^R + f_{Cp_i}(a_1, \dots, a_4, c_1, c_2, \omega) \quad \dots (62)$$

$$V_i^0 = V_i^R + f_{V_i}(a_1, \dots, a_4, c_1, c_2, \omega) \quad \dots (63)$$

where a_{1-4} = constants for volume

c_{1-2} = constants for heat capacity

ω = temperature and pressure property of water

Thus, the equilibrium constant can be determined from the calculation of the above properties.

2.6.2 Application of OLI

As OLI Stream Analyser is a thermodynamic predictive package it can be used to determine how a precipitation system will behave under purely thermodynamic conditions i.e. kinetics are not considered. For application in this work, OLI can be used to determine the thermodynamic:

(i) precipitation products
(ii) yield of precipitate
(iii) solubility products
(iv) activity coefficients
(v) supersaturations

In calculation of the supersaturation ratio, see Equation (12), OLI calculates the exact concentrations of only those species involved in the equilibrium equation. Thus, the contribution due to the formation of other ion complexes is not considered in the calculation of the IAP. OLI reports a parameter known as the 'scaling tendency' which is defined as: *"the ratio of the real-solution solubility product to the thermodynamic limit based on the thermodynamic equilibrium constant."* For this system, the scaling tendency is related to the supersaturation as follows:

$$\text{Scaling Tendency (ST)} = \frac{IAP}{K_{sp}} = S^2 \quad \dots (64)$$

Therefore, the supersaturation ratio can be calculated very easily from Equation (64).

2.7 Kinetic Modelling for Precipitation Systems – The Population Balance

2.7.1 Equations for Nucleation, Growth and Aggregation

The population balance (PBE) is a statement of continuity for particulate systems and is used in modelling precipitation processes (Bramley *et al.*, 1996). The general population balance can be represented as follows

$$\frac{\partial n}{\partial t} + \frac{\partial (Gn)}{\partial L} + n\frac{d(logV)}{dt} = B - D - \sum_k \frac{Q_k n_k}{V} \quad \dots (65)$$

For a well-mixed batch system of constant volume, the population balance is given by Randolph & Larson (1988) as follows

$$\frac{\partial n}{\partial t} + \frac{\partial (Gn)}{\partial L} = B - D \quad \dots (66)$$

where n is the number-density function and B & D are the particle birth and death terms respectively. According to Hounslow *et al.* (1988), if in the system there are dN particles per unit volume of suspension in the size range L to $(L + dL)$, then at that size and time the density function is

$$n(L) = \frac{dN}{dL} \quad \text{... (67)}$$

Equation (66) relates the rate of change of the number of particles in the differential size range L to $(L + dL)$, to the rates of growth into and out of that range and the rates of birth and death in the size range (Hounslow *et al.*, 1988). The growth term in Equation (66) may be simplified by assuming that the growth rate is not a function of length (from the McCabe ΔL law), yielding

$$\frac{\partial n}{\partial t} = -G\frac{\partial n}{\partial L} \quad \text{… (68)}$$

if the birth and death of particles is also assumed to be negligible. Aggregation is represented in the population balance as the birth and death of particles and can be expressed as follows

$$B(L) = \frac{L^2}{2}\int_0^L \frac{\beta\left[(L^3-\lambda^3)^{\frac{1}{3}},\lambda\right] n\left[(L^3-\lambda^3)^{\frac{1}{3}}\right] n(\lambda)d\lambda}{(L^3-\lambda^3)^{\frac{2}{3}}} \quad \text{… (69)}$$

$$D(L) = n(L)\int_0^\infty \beta(L,\lambda)n(\lambda)d\lambda \quad \text{… (70)}$$

with length as the internal coordinate. The nucleation rate, J, is taken to be the rate at which particles of zero size appear. Birth as a result of nucleation can thus be represented as

$$B = J\delta(L) \quad \text{… (71)}$$

where $\delta(L)$ is the Dirac delta function.

2.7.2 The Moment Form

When initial conditions and auxiliary equations are applied to the population balance equations, a set of integro-partial-differential equations of mixed dimension result for which analytical solutions can rarely be found (Hounslow *et al.*, 1988). The moment transform can be used to convert the intractable set of equations into a set of ordinary differential equations which are easily solvable (Hounslow *et al.*, 1988). The j^{th} moment of the number density function, $n(L)$, with respect to its internal coordinate, L, is defined as

$$m_j = \int_0^\infty L^j n(L)dL \quad \text{… (72)}$$

The first four moments are significant as they are related to the total number, length, area, and volume of solid per unit volume of suspension, respectively

$$N_T = m_0 \quad \text{… (73)}$$

$$L_T = k_L m_1 \quad \text{... (74)}$$

$$A_T = k_A m_2 \quad \text{... (75)}$$

$$V_T = k_V m_3 \quad \text{... (76)}$$

The shape factors (k_L, k_A & k_V) are dependent on the shape of the particles and the type of particle size analyzer used. For a Coulter Counter: $k_V = {}^{\pi}/_{6}$, irrespective of particle shape while the analysis of spheres on the Coulter Counter requires $k_L = 1$ and $k_A = \pi$ (Hounslow *et al.*, 1988). The moment transform for the particle number continuity equation (Equation 66), is as follows

$$\frac{dm_j}{dt} - jGm_{j-1} = \bar{B}_j - \bar{D}_j \quad \text{… (77)}$$

with the birth and death terms in Equation (77) being defined as

$$\bar{B}_j = \int_0^\infty L^j B(L)dL \quad \text{… (78)}$$

$$\bar{D}_j = \int_0^\infty L^j D(L)dL \quad \text{… (79)}$$

2.7.3 Analytical and Numerical Solutions

Solving the population balance involves finding the PSD, $n(L,t)$, that will satisfy the population balance equation for the system, subject to the appropriate initial and boundary conditions (Bramley *et al.*, 1996). Analytical solutions to the population balance are very difficult to obtain and significantly more difficult when growth and aggregation occur simultaneously (Bramley *et al.*, 1996). Thus the majority of the solutions to the population balance found in literature are of a numerical nature. According to Bramley *et al*. (1996), numerical methods for solving the population balance can be divided into three groups, namely:

i. Classical numerical methods e.g. finite elements methods
ii. Cubic spline methods
iii. Discretized population balances (DPBs)

In the discretized population balance the size interval is discretized into intervals and some form for $n(L)$ is assumed within each interval. The discretization of the population balance has a major advantage over other numerical techniques as it transforms the population balance into a set of ordinary differential equations which significantly reduces the complexity of the solution.

2.7.4 Analysis of the Discretized Population Balance (DPB)

This section represents an overview of the DPB of Hounslow *et al.* (1988). The DPB ensures the correct prediction of the particle number and volume for the aggregation terms as well as the correct prediction of the first three moments for the growth terms (Hounslow *et al.*, 1988). The method of discretization involves dividing the length domain into intervals in a geometric series which results in the upper and lower bounds of each size interval being in a ratio, $r = \sqrt[3]{2}$. For aggregation the rate of change of particle numbers in the i^{th} interval can be represented by the following discretized equation

$$\frac{dN_i}{dt} = N_{i-1}\sum_{j=1}^{i-2} 2^{j-i+1}\beta_{i-1,j}N_j + \frac{1}{2}\beta_{i-1,i-1}N_{i-1}^2 - N_i\sum_{j=1}^{i-1} 2^{j-i}\beta_{i,j}N_j - N_i\sum_{j=1}^{n_{eq}}\beta_{i,j}N_j \quad \ldots (80)$$

The discretized equation for growth is

$$\frac{dN_i}{dt} = \frac{2G}{(1+r)L_i}\left(\frac{r}{r^2-1}N_{i-1} + N_i - \frac{r}{r^2-1}N_{i+1}\right) \quad \ldots (81)$$

with $i \neq 1$. According to Bramley *et al.* (1996), Equation (81) cannot be used for the first size interval because the total number of particles will not otherwise be predicted correctly. Thus, for the first size interval, the discretized equation is

$$\frac{dN_1}{dt} = \frac{2G}{(1+r)L_1}\left[\left(1 - \frac{r^2}{r^2-1}\right)N_1 - \frac{r}{r^2-1}N_2\right] \quad \ldots (82)$$

2.7.5 Mixed-Suspension-Mixed-Product-Removal (MSMPR) Modelling

Kinetic data for crystallization processes has been frequently determined in the literature assuming MSMPR conditions, analogous to the continuous-stirred tank reactor (CSTR) model in chemical reaction engineering (Zauner & Jones, 2000). According to Randolph & Larson (1988) and Zauner & Jones (2000), the assumptions leading to the basic definition of an ideal MSMPR crystallizer are

i. Continuous steady-state operation
ii. Perfectly-mixed
iii. No agglomeration or disruption i.e. breakage assumed negligible
iv. No classified withdrawal of the product

v. Crystal growth rate independent of crystal size
vi. No seed crystals in the feed

With the above assumptions, Equation (65) reduces to

$$G\frac{dn}{dL}+\frac{n}{\tau}=0 \quad \ldots (83)$$

Differentiation of Equation (83) yields the following equation

$$n=n_0\exp\left(-\frac{\mathrm{L}}{\mathrm{G}\tau}\right) \quad \ldots (84)$$

with n_0 representing the population density of nuclei. The drastic simplification of the population balance makes determining the kinetic parameters a simple task. Equation (84) can be plotted as a line in a logarithmic-linear plot and the growth and nucleation rates can be determined from the gradient and intercept respectively (see Figure 21).

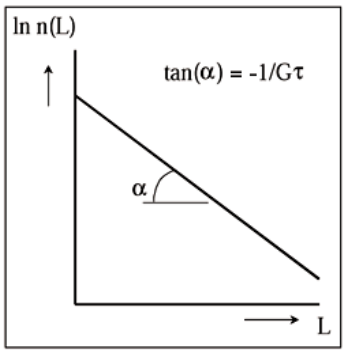

Figure 21: Population balance for an MSMPR crystallizer (Giulietti *et al.*, 2001)

However, during precipitation processes, agglomeration and disruption frequently occur thus the MSMPR assumptions do not hold and the above simplified population balance cannot be used.

2.8 Methods for Determining Precipitation Kinetics

Precipitation kinetics, compared to those of crystallization, are difficult to study as they take place under high supersaturation which results in very fast reactions. The induction times can be of the order of a few milliseconds for precipitation whereas for crystallization these times can be minutes or longer (Aoun *et al.*, 1999). Therefore methods used to determine rates in crystallization processes will not always work for precipitation processes. Traditionally, the approach of determining kinetics requires the experimental separation of the simultaneous processes i.e. nucleation, growth, aggregation etc. however this is not an easy task. It is also important that for validity purposes simultaneous methods are used where the precipitation rates are deduced from a single experiment (Aoun *et al.*, 1999).

The available experimental data that can be used to determine the kinetics of precipitation processes generally consists of concentration profiles obtained from chemical solution analysis and the PSD determined using an analytical technique such as the Malvern Mastersizer or Coulter Counter (Aoun *et al.*, 1999). In steady-state processes, the experiments are time and reagent-consuming while in batch processes experiments can be conducted within a short time period. However, the

mathematical treatment of the experimental results in batch processes is complicated due to both the supersaturation and particle population varying with time (Aoun *et al.*, 1999).

The methods used to determine the rates of different processes can be classified into two groups:

1) Isolation methods
2) Simultaneous methods

Isolation methods allow the independent calculation of the rates of different mechanistic processes from separate experimental results. Isolation methods can be further divided into two subcases:

i. Data is recorded from the same experimental run
ii. Data is recorded from separate runs

The problem with subcase (ii) is that the experimental conditions may be different between runs and thus the mechanisms may have changed somewhat if not significantly. Simultaneous methods determine rates by separating the contributions of each individual mechanism from the observed experimental output variables using a mathematical treatment. However, the mathematical treatment of the data may be very complicated especially if all rates are to be determined accurately (Aoun *et al.*, 1999).

Isolation and simultaneous methods can be based on either a differential or an integral approach. According to Aoun *et al.* (1999), integral methods make use of a wide set of experimental data integrated over a large time interval during precipitations, whereas differential methods are based on instantaneous values of process variables and their variations in a very short time interval. An integral approach involves fitting a kinetic model to an integral form of the rate equations where a number of parameters can be adjusted. For given values of the parameters the experimental data may be simulated by integrating a combination of the rate and kinetic equations. The parameters are usually selected to optimize the fit of the simulated results to those obtained experimentally (Aoun *et al.*, 1999). The drawbacks to this approach are that it is computationally demanding and also requires the knowledge of what constitutes an appropriate kinetic model. Bramley *et al.* (1996) stated that the principal virtue of the differential technique is its simplicity. The problem with this approach is that large errors can be generated in the estimates for the rates of change. Despite this problem, the differential technique is a better discriminator between models than the integral approach (Bramley *et al.*, 1996).

The following sub-sections represent a detailed evaluation of a number of methods for determining the kinetics of various precipitation systems.

2.8.1 Methods for Determining the Nucleation Rate

Nucleation is one of the most difficult and lesser studied kinetic mechanisms due to the size of the particles involved (Aoun *et al.*, 1999). In past literature, nucleation rates have been estimated using experimental data of induction time measured by turbidity and by the counting of particles under a simple optical microscope (Aoun *et al.*, 1999). This technique was tedious and imprecise but has remained the starting point for the development of new techniques.

Aoun *et al.* (1999) developed a new method to derive the rates of nucleation and growth based on the simultaneous measurement of the supersaturation and the crystal size distribution (CSD) during a

batch spontaneous precipitation. In the development of the model, Aoun *et al.* (1999) stated that the primary nucleation rate can be expressed as a function of supersaturation by

$$r_N(t) = k_N exp\left(-\frac{B}{\left(ln\sqrt{C_A C_B/P_S}\right)^2}\right) \quad \text{... (85)}$$

where r_N is the nucleation rate [#.m^{-3}.s^{-1}], k_N is the nucleation rate parameter [#.m^{-3}.s^{-1}], B is the nucleation kinetic parameter, C_A and C_B are the reactant concentrations [mol.m^{-3}], and P_S is the solubility product [mol^2.m^{-6}]. Equation (85) is based on a semi-empirical model deduced from the theory of condensation of gases (Dirksen and Ring, 1991 cited in Aoun *et al.*, 1999). In following the development of the method, this equation is transformed into a differential equation as follows

$$r_N(t) = \frac{d\left(\int_0^\infty \psi(L,t)dL\right)}{dt} \quad \text{... (86)}$$

where ψ is the crystal size distribution density function [#.m^{-4}]. Equation (86) is integrated in order to yield Equation (87) which is less sensitive to experimental errors

$$N(t) - N(t_0) = \int_{t_0}^{t} k_N exp\left(-\frac{B}{\left(ln\sqrt{C_A C_B/P_S}\right)^2}\right)dt \quad \text{... (87)}$$

where N is the particle number concentration [#.m^{-3}]. The kinetic parameters k_N and B are determined by fitting two particle concentration profiles: the first profile is calculated from the experimental CSD and the second is calculated from Equation (87) using the postulated nucleation rate and the experimental supersaturation. Using the above nucleation model Aoun *et al.* (1999) found the following results for the batch precipitation of barium sulphate:

i. The nucleation rate was found to obey an exponential law with a primary heterogeneous dominating process in the concentration range investigated (i.e. between 0.375 and 1.5mol.m^{-3}).
ii. The nucleation rate of barium sulphate under the experimental conditions of the paper is described by the following relationship:

$$r_N = (2.5 \pm 0.5) \times 10^{11} exp\left(\frac{15 \pm 1}{\left(ln\sqrt{C_{Ba}C_{SO_4}/P_S}\right)^2}\right) \quad \text{... (88)}$$

A limitation to the method of Aoun *et al.* (1999) is that only particles with a size larger than L_{min} = 0.1μm can be detected by the particle size analyzer utilized in the study. As a result of this the authors decided to ignore the fraction of the smallest particles at time t. In using this method to measure the nucleation rate, errors may be induced in the calculation of the nucleation rate and this will be most significantly observed at higher supersaturations (or for the precipitation of very insoluble compounds) where a large amount of very small particles are produced.

Salvatori *et al.* (2002) developed a direct method for determining the nucleation rate for barium carbonate precipitation. Nucleation experiments were conducted using a nucleation tube (with a Hartridge-Roughton mixing device) attached to a dilution tank. The nucleation rate was calculated according to Equation (89)

$$r_N = \frac{N}{V_{tube} t_i} \quad \text{… (89)}$$

where N is the total number of nuclei generated by nucleation, V_{tube} is the volume of the nucleation tube, and t_i represents the injection time. Equation (89) is based on a number of conditions including:

a. The mixing time of the reactants must be much lower than the induction period.
b. The dilution must be fast.
c. In the dilution tank, nucleation, agglomeration and breakage must be avoided.

An exponential kinetic expression, similar to that used by Aoun *et al.* (1999), was used to determine the nucleation kinetic parameters. The nucleation rate was expressed as a function of supersaturation by Equation (19). The parameter A in Equation (19) was expressed as an Arrhenius-type equation as follows

$$A = A_0 exp\left(-\frac{E}{RT}\right) \quad \text{... (90)}$$

where E is the activation energy [J.mol^{-1}] and T is the temperature [K or °C]. Salvatori *et al.* (2002) found the following results based on the above equations:

i. The experimental data showed that the nucleation rate of barium carbonate in the supersaturation range investigated was characterized by the primary heterogeneous mechanism and could be expressed by the relation

$$r_N = 6.4 \times 10^{24} exp\left(-\frac{22065}{RT}\right) exp\left[-\frac{58.7}{ln^2 S}\right] \quad \text{... (91)}$$

ii. When Equation (19) was fitted to the experimental data, it was found that the nucleation rate could be calculated with an uncertainty of about 50%, which, according to Salvatori *et al.* (2002), is very satisfactory for this kind of measurement.

Salvatori *et al.* (2002) also found that agglomeration was a problem in the dilution tank as it caused problems with the counting of crystals. The addition of an anti-agglomerant did not work satisfactorily and the use of an ultrasonic probe in order to break the agglomerates also did not work. Thus, assumptions had to be made i.e. it was assumed that the size distribution of elementary particles in the agglomerates was the same as the size distribution of free elementary particles measured by the granulometer.

A significant problem with the nucleation rate method of Salvatori *et al.* (2002) is the way in which the residence time in the nucleation rate equation has been defined. The nucleation rate is defined as the measured particle number concentration divided by a characteristic residence time for the flow in the tube (see Equation 89) (Salvatori *et al.*, 2002). The rate of depletion of supersaturation over the length of the tube is unknown, but the decrease in nucleation rate may be large (Roelands *et al.*, 2004). The use of the residence time over the entire length of the tube may result in an underestimation of the nucleation rate due to the fact that nucleation may be restricted to the first part of the tube.

Roelands *et al.* (2004) developed a new method for measuring the nucleation rates in reactive precipitation. The experimental method is similar to that of Salvatori *et al.* (2002) where the reactant solutions are rapidly mixed in a T-shaped or Y-shaped mixing chamber and the nucleation takes place in a nucleation tube attached to a dilution tank. Figure 22 shows a simple diagram of the experimental method.

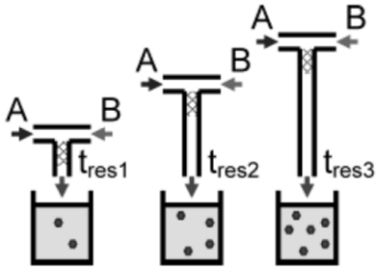

Figure 22: Schematic representation of the method applied to measure nucleation rates (Roelands *et al.*, 2004)

The method for determining the nucleation rates involves varying the tubular length of the reactor, corresponding to different residence times, for different supersaturation levels, corresponding to the reactant concentrations. Roelands *et al.'s* (2004) method is based on the CNT with the stationary nucleation rate being expressed by Equation (19). This is a similar exponential kinetic expression to that used by both Aoun *et al.* (1999) and Salvatori *et al.* (2002). Equations (14) & (15), for the critical nucleus size and nucleation work, can be simplified as follows

$$\frac{W^*}{kT} = \frac{B}{ln^2 S} \quad \text{... (92)}$$

$$n^* = \frac{2B}{ln^3 S} \quad \text{... (93)}$$

According to Roelands *et al.* (2004), the nucleation rate can be determined from the straight line plot of the total number of particles, N, versus the residence time, t_{res} i.e. $J = \Delta N/\Delta t_{res}$. A straight line can be obtained when measurements of the nucleation rate at different levels of supersaturation are plotted according to

$$ln\left(\frac{J}{S}\right) = lnA - \frac{B}{ln^2 S} \quad \text{... (94)}$$

The kinetic parameters A and B can be determined from the intercept of the line with the ordinate and the slope of the line respectively. Roelands *et al.'s* (2004) method is based on the following assumptions and conditions:

a. Spherical nuclei.
b. Nucleation and growth of crystals to an observable size takes place under well-controlled hydrodynamic conditions and at a constant supersaturation.
c. The Y-mixer must promote rapid mixing down to a molecular scale before nucleation takes place.
d. Fully-developed turbulent plug flow must exist in the tubular reactor lengths.
e. The conversion in the tube must be low, ~ 1%, so that the driving force over the length of the tube remains constant (this allows measurement of the "stationary" nucleation rate) i.e. the supersaturation ratio must remain approximately constant over the whole residence time in the tube.

Condition (e) above builds upon the work of Salvatori *et al.* (2002). Roelands *et al.* (2004) used the above theory and experimental method to determine the nucleation rates of H_4EDTA precipitation. The following results were found:

i. An increase in supersaturation ratio resulted in an increase in the nucleation rate. This result is consistent with the findings of Aoun *et al.* (1999), Zauner & Jones (2000), Salvatori *et al.* (2002) and Mangere *et al.* (2009).
ii. The exponential kinetic expression represented by Equation (91) could be used to obtain values for the kinetic parameters of A = (5.7 ± 1.0)×10^{15} $m^{-3}.s^{-1}$ and B = (3.3 ± 2.0)×10^2.
iii. The experimentally obtained value for A indicates heterogeneous nucleation.

Roelands *et al.* (2004) stated that the next step would be to investigate whether this experimental method could be used to measure homogeneous nucleation. This would occur at higher supersaturations thus resulting in faster nucleation, possibly before mixing is completed. Some recommendations by Roelands *et al.* (2004) to improve the methods applicability to homogeneous nucleation include

i. Increasing the mixing intensity to accelerate mixing of the liquids.

ii. Applying ultrasound to break-up the liquid layers and enhance the mixing process.
iii. Shortening the length of the tube to decrease the residence time and thus ensure that the supersaturation remains constant over the tube.
iv. Diluting the solution with a larger volume of saturated solution to achieve sample stability.

Mangere *et al.* (2009) used the same experimental method and CNT as Roelands *et al.* (2004) to determine the nucleation kinetics of selenium (+4) precipitation from an acidic copper sulphate solution. From experiments, Mangere *et al.* (2009) found the following results

i. The kinetic constant A was found to be 3.92×10^{27} $m^{-3}.s^{-1}$ which shows that the nucleation process takes place through a homogeneous mechanism, which is expected due to the high supersaturation levels.
ii. The associated thermodynamic parameter B was determined to be 8.98×10^{4}.
iii. The critical nucleus size is very small for the supersaturation levels investigated and decreases with an increase in supersaturation.
iv. The energy barrier to nucleation (nucleation work) decreases with an increase in supersaturation and the nucleation energy for the system is extremely small.

The findings of Mangere *et al.* (2009) confirm the ability of the experimental method of Roelands *et al.* (2004) to correctly determine nucleation rates in reactive precipitation. They conclude that the method can be used for systems where homogeneous nucleation is dominant which builds upon the findings of Roelands *et al.* (2004) and suggests that this experimental method can be used to predict the nucleation rates of any system (Mangere *et al.*, 2009).

2.8.2 Determining the Induction Time for Precipitating Systems

As discussed in Section 2.1.2.1 the induction time can be used to calculate the nucleation rate for a given system as well as to infer details about the controlling nucleation mechanism. This sub-section deals with methods for the determination of the induction time.

Many related properties including solution conductivity, intensity of transmitted or scattered light, heat released, activity of precipitated ions and pH of solution have been utilized to determine the induction period for both soluble and sparingly soluble systems (Chien *et al.*, 1999). According to Mullin (2001) induction periods are often measured visually but more sensitive techniques are also possible for detecting new crystalline matter e.g. laser light scattering or electric zone sensing methods. Reactant solutions are generally quickly mixed in an agitated vessel and the time recorded when the first physical property change or the first crystals are detected. However, when the induction time is less than 5s complications can arise because the mixing time will be of the same order of magnitude or greater than the induction time. Therefore, in order to measure short induction periods, two things are essential: (i) very rapid mixing, and, (ii) a fast and sensitive method for the detection of the appropriate system changes (Sohnel & Mullin, 1978).

Sohnel & Mullin (1978) used a stopped-flow method where conductivity changes were measured in supersaturated solutions. They investigated the precipitation of various relatively insoluble electrolytes i.e. $CaCO_3$, $BaCO_3$, $SrCO_3$ and $CaMoO_4$ at 25°C. The method worked by instantaneously

mixing two stable solutions which subsequently reacted to form a supersaturated solution. When the system started to precipitate the concentration of the electrically conducive species started to decrease and this caused the solution conductivity to decrease. The time in which the conductivity was constant was inversely proportional to the supersaturation. Sohnel & Mullin (1978) used this method to determine the induction periods, for the substances listed above, in the range of 10s to approximately 5ms. They plotted $\log(t_{ind})$ versus $log\,(S)^{-2}$ (see Figure 6 on page 11) and found interfacial tensions of 83, 109, 116 & 95 mJ/m^2 for $CaCO_3$, $BaCO_3$, $SrCO_3$ and $CaMoO_4$ respectively. Sohnel & Mullin (1978) stated that the present method was a substantial improvement on turbidity methods as these methods rely on the crystal nuclei to grow to sizes large enough to create a turbidity that is dense enough to be detected. Thus, a method utilizing conductivity measurements is able to register changes in the solution physical properties long before turbidity develops and is thus more accurate.

Sohnel & Mullin (1988) investigated the dependence of the induction period on solution supersaturation and found that it was possible to deduce whether the new phase appearance was governed either by nucleation (or nucleation followed by growth) or by growth alone. They also found that, in specific cases, the dependence could also reveal the controlling nucleation mechanisms of nucleation and/or growth (Sohnel & Mullin, 1988).

Verdoes *et al.* (1992) used induction times from seeded and unseeded precipitation experiments in order to determine the nucleation and growth rates for calcium carbonate. The induction times were determined from recordings of the signal of the Ca-ion-selective electrode versus time (Verdoes *et al.*, 1992). van der Leeden *et al.* (1992) used similar theoretical expressions to Verdoes *et al.* (1992) to determine the nucleation and growth of barium sulphate using induction times. A supersaturation range for $BaSO_4$ of S = 4.54 - 11.08 was investigated with the induction times being determined from the time evolution of the conductivity of the solution (van der Leeden *et al.*, 1992). van der Leeden *et al.* (1992) found that in both seeded and unseeded solutions the induction time changed with supersaturation, seed number density and with the presence of an additive. This work was continued by further developing general expressions for the nucleation rate, rate of crystal growth by two-dimensional nucleation, and the induction time in unseeded precipitation in the presence of additives (van der Leeden *et al.*, 1993).

Chien *et al.* (1999) investigated the induction time of the $CaCO_3$ system using a conductivity method similar to Sohnel & Mullin (1978). The induction time was estimated from the desupersaturation curve i.e. plot of solution conductivity versus time (see examples below). In Figure 23, t_v represents the time interval between the instant of supersaturation creation and crystal formation observable to the naked eye.

Chien *et al.* (1999) stated that the induction period was easily determined at high reagent concentrations but at low reagent concentrations it was more difficult to determine. Thus, the conductivity profiles were enlarged to solve this problem. The fluctuation in the conductivity reading between t_{ind} and t_v was explained by Chien *et al.* (1999) as follows: concentration fluctuations in the bulk solution redissolve some nuclei due to the creation of undersaturation. This fluctuation was

found to be more prominent at lower concentrations where the probability to create undersaturation was higher.

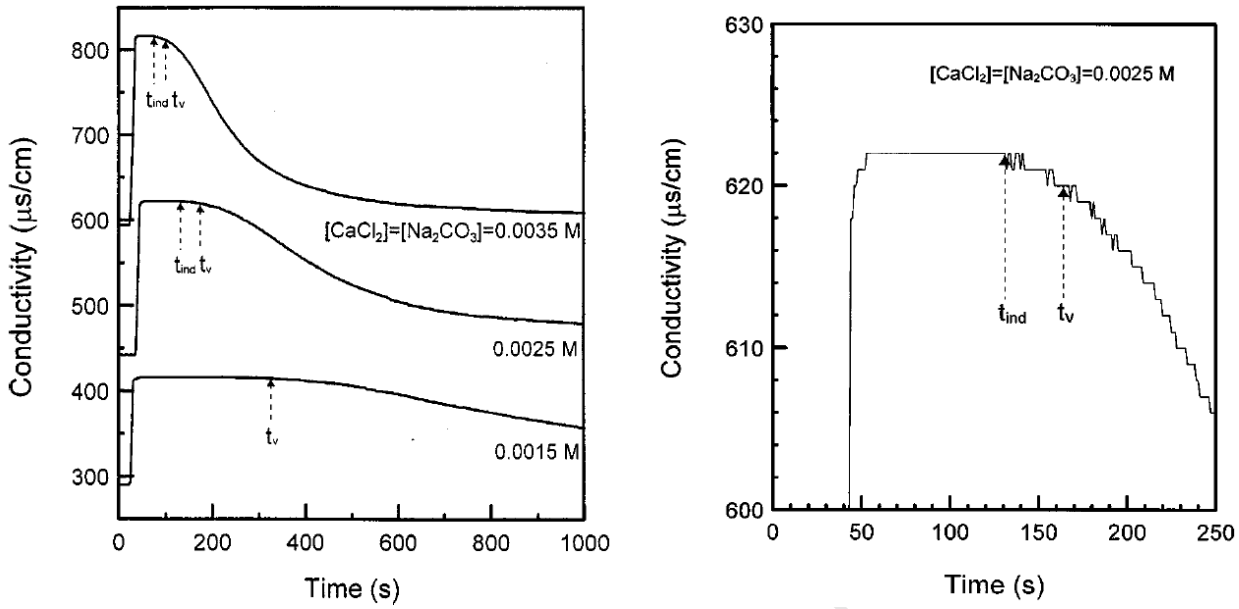

Figure 23: (left) Conductivity profiles for various reagent concentrations, and, (right) Enlarged conductivity-time curve for [$CaCl_2$] = [Na_2CO_3] = 0.0025 M (Chien *et al.*, 1999)

Using the results found by Chien *et al.* (1999) a plot of the induction time versus supersaturation could be determined (see Figure 24 below).

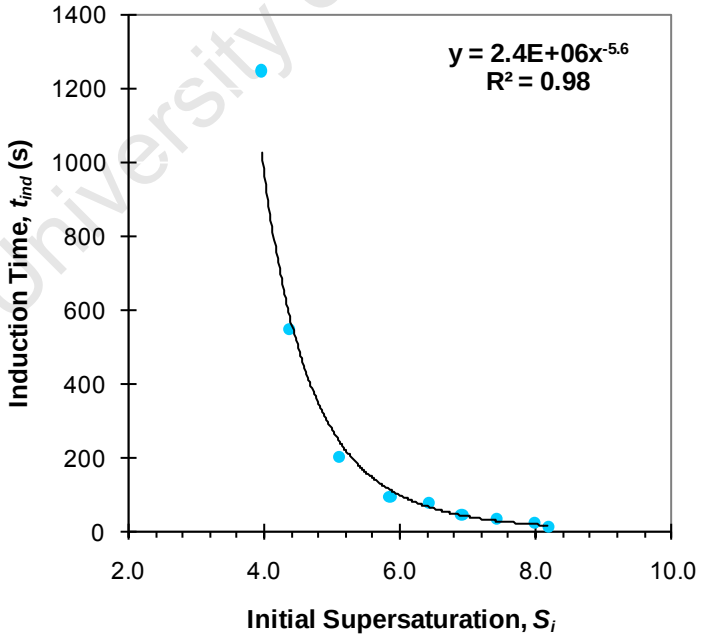

Figure 24: Plot of induction time versus supersaturation developed from the data of Chien *et al.* (1999)

As can be seen from Figure 24, the data fits very well to a power-law trend:

$$t_{ind} = 2.4 \times 10^6 S_i^{-5.6} \quad \text{... (95)}$$

Chien *et al.* (1999) were able to fit their data to an expression derived by van der Leeden *et al.* (1991) (cited in Chien *et al.*, 1999) for unseeded precipitation of $CaCO_3$ and found the theory was capable of describing their data quite well.

Tai & Chien (2003) further extended the work of Chien *et al.* (1999) to interpret the effects of operating variables on the induction period using a cluster coagulation model. The operating variables investigated were supersaturation, temperature, additives and seeds. They found that a decrease in the supersaturation and temperature resulted in an increase in the induction time. They also found that an additive prolonged the induction time whereas the addition of seeds reduced it. In comparison of the experimental and model results, the model was found to be suitable in determining the effects of the operating variables on the induction time (Tai & Chien, 2003).

2.8.3 Methods for Determining the Growth and/or Aggregation Rates

In precipitation processes the crystal growth rate is a significant parameter as it controls the final specific properties of the precipitate, such as the morphology and final particle size distribution (Salvatori *et al.*, 2002). Thus it is important that the growth rate is known or can be easily calculated for a desired precipitation process. According to Lindenberg *et al.* (2008) the determination of agglomeration models and of the corresponding agglomeration rates continues to be a major challenge. A number of authors have reported that a size-independent agglomeration rate can be used to describe their experimental data however others have concluded that the agglomeration process cannot be considered to be a size-independent phenomenon (Lindenberg *et al.*, 2008).

Aoun *et al.* (1999) developed a new method to derive the nucleation and growth rates from batch precipitation experiments by measuring the supersaturation and PSD. According to Aoun *et al.* (1999), the solid concentration during precipitation is given by the following expression

$$C_S(t) = \frac{\rho_c}{M_s}\int_0^t \phi_v L^3 \psi(L,t) dL \quad \text{... (96)}$$

where C_s is the concentration of the solid phase [mol.m^{-3}], ρ_C is the density of the solid phase [kg.m^{-3}], M_S is the molar mass of the solid phase [kg.mol^{-1}], ϕ_V is the volumetric shape factor, L is the crystal size [m], and ψ is the crystal size distribution density function [#.m^{-4}]. Differentiation of Equation (96) yields

$$\frac{dC_S(t)}{dt} = \frac{\rho_C}{M_S}\int_0^\infty \phi_V L^3 \frac{\partial\psi(L,t)}{\partial t} dL \quad \text{... (97)}$$

The classical population balance with negligible agglomeration and breakage is expressed as

$$\frac{\partial\psi(L,t)}{\partial t} + \frac{\partial[\psi(L,t)G(L,t)]}{\partial L} = r_N(t)\delta(L-L^*) \quad \text{... (98)}$$

Aoun *et al.* (1999) make the following assumptions in the development of the model

a. $G(L,t)$ is expressed as the linear growth rate i.e. $G(L,t) = \frac{dL}{dt}$.
b. The variation of solid mass consecutive to nucleation is negligible.

By multiplying Equation (98) by $\phi_V L^3 \rho_c / M_S$ and integrating, Equation (99) is obtained

$$\frac{dC_S(t)}{dt} = \frac{3\rho_C}{M_S}\int_0^\infty \phi_V L^2 G(L,t)\psi(L,t) dL \quad \text{... (99)}$$

Equation (99) is integrated with respect to time in order to avoid excessive errors due to numerical derivation of the experimental data.

$$C_S(t) - C_S(t_0) = \frac{3\phi_V\rho_C}{M_S}\int_{t_0}^t\int_0^\infty L^2\psi(L,t)G(L,t) dL dt \quad \text{... (100)}$$

The extent of precipitation can be calculated from

$$X(t) = \frac{C_S(t)}{C_s(t\to\infty)} \quad \text{... (101)}$$

$$X(t) - X(t_0) = \frac{3\phi_V\rho_C}{M_S C_S(t\to\infty)} \int_{t_0}^{t}\int_0^{\infty} L^2\psi(L,t)G(L,t)dLdt \quad \text{... (102)}$$

The Armenante and Kirwan (1989) correlation, which is especially suited for microparticles (L < 30μm), was chosen by Aoun *et al.* (1999) for calculation of the mass transfer coefficient

$$\frac{k_d L}{D} = 2 + 0.52 \times \left(\frac{L^{\frac{4}{3}} P_S^{\frac{1}{3}}}{v}\right)^{0.52} \left(\frac{v}{D}\right)^{0.33} \quad \text{... (103)}$$

where k_d is the mass transfer coefficient [m.s^{-1}], D is the diffusivity [m^2.s^{-1}], and v is the kinematic viscosity [m^2.s^{-1}]. The crystal growth rate is generally expressed as a function of supersaturation by using different functions containing several kinetic constants (Aoun *et al.*, 1999). A good representation of many mechanisms of the surface reaction model and the surface nucleation model, over a limited supersaturation range, is the following power law expression (Aoun *et al.*, 1999)

$$G(L,t) = k_r[C_{int}(t) - C^*]^r \quad \text{... (104)}$$

where C_{int} is the solid-liquid interface concentration [mol.m^{-3}] and C^* is the equilibrium concentration [mol.m^{-3}]. In conclusion of the development of the model, Aoun *et al.* (1999) express the overall growth rate as the combination of two equations as follows

$$\left[\frac{G(L,t)}{k_r}\right]^{\frac{1}{r}} + \frac{3\rho_C\phi_V G(L,t)}{M_S k_d \phi_S} = C(t) - C^* \quad \text{... (105)}$$

where k_r is a growth rate parameter [m.s^{-1}], r is the crystal growth kinetic order, and ϕ_S is the surface shape factor. Equations (102) & (105) are the primary equations for an iterative non-linear optimization. The growth kinetics were determined by the following procedure:

i. For given values of the parameters, k_r and r, Equation (102) was solved to obtain $G(L,t)$ using $C(t)$ from the experimental desupersaturation curve and $k_d = k_d(L)$ from Equation (103).
ii. The calculated curve of the crystal growth rate $G(L,t)$ was inserted into Equation (102) to yield the calculated profile of the extent of precipitation during the process. A close agreement between this profile and the experimental profile of $X_{exp}(t)$ shows that the postulated G function is an adequate kinetic expression for the crystal growth rate.

From experiments on the batch precipitation of barium sulphate, Aoun *et al.* (1999) found the following results

i. The linear rate of crystal growth followed a 2.1 power law with supersaturation and the process was surface integration limited.
ii. The crystal growth rate for stoichiometric experiments over the entire concentration range was found to be

$$G = (2.5 \pm 0.5) \times 10^{-7}\left(\sqrt{C_{Ba}C_{SO_4}} - \sqrt{P_S}\right)^{(2.1\pm0.1)} \quad \text{... (106)}$$

iii. The assumption that the intrinsic crystal growth rate is independent of crystal size was correct as the values of r and k_r did not vary with initial supersaturations.
iv. The obtained value of r was close to 2 which is a commonly published kinetic order, especially for sparingly soluble salts.

Hove *et al.* (2008) used experimental PSDs in combination with the moment equations in order to determine the kinetics of iron precipitation. The moments were plotted against time to determine the

active precipitation mechanisms. Assuming size independent growth and aggregation and negligible breakage, the nucleation rate, J, molecular growth rate, G, aggregation kernel, β, and the aggregation rate, r_{agg}, were calculated from the first four moments respectively (Hove *et al.*, 2008) (Randolph & Larson, 1988)

$$J = \frac{m_0}{t} \quad \text{... (107)}$$

$$G = \frac{\Delta m_3}{3\Delta t \bar{m}_2} \quad \text{... (108)}$$

$$\beta = \frac{\Delta m_2}{\Delta t(\bar{m}_1)^2} - 2\frac{G}{\bar{m}_1} \quad \text{... (109)}$$

$$r_{agg} = -\frac{\beta m_0^2}{2} \quad \text{... (110)}$$

Equations (107)-(110) were used to compute the respective process rates from the PSD data (Hove *et al.*, 2008). These equations are simple but of limited use as they are not a function of S.

In most precipitating systems, when both growth and aggregation occur simultaneously, it is very difficult to determine the rates of both these size enlargement mechanisms (Bramley *et al.*, 1996). This is because the analytical description of such systems is very complicated except for the most idealized cases (Bramley *et al.*, 1996). Thus, the use of numerical methods is required however the integration of these methods often entails considerable computational effort.

Bramley *et al.* (1996) have introduced a general method that uses the numerical technique of Hounslow *et al.* (1988) to solve a population balance model and determine the rates of growth and aggregation in a batch system. The starting assumptions in the development of the method include

a. Only growth and aggregation occur (no nucleation occurs).
b. The growth rate is independent of length i.e. size-independent growth.
c. Aggregation is size-independent.
d. Growth and aggregation occur simultaneously.

Bramley *et al.* (1996) use a differential technique in combination with the DPB to calculate the rates of growth and aggregation. Hounslow *et al.* (1988) show that for size-independent aggregation in a batch system, using length as the internal co-ordinate, the rate of change of the zeroth and third moments can be represented by

$$\frac{dm_0}{dt} = -\frac{1}{2}\beta_0 m_0^2 \quad \text{... (111)}$$

$$\frac{dm_3}{dt} = 0 \quad \text{... (112)}$$

If a size-independent growth term is included, then Equation (111) remains unchanged because growth does not affect the number of particles in a system. However from Equation (77), the rate of change of the third moment becomes

$$\frac{dm_3}{dt} = 3Gm_2 \quad \text{... (113)}$$

If the rates of change of the zeroth and third moments are known, values of β_0 and G may be calculated directly from the experimental data using Equations (111) and (113) (Bramley *et al.*, 1996). The values for the moments can be easily extracted from the experimental PSDs and the rates of change can be calculated graphically or numerically from these. According to Bramley *et al.* (1996) the above method can be generalized to allow for size-dependent aggregation and a source function. The source function, B_u, accounts for the movement of crystals into the field of view of the particle size analyzer and is defined as the rate of appearance of crystals in the first interval of the size range

covered by the particle size analyzer (Bramley *et al.*, 1996). The differential method is modified in order to allow for the additional variable, B_u, by introducing a time derivative, the rate of change of the crystal number in the first size interval, $\dot{N}_1$. For aggregation only

$$\Phi_0 = \frac{\dot{m}_0|_{agg}}{\beta_0} \quad \text{... (114)}$$

$$\Phi_1 = \frac{\dot{N}_1|_{agg}}{\beta_0} \quad \text{... (115)}$$

By recalling that m_0 is the total number of particles in a system, it follows that

$$\dot{m}_0|_{agg} = \sum_{i=1}^{n_{eq}} \dot{N}_i|_{agg} \quad \text{... (116)}$$

Using Equation (80) and Equation (43) for a size-dependent kernel then

$$\phi_0 = \sum_{i=1}^{n_{eq}} N_{i-1} \sum_{j=1}^{i-2} 2^{j-1+1} f(\bar{L}_{i-1}, \bar{L}_j) N_j + \sum_{i=1}^{n_{eq}} \frac{1}{2} f(\bar{L}_{i-1}, \bar{L}_{i-1}) N_{i-1}^2 - \sum_{i=1}^{n_{eq}} N_i \sum_{j=1}^{i-1} 2^{j-1} \times f(\bar{L}_i, \bar{L}_j) N_j - \sum_{i=1}^{n_{eq}} N_i \sum_{j=1}^{n_{eq}} f(\bar{L}_i, \bar{L}_j) N_j \quad \text{... (117)}$$

where, for example, $\bar{L}_i$ is the arithmetic average of the upper and lower sizes of interval i (Bramley *et al.*, 1996). Also from Equation (80) with $i = 1$,

$$\Phi_1 = -N_1 \sum_{j=1}^{n_{eq}} f(\bar{L}_1, \bar{L}_j)\, N_j \quad \text{... (118)}$$

Similarly for growth only

$$\Phi_2 = \frac{\dot{N}_1|_g}{G} \quad \text{... (119)}$$

$$\Phi_3 = \frac{\dot{m}_3|_g}{G} \quad \text{... (120)}$$

Using Equation (82) gives

$$\Phi_2 = \frac{2}{(1+r)L_1}\left[\left(1 - \frac{r^2}{r^2-1}\right) N_1 - \frac{r}{r^2-1} N_2\right] \quad \text{... (121)}$$

To evaluate Equation (120) an expression for the discrete form of the moments of a PSD is required. Hounslow *et al.* (1988) show an appropriate equation is

$$m_j = \sum_{i=1}^{n_{eq}} \bar{L}_i^j N_i \quad \text{... (122)}$$

where $\bar{L}_i$ is the arithmetic average of the upper and lower sizes of interval i. Thus using Equation (122) together with Equations (81) and (82), Φ_3 is given by

$$\Phi_3 = \frac{2}{(1+r)L_1}\left[\left(1 - \frac{r^2}{r^2-1}\right) N_1 - \frac{r}{r^2-1} N_2\right] \bar{L}_1^3 + \sum_{i=2}^{n_{eq}} \frac{2}{(1+r)L_i}\left[\frac{r}{r^2-1} N_{i-1} + N_i - \frac{r}{r^2-1} N_{i+1}\right] \bar{L}_i^3 \quad \text{... (123)}$$

Equations (114), (115), (119) and (120) may be written as three equations in terms of the three unknown rate constants as follows

$$\dot{m}_0 = \beta_0 \Phi_0 + B_u \quad \text{... (124)}$$

$$\dot{m}_3 = G \Phi_3 + B_u \bar{L}_1^3 \quad \text{... (125)}$$

$$\dot{N}_1 = G \Phi_2 + \beta_0 \Phi_1 + B_u \quad \text{... (126)}$$

The method for determining the growth and aggregation kinetics using the model developed by Bramley *et al.* (1996) is as follows

i. The values of $\dot{m}_0$, $\dot{m}_3$, $\dot{N}_1$, Φ_0, Φ_1, Φ_2, and Φ_3 can all be calculated from the experimental PSDs.
ii. Equations (124), (125) and (126) can then be solved to obtain the rate constants.
iii. A model can be fitted to the rate constants. The growth and aggregation rates and the source function will often depend on supersaturation. According to Bramley *et al.* (1996) from the variations in the reactant concentrations with time, some measure of supersaturation can be calculated and correlations of the dependence of B_u, G and β_0 on supersaturation can be determined.

iv. Using an experimental PSD as the initial condition and the dependence of the source function, growth, and aggregation on supersaturation to calculate the rates, a batch experiment can be simulated.

v. The predicted and experimental moments and PSDs may be compared to determine which aggregation kernel best describes the experimental data.

Bramley *et al.* (1996) tested the above method on the precipitation of calcium oxalate monohydrate (COM). In order to calculate the total calcium and oxalate concentrations (for calculation of the change in supersaturation over time), the following mass balance equations were used. If W_0 is the initial concentration of seeds [kg.m^{-3}] at time t, the total number of moles of calcium oxalate deposited per unit volume, Δn, is given by

$$\Delta n = \frac{W_t - W_0}{M} \quad \text{... (127)}$$

where M is the molecular weight of COM [kg.kmol^{-1}] and W_t is the solids concentration [kg.m^{-3}] at time t, which can be calculated by recalling that the third moment is proportional to the volume of particulate matter, yielding

$$W_t = \rho_s \frac{\pi}{6} m_3 \quad \text{... (128)}$$

where ρ_s is the density of COM [kg.m^{-3}]. The total ion concentrations at time t can then be calculated from

$$T_{Ca^{2+}} = T^0_{Ca^{2+}} - \Delta n \quad \text{... (129)}$$

$$T_{Ox^{2-}} = T^0_{Ox^{2-}} - \Delta n \quad \text{... (130)}$$

Thus, from the concentrations in Equations (129) and (130) the solution supersaturation can be calculated.

Bramley *et al.* (1996) concluded with the following findings

i. The number of crystals decreased and the PSDs broadened as the experiment proceeded, which is characteristic of aggregation. Also, the total volume of particulate matter increased as a consequence of growth (see Figure 25 below).

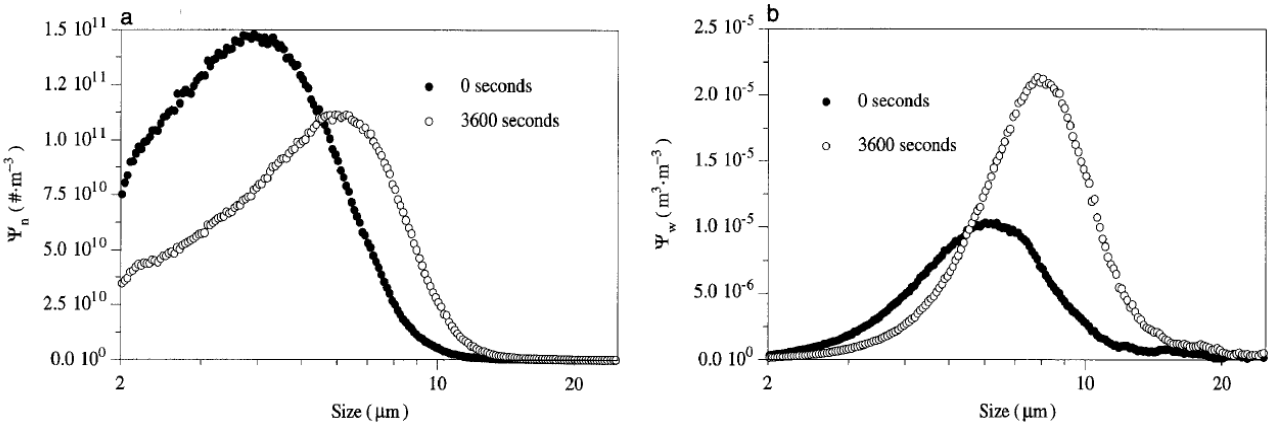

Figure 25: Typical PSDs at the beginning and completion of a batch precipitation experiment by (a) number and (b) volume (Bramley *et al.*, 1996)

ii. The growth rate could be determined without specific knowledge of the aggregation kernel.

iii. The aggregation rate constants could be determined for different types of aggregation kernels.
iv. Comparison of the simulated and experimental PSDs and their moments showed that it is possible to distinguish between the kernels and determine which is appropriate for modelling the aggregation of the test system.
v. A size-independent aggregation kernel was found to be most appropriate to model COM precipitation.
vi. The results show that the growth of COM is well described by McCabe's ΔL law and is independent of the form of the aggregation kernel.

Bramley *et al.*s (1996) method has been extensively cited in literature and has been successfully used by Bramley *et al.* (1997), Andreassen & Hounslow (2004) and Collier & Hounslow (1999) (to name a few) for extracting the growth and aggregation rates from a chosen precipitation system.

2.9 Model System – Calcium Oxalate Monohydrate

2.9.1 Choice of a Moderately Soluble System

For purposes of this work, a moderately soluble system is defined as a system exhibiting a solubility product somewhere between that of a soluble system (e.g. Na_2SO_4 with K_{sp} (25°C) ~ 10^4 (mol.dm^{-3})^2) and a sparingly soluble system (e.g. NiS with K_{sp} (25°C) ~ 10^{31} (mol.dm^{-3})^2).

The model system for this dissertation was chosen to be calcium oxalate monohydrate (COM). COM was chosen as there has been numerous research conducted on this compound in the medical, chemical and chemical engineering industries. Adequate kinetic research is also readily available which can be used for comparison purposes.

2.9.2 General Information and Significance

Research into the crystallization of calcium oxalate hydrates is of significance as they are the major inorganic constituent of human kidney stones (Bramley *et al.*, 1997). The growth and aggregation of calcium oxalate crystals is known to lead to stone formation and thus a better understanding of the underlying mechanisms will aid in prevention of the disease. However, this will not be directly investigated in this dissertation.

2.9.3 Physical and Chemical Properties

2.9.3.1 Behaviour and Solubility

Calcium oxalate monohydrate is an ionic crystal which dissociates into anions and cations as follows

$$CaC_2O_4 \cdot H_2O \leftrightarrow Ca^{2+} + C_2O_4^{2-} + H_2O \quad \text{... (131)}$$

The supersaturation ratio for calcium oxalate monohydrate can be calculated from the following equation

$$S = \left[\frac{\gamma_{Ca^{2+}} \cdot C_{Ca^{2+}} \cdot \gamma_{C_2O_4{}^{2-}} \cdot C_{C_2O_4{}^{2-}} \cdot a_{H_2O}}{K_{sp}}\right]^{\frac{1}{2}} \quad \text{... (132)}$$

Previous literature has found that calcium oxalate can precipitate in either the monohydrate, dihydrate (COD) or trihydrate (COT) form or as a combination of these hydrates (see Section 2.9.3.2). The solubility products of these hydrates at different temperatures have been found in literature as follows:

Table 6: Solubility products for calcium oxalate hydrates at T = 25 & 37°C

Hydrate	Temperature [°C]	K_{sp} x 10^{-9} $[mol.dm^{-3}]^2$	Reference
COM	25	2.00	Nancollas & Gardner (1974)
		2.15	Calculated by OLI Stream Analyser (2008)
		2.32	Generalic (2003)
	37	2.24	Bramley *et al.* (1996)
		2.47	Calculated by OLI Stream Analyser (2008)
		2.51	Garside *et al.* (1982)
COD	25	3.70	Garside *et al.* (1982)
COT	25	5.30	Garside *et al.* (1982)
	37	8.20	Garside *et al.* (1982)

Calcium oxalate monohydrate has a density of 2.2g.cm^{-3} and a molar mass of 146.1g.mol^{-1} (Mullin, 2001).

2.9.3.2 Morphology and Polymorphism

As previously mentioned, calcium oxalate exhibits pseudo polymorphism and thus can precipitate as either monoclinic monohydrate, tetragonal dihydrate, or, triclinic trihydrate, depending on the process conditions. Nancollas & Gardner (1974) stated that the different hydrates (or a mixture of them) will precipitate depending on the initial supersaturation, temperature and calcium to oxalate molar ratio. Thus, the kinetics of nucleation and growth of the individual hydrates may be quite different (Nancollas & Gardner, 1974). Garside *et al.* (1982) discussed the formation of different hydrates at various temperatures in their MSMPR reactor:

At T = 9°C: COT only
T = 20 - 30°C: Mixture of COM, COD and COT likely
T = 25°C: COM is stable, while COD and COT are metastable
T = 37°C: fully COM

They concluded that COT was the predominant phase below 25°C while COM dominated above 30°C. They also stated the particular hydrate formed is ultimately governed by kinetic rather than thermodynamic factors (Garside *et al.*, 1982). Bretherton & Rodgers (1998) found that the favoured phases were COT at 18°C, COD at 38°C and COM at 58°C. They also stated that since COD and COT are thermodynamically unstable with respect to COM, their higher solubilities make them the kinetically favoured phases. Other literature found that calcium oxalate precipitated fully as COM at

25 and 37°C (Sohnel *et al.*, 1997). Thongboonkerd *et al.* (2006) found in their experiments that the most frequently crystallized hydrate was COM. At higher concentrations they found COM dendrites forming. Houcine *et al.* (1997) found that in continuous experiments, the total product consisted only of COT, while in semi-batch single feed experiments the product mostly consisted of COM and COD.
A number of images showing the morphology and various forms of calcium oxalate can be found below. These images show that calcium oxalate exhibits different morphologies for the three polymorphs and can form agglomerates, dendrites, intergrowths and twins under various operating conditions.

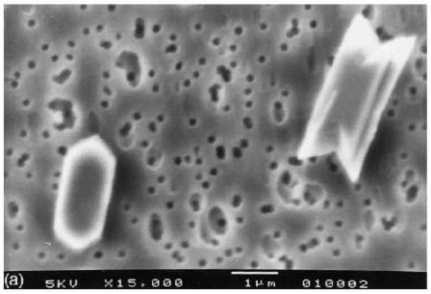

Figure 26: SEM photograph of COM (Houcine *et al.*, 1997)

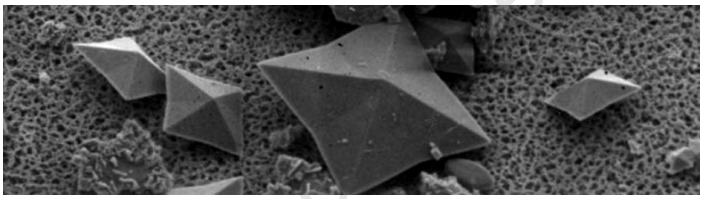

Figure 27: SEM photograph of COD crystals – mag. 1040x (Bretherton & Rodgers, 1998)

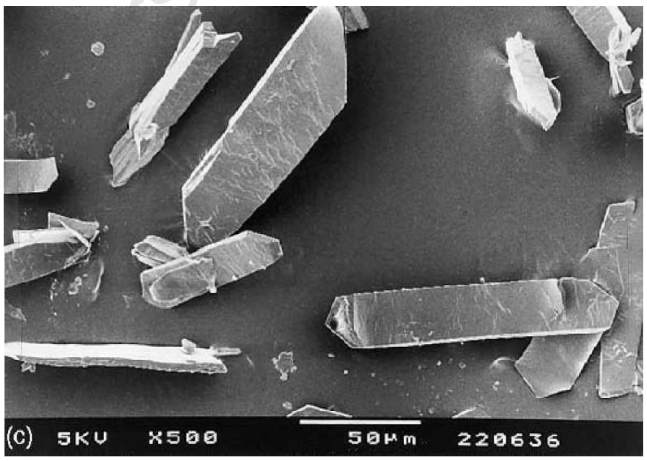

Figure 28: SEM photograph of COT (Houcine *et al.*, 1997)

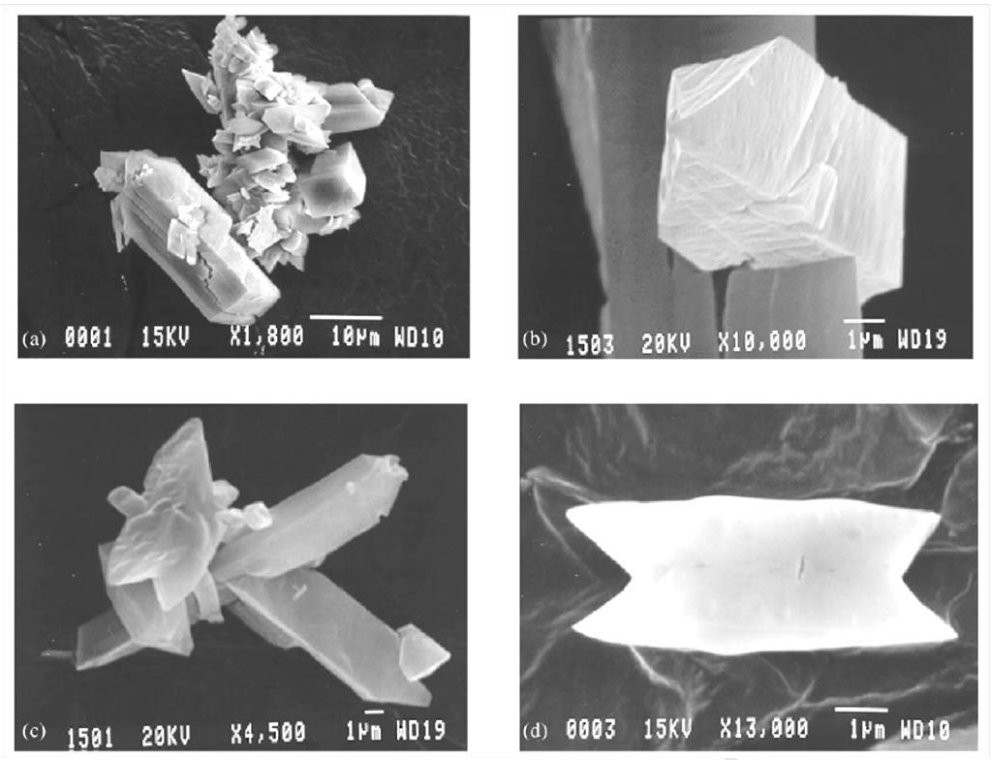

Figure 29: SEM images of calcium oxalate crystals – (a) calcium oxalate agglomerate, (b) Intergrowth of particles, (c) Agglomeration and disruption effects, and, (d) Twinned particle (Zauner & Jones, 2000)

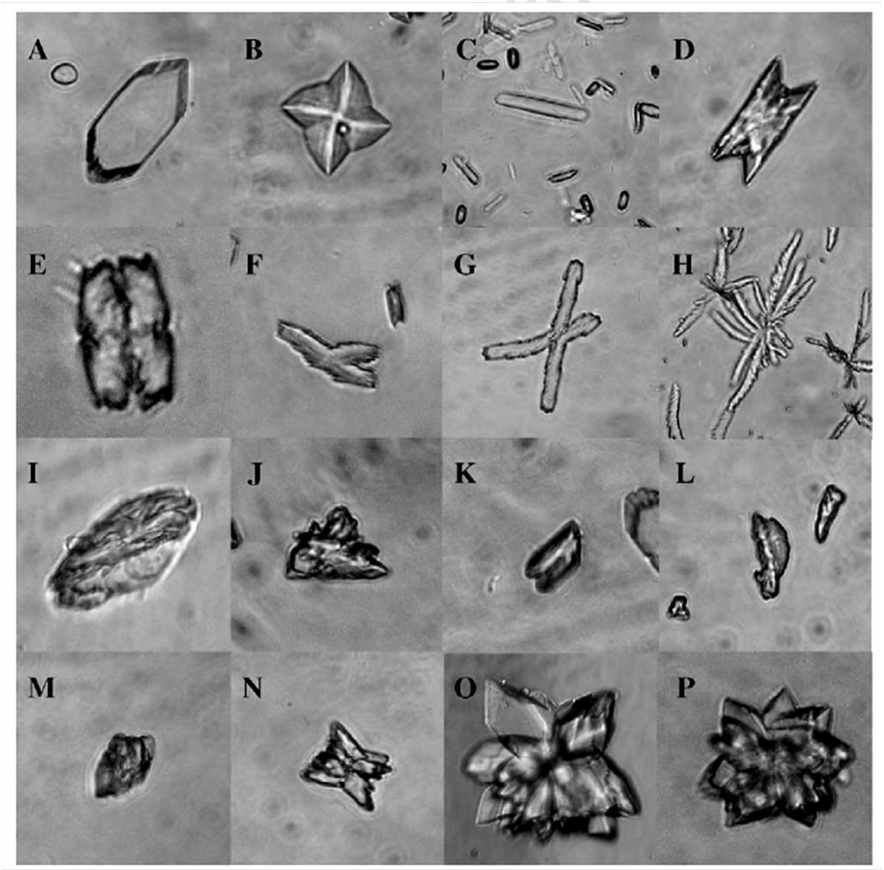

Figure 30: Different forms of calcium oxalate viewed under an optical microscope: A – monoclinic prismatic COM, B – weddellite COD, C –COT needles, D & E – COM twins, F to H – COM dendrites, I to M – atypical forms, N to P – COM agglomerates (Thongboonkerd *et al.*, 2006)

A diagram showing the precipitation boundary for calcium oxalate at 25°C is illustrated in Figure 31 below. The diagram shows the solubility boundary as well as the metastable region. It also gives an indication of the concentrations at which different morphologies of calcium oxalate are formed.

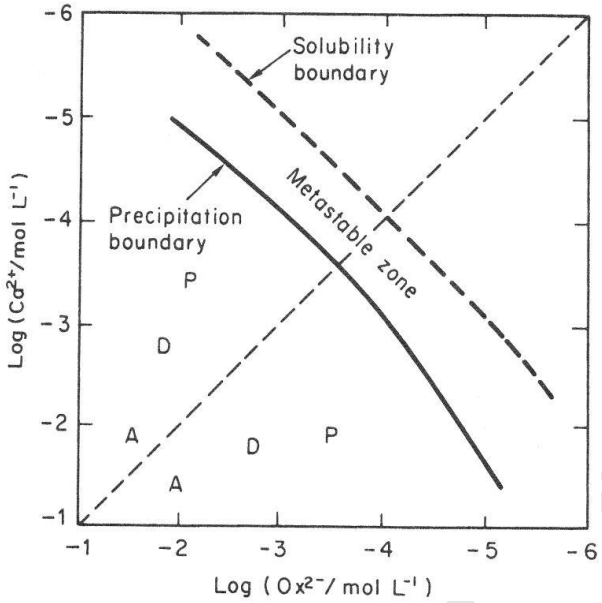

Figure 31: Precipitation boundary (24hr) for calcium oxalate at 25°C. P = plates, D = dendrites, and, A = agglomerates (Mullin, 2001)

2.9.4 Kinetics and Mechanisms

From an analysis of the current literature, not much can be found with regards to the nucleation and disruption kinetics of calcium oxalate. However, a reasonably large amount of research has been conducted on the growth and aggregation kinetics. The main reason for this is due to the fact that the growth and aggregation of calcium oxalate are of a greater importance in medical research related to kidney stone formation.

2.9.4.1 Nucleation Kinetics

Nielsen (1955) (cited in Finlayson, 1978) has shown that in filtered solutions of poorly soluble salts, the induction time for precipitation obeys

$$t_{ind} = gC^n \quad \ldots (133)$$

where C is the square root of the molar ion concentration product of the precipitation salt and g and n are empirical constants. It was found that for calcium oxalate at 25°C, g = 1.03×10^{-7} s and n = -3.33 (Finlayson, 1978).

Garside *et al.* (1982) determined nucleation rates for calcium oxalate monohydrate of J = 2.78×10^7 to 8.33×10^7 m^{-3}.s^{-1} for a feed concentration of 0.001 M and T = 37°C (cited in Zauner & Jones, 2000).

Brown *et al.* (1991) measured the change in turbidity over an initial relative supersaturation range of σ = 10.5 - 32. For COM precipitation at 37°C the values of A and B for the CNT were determined to be (Brown *et al.*, 1991)

$$J = 2.344 \times 10^7 exp\left[-52.09/(lnS)^2\right] \quad \ldots (134)$$

Zauner & Jones (2000) used the data found by Brown *et al.* (1991) to determine the nucleation rates such that a comparison could be made with their own work. They calculated the nucleation rates to be in the range of J = 2.78×10^{4} to 2.7×10^{10} m^{-3}.s^{-1} for Brown *et al.*'s (1991) work.

Zauner & Jones (2000) investigated the kinetics of calcium oxalate using a 300mL draft tube baffled (DTB) precipitation reactor under continuous operation. The kinetics were investigated for a number of parameters including feed concentrations of 0.01 and 0.04 M, various residence times and feed point positions, stirrer speeds of 4.2 - 33.4 Hz, and a temperature of 37°C. Zauner & Jones (2000) found nucleation rates over the range of J = 5.6×10^{8} to 2.8×10^{11} m^{-3}.s^{-1}. They also concluded that the nucleation rate was dependent on the power input and the feed point position, suggesting a mixing-controlled nucleation process.

2.9.4.2 Growth Kinetics

Nielsen (1960) investigated the growth kinetics of the precipitation of calcium oxalate by measuring the change in electrical conductance of the solution. Below 1 mM it was found that the linear rate of crystal growth was proportional to the 3.3rd power (surface-reaction controlled), while above 1 mM the rate was proportional to the concentration (diffusion controlled) (Nielsen, 1960).

Nielsen & Toft (1984) found growth rates in the range of G = 2.8×10^{-10} to 1.11×10^{-8} m.s^{-1}, Garside *et al.* (1982) determined growth rates in the range of G = 3.4×10^{-9} to 5.0×10^{-8} m.s^{-1}, while Kavanagh (1992) (cited in Zauner & Jones, 2000) found a growth rate of G = 1.08×10^{-8} m.s^{-1}, all for COM precipitation.

Nancollas & Gardner (1974) investigated the growth kinetics of COM by inoculating supersaturated solutions with seed crystals and following the rate of crystal growth conductimetrically. They found that the growth of COM was surface-reaction controlled and exhibited a second-order power law relationship with supersaturation. Other literature found the same second-order dependence of supersaturation on the growth rate (Gardner & Nancollas, 1975).

Sohnel *et al.* (1997) used an isoperibolic reaction twin calorimeter to study the kinetics of calcium oxalate monohydrate at 25 and 37°C. They used a crystal growth rate expression of

$$G = k_g(C - C^*)^g \quad \ldots (135)$$

and found the kinetic constant and order of crystal growth to be k_g = 0.090 ml^{2}.s^{-1}.mol^{-1} and g = 2.47 at 25°C and k_g = 4.27×10^{-3} ml^{2}.s^{-1}.mol^{-1} and g = 1.65 at 37°C respectively. These results were determined for supersaturation ranges of ΔC = (1.18-4.95)×10^{-3} mol.dm^{-3} at 25°C and ΔC = (1.7-5.4)×10^{-3} mol.dm^{-3} at 37°C.

In the batch precipitation of calcium oxalate monohydrate from a seeded system at 37°C with S_i = 2.34 – 3.61, Bramley *et al.* (1997) determined the growth rate expression to be

$$G = 1.45 \times 10^{-9}(S - 1)^2 \quad \ldots (136)$$

with the range of G being shown in Figure 32 below. Bramley *et al.* (1997) stated that the results for experiments using shaken flasks were indistinguishable to those found for experiments using a stirred tank reactor. They concluded (from Figure 32) that the growth rate data gave a very good fit to a parabolic rate law (consistent with the spiral growth mechanism).

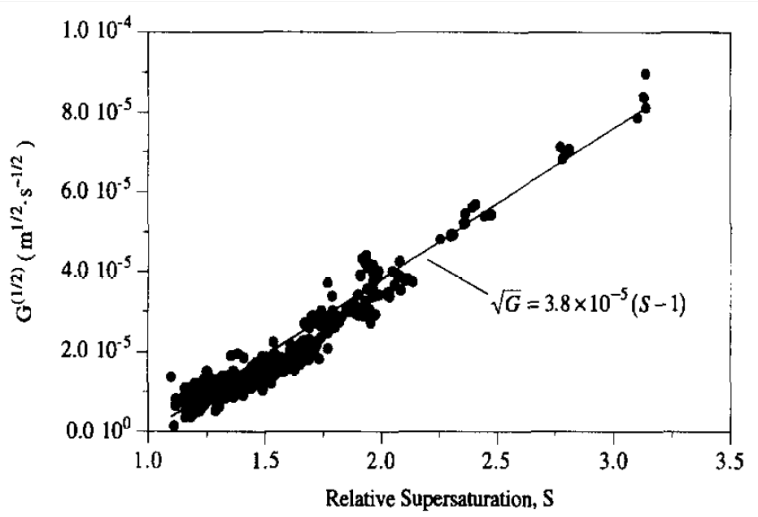

Figure 32: The dependence of growth rate on supersaturation for all experiments (Bramley *et al.*, 1997)

Bramley *et al.* (1997) also found that the growth of calcium oxalate was independent of the agitation of the system (agitation rate = 1.33 - 1.83Hz). This was explained by the idea that if the growth rate depends on the stirring rate then the growth is transport controlled. However, if the growth rate does not change with the stirring rate, then the growth is surface controlled. Thus, the results were concluded to be correct as the growth rate was independent of the agitation rate and fitted well to a surface-controlled growth mechanism. In similar experiments to Bramley *et al.* (1997), Bramley *et al.* (1996) found that the growth rate of calcium oxalate monohydrate was well described by McCabe's ΔL law i.e. size-independent growth and was independent of the form of the aggregation kernel.

Zauner & Jones (2000) found crystal growth rates in the range of G = 0.75×10^{-8} to 4.7×10^{-8} m.s^{-1} for calcium oxalate. The crystal growth rate was found to be virtually independent of the stirrer speed thus indicating a surface-integration controlled growth mechanism, in agreement with the above literature findings. Thus, Zauner & Jones (2000) used a power-law relationship (see Equation 41) and found a growth rate constant of k_g = 5.9×10^{-10} m.s^{-1} with an order of growth of g = 2. Figure 33 shows the linear relationship of the square root of the growth rate versus the relative supersaturation found by Zauner & Jones (2000).

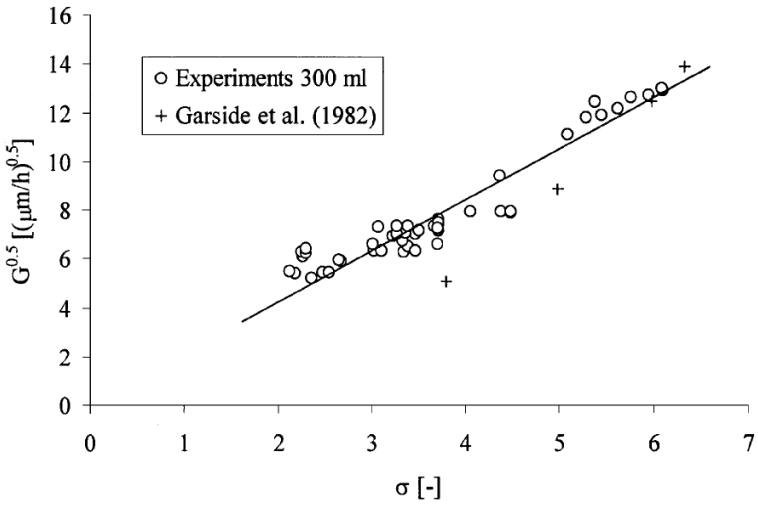

Figure 33: Growth rate of calcium oxalate versus supersaturation (Zauner & Jones, 2000)

Millan *et al.* (1997) investigated the influence of the crystal morphology on the growth kinetics of COM. They found that the crystal growth kinetics were dependent on the crystal morphology, crystal perfection, and degree of aggregation.

2.9.4.3 Aggregation Kinetics

Bramley *et al.* (1996) investigated a number of aggregation kernels (see Table 1) in order to determine the best-fit kernel for the batch precipitation of calcium oxalate monohydrate at 37°C. The kernels were compared to the PSDs and moments and Bramley *et al.* (1996) concluded that the size-independent kernel yielded the best fit to the experimental data. In similar experiments, over a wider range of conditions, Bramley *et al.* (1997) also found that the size-independent aggregation kernel best described the precipitation of COM. Figure 34 shows the aggregation rate constants determined by Bramley *et al.* (1997). It was found that the aggregation rate was dependent on the agitation rate and the oxalate ion concentration.

Mumtaz & Hounslow (2000) developed a novel Poiseuille flow crystallizer (PFC) to investigate the effect of the process conditions on the aggregation of COM. They found that, at low shear rates, the aggregation rate constant varied linearly with the shear rate, while a maximum point was observed as the shear rate was increased. It was also found that the aggregation rate was independent of the solution ion ratio at a constant supersaturation (Mumtaz & Hounslow, 2000). This is in agreement with what was found previously by Bramley *et al.* (1997).

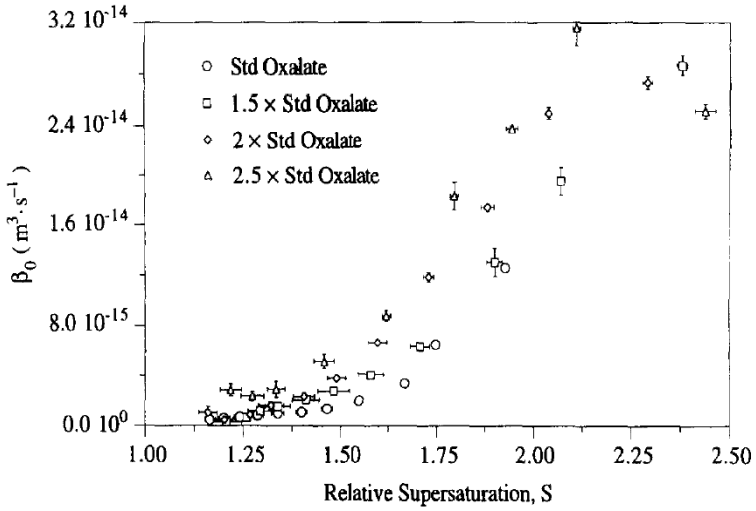

Figure 34: The dependence of the aggregation rate constant on supersaturation (Bramley *et al.*, 1997)

Zauner & Jones (2000) found the agglomeration rate to increase with power input, exhibiting a maximum point (see Figure 35). From previous literature, which found that the agglomeration kernel increased linearly with the growth rate, Zauner & Jones (2000) proposed the following final modeling equation for the agglomeration kernel

$$\beta_{aggl} = 5.431 \times 10^{-17}(1 + 2.296\varepsilon^{0.5} - 2.429\varepsilon)S^{2.15} \quad \ldots (137)$$

The first term of the equation relates to the agglomeration effects independent of the power input while the bracketed term relates to the agglomeration effects due to shear (Smoluchowski's theory).

The final term describes the reduced agglomeration efficiency found experimentally at higher shear rates (Zauner & Jones, 2000).

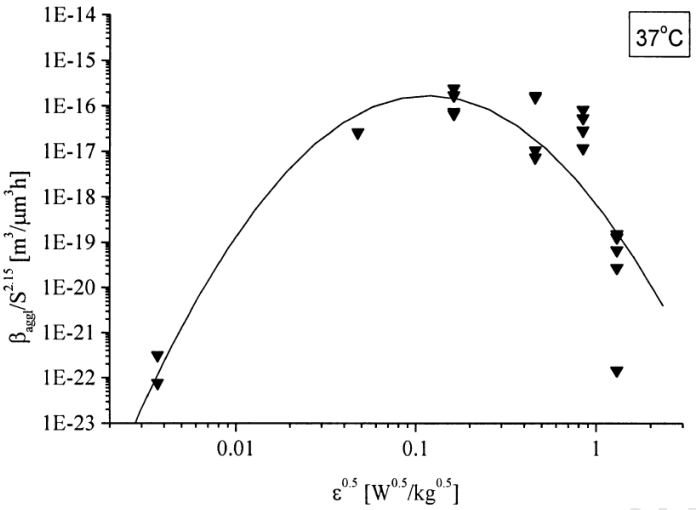

Figure 35: Agglomeration rate of calcium oxalate versus energy dissipation (Zauner & Jones, 2000)

Zauner & Jones (2000) also concluded that both decreased agglomeration efficiency and increased breakage lead to a decrease in the number of agglomerates observed at higher stirrer speeds.

Liew *et al.* (2003) investigated the seeded batch precipitation of calcium oxalate at varying stirring speeds (600 - 1000rpm), ion ratios (1 - 5) and mean particle sizes (5.3 - 17.9µm). From literature findings they expected the aggregation rate constant to be dependent on the growth rate, mean particle size and stirrer speed. From multiple linear regression they found the following expression

$$\beta_0 \propto G^{0.983} \bar{d}_{3,0}{}^{1.085} N^{-1.278} \quad \ldots (138)$$

with the resulting fit being shown in Figure 36 below.

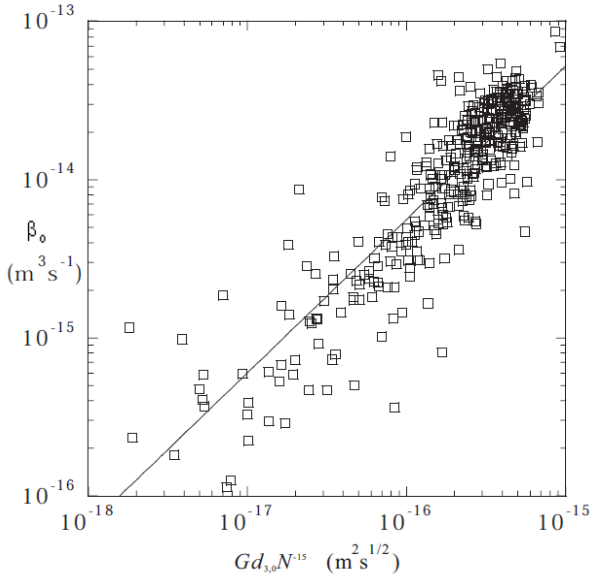

Figure 36: Correlation between the aggregation rate constant to the instantaneous growth rates, average particle diameter and stirrer speed (Liew *et al.*, 2003)

2.9.4.4 Breakage Kinetics

Zauner & Jones (2000) found the disruption kinetics for COM, accounting for breakage due to both particle splitting and attrition, to increase linearly with power input. They also assumed, from previous literature findings, that the disruption kernel decreased linearly with the growth rate resulting in the following proposed relationship

$$\beta_{disr} = 6.25 \times 10^{-5} \varepsilon \, S^{-2.15} \quad \ldots (139)$$

2.10 Overall Objectives and Key Questions

From an extensive literature review the overall objectives of the dissertation are as follows:

i. To investigate the precipitation behaviour of a moderately soluble system i.e. calcium oxalate under varying operational parameters. This investigation will aid in the decision about a suitable seed preparation technique which will be used to produce seeds for the kinetic experiments.
ii. To determine the growth and aggregation kinetics for the calcium oxalate system by at first repeating the experimental work of Bramley *et al.* (1996). Higher initial supersaturation levels will be investigated as well as higher seed masses.
iii. To determine whether experimental methods (such as that of Bramley *et al.* (1996)) for determining the growth and aggregation kinetics is viable for more insoluble systems. The determination of the induction time for calcium oxalate monohydrate will aid with this decision.

The following key questions have been formulated:

i. Is the mixing in the batch reactor sufficient such that supersaturation gradients are avoided?
ii. How does the level of supersaturation with respect to concentrations, agitation rate, addition rate and addition method affect the size and morphology of precipitated particles?
iii. What are the conditions necessary to produce seeds that satisfy the criteria for use in the kinetic experiments?
iv. What combinations of initial supersaturation and mass of seeds effectively suppress nucleation from occurring during the kinetic experiments?
v. How do the growth and aggregation kinetics for calcium oxalate compare to those found in literature?
vi. Do seed samples with similar sizes but different morphologies yield the same kinetic results?
vii. What is the limit on the initial supersaturation, such that Bramley *et al.*'s (1996) experimental method is still viable?

Chapter 3

PREPARATION OF SEEDS FOR A MODERATELY SOLUBLE SYSTEM

3.1 Introduction

Methods for preparing suitable seeds for precipitation systems are not easily found in literature and are generally not known. Of those seed preparation methods available, most are system specific and thus cannot be utilized in other situations. For systems that are moderately to sparingly soluble i.e. $K_{sp} \leq 10^{-8}$ $(mol^2.dm^{-3})^2$ preparing satisfactory seeds can be very difficult. These systems incur high supersaturations due to the order of the solubility products and thus are governed by homogeneous nucleation. This results in the production of a large number of very small particles which makes measuring the PSD very difficult. Also, good mixing in the reactor becomes a significant factor. Poor mixing results in supersaturation gradients which can alter the seed population with regards to size and shape quite dramatically. This means that good mixing is required for the production of a reproducible seed population.

This chapter is dedicated to determining a suitable preparation technique for calcium oxalate monohydrate seeds. This will be done by investigating how operating parameters such as the supersaturation, agitation rate, reactant addition rate and addition method affect the size and morphology of precipitated calcium oxalate particles. Thus, this will aid in understanding the precipitation behaviour of the chosen system. The best seeds produced will be utilized in the following chapter of this dissertation.

3.2 Materials and Methods

3.2.1 Seed Preparation Guidelines

With reference to Section 2.5 the following constraints have been imposed on the precipitated particles such that a desired seed population is produced:

a. The precipitate must be pure COM.
b. The PSD of the seeds must lie within the range of 2 - 60μm as a 100μm aperture tube will be utilized in the Coulter Counter for measurement of the PSD.
c. The PSD must be monodisperse with respect to both number and volume.
d. The PSD must be narrow and the maximum size of the particles must not exceed 50μm. This is to ensure that the seeds do not grow out of the field of view of the Coulter Counter when utilized in the kinetic experiments.
e. The precipitated particles must be well-grown and possibly not agglomerated.
f. A reasonable yield of precipitate must be produced such that the seeds may be further utilized in the kinetic experiments.

3.2.2 Reagents

De-ionized water (Milli-Q Water Purification System, Millipore, USA) was utilized in all cases. All chemicals used in the preparation of solutions were analytical grade. These included: anhydrous calcium chloride ($CaCl_2$) (Merck, South Africa), sodium oxalate ($Na_2C_2O_4$) (Sigma-Aldrich Co., Germany) and sodium chloride (NaCl) (Merck, South Africa). Purchased COM powder ($CaC_2O_4.H_2O$) (Merck, South Africa) was used as a base case for comparison with the prepared seed PSD and SEM results.

3.2.3 Experimental Set-Up and Operating Conditions

The seed preparation experiments were conducted in a 1L jacketed and baffled glass reactor (see figure below for the experimental set-up).

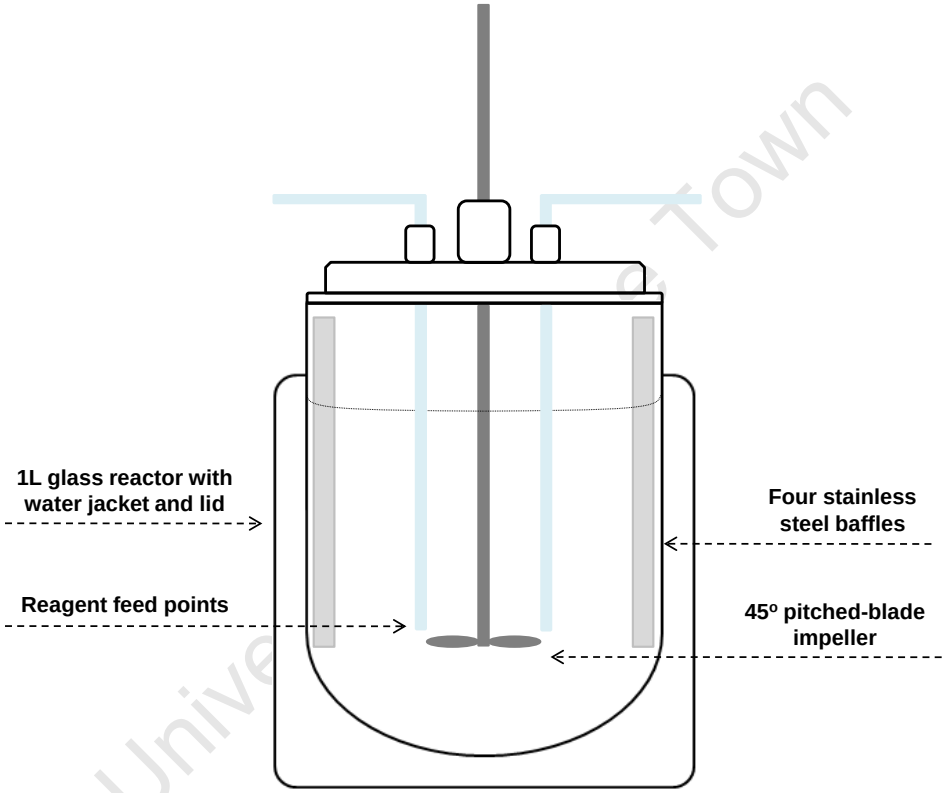

Figure 37: Reactor set-up for seed preparation experiments

All seed preparation experiments were conducted at a constant temperature of 37±2°C. Twenty-four different combinations of the operating parameters, shown in Table 7 below, were used to investigate the behaviour of the calcium oxalate system. All experiments were repeated three times for reproducibility and error analysis.

Table 7: Operating variables for seed experiments

Addition Methods	S_i	N (rpm)	Addition Rate
Single-jet (A) Double-jet (B)	10 (1) 17 (2) 30 (3)	300 (1) 900 (2)	Slow – over 60min (1) Fast – over 5min (2)

The letters/numbers in brackets represent the seed sample I.D. e.g. A.1.2.1 represents a seed sample prepared with the following combination of variables: (i) single-jet addition method, (ii) S_i = 10, (iii) N = 900rpm and (iv) slow addition of reactants. The supersaturation was calculated using OLI Stream Analyser (OLI Systems, 2008) and Equation (64). The supersaturation values listed in Table 7 refer to the initial maximum supersaturation that would be reached if both reagent solutions were instantaneously mixed together. For the single-jet addition method only one of the reagent feed pipes shown in Figure 37 was utilized.

It was decided not to investigate supersaturations below 10 as the yield of precipitate per experiment was too low. Also, a maximum agitation rate of 900 rpm was chosen as the turbulence in the reactor was quite high at this value and thus in order to prevent the breakage of particles higher agitations were not investigated.

3.2.4 Reactant Addition Methods

Two reactant addition methods were investigated viz. single-jet and double-jet methods. For both methods the reagent piping was placed perpendicular to the impeller blades such that the reactant feed points were positioned just above the impeller tips (see Figure 37). For both methods the reactant solutions were heated to 37±2°C in a water bath before use.

3.2.4.1 Single-Jet Method

500mL of $Na_2C_2O_4$ was pumped into the reactor initially containing 500mL of $CaCl_2$ using a peristaltic pump. For the slow reactant addition rate, $Q_{Na_2C_2O_4}$ = 8.33 mL.min^{-1} for 60 minutes. The solution was left to equilibrate for a further 15min. For the fast reactant addition rate, $Q_{Na_2C_2O_4}$ = 100 mL.min^{-1} for 5 minutes. The solution was left to equilibrate for a further 30 minutes.

3.2.4.2 Double-Jet Method

250mL each of $CaCl_2$ and $Na_2C_2O_4$ were pumped simultaneously into the reactor initially containing 500mL of de-ionized water. For the slow reactant addition rate, $Q_{CaCl_2} = Q_{Na_2C_2O_4}$ = 4.17 mL.min^{-1} over 60 minutes. The solution was left to equilibrate for a further 15 minutes. For the fast reactant addition rate, $Q_{CaCl_2} = Q_{Na_2C_2O_4}$ = 50 mL.min^{-1} for 5 minutes. The solution was then left to equilibrate for a further 30 minutes.

3.2.5 Filtering and Storage

Once the prescribed reaction time had been reached the bulk solution in the reactor was vacuum filtered using 0.22µm cellulose membranes (Millipore, USA). The precipitate was dried in an oven, weighed (for calculation of the yield) and then transferred to a storage container.

3.2.6 Particle Size and Morphology Analysis

3.2.6.1 Beckman Coulter Multisizer III – Coulter Counter

The PSD of each seed sample was measured using the electrical sensing zone technique as discussed in Section 2.4.3. The Coulter Counter was fitted with a 100μm aperture tube which enabled particles within the size range of 2 - 60μm to be measured. A 4wt% NaCl saturated CaC_2O_4 solution was utilized as the electrolyte in the Coulter Counter as it was found that the COM particles were slightly soluble in water-based electrolytes. The electrolyte solution was filtered twice using 0.22μm cellulose membranes (Millipore, USA) before use to ensure a low background count of particles. Also, filtering the solution reduced the possibility of the aperture tube becoming blocked during readings due to foreign particles in the solution.

A specific mass of the dried seed sample was weighed out and suspended in 10mL of electrolyte solution. An aliquot of the seed suspension was transferred to the Coulter Counter beaker containing 150mL of electrolyte. The seed PSD was then measured using a control mode of 1000μL. The PSD of each sample was measured three times for reproducibility and error analysis purposes.

3.2.6.2 Scanning Electron Microscopy (SEM)

Photographs of the seed samples were conducted using a Scanning Electron Microscope (Nova NanoSEM 230, FEI). Images were taken using a voltage of 5.0 keV, ETD detector (SE mode) and with magnifications of between 1000 and 10 000x. The SEM images were used to determine the shape of the particles and to investigate the state of the particles i.e. polymorphs, agglomerates, intergrowths, twins etc.

3.2.6.3 X-Ray Diffraction (XRD)

All seed samples were analysed using a D8 Advance X-ray laboratory diffractometer (Bruker AXS). The diffractometer had a Co source ($\lambda_{K\alpha 1}$ = 0.178897 nm) and a VÅNTEC position-sensitive detector. The XRD patterns were used for confirmation of the precipitated product i.e. calcium oxalate as well as for determination of the level of hydration i.e. mono-, di- or tri-hydrate.

3.2.7 Dye Visualization Experiments

Dye visualization experiments were conducted to observe the mixing in the batch reactor. Two solutions containing coloured dye (red and blue) were pumped into the reactor initially containing 500mL of water using the double-jet reactant addition method. The reactor was agitated at 600rpm and the rate of addition of the solutions was relatively fast (approximately Q = 153 mL.min^{-1}). A high reactant addition rate was used to observe the mixing of the reactants under extreme conditions. The addition of the solutions was filmed using a Casio EXILIM Pro EX-F1 Digital Camera operating at 600 fps. It was decided that only the double-jet method would be imaged as conclusions for the single-jet method could be drawn by looking at a single jet stream.

Image processing was conducted using MATLAB (MathWorks, 2011) to improve the viewing quality of the images (i.e. to highlight the addition of the reactants and their dispersion into the bulk liquid).

3.3 Results

3.3.1 Mixing in the Batch Reactor

3.3.1.1 Mixing Times and Scales

The macro, meso and micro mixing times as well as the Reynolds number, average energy dissipation rate and impeller power were calculated according to the equations in Section 2.3.3 of the Literature Review chapter (sample calculations can be found in Appendix C.1). As mentioned by Perry *et al*. (1997) fully turbulent flow exists for Reynolds numbers above 10^4. As can be seen from Figure 38, Re = 10^4 at approximately N = 168 rpm. Thus the system is fully turbulent for the two impeller speeds investigated in the seed preparation experiments i.e. N = 300 & 900 rpm.

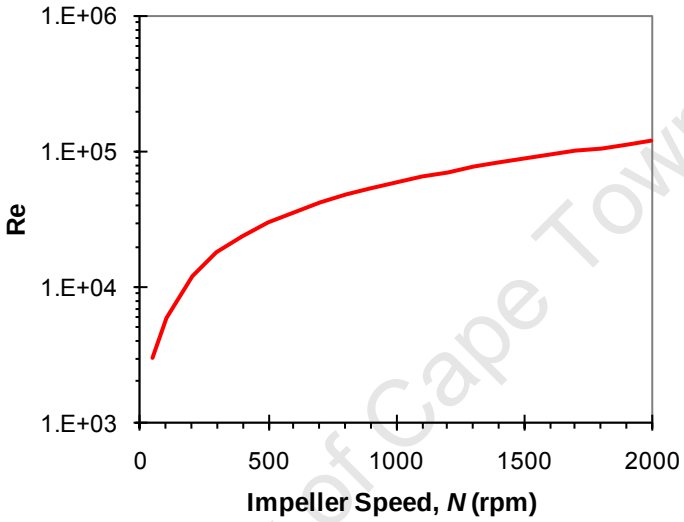

Figure 38: Reynolds number versus impeller speed

The macro, meso and micro mixing times for various impeller speeds are shown in Figure 39 below. All three mixing times were calculated for a total reactor volume of 1L.

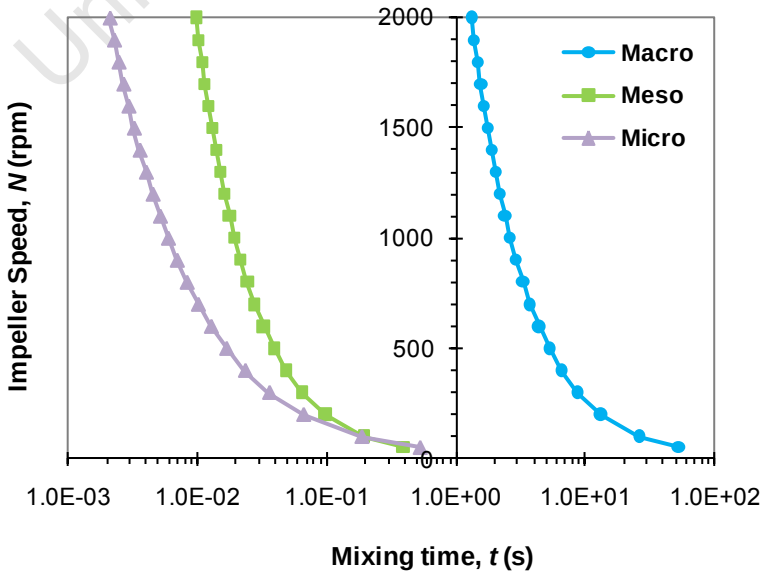

Figure 39: Macro, meso and micro mixing times in the batch reactor with V = 1L versus impeller speed

As expected the macro, meso and micro mixing times all decrease with an increase in the impeller speed. Figure 39 shows a region below N = 100rpm where the meso and micro mixing times overlap i.e. point of overlap → (t, N) = (0.212, 91.8). This could possibly be due to the fact that the system is not fully turbulent below an impeller speed of 168rpm.

The seed experiments were conducted using a semi-batch approach thus the volume of the bulk solution changed with time as the reactants were pumped into the reactor. Initially V = 0.5L and over a specified period of time the reactants were added until the total volume in the reactor was 1L. Thus, both the macro and meso mixing times increased as the total volume increased (see Figures 40 & 41 below).

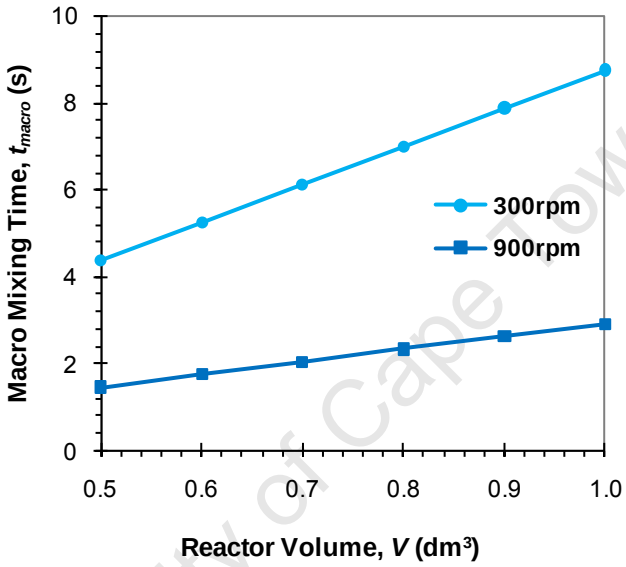

Figure 40: Macro mixing time as a function of reactor volume

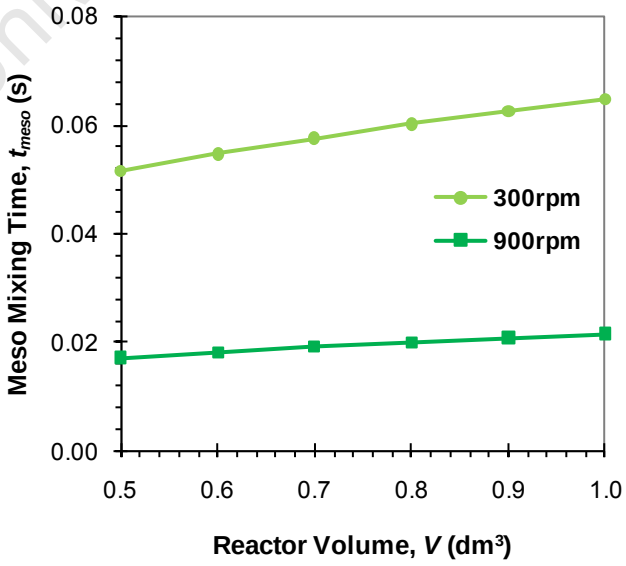

Figure 41: Meso mixing time as a function of reactor volume

It is interesting to note from Figures 40 & 41 that a lower agitation rate appears to have a more significant influence on the mixing times, with respect to an increase in the reactor volume, in comparison to a higher agitation rate (shown by the steeper slope).

A plot of the impeller power and average energy dissipation rate versus the agitation rate can be found in Figure 42 below. Both variables show a power-law trend with impeller speed.

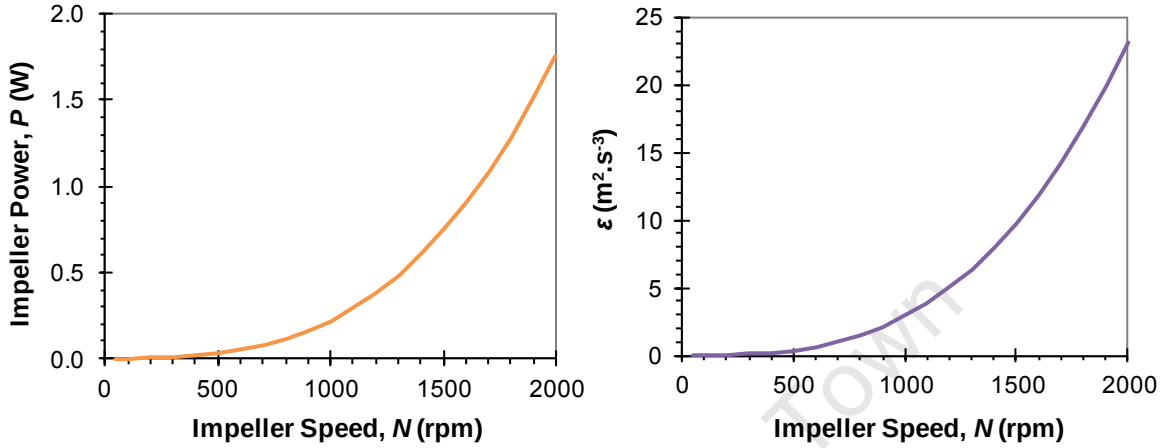

Figure 42: Impeller power (left) and average energy dissipation rate (right) versus impeller speed

A summary of the mixing times and variables at the start of a seed experiment can be found in Table 8 below.

Table 8: Mixing times and variables for N = 300 & 900 rpm at the start of a seed experiment i.e. V = 0.5L

Mixing Variables	300 rpm	900 rpm
t_{macro} (s)	4.38	1.46
t_{meso} (s)	0.0515	0.0172
t_{micro} (s)	0.0359	0.0069
Re	1.79×10^{4}	5.37×10^{4}
q_C ($m^3.s^{-1}$)	4.56×10^{-4}	1.37×10^{-3}
P (W)	5.94×10^{-3}	1.60×10^{-1}
$\bar{\varepsilon}$ ($m^2.s^{-3}$)	0.234	6.33

The macro mixing time for an agitation rate of 300rpm is relatively high at the start of a seed experiment. This will most likely create different environments, with respect to supersaturation, within the batch reactor especially for the fast reactant addition rate.

3.3.1.2 Dye Visualization Experiments

Figure 43 below shows images from the dye visualization experiments where the image on the right-hand side has undergone image processing as discussed in Section 3.2.7. The left-hand image of Figure 43 shows the positions of the baffles, impeller, reactant feed points as well as the height of the

bulk solution. The reactant feed points were manually positioned as close to the impeller as possible however as can be seen from Figure 43 this distance is not ideal.

Figure 43: Mixing image before (left) and after (right) additional image processing

From the dye visualization experiments the addition of "reactant" solutions and their dispersion into the bulk liquid could be observed. Figure 44 shows a number of images with a time interval of 0.0167s between each frame and a total time from frame (a) to (l) of 0.183 seconds. As a peristaltic pump was utilized in all experiments the "time between pumps" of the peristaltic pump seems to be approximately the same time as that from frame (a) to (l). This however corresponds only to the chosen addition rate of Q = 153 mL.min^{-1}.

The 45° pitched-blade impeller rotated in a clockwise direction and had a downwards pumping action. The blue reagent stream is swept to the back of the reactor while the red reagent stream is swept to the front. From the progression of images in Figure 44 it can be seen that both reagent streams are forced to the bottom of the reactor below the impeller. The reagents appear to mix beneath the impeller; however this is difficult to observe. The most likely case for mixing in the reactor is that after the reagent solutions are forced to the bottom of the reactor, they are swept to the sides of the reactor and back up towards the liquid surface in a "circular" motion. This is what is expected from the chosen axial-flow impeller and baffled reactor (see Figure 15 in Section 2.3.2). However, this cannot be completely quantified by the images in Figure 44.

Figure 44 shows that the mixing in the batch reactor is relatively good; nevertheless this is highly dependent on a number of factors e.g. agitation rate and addition rate. At the high addition rate investigated the reactants are not dispersed instantaneously throughout the bulk and seem to stay near the bottom of the reactor without mixing for longer than desired. However, the addition rates for the actual seed experiments are considerably lower. Thus, the reactants would be dispersed more effectively throughout the bulk solution. Problems with mixing may be observed for the single-jet method-high addition rate combination since one reagent is added to the bulk of another. This will most likely produce very high points of local supersaturation thus resulting in different environments throughout the reactor.

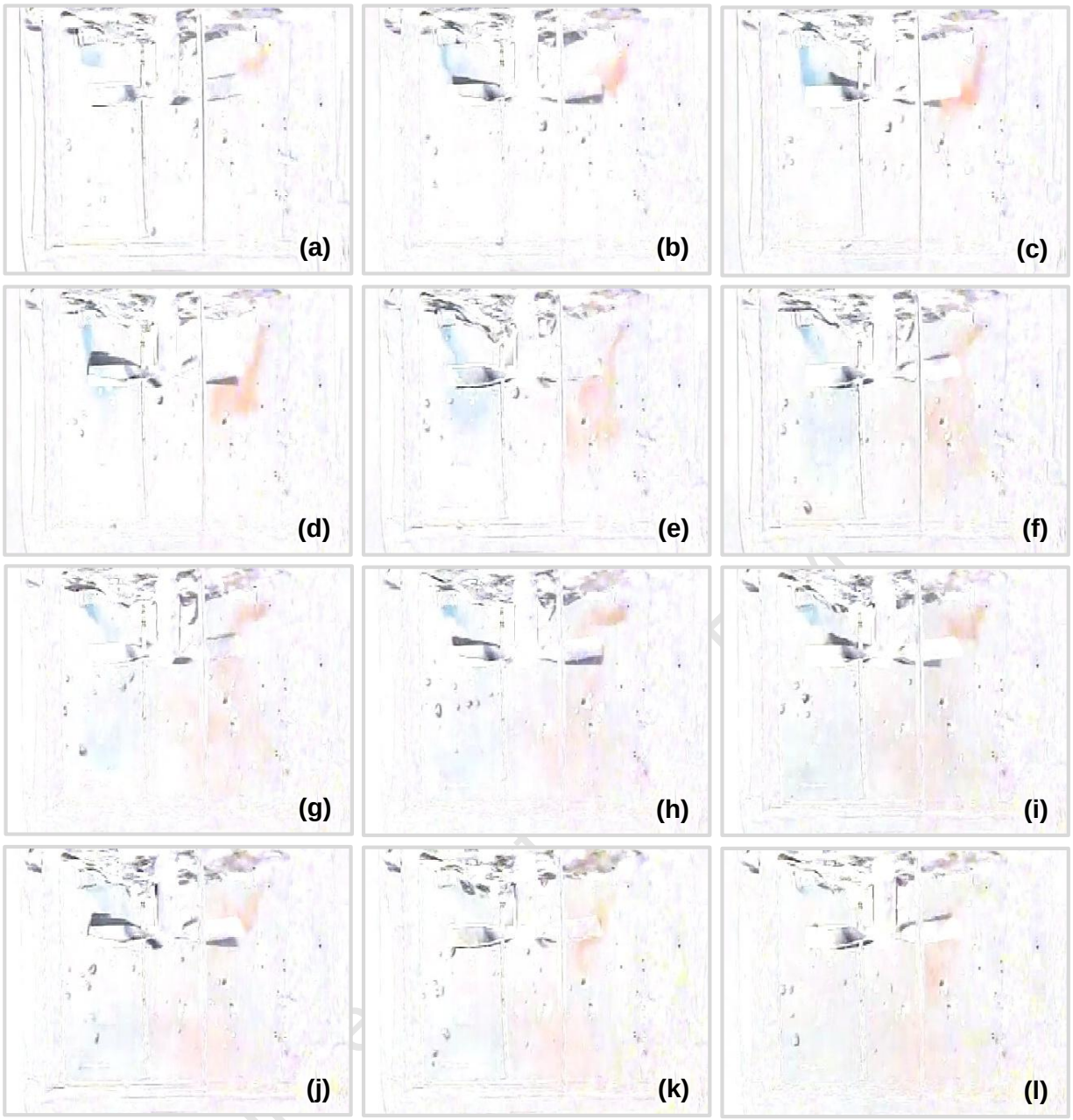

Figure 44: Images highlighting the addition of reagents and their dispersion into the bulk solution

3.3.2 Seed Particle Size Distributions

A complete set of PSDs for each of the seed samples can be found in Appendix A. Number and volume PSDs for a purchased COM sample have been included for comparison purposes. Raw data and sample calculations can be found in Appendix C.1.

The following combined PSDs highlight the similarities and differences between the seed samples. It was decided to plot the PSDs with varying supersaturation in each of the figures so that, for a given combination of conditions, a direct comparison could be made between the different levels of initial supersaturation investigated. Also, by making cross-comparisons between figures the effect of agitation rate, addition rate and addition method on the PSD could be deduced.

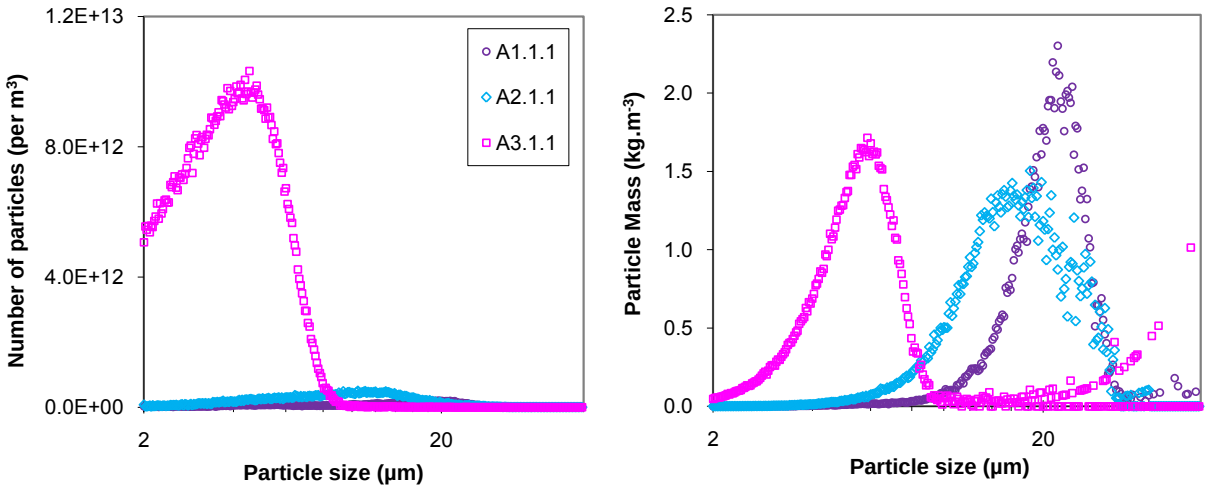

Figure 45: Single-jet, N = 300rpm & slow addition seed PSDs at varying S_i

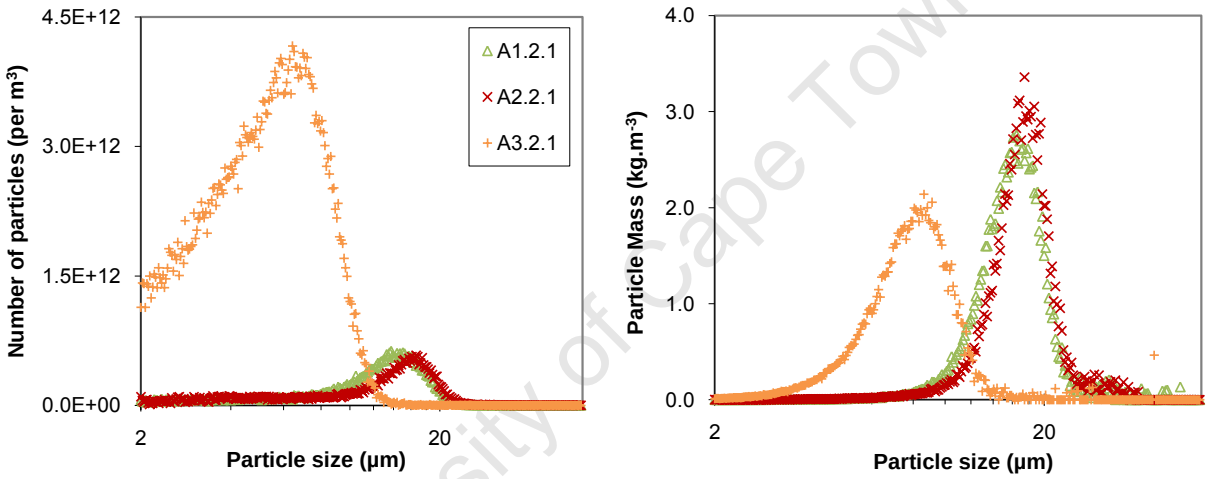

Figure 46: Single-jet, N = 900rpm & slow addition seed PSDs at varying S_i

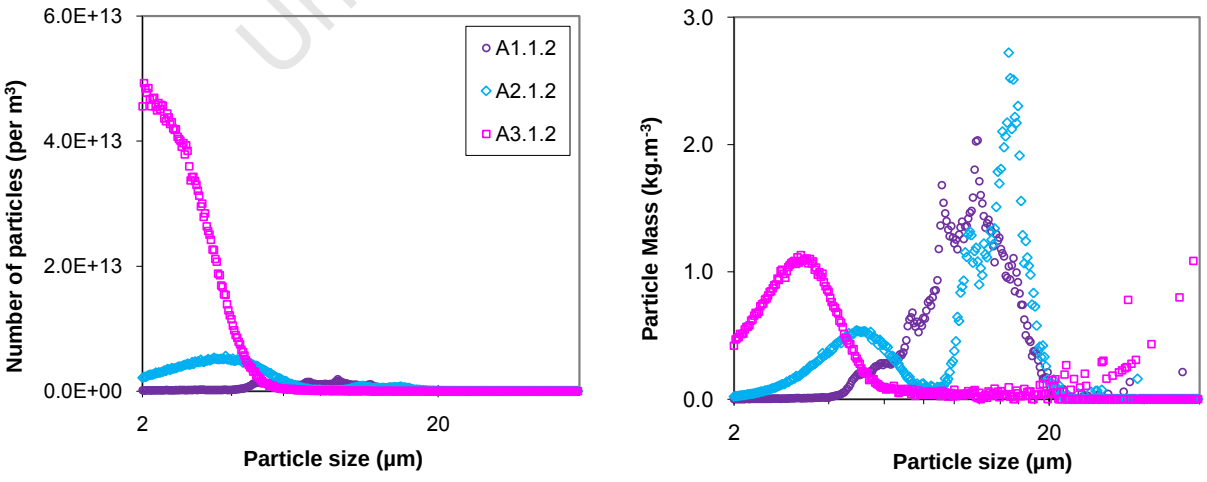

Figure 47: Single-jet, N = 300rpm & fast addition seed PSDs at varying S_i

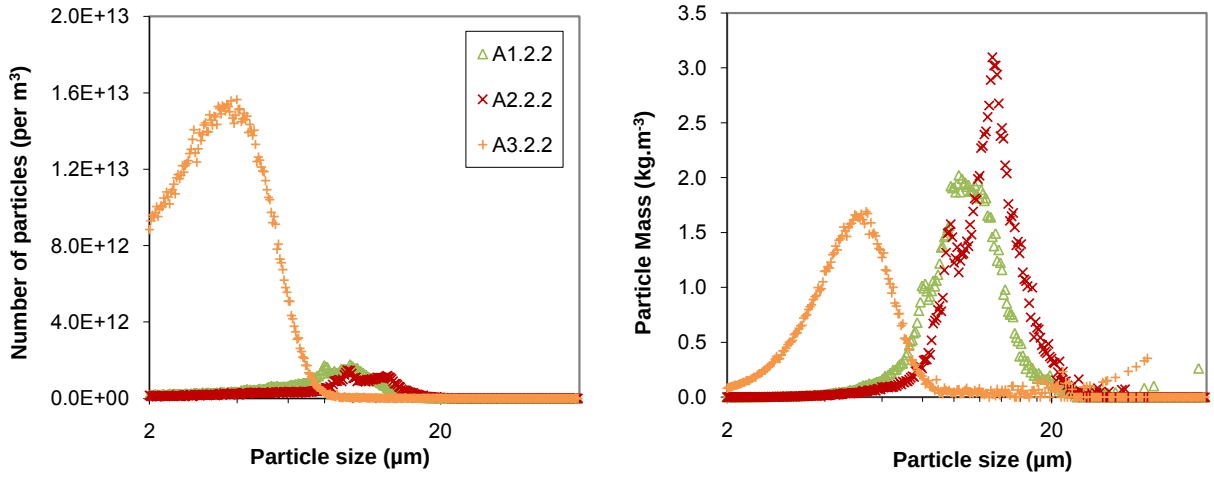

Figure 48: Single-jet, N = 900rpm & fast addition seed PSDs at varying S_i

It is clear from the number distributions for the single-jet method that the highest number of particles exist for experiments at S_i = 30. Also experiments with this supersaturation exhibit the smallest particles with regards to both number and volume (see Table 9 for exact values). For the single-jet method the largest particles were produced with a combination of S_i = 10 or 17 and with a slow reactant addition rate. From the above PSDs it can be seen that the shapes of the distributions, at a specific supersaturation, are very similar for Figures 46 & 48.

For the double-jet method the PSDs at varying supersaturation levels are quite similar for a specific combination of operating conditions. Also, when comparing across the double-jet figures the shapes of the PSDs are quite similar specifically at a high reagent addition rate i.e. Figures 51 & 52. The precipitated particles are considerably larger than those for the single-jet method with the largest particles being produced with a slow addition rate (see Table 9). The double-jet method seems to have more reproducible results in comparison to the single-jet method as there is not a large difference in the results at varying supersaturations. For both addition methods, the volume distributions are narrower at a higher agitation rate. The purchased COM powder exhibits a very similar distribution and mean particle size to seed sample A3.2.1 (see Figure 134 and Table 9).

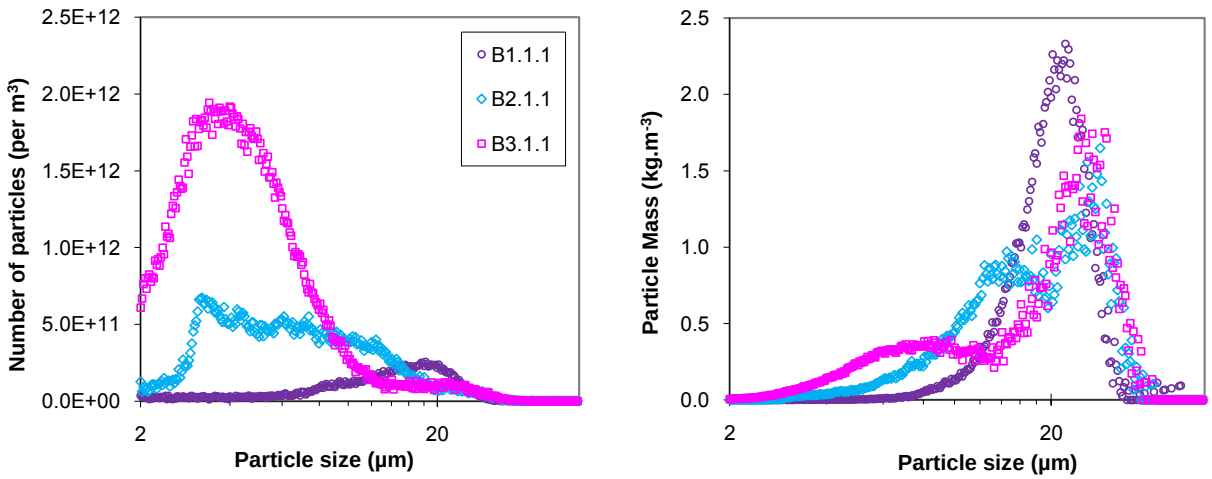

Figure 49: Double-jet, N = 300rpm & slow addition seed PSDs at varying S_i

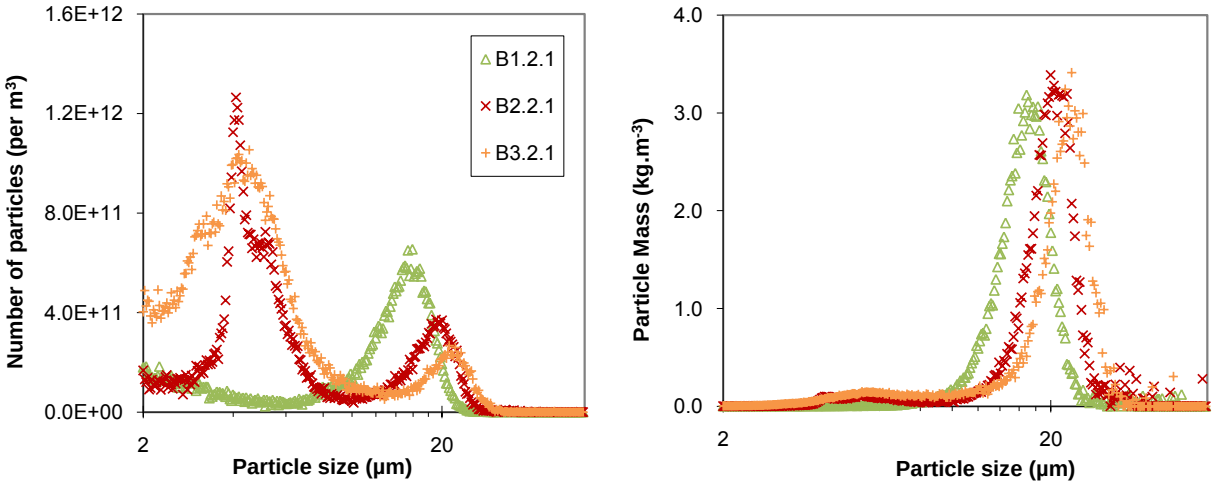

Figure 50: Double-jet, N = 900rpm & slow addition seed PSDs at varying S_i

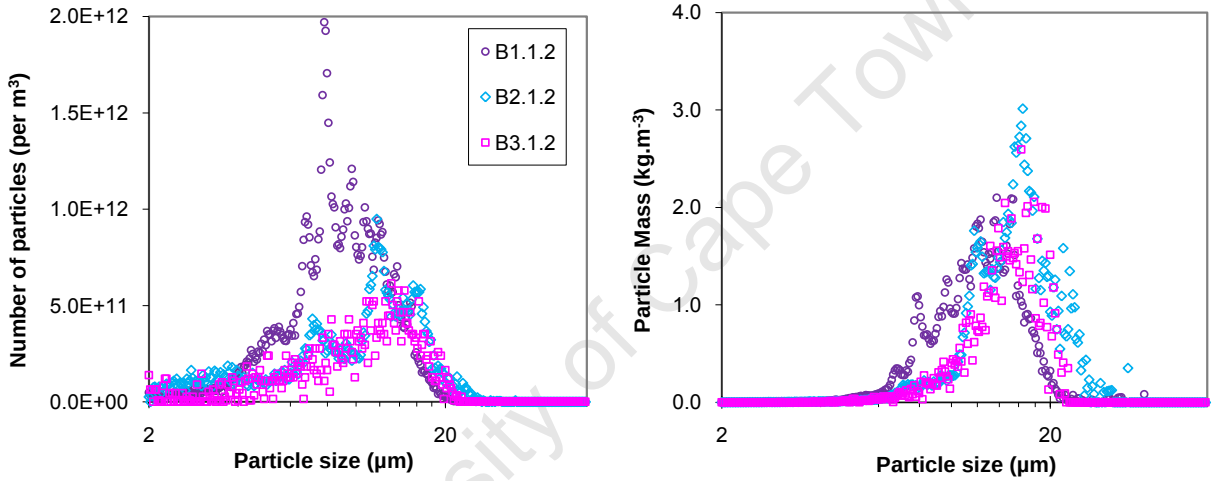

Figure 51: Double-jet, N = 300rpm & fast addition seed PSDs at varying S_i

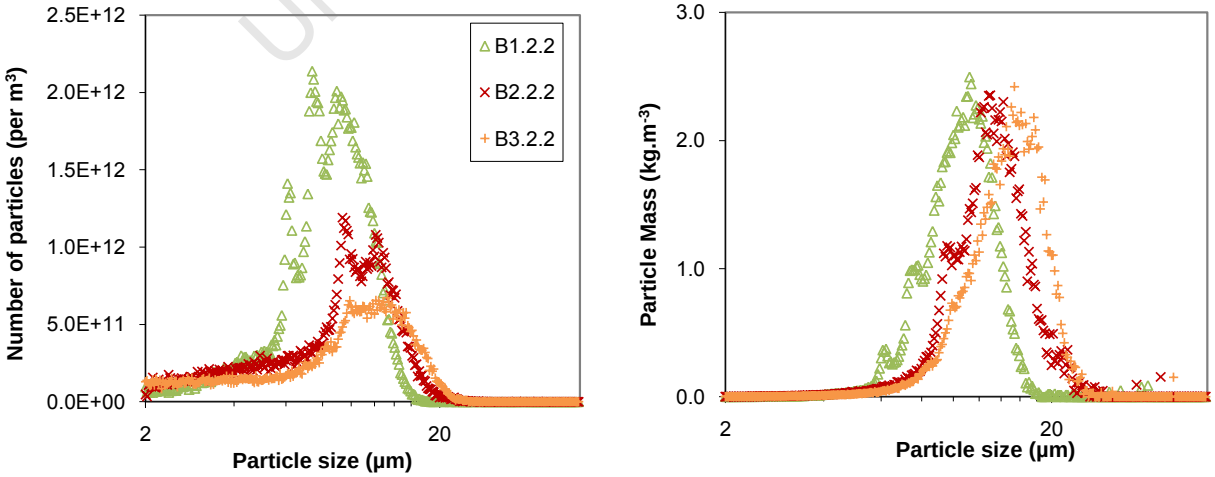

Figure 52: Double-jet, N = 900rpm & fast addition seed PSDs at varying S_i

3.3.3 Morphology Charts

A complete set of SEM photographs for each of the seed samples can be found in Appendix A. In summarising the results from the seed experiments, Figures 53 & 54 were developed for the single-jet and double-jet methods. The 3D axes for the morphology charts were produced using STATISTICA 10 (StatSoft, 2011). A number of different morphologies were observed across the various seed samples. These included single monoclinic particles, twinned particles, intergrowths, agglomerates, large needle-like flat plates, small jagged rectangular plates and dendrites. A sample SEM photograph for each seed experiment was used to represent the morphology found at each combination of operating parameters.

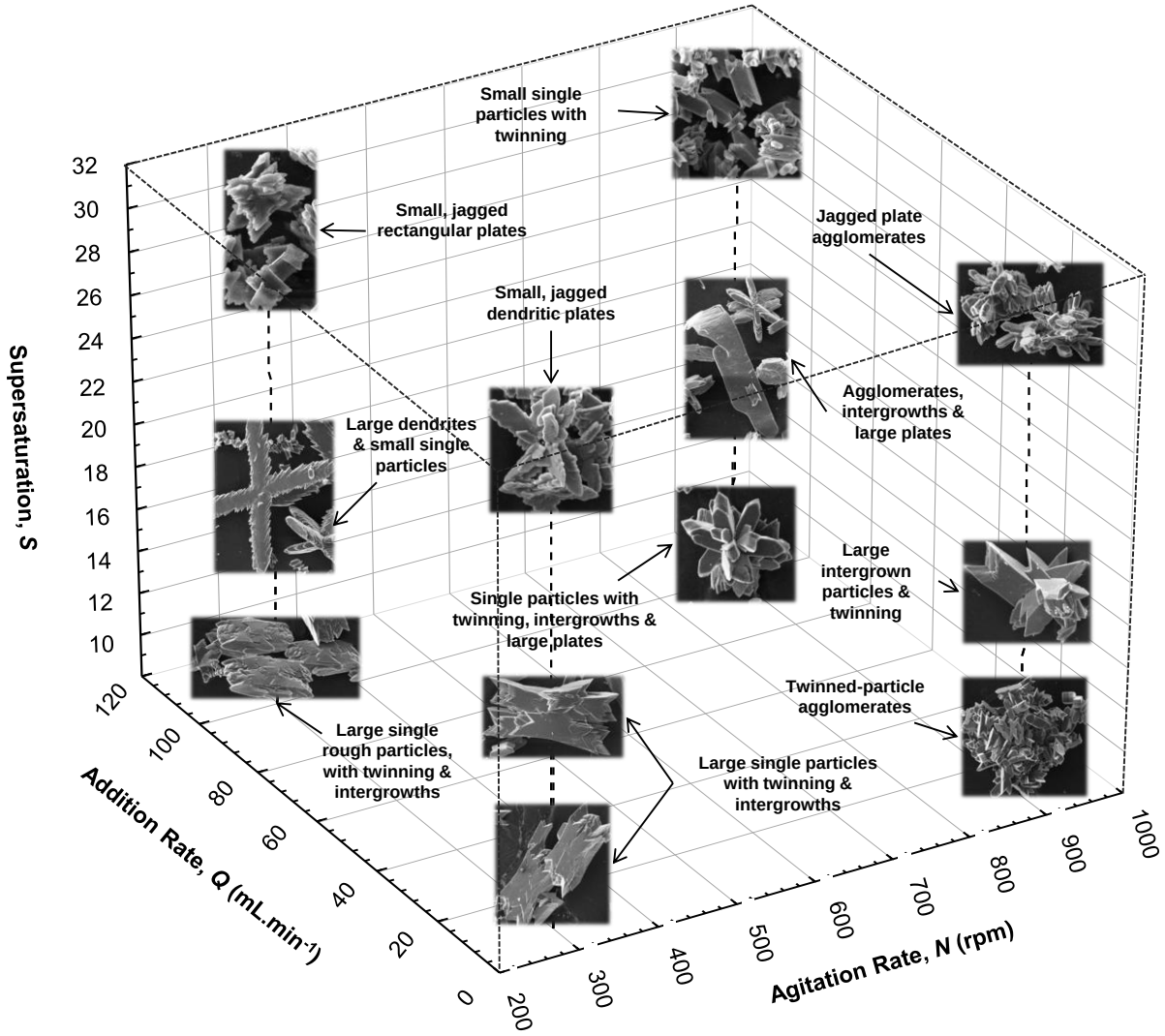

Figure 53: 3D chart showing the morphologies of calcium oxalate at various conditions for the single-jet addition method

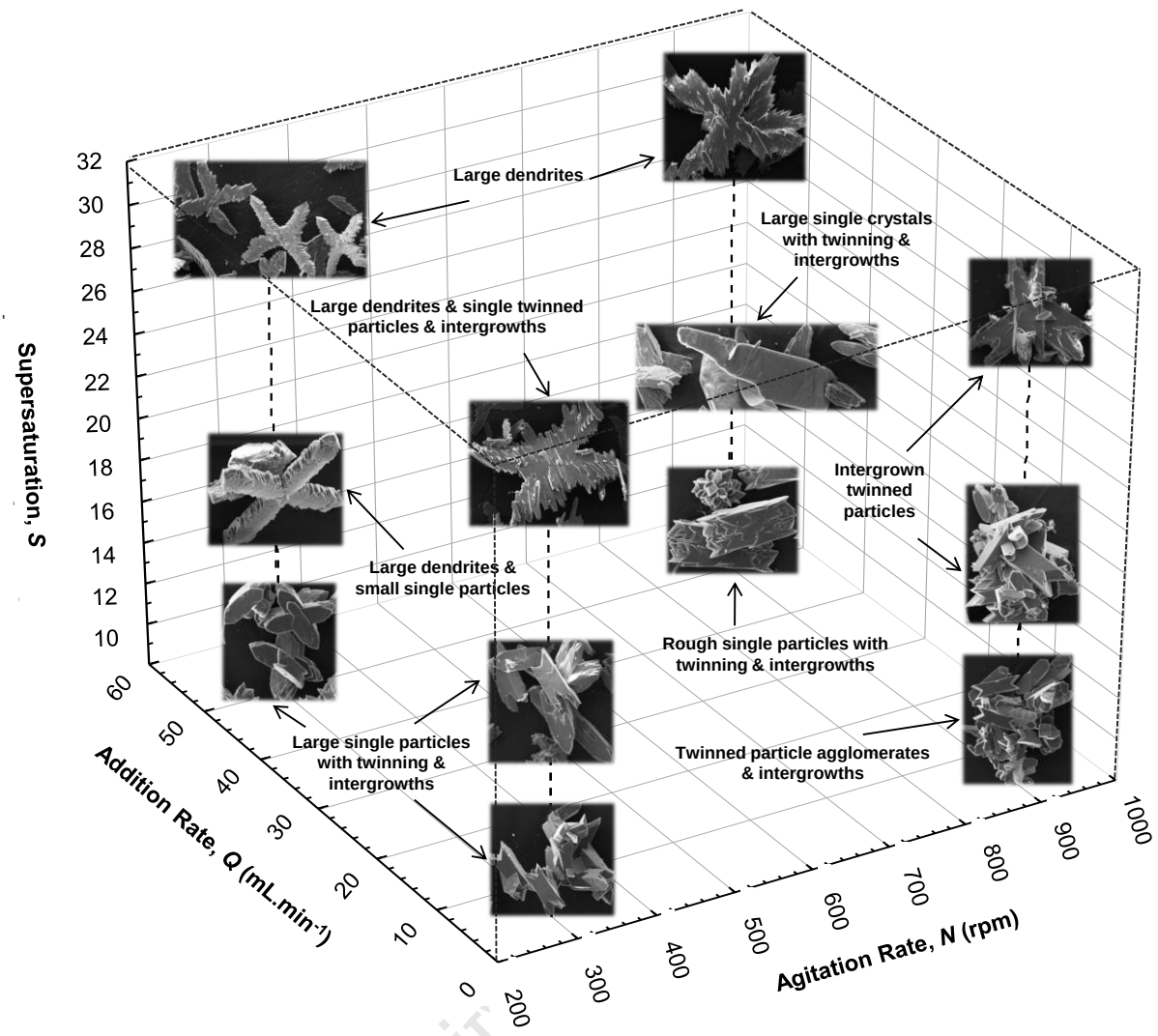

Figure 54: 3D chart showing the morphologies of calcium oxalate at various conditions for the double-jet addition method

3.3.4 Polymorphism in the Seed Samples

The XRD spectra confirmed that all of the seed samples were calcium oxalate and consisted mainly of COM. Both COD and COT were found to be present in only a few of the seed samples. The characteristic monoclinic, tetragonal and triclinic forms of the three hydrates were confirmed by the SEM images. Some SEM images showed a few COD and COT crystals for seed samples where the XRD confirmed only COM e.g. SEM images showed COD and/or COT in seed samples B2.1.1, B2.2.1, B3.1.2, B3.2.2. Possible reasons for this discrepancy are that the SEM sample could have become contaminated by powder from a previous sample containing these hydrates or that the X-rays in the diffractometer did not penetrate the entire seed sample thus only showing COM as the present phase.

COT was characterized by large flat needle-shaped plates (triclinic) and was easily observed in the SEM images of the seed samples where it was present (Figure 55). COD, however, was not easily observed in the SEM images. A dendritic tetragonal COD crystal was found in seed sample B3.1.2

(Figure 56). COD and COT tended to occur in the seed experiments where the fast addition of reactants was implemented.

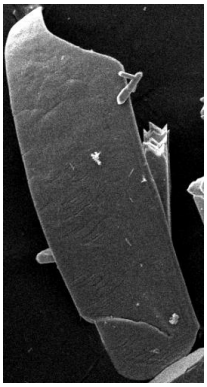

Figure 55: Flat needle-like COT plate found in seed sample B2.1.1 (approximately 60µm in length)

Figure 56: Dendritic COD crystal found in seed sample B3.1.2 (approximately 40µm in diameter)

The XRD spectra in the figures below show examples of the major peaks for each of the different hydration forms found in the seed samples.

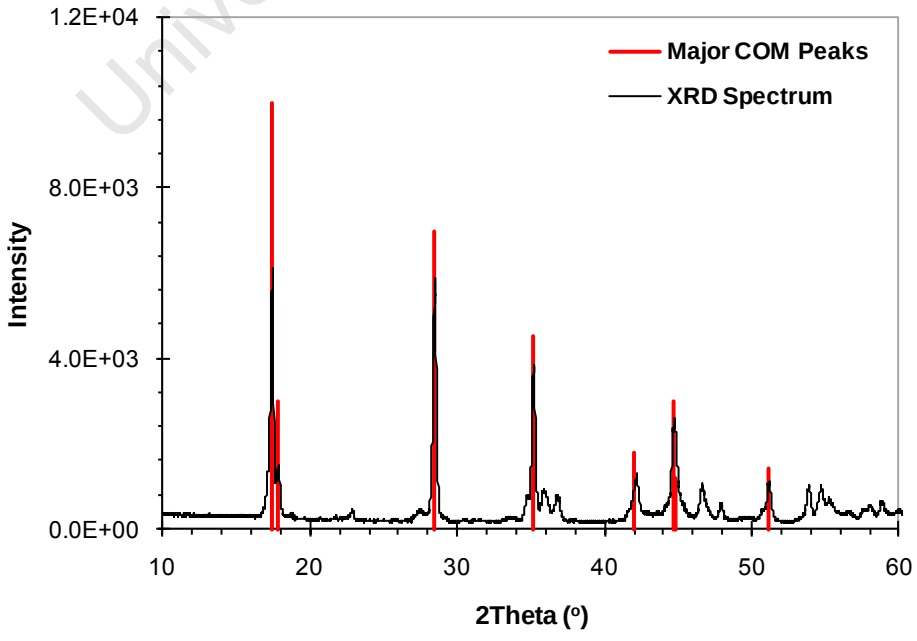

Figure 57: XRD spectrum for pure COM from seed sample A1.1.1

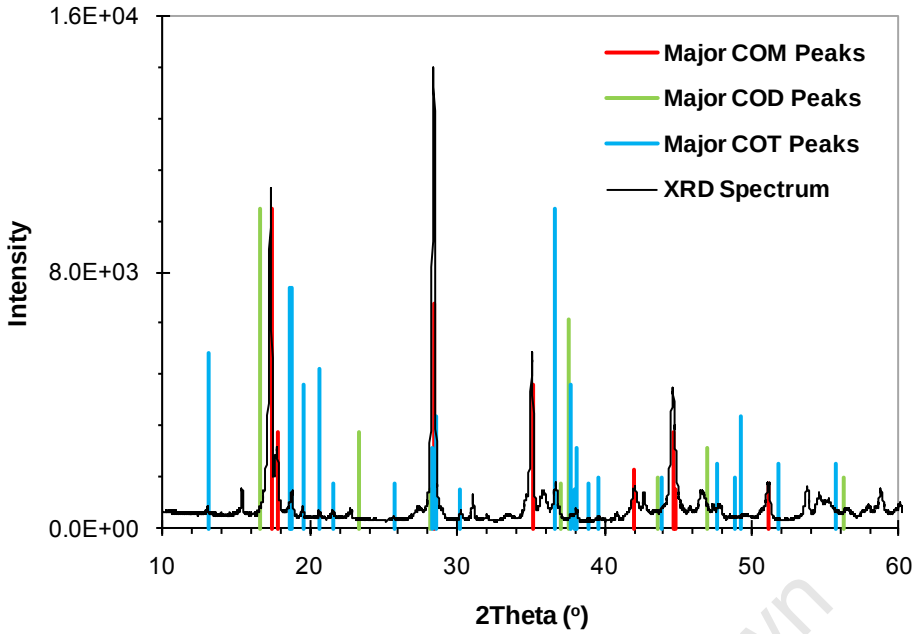

Figure 58: XRD spectrum showing peaks for COM, COD & COT from seed sample B2.2.2

It is important to note that the peaks for COD in the XRD spectra were found to be shifted to the left of the reference spectra for COD. This was because a Co source was used in the diffractometer instead of a typical Cu source. The Co source will shift the peaks but the pattern remains the same. Table 9 displays the full polymorphic results from the XRD analysis.

3.3.5 Summary Table

Table 9 below is a full summary of the results from the PSDs, SEM photographs and XRD analyses.

It was found that the yield of precipitate increased with supersaturation and was the highest for the fast reagent addition rate across the supersaturation levels investigated.

Table 9: Summary of seed preparation findings

Seed Sample	Total No. of Particles, N_T	Total Mass of Particles, M_T	Average Size (µm)		PSD mode	Morphology (SEM)						Polymorph/s (XRD)	Yield
	(#.m^{-3})	(kg.m^{-3})	$d_{1,0}$	$d_{4,3}$		Single particles	Twinning	Inter-growths	Dendrites	Plates	Agglomerates		(%)
A1.1.1	1.91x10^{13}	100	13.5	21.3	Bimodal	x	x	x	-	-	-	COM	35
A1.2.1	4.07x10^{13}	119	11.9	16.4	Monomodal	-	x	x	-	-	x	COM	55
A1.1.2	1.25x10^{14}	102	7.73	11.4	Monomodal	x	x	x	-	-	-	COM	62
A1.2.2	1.21x10^{14}	106	8.00	11.3	Monomodal	x	x	x	-	x	-	COM, COD & COT	64
B1.1.1	2.16x10^{13}	112	14.1	20.4	Monomodal	x	x	x	-	-	-	COM	47
B1.2.1	3.71x10^{13}	117	11.8	16.9	Bimodal	-	x	x	-	-	x	COM	48
B1.1.2	8.51x10^{13}	104	9.10	12.4	Monomodal	x	x	x	-	-	-	COM	64
B1.2.2	1.26x10^{13}	115	8.49	10.7	Monomodal	x	x	x	-	-	-	COM	69
A2.1.1	5.40x10^{13}	113	9.81	17.4	Monomodal	x	x	x	-	-	-	COM, COD & COT	86
A2.2.1	3.44x10^{13}	118	12.3	17.4	Monomodal	-	x	x	-	-	x	COM, COD & COT	73
A2.1.2	4.29x10^{14}	111	4.37	11.5	Bimodal	x	x	x	x	-	-	COM	90
A2.2.2	8.68x10^{13}	121	9.27	12.9	Monomodal	-	x	x	x	x	x	COM, COD & COT	86
B2.1.1	7.65x10^{13}	111	7.59	19.1	Monomodal	x	x	x	-	x	-	COM	76
B2.2.1	5.90x10^{13}	117	7.92	19.6	Bimodal	x	x	x	-	-	x	COM	71
B2.1.2	5.27x10^{13}	122	10.7	15.9	Monomodal	x	x	x	x	-	-	COM, COD & COT	83
B2.2.2	7.54x10^{13}	112	9.43	13.4	Monomodal	x	x	x	-	x	-	COM, COD & COT	87
A3.1.1	8.74x10^{14}	101	4.08	7.55	Monomodal	x	x	x	-	x	-	COM	94
A3.2.1	3.88x10^{14}	115	5.50	8.20	Monomodal	x	x	x	x	x	x	COM	94
A3.1.2	2.25x10^{15}	78.4	2.81	6.94	Monomodal	x	x	x	-	x	-	COM	94
A3.2.2	1.24x10^{15}	104	3.73	5.89	Monomodal	x	x	-	-	-	x	COM	96
B3.1.1	1.89x10^{14}	115	5.17	19.4	Bimodal	x	x	x	x	-	-	COM	87
B3.2.1	9.04x10^{13}	117	6.18	20.6	Bimodal	x	x	x	-	x	x	COM	87
B3.1.2	3.77x10^{13}	83.8	10.9	15.0	Monomodal	x	-	-	x	x	-	COM	96
B3.2.2	5.80x10^{13}	115	10.2	14.9	Monomodal	x	x	-	x	x	-	COM	95
Purch.	3.20x10^{14}	101	5.25	10.2	Monomodal	x	-	-	-	-	x	COM	-

3.4 Discussion

3.4.1 Factors Effecting Particle Size and Morphology

3.4.1.1 Supersaturation

The level of supersaturation at a specific point in the reactor and at a specific time is dependent on the concentrations of the reagent solutions, agitation rate, addition rate and addition method. Thus, the efficiency of the mixing process is a very significant factor. As already shown in the results section, the reactor system is considered to be fully turbulent at the two agitation rates employed i.e. $Re > 10^4$ for both N = 300 & 900 rpm. Although the dye visualization experiments showed that the reagent solutions dispersed relatively quickly throughout the reactor bulk, frame (e) from Figure 44 for example shows that there is a point in time in which the reagent feed solutions are not instantaneously mixed but rather form highly supersaturated plumes of solution. These points of high local supersaturation would result in different environments within the reactor which would cause particles of different sizes and morphologies to precipitate. This would be expected at high initial supersaturation levels and for a fast addition rate where the mixing could become a controlling factor. Under these operating conditions the agitation rate would need to be increased to such a level that supersaturation gradients are prevented. Both the PSD and SEM results from a number of the seed experiments confirm that mixing was a controlling factor in the precipitation process. This was specifically observed for combinations of a fast reagent addition rate and slow agitation rate. For example, various sizes and morphologies of calcium oxalate particles were found in seed sample A2.1.2. Two completely different seed populations exist within the sample i.e. large dendritic particles and small monoclinic particles (see Figure 107). Figure 106 also shows bimodal PSDs representative of the two populations within the seed sample.

Scaling was observed on the reactor walls, baffles and impeller at a low supersaturation and slow addition rate and these are the conditions where the yield of precipitate was the lowest (see Table 9). The reason for the scaling and subsequent low yield is most likely due to heterogeneous nucleation. The supersaturation in the reactor was initially low due to the slow addition of reactants. As the reagent solutions were pumped into the reactor, the supersaturation increased until it reached the critical value for homogeneous nucleation to occur. However, before this point, the supersaturation was sustained at a level where heterogeneous nucleation could occur. The reason for the yield being slightly higher at a high agitation rate is possibly due to the fact that the higher turbulence reduced particle sticking to the reactor walls, baffles and impeller.

The results in Table 9 show that the total number of particles increased and their size decreased as the initial supersaturation level was increased. This is because a higher supersaturation level results in a greater extent of homogeneous nucleation. The single-jet method exhibited the most noticeable contrast between the supersaturation levels. In the single-jet method one concentrated solution is added to the bulk of another concentrated solution which would result in points of high local supersaturation. In the double-jet method, however, the reagent solutions have time to disperse throughout the bulk before mixing. Thus, the double-jet method exhibits a better control of the supersaturation (compare Figures 45 & 49 or 48 & 52). These figures show that the distributions are narrower and more uniform for the double-jet method confirming better control of the supersaturation.

In the double-jet method there is less nucleation due to lower levels of local supersaturation. This results in a lower number of larger particles e.g. at S_i = 30, the double-jet method precipitated large dendrites showing that homogeneous nucleation was suppressed and the process was dominated by fast growth (see Figure 54). However, for the exact same operating conditions, the single-jet method precipitated a high number of considerably smaller plate-like particles (see Figure 53). Due to the higher local supersaturation the initial large burst of homogeneous nucleation consumed the majority of the supersaturation thereby allowing only a small amount of growth to occur. In comparing the similar jagged-plate morphologies of seed samples A3.1.1 and A3.1.2 in Figure 53, it is interesting to note that the sample with the slow addition rate yielded plates with a dendritic-like structure. Because of the slow addition rate not as much nucleation would have occurred, in comparison to the fast addition rate, thus allowing the particles to grow larger.

The morphology of the seed particles changed quite considerably with an increase in the initial supersaturation level. Dendrites and jagged plates were prevalent at the highest supersaturation level investigated whereas the typical monoclinic COM form (with twinning and intergrowths) were prevalent at S_i = 10, 17 & 30. Figure 31 (Section 2.9.3.2) from Mullin (2001) showed that calcium oxalate agglomerates, dendrites and then plates would precipitate as the concentration of the reagent solutions was increased. Although this diagram was for a temperature of 25°C, similar results were found in the current work (see Figures 53 & 54). As discussed in the previous chapter, dendrites generally precipitate from highly supersaturated solutions and usually form in the early stages of crystallization. Also agitation tends to suppress dendritic growth. Although dendrites were observed at high supersaturations, they also occurred in highly agitated solutions i,e. N = 900rpm. Thongboonkerd *et al.* (2006) also found COM dendrites at high concentrations. According to Mullin (2001) twinning is most frequently encountered by the orthorhombic and monoclinic crystal systems. Twinning was observed in almost all of the seed experiments and as COM exhibits a monoclinic crystal system, this confirms the theoretical predictions. Also, twinning tends to occur in systems where there is poor agitation, seeding at high supersaturation, overcrowding in the crystallizer etc. Thus, from the results, this could support the findings that the batch reactor was not well-mixed thereby resulting in supersaturation gradients. The high degree of twinning found in almost all of the experiments could also be as a result of the specific supersaturation range investigated i.e. if S_i < 10 or > 30, twinning may not occur at all. Literature suggests that agglomeration tends to occur at higher supersaturations so it was expected that the degree of agglomeration observed may be the highest for S_i = 30. This was not the case as agglomerates were found for various supersaturation levels where slow reagent addition and high agitation rates were implemented (see Figures 53 & 54).

At the chosen operational temperature of 37°C it was expected that COM would be the only stable hydrate as found by Garside *et al.* (1992) and Sohnel *et al.* (1997). The results from the XRD analyses showed that COM was the most prevalent calcium oxalate hydrate in the seed samples while a few of the seed samples contained COD and COT as well. COD and COT were usually found in the seed samples where higher initial supersaturations and the fast addition of reactants were implemented. According to Ostwald's rule of stages it is likely that COT would be the first hydrate to precipitate (due to its considerably higher solubility, see Table 6 in Chapter 2). Over time, COT would dissolve and re-precipitate as the more stable COD. Eventually COM would be the final phase as it is the most thermodynamically stable. Bretherton & Rodgers (1998) also stated that since COD and

COT are thermodynamically unstable with respect to COM, their higher solubilities make them the kinetically favoured phases. This could explain the reason why COD and COT were mostly found in samples where the fast addition of reagents was employed. As the total time for these runs was only 35 minutes (in comparison to 75 minutes for the slow addition method), COT and COD may not have had the time necessary to transform completely to COM.

3.4.1.2 Agitation Rate

In comparing the PSD results from both low and high agitation rates it is obvious that the higher agitation rate yields a narrower distribution (see Figures 51 & 52). The higher agitation improves the mixing within the reactor and thus the distribution of supersaturation. This yields a better control of the precipitation process thus creating particles with a more even size and shape. This can be further supported by Figures 86 & 88 where the number and volume PSDs at a higher agitation rate are narrower than those at a lower agitation rate.

Agglomerates were only observed at a higher agitation rate which is what was expected from theory and literature findings. A higher energy dissipation rate yields a higher agglomeration rate due to the increase in particle collisions (Giulietti *et al.*, 2001). Zauner & Jones (2000) also found calcium oxalate agglomerates at high agitation rates i.e. 1000 and 1500 rpm. The "agglomerates" found by Thongboonkerd *et al.* (2006), however, appear to be crystal intergrowths and not agglomerates (see Figure 30 on page 51).

3.4.1.3 Addition Rate

A slow addition rate was investigated as it was expected that this would help to control the supersaturation thereby preventing excessive homogeneous nucleation. Also, the slow addition of the reagent solutions would help to promote the growth of particles resulting in a distribution consisting of a low number of large particles. However, as discussed already, at S_i = 10 the supersaturation was sustained in the beginning of the experiments at a level that was too low for homogeneous nucleation but within the correct region for heterogeneous nucleation. This produced scaling on the impeller, baffles and reactor walls and negatively impacted the yield of precipitate. Nonetheless, the slow reagent addition rate resulted in the largest precipitated particles in comparison to the fast addition rate viz. $d_{4,3}$ = 21.4 and 11.4μm for seed samples A1.1.1 & A 1.1.2 respectively (see Table 9). The precipitated particles from a slow addition method were generally well-grown even at a high initial supersaturation of S_i = 30.

For seed experiments where the fast reagent addition rate was employed, there were a significantly higher number of particles of a smaller size in comparison to the slow reagent addition method (see Table 9). The fast addition rate resulted in higher supersaturation within the reactor which in turn produced more homogeneous nucleation. This consumed the bulk of the supersaturation and prevented a large amount of growth. The significantly higher number of smaller particles was thus a result of the larger amount of homogeneous nucleation. Figures 53 & 54 show that particles in seed samples A1.1.2 and B1.2.2 have rough surfaces in comparison to those using the slow addition rate i.e. A1.1.1 and B1.2.1. This observation confirms that the fast reagent addition rate produces higher supersaturations as the rough surface growth mechanism generally occurs at high supersaturations

where the growth units attach at any point on the crystal surface e.g. terraces, steps or kinks and as a result the crystal surface becomes rough.

It is important to note that the addition rate is significantly influenced by the addition method as the addition rates show considerably different results between the two methods.

3.4.1.4 Addition Method

As discussed in Section 3.4.1.1 the double-jet method shows a better control of the supersaturation than the single-jet method. From the results it can be justified that the efficiency of the mixing in the batch reactor is a much more significant factor for the single-jet method. At specifically higher supersaturations the particles are considerably smaller for the single-jet method (e.g. $d_{4,3}$ = 7.55μm for A3.1.1 versus $d_{4,3}$ = 19.4μm for B3.1.1). Many different morphologies exist for the precipitated particles highlighting the fact that there are different environments within the reactor and thus it is not well-mixed. The PSDs also show that the double-jet method yields a better control of the supersaturation. The PSDs are narrower and more uniform across supersaturation levels (compare Figures 47 & 51).

3.4.2 Choice of Seeds for the Kinetic Experiments

Seed experiments where an initial supersaturation level of S_i = 10 was used conflicted with point (f) of the seed preparation guidelines i.e. not enough precipitate was produced per experiment, thus these seed samples were not considered for use in the kinetic experiments. It was decided that seed particles with a dendritic morphology would not be utilized as these tended to block the aperture very easily. Also, the sizes of the dendritic particles observed in the SEM images seem to be larger than those portrayed by the respective PSDs. Thus, the actual average sizes of the dendrites are probably considerably larger than what is displayed in Table 9. Seed samples consisting of all three hydrates were not considered because a pure monohydrate sample is required for the kinetic experiments. If other hydrates are present, the kinetics of each of these will influence the overall kinetic results. Seed samples which had bimodal PSDs and/or had PSDs which lay completely out of the 2 - 60μm range, did not satisfy the seed preparation guidelines and were thus not considered.

From the above results and discussion as well as the seed preparation guidelines i.e. Section 3.2.1 it was decided that the following seed samples could possibly be utilized in the kinetic experiments: A3.1.1, A3.2.1 and A3.2.2. Although these seed samples did not completely satisfy point (b) of the seed preparation guidelines it was decided that this was a less significant point. Also, the PSDs and average sizes of these seed samples best represented the seeds used by Bramley *et al.* (1996) and Bramley *et al*. (1997) (see Figure 25 on page 47). The mean size and PSDs of the purchased COM sample are very similar to the chosen seed samples above. As it is readily available it would most likely be the best choice for seeds in the kinetic experiments.

3.5 Preliminary Conclusions

The aims of this chapter were twofold: firstly, the behaviour of the moderately soluble calcium oxalate system was investigated by varying the initial supersaturation, agitation rate, addition rate and addition method. Secondly, the conditions necessary for preparing suitable seeds that satisfied the seed preparation guidelines outlined in Section 3.2.1 were determined. The following preliminary conclusions have been formulated from the results and discussion sections:

i. The batch reactor system was determined to be fully turbulent, for the agitation rates investigated, according to the theoretical Reynolds number equation. The mixing in the batch reactor was reasonably good however at the high supersaturations and fast reagent addition rate investigated in this chapter, the mixing appeared to be insufficient. This created points of high local supersaturation which resulted in different environments within the reactor. Thus, particles with various sizes and morphologies were found throughout a number of the seed samples. Better mixing is required in the batch reactor, especially for high supersaturations or more insoluble compounds, such that the PSD and morphology of the precipitate can be better controlled.

ii. The double-jet reactant addition method exhibited a better control of the superstation in comparison to the single-jet method. The PSDs for the double-jet method were narrower and more uniform across the supersaturation levels investigated. Also there were a lower total number of particles and larger-sized particles for the seed samples prepared with the double-jet method e.g. large dendrites versus small jagged plates.

iii. The fast addition of reactants was found to produce a high number of small particles due to the promotion of homogeneous nucleation. Slow addition, on the other hand, promoted growth yielding a lower number of larger particles. In some experiments, at low S_i, the fast addition rate produced particles with rough surfaces confirming the rough surface growth mechanism.

iv. A higher agitation rate produced narrower and more uniform PSDs in comparison to a lower agitation rate. Agglomerates were only found for seed samples where a high agitation rate had been utilized.

v. At a low initial supersaturation, large well-grown monoclinic COM particles precipitated. However, at higher supersaturations dendrites and plates were formed. Twinning was present in almost all of the seed samples and is a characteristic of the monoclinic crystal system. A large amount of intergrowths also occurred throughout the seed samples.

vi. At the operational temperature of 37°C it was expected that COM would be the only hydrate present in the seed samples. All of the seed samples contained COM while some contained COD and COT as well. The presence of COD and COT, particularly in seed experiments utilizing the fast addition of reagents, was determined to be a thermodynamic effect. Thus COD and COT did not have enough time to transform to the thermodynamically stable monoclinic form of calcium oxalate.

vii. Seed samples A3.1.1, A3.2.1 and A3.2.2 satisfied the seed preparation guidelines to the highest degree. It was decided, however, that the purchased COM powder would be utilized for the kinetic experiments as it is readily available and has a very similar PSD and mean particle size to that used by Bramley *et al.* (1996) and Bramley *et al.* (1997).

Chapter 4

DETERMINATION OF THE GROWTH & AGGREGATION KINETICS

4.1 Introduction

Understanding the kinetics of precipitation processes is very important as they govern the relative rates of nucleation, growth, aggregation, and breakage. Thus, reliable kinetic data is of fundamental importance for successful modelling and scale-up of precipitation processes as well as for the control of the specific properties of a precipitate. As already discussed in the literature review chapter, numerous methods can be found for measuring and predicting the rates of nucleation, crystal growth and, to a lesser extent, secondary processes such as aggregation and breakage. These techniques are generally specific to the chemistry and operating conditions of the system of choice and thus cannot be directly used for other processes. Also, in the modelling of crystallization processes, it is possible to make the assumption of perfect mixing which simplifies the problem considerably. It is also possible to confine the mechanisms to nucleation and growth only. However, neither of these assumptions is valid in precipitation problems, which makes them highly non-linear and more difficult to solve.

This chapter aims to determine the growth and aggregation kinetics for the moderately soluble COM system using the experimental kinetic method utilized by Bramley *et al.* (1996), Bramley *et al.* (1997) and Andreassen (2001) to name a few. The experimental work of Bramley *et al.* (1996) will be repeated with higher initial supersaturation levels and higher seed masses being investigated as well.

4.2 Materials and Methods

4.2.1 Reagents

De-ionized water (Milli-Q Water Purification System, Millipore, USA) was utilized in all cases. All chemicals used in the preparation of solutions were analytical grade. These included: anhydrous calcium chloride ($CaCl_2$) (Merck, South Africa), sodium oxalate ($Na_2C_2O_4$) (Sigma-Aldrich Co., Germany), sodium chloride (NaCl) (Merck, South Africa) and COM ($CaC_2O_4.H_2O$) (Merck, South Africa).

4.2.2 Experimental Set-Up and Procedure

Kinetic experiments were conducted in a similar manner to that of Bramley *et al.* (1996), Bramley *et al.* (1997) and Andreassen (2001). In this work, seeds were added to a metastable solution and samples were taken at regular time intervals in order to determine the evolution of the PSD. Four initial supersaturation levels were investigated in this work. A comparison between these and those investigated by Bramley *et al.* (1997) can be found in Table 10 below. It was decided to further Bramley *et al.*'s (1997) work by investigating initial supersaturation levels above those already investigated.

Table 10: Supersaturation levels investigated by Bramley *et al.* (1997) and the current work

Initial Supersaturation, S_i	
Bramley *et al.* (1997)	**Current Work**
2.3	2.3
2.8	3.3
3.3	4.6
3.6	5.8

As Bramley *et al.* (1997) used a different program to calculate their initial supersaturations, it was decided, for comparison purposes, to recalculate the supersaturations using OLI Stream Analyser (OLI Systems, 2008) and Equation (64). The resulting supersaturations are shown in Figure 59 below.

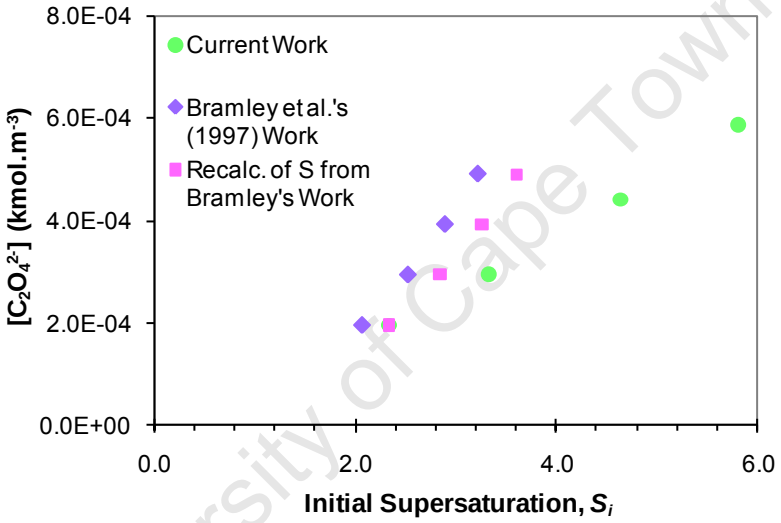

Figure 59: Comparison of initial supersaturation levels used by Bramley *et al.* (1997) and used in this work

The kinetic experiments were conducted in the same 1L jacketed and baffled glass reactor as utilized in the seed experiments (see Figure 37 in Section 3.2.3). In all experiments the jacketed reactor operated at a temperature of 37±2°C and an agitation rate of 600±10rpm (P = 4.8x10^{-2} W).

Reactant solutions ($CaCl_2$ & $Na_2C_2O_4$) were filtered once using 0.22µm cellulose membranes (Millipore, USA) and then heated to 37±2°C in a water bath before use in the experiments. A metastable solution was prepared by pumping 250mL each of the reactant solutions simultaneously into a 1L glass reactor containing 500mL of de-ionized water. NaCl was added to the solution such that an initial ionic strength of 0.158kmol.m^{-3} was achieved. All experiments had an initial Ca^{2+} to $C_2O_4^{2-}$ ion ratio of 5:1.

From the previous chapter it was decided that the primary seeds utilized in the kinetic experiments would be the purchased COM sample (viz. the purchased powder is readily available and has a very similar PSD and mean particle size to the seeds used by Bramley *et al.* (1996) & Bramley *et al.* (1997)). A certain mass (either 0.3 or 0.5g) of seeds were placed in 10mL of saturated CaC_2O_4

solution (σ = 0). Either 1 or 3mL of this seed solution was then added to the metastable solution to yield an initial seed concentration of approximately 0.03 or 0.15g/L respectively.

Table 11: Properties of the two seed concentrations used in the kinetic experiments

Seed Concentration ($g.dm^{-3}$)	Volume % of Seeds	Average Surface Area ($\mu m^2.m^{-3}$)	Mean Seed Size (μm)	
			$d_{1,0}$	$d_{4,3}$
0.03	$1.4x10^{-3}$	$1.1x10^{13}$	5.3±0.1	10.4±0.2
0.15	$6.8x10^{-3}$	$5.3x10^{13}$		

Experiments were also conducted using a second seed sample (A3.2.1) in order to determine whether the size or morphology of the seed material affected the kinetic results. For these experiments an initial supersaturation level of S_i = 3.3 was investigated and a mass of seeds corresponding to a surface area of 1.1×10^{13} $\mu m^2.m^{-3}$ was utilized. As seed sample A.3.2.1 had a higher surface area as compared to the primary seed sample a conversion factor of 0.84 was applied to the mass of the seeds to ensure the same surface area in the experiments. Seed sample A3.2.1 had a mean particle size with regards to number and volume of $d_{1,0}$ = 5.7±0.1μm & $d_{4,3}$ = 8.4±0.1μm respectively.

4.2.3 Preventing Nucleation in the Kinetic Experiments

Nucleation was an unwanted mechanism in the kinetic experiments as only the growth and aggregation of the particles was being investigated. Nucleation was most likely to take place in two instances during the course of the experiments:

i. The “metastable” solution could spontaneously nucleate before the seeds had been added (homogeneous nucleation).
ii. Nucleation could take place when the seeds were added to the metastable solution.

The metastable solution was in fact only “metastable” for a period of time until the thermodynamic activation energy was surpassed and nucleation could take place spontaneously. Thus, the seeds needed to be added to the metastable solution before any nucleation took place (observed by the solution turning from clear to cloudy). Nucleation could also take place when the seeds were added to the metastable solution. This would be due to the surface area of the seed material not being high enough to consume the supersaturation of the solution. Thus, in order to prevent nucleation from occurring, the surface area of the seeds would have to be increased. This could be done in two ways, either: (i) a higher number of seeds or (ii) larger sized particles could be added.

Nucleation was prevented in the kinetics experiments by increasing the mass of seeds added to the metastable solution. The highest supersaturation level i.e. S_i = 5.8 was initially investigated with a seed concentration of C_{seeds} = 0.03$g.dm^{-3}$. As nucleation occurred in this experiment the seed concentration was increased until no nucleation was observed. Similar preliminary experiments were conducted for the other supersaturation levels.

4.2.4 Sampling and PSD Measurements

5-10mL samples were taken at 5, 10, 15, 20, 30, 45 and 60 minutes after the addition of the seeds to the metastable solution. The samples were placed in 80mL of electrolyte solution and analyzed using the electrical sensing zone technique (as discussed in Section 2.4.3) in order to determine the PSD.

The Coulter Counter was fitted with a 100µm aperture tube which enabled particles within the size range of 2 - 60µm to be measured. A control mode of 2000µl was utilized in all measurements. A 4wt% NaCl saturated CaC_2O_4 solution was utilized as the electrolyte in the Coulter Counter as it was found that the COM particles were slightly soluble in water-based electrolytes. The electrolyte solution was filtered twice using 0.22µm cellulose membranes (Millipore, USA) before use to ensure a low background count of particles. Also, filtering the solution reduced the possibility of the aperture tube becoming blocked during readings due to foreign particles in the solution.

4.2.5 Repeatability and Error Analysis

All experiments were repeated at least four times to ensure repeatability of the measurements and for error analysis. According to Andreassen (2001), experiments should be repeated a number of times in order to minimise the uncertainty in the estimated kinetic parameters. This is because the determination of the increase in particle volume by growth and the decrease in particle numbers by aggregation at low relative supersaturation is affected by the error in the Coulter Counter measurements. This leads to a spread in the results at low relative supersaturation levels and thus repeating the experiments minimizes the error in the determination of the growth and aggregation rates (Andreassen, 2001). Thus, the experiments conducted at lower initial supersaturation levels and seed masses were repeated more than ten times in order to improve the accuracy in the results.

4.2.6 Filtering and Storage

After the final sample had been taken at 60 minutes the remaining solution was vacuum filtered using 0.22µm cellulose membranes (Millipore, USA). The precipitate was dried in an oven and then transferred to a storage container.

4.2.7 Other Analyses

4.2.7.1 Scanning Electron Microscopy

Photographs of the kinetic samples were conducted using a Scanning Electron Microscope (Nova NanoSEM 230, FEI). Images were taken using a voltage of 5.0 keV, ETD detector (SE mode) and with magnifications of between 1000 and 10 000x. The purpose of conducting SEM was in order to determine the morphology of the particles and to confirm that both growth and aggregation had occurred within the kinetic experiments.

4.2.7.2 X-Ray Diffraction

All kinetic samples were analysed using a D8 Advance X-ray laboratory diffractometer (Bruker AXS). The diffractometer had a Co source ($\lambda_{K\alpha 1}$ = 0.178897 nm) and a VÅNTEC position-sensitive detector. The XRD patterns were used for confirmation of COM as the only precipitated product.

4.2.8 Calculation of G and β_0

In order to calculate the growth and aggregation kinetics the following procedure was followed:

i. Size-independent growth and aggregation of COM was assumed (as found in literature).
ii. The moments from the experimental PSDs i.e. m_0, m_2 & m_3 were determined.
iii. The rates of change of the zeroth & third moments were calculated numerically.
iv. β_0 and G were calculated using Equations (111) and (113) respectively.
v. S at each sample time was calculated using Equations (127) – (130) and Equation (132).
vi. A parabolic (spiral) surface growth mechanism for COM was assumed (as found in literature).
vii. $G^{0.5}$ versus σ was plotted in order to determine a kinetic expression for the growth rate in terms of the supersaturation.

Raw data and sample calculations can be found in Appendix C.2.

4.3 Results

4.3.1 Nucleation in the Experiments

The following figures show the case when nucleation took place during the kinetic experiments. This was for an initial supersaturation level of S_i = 5.8 and an initial seed concentration of C_{seeds} = 0.03g.dm^{-3}. Nucleation could have occurred either because homogeneous nucleation occurred before the seeds had been added or because the surface area of the seeds was too small to consume the supersaturation when they were added. The most likely explanation is that the seed surface area was not high enough. Figure 60 shows that there is an increase in the total number of particles between 0 and 5 minutes which confirms that nucleation took place.

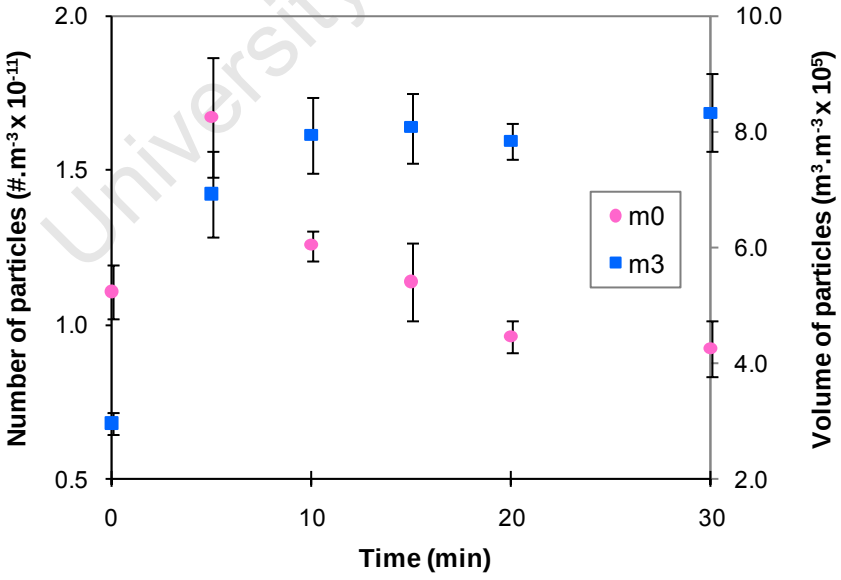

Figure 60: Evolution of m_0 and m_3 for the case when nucleation occurred in the experiments

Nucleation is also evident from the PSDs in Figure 61. There is a significant increase in the number of particles between 0 and 5 minutes i.e. the number distribution for the seed particles is considerably smaller than that of the number distribution at 5 minutes. There is also an increase in the number of particles at the lower end of the size range (at and below 2μm) which is indicative of nucleation. It is

possible that because the initial supersaturation level was relatively high the particles that nucleated at the point of seed addition grew to a larger size within the first 5 minutes of the experiment. Thus, the most likely explanation is that there was nucleation and subsequent fast growth of the nuclei into the field of view of the particle size analyser. This would explain the increase in the major peak of the number distribution at approximately 5µm between 0 and 5 minutes.

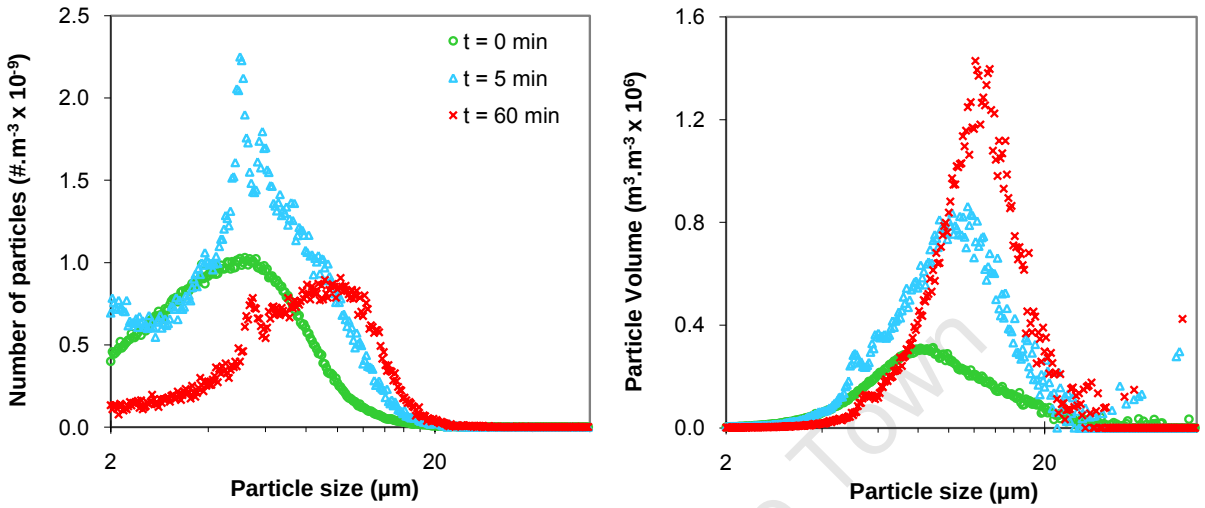

Figure 61: Number (left) and volume (right) size distributions for the case when nucleation occurred in the experiments

There is also only a small decrease in the total number of particles over 60 minutes and if the error bars are taken into account it is quite possible that the total number of particles does not change at all. This could either be explained by the fact that agglomeration did not occur within the system (or was not a significant mechanism) however this is unlikely. The more likely explanation is that nucleation did occur at the point of seed addition and increased the total number of particles within the system. Because of the significant initial supersaturation level, nucleation would occur and consume the majority of the supersaturation. Rapid growth would then increase the size of the nucleated and seed particles over the next 5 minutes. Finally, the remaining supersaturation would be consumed by a small amount of growth as well as aggregation of the particles, which would also decrease the total number of particles within the system.

4.3.2 Evolution of the Zeroth and Third Moments

The PSDs for the kinetic experiments at varying initial supersaturations and seed concentrations are presented below. For all the supersaturation levels investigated (apart from S_i = 5.8 & 4.6) both seed concentrations listed in Table 11 were utilized. The evolution of the zeroth moment i.e. total number of particles per m^3 indicated that no nucleation took place. In all cases the zeroth moment decreased over the course of the experiments showing that aggregation was an active mechanism in the process. Also, the third moment increased indicating that growth of the seeds took place. The full moment and PSD results for each kinetic experiment can be found in Appendix B.1.

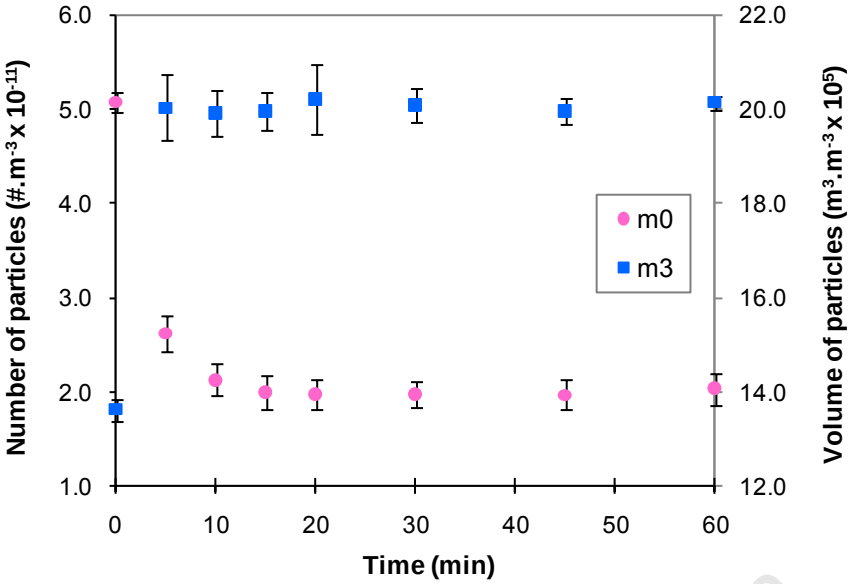

Figure 62: Evolution of m_0 and m_3 for S_i = 5.8 & C_{seeds} = 0.15g.dm^{-3}

For all the kinetic experiments the PSDs show a shift in the distribution from smaller to larger sizes thus supporting the theory that both aggregation and growth are active mechanisms in the system. The number distributions decrease in number and shift to larger sized particles over time whereas the volume distributions show an increase in volume and also a shift to larger sized particles.

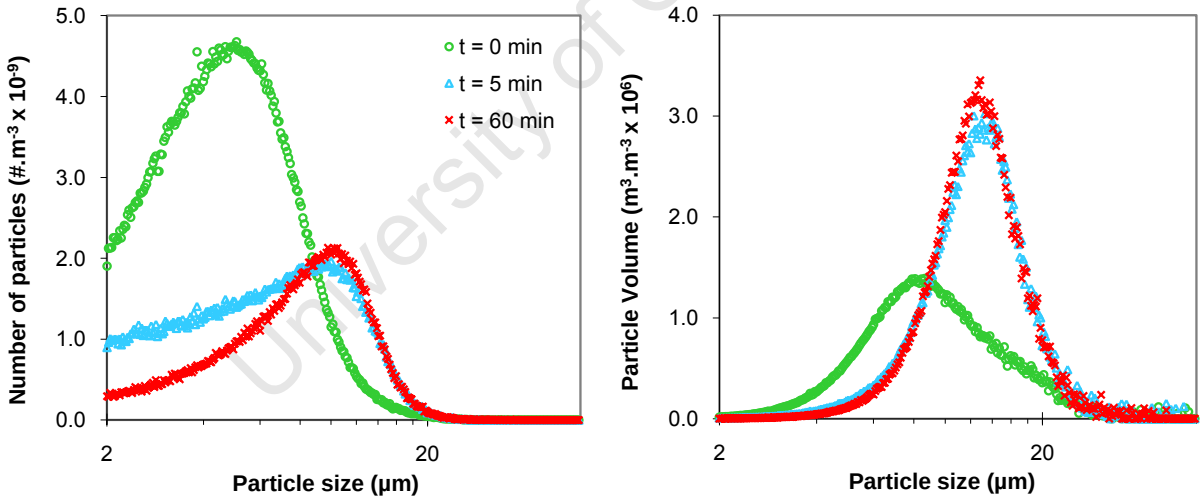

Figure 63: Number (left) and volume (right) size distributions for S_i = 5.8 & C_{seeds} = 0.15g.dm^{-3}

In all experiments where the highest seed concentration was investigated i.e. C_{seeds} = 0.15g.dm^{-3} the zeroth and third moments as well as the PSDs are relatively constant after approximately 20-30 minutes. This indicates that the system had reached equilibrium (see Figure 64 below). However, for the lower seed concentration it appears that this is not the case.

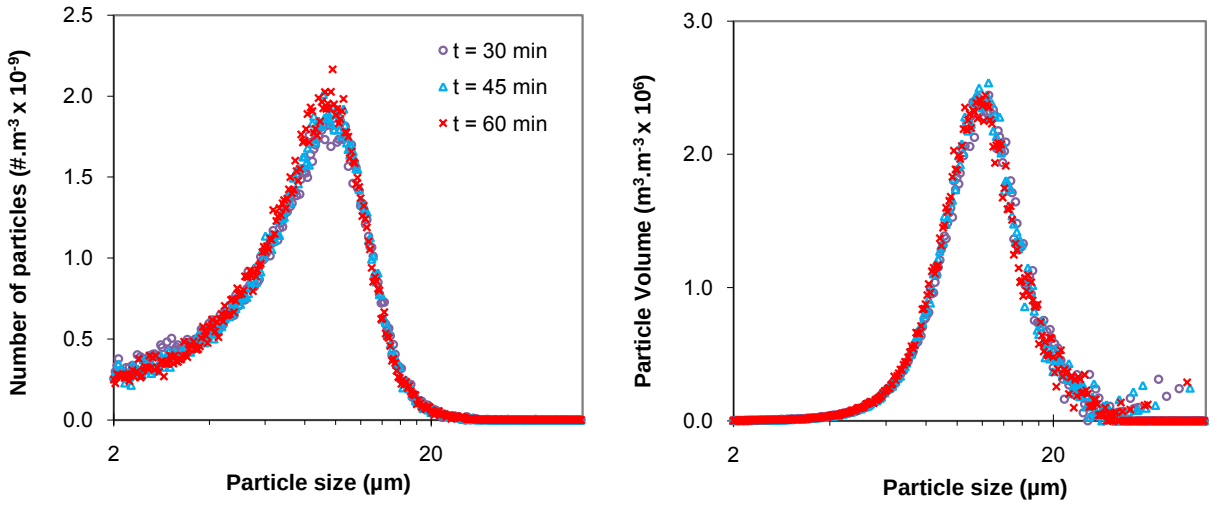

Figure 64: Number (left) and volume (right) size distributions for S_i = 2.3 & C_{seeds} = 0.15g.dm^{-3} confirming equilibration of the system

The kinetic experiments where a lower seed concentration was utilized exhibit a slower approach to equilibrium. This can be seen in comparing Figures 62 & 63 with Figures 65 & 66 (also see Figures 136-145 in Appendix B.1)

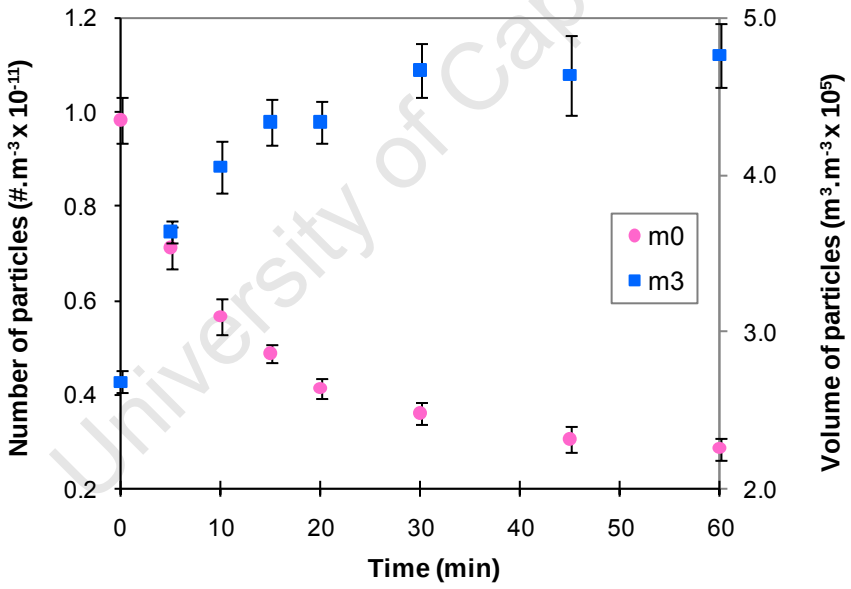

Figure 65: Evolution of m_0 and m_3 for S_i = 3.3 & C_{seeds} = 0.03g.dm^{-3}

The growth and aggregation of the particles (i.e. increase in seed particle volume and decrease in number) is slower for a lower seed concentration. Figures 144 & 145 in Appendix B.1 show that the alternative seed sample (A3.2.1) exhibits the same precipitation behaviour as the purchased seed sample. The total number of particles decrease, the total volume of particles increase and the average size of the particles shift to a larger size over time.

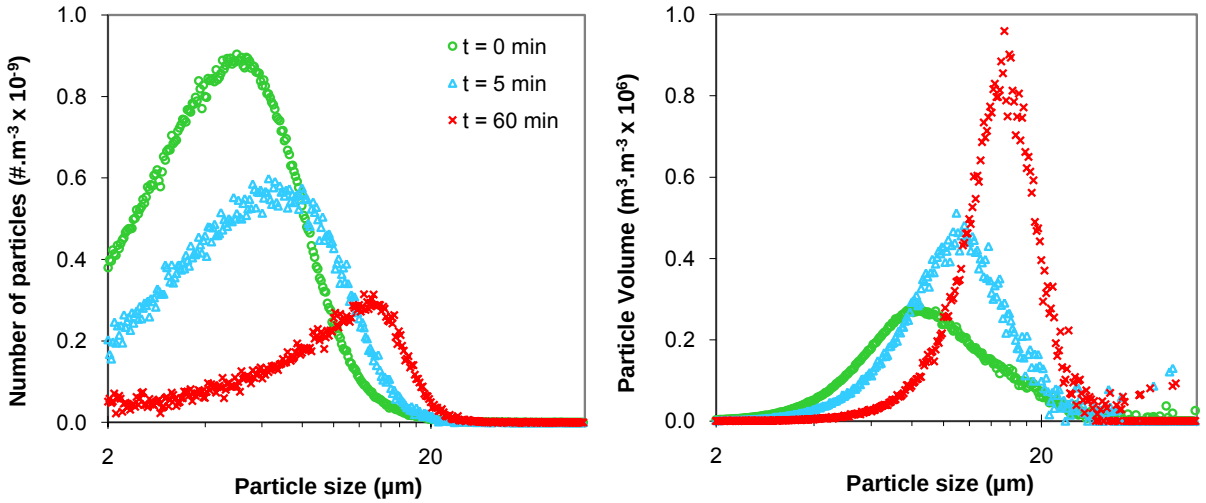

Figure 66: Number (left) and volume (right) size distributions for S_i = 3.3 & C_{seeds} = 0.03g.dm^{-3}

4.3.3 Morphology and Size of Particles

The evolution of the average particle size by both number and volume is shown in Figure 67 below. Error bars were not included on the plots in order to improve the readability.

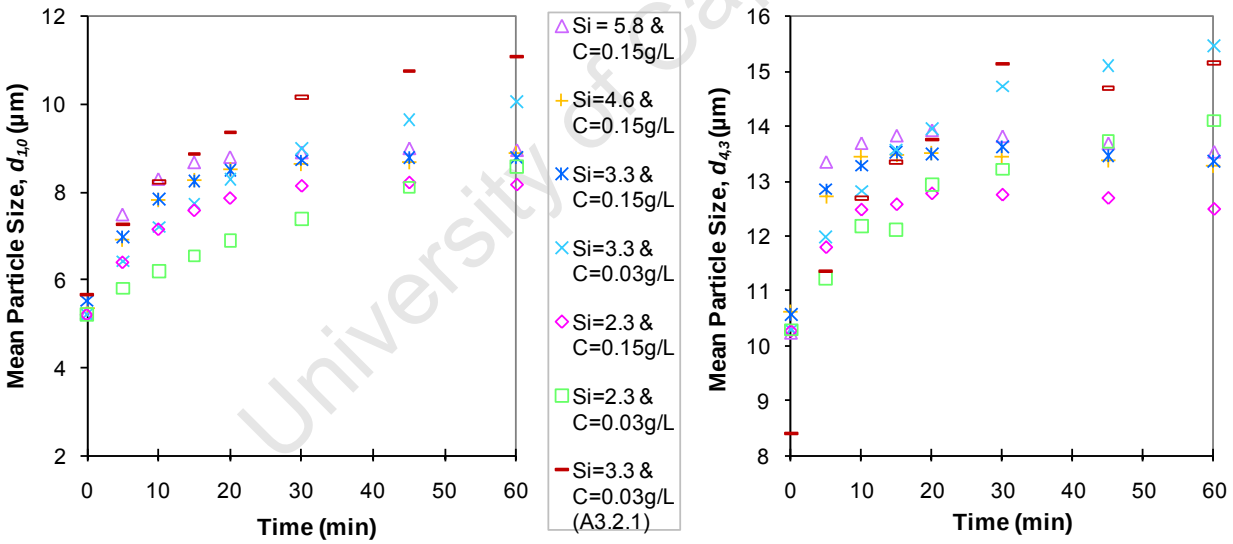

Figure 67: Change in mean particle size, $d_{1,0}$ (right) & $d_{4,3}$ (left), with time for the various kinetic experiments

Figure 67 shows that the mean particle sizes increase over time for all the kinetic experiments. The largest particles were produced where an initial supersaturation level of S_i = 3.3 and a seed concentration of C_{seeds} = 0.03g.dm^{-3} was utilized. The figure also confirms that the system had reached equilibrium for experiments with a high seed concentration.

The SEM images for the purchased and A3.2.1 seed samples are shown below. Both seed samples have similar mean sizes, as discussed earlier, but different morphologies. Both samples also appear to be relatively agglomerated.

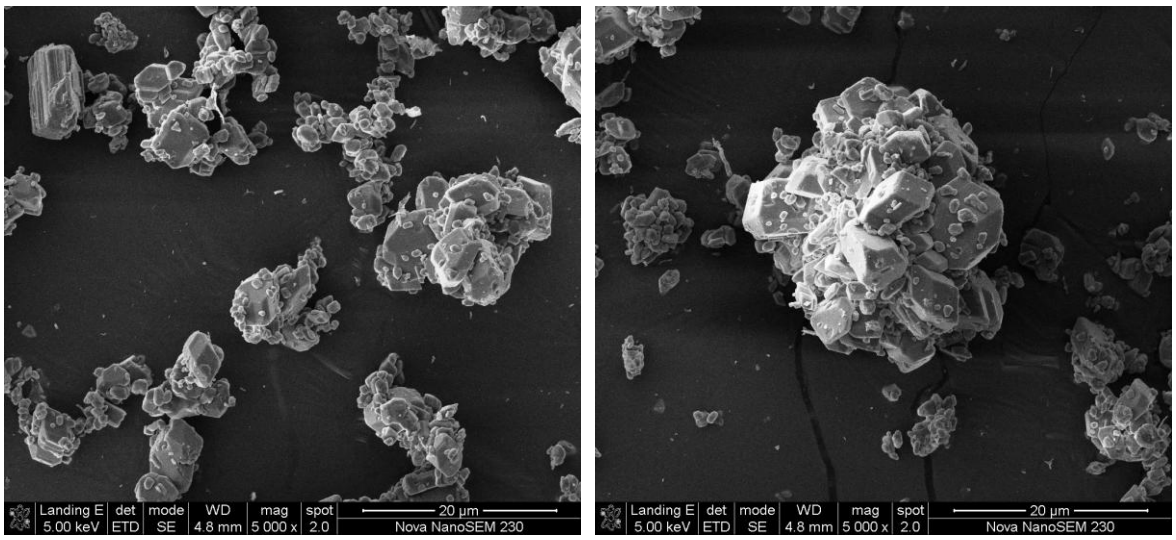

Figure 68: SEM images of purchased $CaC_2O_4.H_2O$ seed material

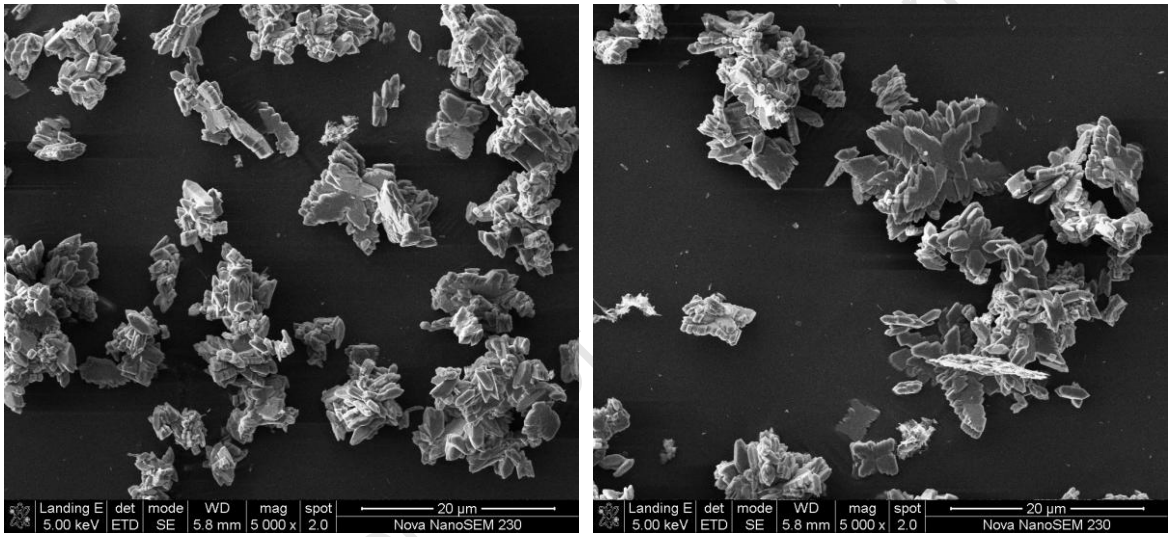

Figure 69: SEM images of A3.2.1 seed material

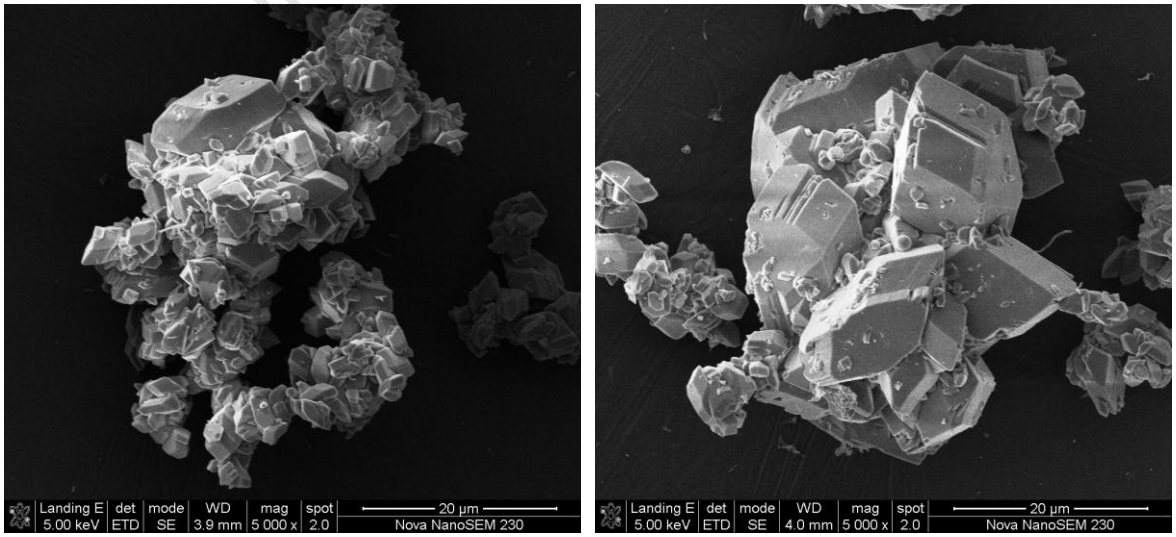

Figure 70: SEM images from kinetic experiment with S_i = 3.3 & C_{seeds} = 0.03g.dm^{-3}

Figure 70 shows an example of the particles produced at the end of a kinetic experiment. The particles appear to have a larger size and morphology to the seed particles. The particles in Figure 70 seem to exhibit a higher degree of agglomeration and the individual particles have more shape i.e. the edges of the seed particles are rounded whereas those at the end of a kinetic experiment have more defined edges. This would support growth as an active mechanism in the kinetic experiments. Figure 151 in Appendix B.2 shows that the particles produced from seed sample A3.2.1 are more agglomerated at the end of the kinetic experiment then what was previously observed. Similar results were found for the other kinetic experiments and the SEM photographs can be found in Appendix B.2.

XRD analysis confirmed that all samples produced in the kinetic experiments were pure COM. Figure 71 below shows an example of the XRD spectrum obtained for every kinetic experiment sample.

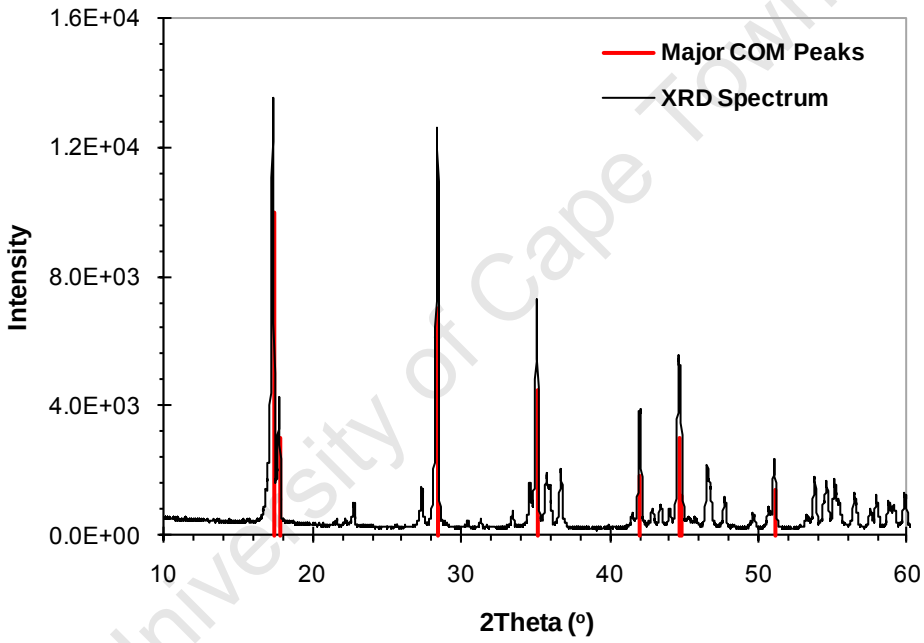

Figure 71: XRD spectrum showing fit to major COM peaks for kinetic experiment with S_i = 5.8 & C_{seeds} = 0.15g.dm^{-3}

4.3.4 Growth and Aggregation Kinetics

The growth and aggregation kinetics were determined by following the procedure set out in Section 4.2.8. The supersaturation profiles and individual plots of growth rate versus relative supersaturation for each kinetic experiment can be found in Appendix B.3. All of the supersaturation profiles exhibit a decrease in the supersaturation over time, as what was expected. The error bars, specifically for the low initial supersaturation levels and seed concentrations, are quite large suggesting scatter in the data at these conditions. The individual plots of the growth rate versus relative supersaturation were fitted with parabolic trendlines and the respective equations and R^2-values are shown in Figures 152 to 158 in Appendix B.3. These figures also confirm the high scatter in the data at low supersaturations and seed concentrations as found by Andreassen (2001). The best fit of the data

was found for the highest supersaturation level investigated. A summarised plot of all the growth rates determined from the kinetic experiments can be found in Figure 72 below.

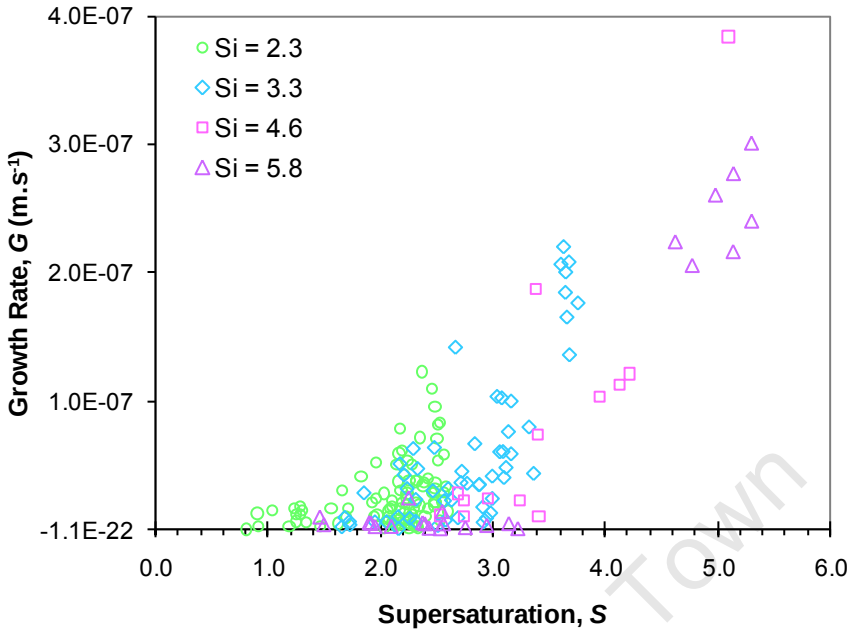

Figure 72: Summary of all determined growth rates at various initial supersaturations

From all the kinetic experiments the growth rates were found to be in a range of G = 1.4×10^{-10} to 3.8×10^{-7} m.s^{-1}. A plot of the square root of the growth rate versus the relative supersaturation was produced in order to determine an expression for the growth rate in terms of supersaturation (Figure 73 below).

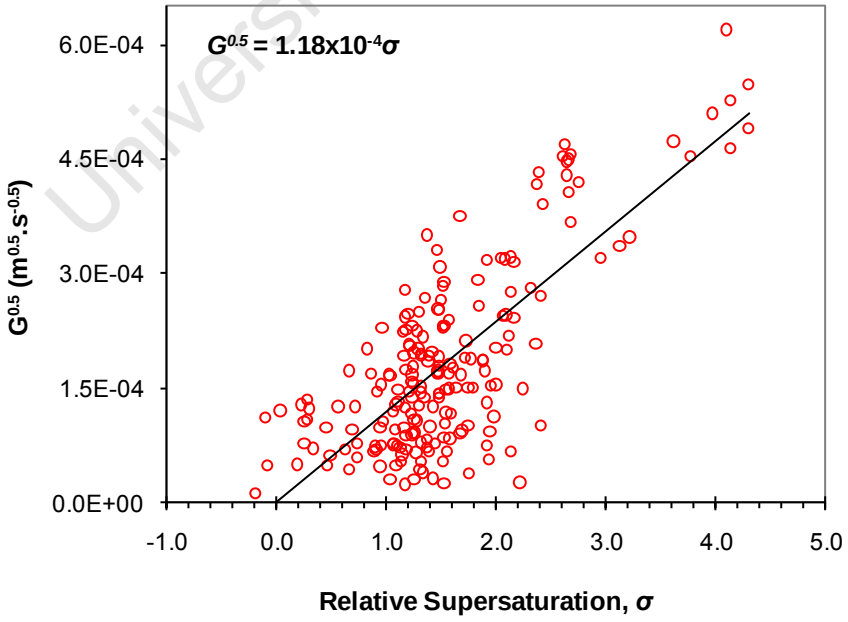

Figure 73: Overall growth rate plot to determine the growth rate constant

The resulting equation was as follows:

$$G = 1.40 \times 10^{-8}(S-1)^2 \quad \text{... (137)}$$

or in terms of the rate of change of the particle radius:

$$r = 7.02 \times 10^{-9}(S-1)^2 \quad \text{... (138)}$$

The coefficient of determination was relatively low for Figure 73 i.e. R^2 = 57%. This was due to the scatter in the data at low relative supersaturations.

The average aggregation rate constant profiles and aggregation rate constant plots versus supersaturation for each of the kinetic experiments can be found in Appendix B.4. These plots show that the aggregation rate constant decreased over time in the kinetic experiments with a maximum value being obtained within the first 5 minutes of the experiment. Figure 74 below shows a summarised diagram of the change in the aggregation rate constant over time in the kinetic experiments.

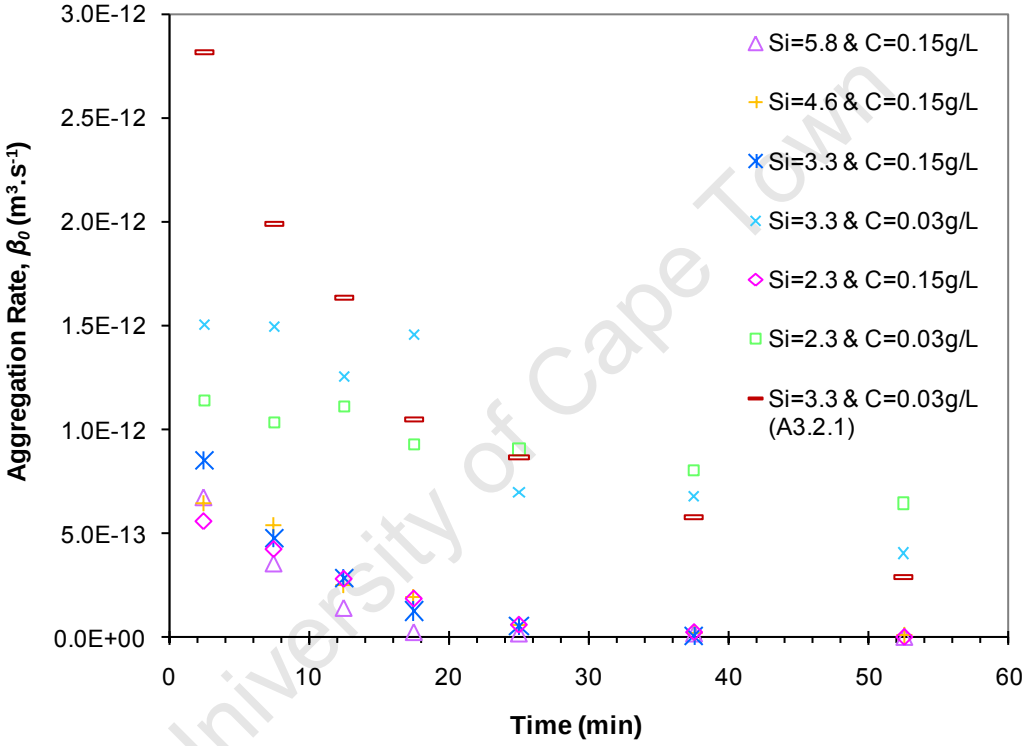

Figure 74: Average aggregation rate constant profiles for different combinations of initial supersaturation and seed concentration

The figure above shows that the profiles for a high seed concentration i.e. C_{seeds} = 0.15g.dm^{-3} all exhibit very similar aggregation rate constants at the same point in time. Where a lower seed concentration was utilized, a higher aggregation rate per time period was observed in comparison to the higher seed concentration. The highest aggregation rates were observed for an initial supersaturation level of S_i = 3.3 and seed concentration of C_{seeds} = 0.03g.dm^{-3}. Kinetic experiments where the A3.2.1 seed sample was utilized appears to initially exhibit higher aggregation rate constants than experiments where the purchased seed sample was used.

As aggregation is a function of both supersaturation and seed concentration (surface area) the results for each kinetic experiment are shown below.

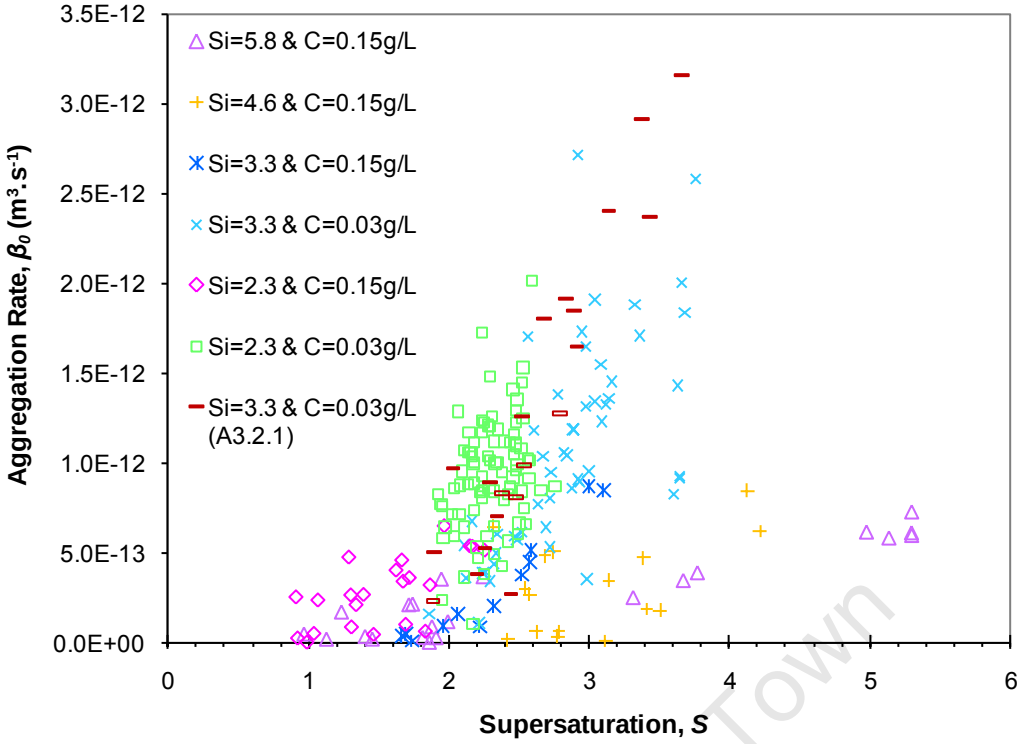

Figure 75: Aggregation rate constants versus supersaturation for various combinations of initial supersaturation and seed concentration

Figure 75 shows that for all the kinetic experiments the aggregation rate constant increases as the supersaturation is increased. The aggregation rate constant does not increase as rapidly however for experiments where an initial supersaturation level of S_i = 5.8 or 4.6 was used. For all the kinetic experiments the aggregation rate constants were found to be in the range of β_0 = 1.3×10^{-16} to 3.2×10^{-12} m^3.s^{-1}.

A comparison of the growth and aggregation results for the two seed samples is shown below in Figure 76. Both the growth rates and aggregation rate constants appear to be very similar between the two seed samples.

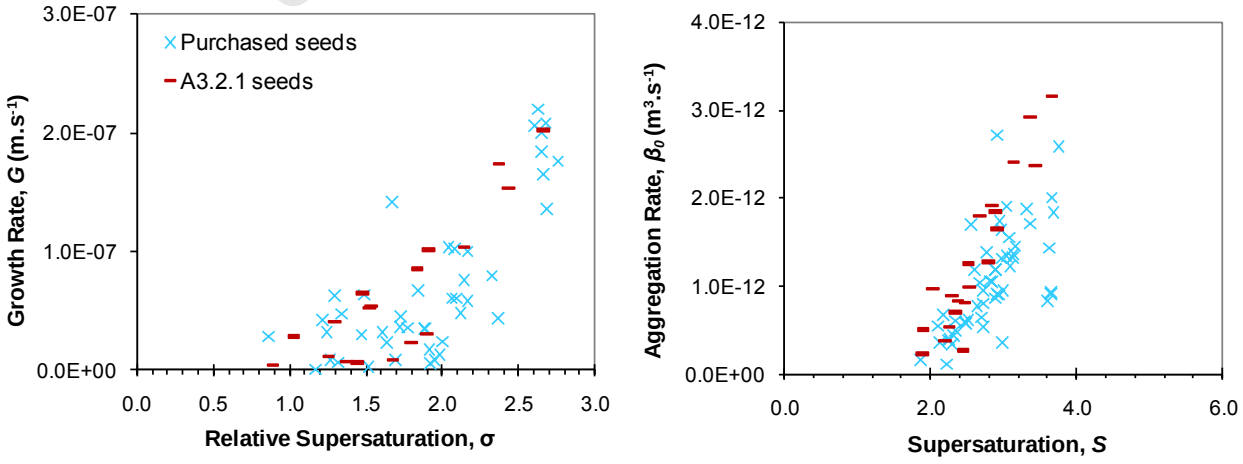

Figure 76: Comparison of the growth and aggregation rates for two different seed samples with S_i = 3.3 & C_{seeds} = 0.03g.dm^{-3}

4.4 Discussion

4.4.1 Effect of Supersaturation and Seed Concentration on Growth and Aggregation

The PSD results for all of the kinetic experiments agreed with those found by Bramley *et al.* (1996) (see Figure 25 in Chapter 2). The number of particles decreased and the PSDs broadened as the experiment proceeded which is characteristic of aggregation and therefore supported that aggregation was an active mechanism within the kinetic experiments. The total volume of particles in the system increased over time confirming that growth was also an active mechanism. Nucleation did not occur in any of the kinetic experiments apart from those operated with a combination of high initial supersaturation (S_i = 5.8) and low seed concentration (C_{seeds} = 0.03g.dm^{-3}). The results from these were thus not used in further calculations.

The results showed that the seed concentration had an effect on the approach to equilibrium of both the zeroth and third moments e.g. compare Figures 65 & 66 with Figures 138 & 139 in Appendix B.1. It was found in all experiments with a high seed concentration (C_{seeds} = 0.15g.dm^{-3}) that the approach to equilibrium was fast and the system had reached equilibrium by approximately 20 to 30 minutes (as seen in Figure 64). When considering the particle volume (third moment) for the high initial supersaturations of S_i = 4.6 & 5.8 it appears that these systems have reached equilibrium within the first 5 to 10 minutes. Thus, it is evident that the approach to equilibrium for the higher supersaturation levels is considerably faster than for the lower ones. This is what was expected as there is a greater driving force for the higher supersaturations. The kinetic experiments with a low seed concentration (C_{seeds} = 0.03g.dm^{-3}) appear to have not reached equilibrium within the time frame of the experiment.

As growth was assumed to be size independent and growth rate dispersion was not considered it was expected that the growth of the particles would not be affected by the concentration of seeds (i.e. number of particles and surface area). The results show that the change in the third moment and volume PSDs over time is faster for a higher initial supersaturation level (compare Figures 62 & 63 with Figures 65 & 66). This agrees with what was expected as a higher supersaturation has a greater driving force. Thus, the growth of the particles will be faster at a higher initial supersaturation level. From the results it was found that the largest particles were produced for conditions of S_i = 3.3 & C_{seeds} = 0.03g.dm^{-3} (see Figure 67). For a combination of high initial supersaturation and high seed concentration, fast growth occurs onto a large number of particles. Thus, the supersaturation has to be distributed amongst the large number of particles and the change in size of the particles is not as great as it would be for a lower seed concentration. Even though the increase in the total particle volume after 60 minutes is the greatest for S_i = 5.8, the high seed concentration (to prevent nucleation) does not allow the individual particles to grow to the largest size. Also, for a combination of low initial supersaturation and high seed concentration, we would expect the resulting particles to be of the smallest size (see Figure 67). This is because there is only a small amount of supersaturation that can be deposited upon a large number of particles, thus the growth of each individual particle is small. The medium supersaturation and low seed concentration yielded the largest particles due to there being only a small number of particles for the supersaturation to be deposited upon resulting in the largest particles.

The aggregation rate is a function of the supersaturation, energy input (agitation rate), number of particles, surface area etc. i.e. $\beta_0 = f(S, \bar{\varepsilon}, m_0^2, m_2, \ldots)$. Thus, it was expected that the initial supersaturation level as well as the seed concentration would directly influence the rate of aggregation. A higher seed concentration has a higher total number of particles and consequently a higher surface area. In the current work the surface area of the higher seed concentration was five times that of the low seed concentration (see Table 11). The evolution of the zeroth and third moments of the PSDs show indirectly that the rate of aggregation was faster for a higher initial supersaturation level and seed concentration e.g. compare Figures 140 & 141 with Figures 62 & 63 and Figures 142 & 143 in Appendix B.1. In comparing these figures it is obvious that the change in the zeroth moment and number PSDs over time was considerably faster for a higher initial supersaturation level and/or seed concentration, which is in agreement with literature expectations.

4.4.2 Growth Kinetics

The growth kinetics determined in the current work i.e. G = 1.4×10^{-10} to 3.8×10^{-7} m.s^{-1} are within the same range as those found by Nielsen & Toft (1984), Garside *et al.* (1982), Kavanagh (1992) and Zauner & Jones (2000). However, the maximum growth rate found by any of these literature sources was generally of the order of 10^{-8} whereas higher growth rates were found in the present work. All the growth rates tend to zero at S = 1 which is what was expected from literature. Conclusions from literature that the growth of COM is controlled by the spiral growth mechanism and exhibits a second-order dependence of supersaturation on the growth rate (as found by Nancollas & Gardner (1974), Gardner & Nancollas (1975), Bramley *et al.* (1997) and Zauner & Jones (2000)) agrees with the findings of the current work. Most of the growth rate data fitted well to a parabolic trendline supporting the spiral growth mechanism. However, the low R^2-values found at the low initial supersaturations and seed concentrations were expected due to the error in the Coulter Counter measurements. Andreassen (2001) stated that due to the small change in both the particle number and volume at low supersaturations, the spread in the results from the Coulter Counter measurements was quite considerable. This is in agreement with what was found in the current work. Even though the experiments were repeated numerous times, the coefficients of determination were still quite low, specifically for the experiment where a combination of low initial supersaturation and seed concentration was utilized (see Figure 157 in Appendix B.2). The best fits to the parabolic trendline were found for the higher initial supersaturations as determined by Andreassen (2001).

The growth rate constant found for the current work is considerably higher than that found by other literature i.e. k_g = 1.40×10^{-8} for the current work, k_g = 1.45×10^{-9} from the work of Bramley *et al.* (1997) and k_g = 5.90×10^{-10} from the work of Zauner & Jones (2000). The difference in the growth rate constants could be explained by the fact that higher initial supersaturation levels were investigated in the current work as compared to the work of Bramley *et al.* (1997). A higher initial supersaturation would result in faster kinetics and thus a higher growth rate constant. Another explanation could be that due to the large spread in the data, specifically at the low supersaturation levels, there is a reasonable amount of uncertainty in the determination of the growth rate constant (R^2 = 57%). The most likely explanation for the deviation, however, is that growth into the field of view of the particle size analyser was not accounted for in the present work (Bramley *et al.* (1997) incorporated this effect into their model and thus this would result in a lower growth rate constant).

Growth into the field of view would affect the value of the growth rate because the total volume of particles would increase not only by the growth of particles from the available supersaturation but also because of the appearance of more particles into the detectable size range of the Coulter Counter. Because the growth rate is calculated from the change in the third moment over time, the results would yield higher growth rates and in turn a higher growth rate constant.

4.4.3 Aggregation Kinetics

The aggregation rate constants for the current work i.e. β_0 = 1.3×10^{-16} to 3.2×10^{-12} $m^3.s^{-1}$ are similar to those found by other literature. The maximum aggregation rates, however, are higher than those found by Bramley *et al.* (1997) i.e. maximum β_0 ~ 3.2×10^{-14} $m^3.s^{-1}$. This can be explained by the fact that higher initial supersaturations were investigated and more importantly that considerably higher seed concentrations were utilized. The initial seed concentration used by Bramley *et al.* (1997) was approximately 0.0161g.dm^{-3} which is between 2 - 9 times smaller than those used in the current work. As discussed already, a higher seed concentration has a higher number of particles and because the aggregation rate constant is directly proportional to the square of the number of particles it is expected that the aggregation rate would be considerably higher for a greater concentration of seeds. This agrees with what was found in the current work.

For experiments where the high seed concentration was utilized, it was expected that the aggregation rate would be higher than for those utilizing the low seed concentration. This is because the higher particle concentration would increase the number of collisions and the aggregation efficiency would increase. This, however, was not the case (see Figure 74). The most likely explanation for these results is due to the growth of new particles into the field of view of the Coulter Counter. As this effect would be most noticeable at the higher supersaturation levels, the aggregation rate constants would appear to be lower than what was expected. The growth of particles into the detectable size range of the particle size analyser would increase the total number of particles in the system. As the aggregation rate constant is calculated from the change in particle number with time as well as the square of the particle number at a specific time, the increased total number of particles would result in a lower aggregation rate constant. Figure 75 shows that the aggregation rate constants for the two highest initial supersaturations investigated do not follow the same upwards trend with supersaturation i.e. the gradients are not as steep. Thus the aggregation mechanism is most likely competing with the effect of the growth of particles into the field of view. Since the total number of particles decreases continually over time it can be assumed that decrease in particle number due to aggregation > increase in particle number due to growth into the field of view.

4.4.4 Influence of Particle Size and Morphology on the Kinetics

Kinetic experiments were run for an alternative seed sample, A3.2.1, in order to determine whether the particles size or morphology had a significant influence on the growth and/or aggregation kinetics. From Figure 76 it is clear that both the growth and aggregation kinetics for experiments with the same operating conditions but different seed samples yield very similar results. Thus, the assumption that both growth and aggregation are size independent appears to be correct. It is important to note that the average sizes of the two seed samples were quite similar and thus if considerably smaller or larger sized particles were to be investigated, significantly different kinetic results may be found.

4.4.5 Applicability of Bramley *et al.*'s (1996) Method to Precipitation Systems

The experimental kinetic method of Bramley *et al.* (1996) has been found to be a simple technique for the determination of the growth and aggregation kinetics for the COM system. However, if higher supersaturation levels were to be investigated or more insoluble systems, this method would not be viable. The main reason for this is because the method relies on the fact that a "metastable" solution is able to be prepared and seeds are able to be added to this solution before nucleation takes place. More insoluble systems, due to their low solubility products, would precipitate very quickly and thus the level of initial supersaturation would be limited by the corresponding induction time. Also, higher supersaturations would require larger seed concentrations in order to prevent nucleation from occurring when the seeds are added to the metastable solution. This would also limit the initial supersaturation level investigated because, as found in the current work, a higher seed concentration shortens the approach to equilibrium. Thus, the sampling time would have to be decreased in order to account for the increased kinetics. Other factors to consider would be the seed particles as well as the particle size analyser. The size of the particles would influence the choice of the particle size analyser and for more insoluble systems the mean size of the particles would most likely be considerably smaller than those used in the present work.

Quantitative results showing the limit on the level of the initial supersaturation that is viable for the use of Bramley *et al.*'s (1996) experimental method will be discussed in the final chapter of this dissertation.

4.5 Preliminary Conclusions

From the results and discussion sections the following conclusions have been formulated:

i. The growth and aggregation kinetics for COM could be determined using the experimental kinetic method of Bramley *et al.* (1996).
ii. The kinetics were determined for various initial supersaturation levels ranging from S_i = 2.3 to 5.8 and seed concentrations of C_{seeds} = 0.03 and 0.15g.dm^{-3}. Nucleation was found to occur where a combination of high supersaturation and low concentration of seeds was utilized and thus these results were not included in the final kinetics determination.
iii. The growth rates for COM were found to be in the range of G = 1.4×10^{-10} to 3.8×10^{-7} m.s^{-1} and a kinetic expression for the growth rate versus supersaturation was determined to be: $G = 1.40 \times 10^{-8}(S-1)^2$. The growth rates agreed with those found in literature; however the growth rate constant was considerably higher than that found in literature most likely due to growth of particles into the field of view.
iv. The aggregation rate constants for COM were determined to be within the range of β_0 = 1.3×10^{-16} to 3.2×10^{-12} m^3.s^{-1} with the highest values being found at the start of the experiments. These values also agreed with literature findings however the aggregation rate constants at high initial supersaturations were lower than what was expected due to growth of particles into the size detection limit of the Coulter Counter.
v. SEM images confirmed that both growth and aggregation of the seed particles occurred within the kinetic experiments. XRD analysis confirmed the product as COM only.

vi. The purchased and A3.2.1 seed samples were found to yield very similar growth and aggregation kinetics. However, the mean sizes of the two samples were similar and seeds with considerably smaller or larger sized particles may yield significantly different results.

Chapter 5

DETERMINATION OF THE INDUCTION PERIOD

5.1 Introduction

Although the induction time is a measurement that does not have any real physical significance, gaining a general idea about this variable for a precipitating system can be useful. The induction period yields information about how quickly a system will precipitate at specific supersaturations and temperatures and can also aid in determining the nucleation kinetics.

The aims of this chapter are to:

i. Determine the induction period at various initial supersaturations for the calcium oxalate monohydrate system.
ii. Conclude about the applicability of experimental kinetic methods, such as that utilized by Bramley *et al.* (1996), for use with more insoluble systems.

5.2 Materials and Methods

5.2.1 Reagents

De-ionized water (Milli-Q Water Purification System, Millipore, USA) was utilized in all cases. Analytical grade anhydrous calcium chloride ($CaCl_2$) (Merck, South Africa) and sodium oxalate ($Na_2C_2O_4$) (Sigma-Aldrich Co., Germany) were used in the preparation of all reagent solutions.

5.2.2 Experimental Set-Up and Procedure

The induction period experiments were conducted in a 1L jacketed and baffled glass reactor analogous to that utilized in the seed and kinetic experiments (see Figure 37 in Section 3.2.3). In all experiments the reactor operated at a constant temperature of T = 37±2°C and an agitation rate of N = 1500±10 rpm ($\bar{\varepsilon}$ = 14.7 $m^2.s^{-3}$, Re = 9.0x10^4). This mixing rate was chosen as it proved to be either at or above the critical impeller speed for all initial supersaturation levels investigated i.e. t_{ind} did not change for impeller speeds above this value. Also, higher agitation rates caused disturbances in the conductivity readings (possibly due to the large amount of bubbles in the system at these high turbulences). The induction times for a large range of supersaturation levels viz. S_i = 2.1 to 9.7 were investigated. For supersaturations below 2.1 the change in conductivity was too small for accurate readings to be established. While, for supersaturations above 9.7 the induction time proved to be of the same order of magnitude as the mixing time.

500mL of deionized water was placed in the reactor and allowed to thermally stabilize. The reactant solutions were also heated to T = 37±2°C in a water bath before use. An AZ86555 conductivity meter (AZ Instruments, South Africa) and data logging system ("HandHeld") was used to read and record the solution conductivity at 1 second intervals. The conductivity probe was placed inside the reactor

and once the conductivity reading had stabilized, 250mL each of the $CaCl_2$ and $Na_2C_2O_4$ solutions were poured simultaneously into the reactor. The experiment was concluded after 20 minutes.

All experiments were repeated four times for repeatability and error analysis purposes.

5.2.3 Determining the Induction Period from the Conductivity Profiles

The induction period for each initial supersaturation level investigated was determined from the experimental conductivity profiles. A typical conductivity profile for the induction period experiments is shown below.

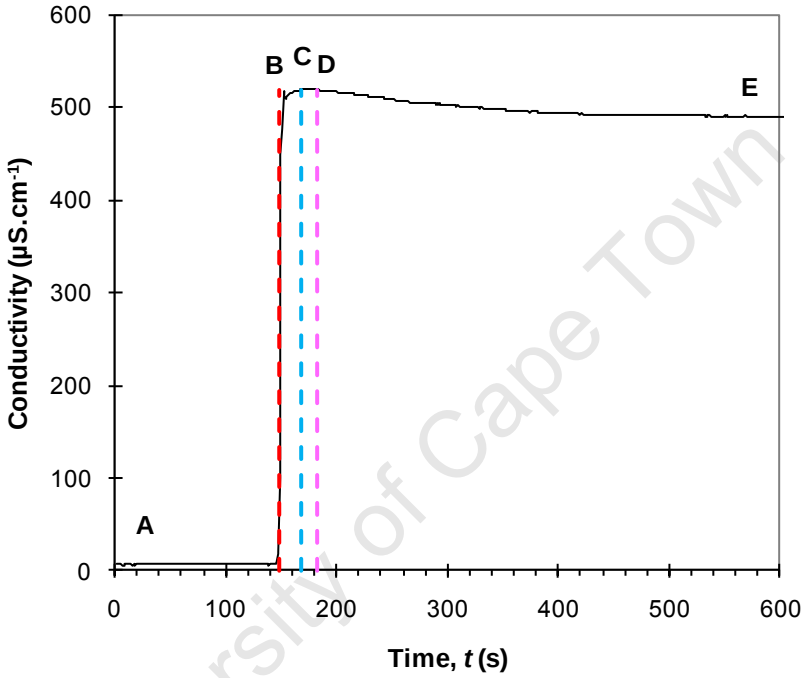

Figure 77: Typical conductivity profile for the induction time experiments where S_i = 6.5

Each conductivity profile consisted of four distinct regions as follows:

$A \rightarrow B$: Stabilization of the conductivity meter reading. This was to ensure thermal equilibration of the initial 500mL of deionized water in the reactor.

$B \rightarrow C$: Instantaneous addition of the reactant solutions. This resulted in a sharp rise in the conductivity reading and subsequent creation of the initial supersaturation level.

$C \rightarrow D$: Invariable solution conductivity. This region was analogous to the induction period.

$D \rightarrow E$: Steady decrease in the solution conductivity until equilibrium was reached. The start of this region indicated the onset of precipitation.

For every conductivity experiment the induction period was read-off from the conductivity profiles by locating region $C \rightarrow D$ (see Figure 78 below). Raw data and sample calculations can be found in Appendix C.3.

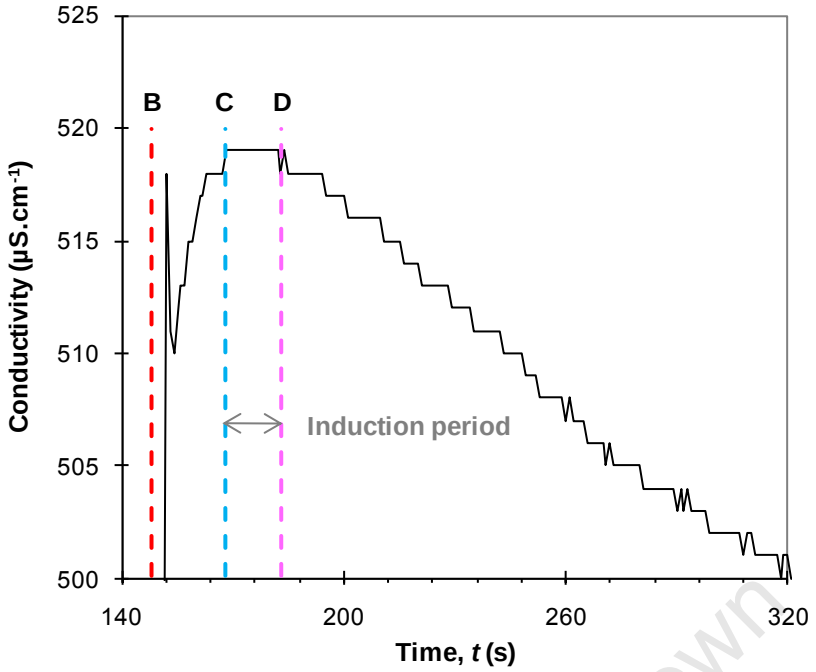

Figure 78: Zoomed-in conductivity profile clearly showing the induction period and onset of precipitation

The four regions were easily identifiable in all of the experiments however at the highest and lowest supersaturations investigated some errors may have occurred. At the low supersaturations the start of precipitation and/or end of the induction period was not easy to identify due to the very small decrease in the conductivity value. Also, at high supersaturations the induction time was short and the onset of precipitation occurred quickly after the addition of the reactants.

5.3 Results

The conductivity profiles for all supersaturation levels investigated can be seen in Figure 79 below.

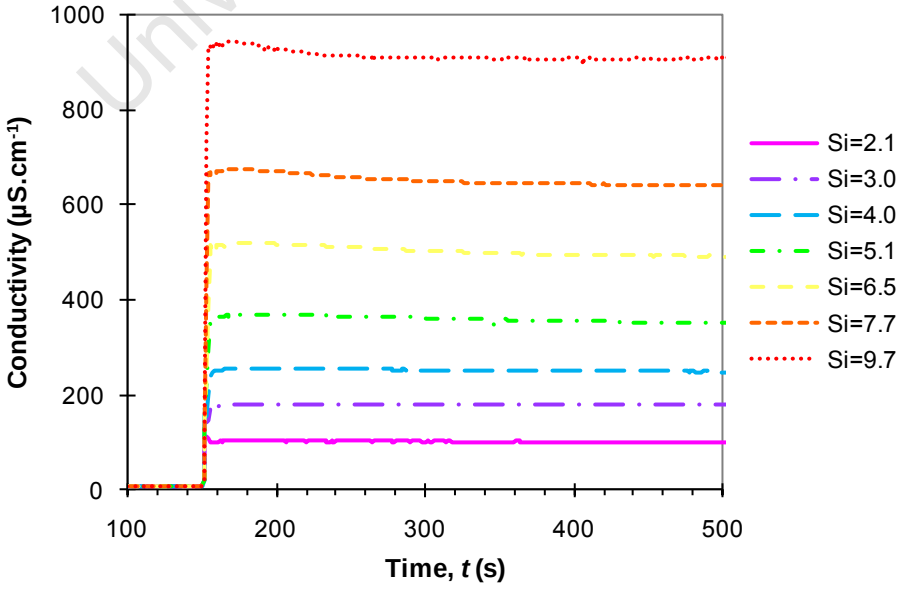

Figure 79: Conductivity profiles for varying initial supersaturation levels

The profiles show that equilibrium is reached in a shorter period of time for higher initial supersaturation levels.

Table 12 shows a summary of the induction times found at each initial supersaturation investigated. As expected the induction time decreases as the supersaturation is increased.

Table 12: Summary of results from induction time experiments

Supersaturation, S_i	Induction Time, t_{ind} (s)	Controlling Nucleation Mechanism	
		Visual Observation	From Figure 81
2.1	345 ± 45	Heterogeneous	Heterogeneous
3.0	118 ± 8	Heterogeneous	Hetero/Homogeneous
4.0	82 ± 14	Hetero/Homogeneous	Homo/Heterogeneous
5.1	34 ± 8	Homo/Heterogeneous	Homogeneous
6.5	20 ± 4	Homogeneous	Homogeneous
7.7	14 ± 2	Homogeneous	Homogeneous
9.7	6 ± 2	Homogeneous	Homogeneous

It is clear to see that there is a higher amount of uncertainty in the induction times found at lower concentrations. As discussed earlier this is due to the small change in the solution conductivity over time. Table 12 also shows that the controlling nucleation mechanism at low supersaturations is heterogeneous while at high supersaturations it is homogeneous, as expected from literature predictions. Heterogeneous nucleation was observed in the experiments from scaling on the reactor walls, impeller and baffles. Homogeneous nucleation, on the other hand, was observed from the bulk solution turning cloudy.

Figure 80 shows a plot of the determined induction times at each initial supersaturation level investigated.

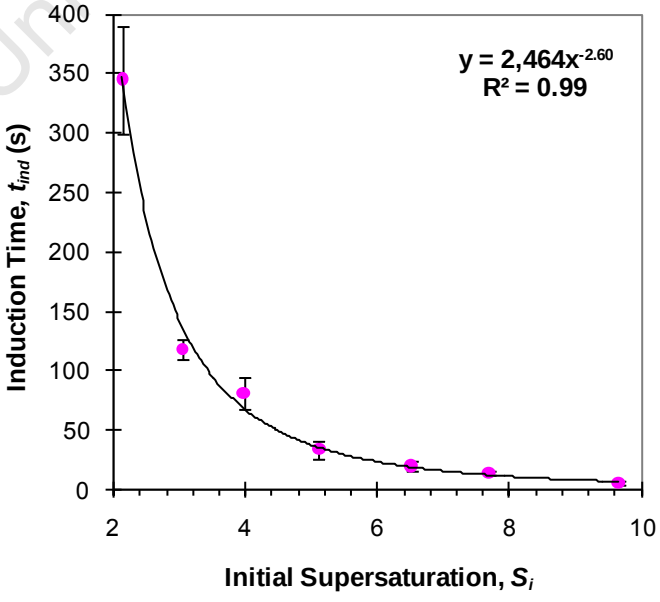

Figure 80: Power law fit of induction time versus initial supersaturation for COM

The data fitted very well to a power law trendline, with the resulting equation being expressed as follows:

$$t_{ind} = 2464S_i^{-2.6} \quad \ldots (139)$$

Plots of $log(t_{ind})$ versus $log(\sigma)$ & $log(S_i)^{-2}$ were compiled in order to characterize the mechanisms of nucleation in the experiments. Figure 81 shows that there were three possible nucleation regions occurring in the induction time experiments.

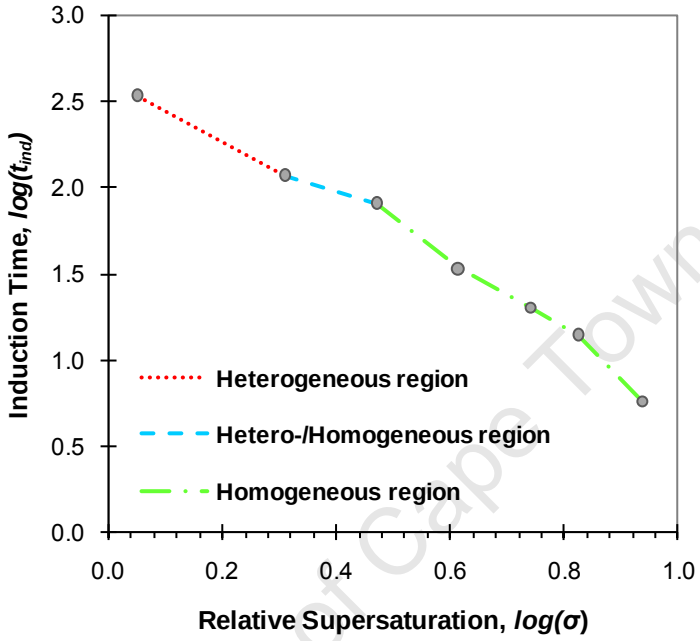

Figure 81: Plot of $log(t_{ind})$ versus $log(\sigma)$

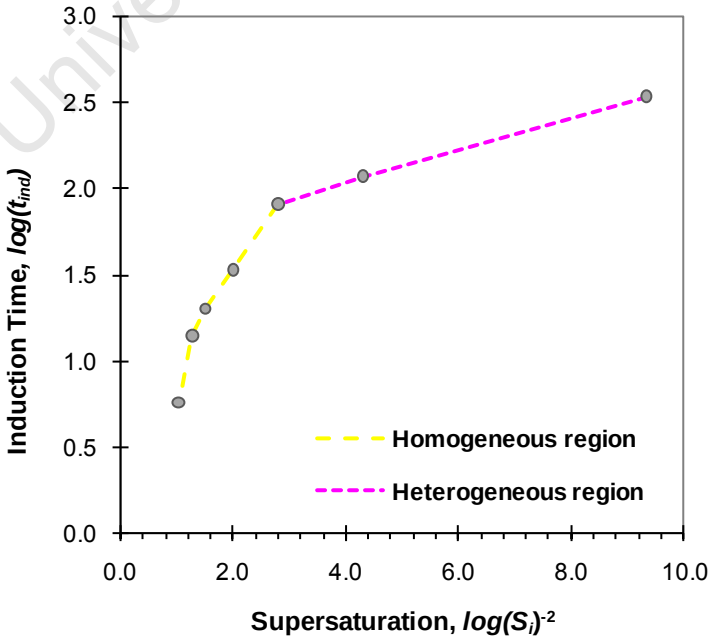

Figure 82: Plot of $log(t_{ind})$ versus $log(S_i)^{-2}$

Figure 82 also shows that both heterogeneous and homogeneous nucleation occurred in the experiments.

Figures 83 & 84 below show a comparison between the induction times found in the current work for COM with those found in literature for other substances using various methods (Sohnel & Mullin (1978), Sohnel & Mullin (1987) (cited in Sohnel & Mullin, 1988), Spanos & Koutsoukos (1998), Chien *et al.* (1999), Sohnel & Mullin (1979) (cited in Myerson, 2002), Mahajan & Kirwan (1993), Lancia *et al.* (1999), Bouropoulos & Koutsoukos (2000) & Scholl *et al.* (2006)).

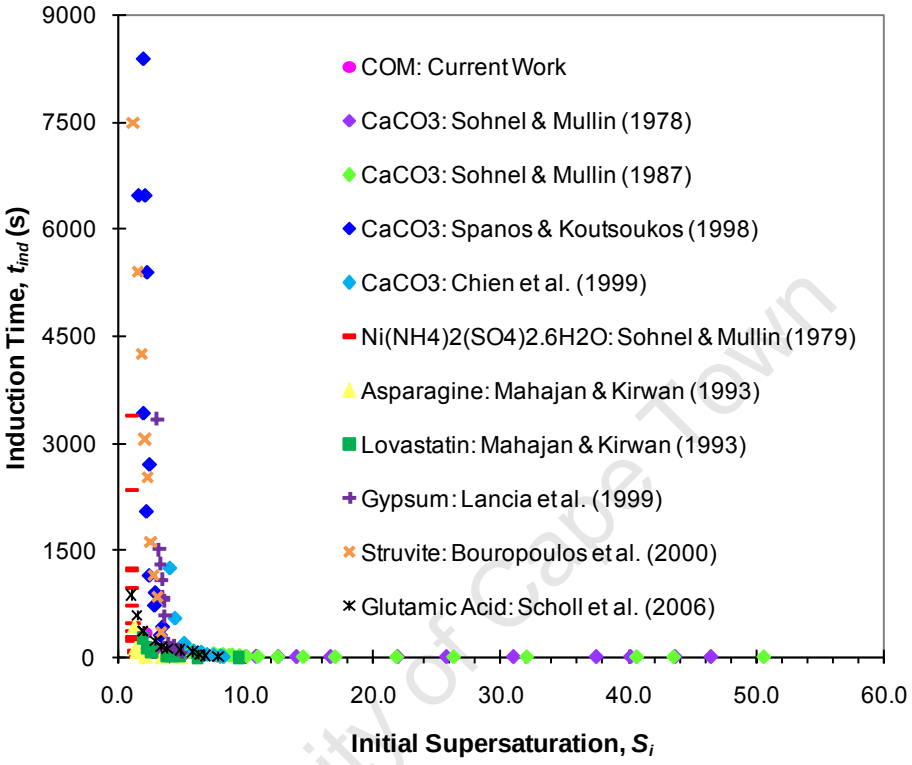

Figure 83: Comparison of induction times for various compounds

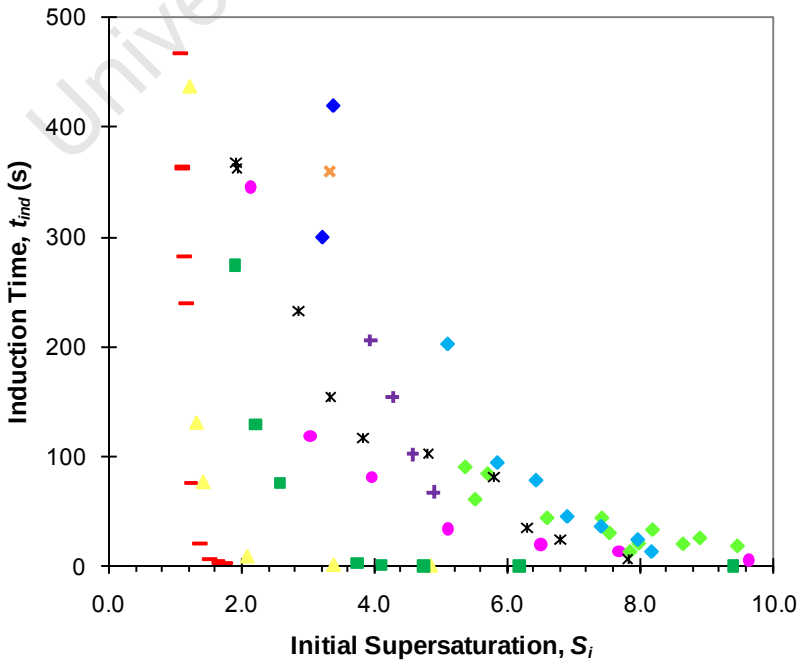

Figure 84: Zoomed-in plot of induction time versus supersaturation (see legend in Figure 83)

Figure 83 shows that the induction time data for all compounds exhibits similar power law trends when plotted against supersaturation. By zooming-in to the data, Figure 84 shows, however, that the data from various compounds does not necessarily fit to a single general curve. If a power law trendline is fitted to all the data, a coefficient of variation of R^2 = 71% is achieved (see Figure 85).

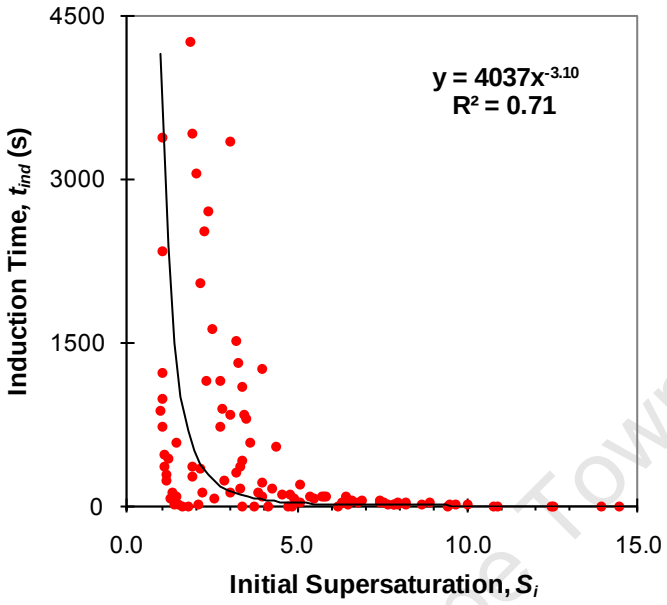

Figure 85: Fit of all induction time data to a power law trendline

Tables 13 & 14 below show a comparison between three compounds (from moderately to sparingly soluble in nature).

Table 13: Solubility products for three precipitation systems calculated using OLI Stream Analyser (OLI Systems, 2008)

Compound	K_{sp} (@ 25°C) (kmol.m^{-3})^2
$CaC_2O_4.H_2O$	2.2×10^{-9}
$BaSO_4$	9.9×10^{-11}
NiS	4.1×10^{-26}

As can be seen in Table 14, for constant reagent concentrations, the supersaturation varies considerably between the three compounds due to the differences in the solubility products.

Table 14: Comparison of supersaturations for different precipitation systems @ 25°C

Compound	C_A (kmol.m^{-3})	C_B (kmol.m^{-3})	S_i
$CaC_2O_4.H_2O$	3.9×10^{-4}	7.8×10^{-5}	2.6
$BaSO_4$			14.5
NiS			513

$CaC_2O_4.H_2O$			10.6
$BaSO_4$	$2.9x10^{-3}$	$5.9x10^{-4}$	77.5
NiS			1404

Note: In Table 14, A = $CaCl_2$, $BaCl_2$ or $NiSO_4$ & B = $Na_2C_2O_4$, Na_2SO_4 or $(NH_4)_2S$ respectively.

5.4 Discussion

The conductivity profiles found in the induction time experiments were very similar to those determined by Chien *et al.* (1999) using a similar method (see Figure 23 in Section 2.8.2). The determined induction times for COM followed a similar power law fit with supersaturation when compared to the data for other compounds found in literature. During the induction time experiments it was observed that the solution conductivity started to decrease before a change could be visually observed i.e. the solution conductivity started to decrease before the solution turned "milky". This is because the visual detection of nucleation (hence end of the induction period) was only possible once the nuclei grew to a detectable size. However, the solution conductivity would most likely have already started to decrease. Thus, techniques utilizing a method of visual observation will inherently encounter inaccuracies in the determination of the induction period.

Figures 83 & 84 show that although the trends are similar for each compound, the exact induction times are not necessarily the same. This could be because different techniques were used to source the induction times and thus there are some inaccuracies in the results. Also, the experiments for the different compounds were conducted at different temperatures and pH levels. Temperature would influence the data in Figures 83 & 84 by either increasing or decreasing the initial supersaturation level.

From the results section it is clear that experimental methods (for kinetics determination) where a metastable solution is required are only suitable for systems where the supersaturation can be kept below a certain limit. This limit is dependent on the system as, from Figure 84, it is clear that the induction time data for various systems does not fall directly upon the same trendline. However, this limit may be approximated at S_i = 6. In order to prepare the initial "metastable" solution the reagent solutions have to be mixed together. Depending on the efficiency of the mixing process, this may take up to 15 - 30 seconds. Also, time is required for the addition of the seeds. Thus, it is proposed that an approximate lower limit of around 30 seconds is sufficient in order to ensure no homogeneous nucleation before the addition of the seed particles. This means that initial supersaturations that yield an induction time below 30 seconds should not be considered for kinetic experiments. Another aspect of this discussion point is that higher supersaturations require higher seed concentrations (surface area) in order to prevent nucleation on addition of the seeds to the metastable solution. As found in the kinetic experiments, higher seed concentrations cause a faster approach to equilibrium. Therefore, shorter sampling times and faster PSD measurements are required which can cause the method to be unfeasible.

When considering the utilization of Bramley *et al.*'s (1996) method for insoluble systems, Tables 13 & 14 present significant results. $BaSO_4$ and NiS were used in the comparison as they represent

different precipitation systems with subsequently lower solubility products then that of COM. At constant reagent concentrations, Table 14 shows that the supersaturations are significantly different between the three compounds due to the differences in the solubility products. This shows that if similar reagent concentrations were to be investigated between different systems, Bramley *et al.*'s (1996) method would not be feasible. This is because the supersaturations for both $BaSO_4$ and NiS are so high that no induction time would exist and the solutions would homogeneously precipitate. Thus, if more insoluble systems are to be investigated, the reagent concentrations must be very low in order to counteract the extremely low K_{sp} of the compound. The low reagent concentrations would impose a constraint on the use of Bramley *et al.*'s (1996) method because a point would be reached when the mass of the reactants would be so low that their preparation would be impractical. Also, if kinetics were to be determined at industrial concentrations, which are generally significantly higher than those investigated in this work, Bramley *et al*.'s (1996) method would not be feasible.

5.5 Preliminary Conclusions

The following preliminary conclusions have been developed from the results and discussion section:

i. The induction time for COM was determined over an initial supersaturation range of S_i = 2.1-9.7. A plot of t_{ind} versus S_i was found to fit very well to a power law trendline which could be expressed by: $t_{ind} = 2464 S_i^{-2.6}$.
ii. Over the supersaturation range investigated it was found that the COM system exhibited three nucleation regions: homogeneous, heterogeneous & a region where both nucleation mechanisms occurred.
iii. Induction time measurements utilizing solution properties e.g. conductivity are proposed to be more accurate than those utilizing visual detection.
iv. Bramley *et al.*'s (1996) experimental method for the determination of the growth and aggregation kinetics was found to be viable for more insoluble systems as long as the initial supersaturation level is kept below a certain value, approximately S_i = 6. The method cannot be used for higher initial supersaturations because the solution will not retain its metastability for a long enough period of time. Also higher seed concentrations, required at higher supersaturations, would cause a fast approach to equilibrium which would create problems with sample time and PSD measurement.
v. The feasibility of solution preparation at very low concentrations is another factor that has to be taken into account when considering the feasibility of Bramley *et al.*'s (1996) method with insoluble systems.

Chapter 6

FINAL CONCLUSIONS & RECOMMENDATIONS

This dissertation consisted of three main chapters of work: (i) Preparation of seeds, (ii) Determination of the growth and aggregation kinetics, and (iii) Determination of the induction period, all for the moderately soluble COM system. The results found in each chapter were subsequently used to improve the experimental methods of the following chapters of work.

The overall objective of Chapter 3 was to investigate the precipitation behaviour of the COM system, and in so doing develop a suitable seed preparation technique for the kinetic experiments. Many significant results were found during the experimental investigations of Chapter 3. The mixing in the reactor was found to be inadequate, especially at high supersaturations (e.g. $S_i > 10$) and at a fast reagent addition rate. Due to the insufficient agitation at these conditions, points of high local supersaturation were created which resulted in particles of various sizes and morphologies being produced in a number of the seed samples. From this result it is recommended that better mixing is employed, when moderately or sparingly soluble systems are investigated, in order to ensure an equal distribution of supersaturation within the reactor. This could be accomplished by either operating at a higher agitation rate or by using premixing devices, such as T-mixers, Y-mixers, Hartridge-Roughton mixers etc., to yield a better control over the initial supersaturation level. Also, as stirred-tank reactors are not well adapted to control precipitation processes (due to the complex internal hydrodynamics), it is recommended that new reactor technologies and set-ups are investigated to improve the control of the mixing process.

Another significant finding of Chapter 3 was that the double-jet reactant addition method exhibited a better control of the supersaturation in comparison to the single-jet method. Across the three supersaturation levels investigated, the PSDs associated with the double-jet method were narrower and more uniform than those for the single-jet method. Due to this conclusion it is recommended that for semi-batch or continuous precipitation processes the double-jet reactant addition method is utilized and that the reagent feed points are placed as close to the impeller tips as is possible. Also this method can be utilized in conjunction with a premixing device if desired.

The results from Chapter 3 showed that a suitable seed preparation technique could be developed, depending on the constraints imposed on the seed sample. One of the biggest challenges to producing an appropriate seed sample was the available size range of the particle size analyser. The PSDs either did not fit within the 2 - 60μm size range or were too broad and thus the seeds would probably grow out of the field of view when used in the kinetic experiments. In future work it is suggested that the Malvern Mastersizer is utilized instead of the Coulter Counter as the detectable size range is significantly greater. One of the constraints of the Malvern Mastersizer, however, is that it cannot measure very dilute samples (with regards to particle concentration) and thus a larger reactor would need to be utilized in order to allow larger volumes of sample to be taken per kinetic experiment. The larger sample volumes would contain a higher number of particles which would permit the measurement of the PSD using a Malvern Mastersizer.

The objective of Chapter 4 was to determine the growth and aggregation kinetics for the COM system by using the experimental kinetic method of Bramley *et al.* (1996). The kinetics were determined for an initial supersaturation range of S_i = 2.3 – 5.8 and seed concentrations of C_{seeds} = 0.03 and 0.15 g.dm^{-3}. The results showed that nucleation was suppressed when a high seed concentration was utilized with any of the supersaturations but that nucleation occurred when a combination of high supersaturation and low seed concentration was utilized. Both the growth and aggregation kinetics were determined to be within the ranges found in literature however the results cannot be fully trusted due to the process of growth into the field of view not being accounted for. Thus, if the kinetics are to be determined from the experimental PSDs and the initial seed PSD lies outside of the field of view of the particle size analyser, then it is recommended that a source function be included in the calculation of the kinetics to ensure that an over-prediction of the growth rates and an under-prediction of the aggregation rate constants are avoided. This means that a more rigorous calculation method is required such as that proposed by Bramley *et al.* (1996). However, another solution to the "growth into the field of view" problem would be to use an alternative particle size analyzer with a wider size detection limit e.g. the Malvern Mastersizer. As discussed above, a larger reactor would need to be utilized in order to offset the low concentrations of the samples.
The two seed samples utilized in Chapter 4 yielded comparable kinetic results; though this was expected because the seed samples had similar mean sizes and only differed in shape. From this result it is suggested that a detailed investigation be conducted with seeds of various shapes and sizes in order to determine whether the assumptions of size independent growth and aggregation and no growth rate dispersion are in fact correct.

In Chapter 5 the induction time for the COM system was determined over an initial supersaturation range of S_i = 2.1 – 9.7. The induction periods were determined from solution conductivity profiles. It was concluded that induction time measurements utilizing solution properties are significantly more accurate than those using visual techniques. This is because a solution property such as conductivity will exhibit a change as soon as nucleation occurs whereas a visual technique involves a time lag as the nuclei are required to first grow to a detectable size. Thus it is recommended that when determining the induction time for precipitation systems a method utilizing solution properties is used rather than one using a visual technique.
The results in Chapter 5 showed that the induction time-supersaturation data fitted very well to a power law trendline. This result agreed with literature results for various other compounds. A recommendation for future work would be that induction times be determined for various precipitation systems using solution conductivity measurements. The results from these experiments could be superimposed in order to determine whether the induction times at the same initial supersaturations for various compounds fit a general power law curve when using the same method.

The ultimate objective of this dissertation was to determine whether the experimental kinetic method of Bramley *et al.* (1996) is viable for more insoluble systems. From Chapters 4 & 5 it can be concluded that the method is feasible for sparingly soluble systems as long as the following points can be satisfied:

(i) Nucleation is prevented by using a high enough seed concentration dependent on the initial supersaturation level.

(ii) The initial supersaturation is kept below a value of approximately S_i = 6 to ensure that a metastable solution can be prepared and can remain in metastability until the seeds are added. The method cannot be used for higher supersaturations because the initial solution will not retain its metastability for a long enough period of time. Thus, homogeneous nucleation will most likely occur before the seeds are able to be added to the solution. Another problem with utilizing higher supersaturation levels is that these require higher seed concentrations which would result in a fast approach to equilibrium and thus create problems with sample time and PSD measurement.

(iii) The PSDs lie within the size range of the particle size analyser of choice. If the seeds lie partially outside of the size range but grow into the field of view during the kinetic experiments, a source function can be utilized to correct the kinetic results.

(iv) The volume of the sample from the reactor is large enough so that an accurate PSD measurement can be conducted.

(v) The reagent solutions can be accurately prepared. This point may create a limit on the viability of the method as for sparingly soluble systems e.g. NiS, with extremely low solubility products, the mass concentrations corresponding to $S_i \leq 6$ will be very small.

Finally, it is recommended that the experimental kinetic method of Bramley *et al.* (1996) be investigated for use with more insoluble systems, utilizing initial supersaturations below S_i = 6, in order to quantitatively determine its viability.

References

Andreassen, J. 2001. Growth and Aggregation Phenomena in Precipitation of Calcium Carbonate. Dr. Ing. Department of Chemical Engineering, Norwegian University of Science and Technology.

Andreassen, J. & Hounslow, M.J. 2004. Growth and Aggregation of Vaterite in Seeded-Batch Experiments. *American Institute of Chemical Engineers Journal.* 50(11):2772-2782.

Aoun, M., Plasari, E., David, R. & Villermaux, J. 1999. A simultaneous determination of nucleation and growth rates from batch spontaneous precipitation. *Chemical Engineering Science.* 54:1161-1180.

Baldyga, J., Bourne, J.R. & Hearn, S.J. 1997. Interaction between chemical reactions and mixing on various scales. *Chemical Engineering Science.* 52(4):457-466.

Beckman Coulter Inc. 2011. *Particle Technologies: The Coulter Principle.* Available: https://www.beckmancoulter.com/wsrportal/wsr/industrial/particle-technologies/coulter-principle/index.htm [2011, July, 24].

Benet, N., Muhr, H., Plasari, E. & Rousseaux, J.M. 2002. New technologies for the precipitation of solid particles with controlled properties. *Powder Technology.* 128:93-98.

Bouropoulos, N. & Koutsoukos, P.G. 2000. Spontaneous precipitation of struvite from aqueous solutions. *Journal of Crystal Growth.* 213:381-388.

Bramley, A.S., Hounslow, M.J. & Ryall, R.L. 1996. Aggregation during Precipitation from Solution: A Method for Extracting Rates from Experimental Data. *Journal of Colloid and Interface Science.* 183(1):155-165.

Bramley, A.S., Hounslow, M.J. & Ryall, R.L. 1997. Aggregation during precipitation from solution. Kinetics for calcium oxalate monohydrate. *Chemical Engineering Science.* 52(5):747-757.

Bretherton, T. & Rodgers, A. 1998. Crystallization of calcium oxalate in minimally diluted urine. *Journal of Crystal Growth.* 192:448-455.

Brown, C.M., Ackermann, D.K., Purich, D.L. & Finlayson, B. 1991. Nucleation of calcium oxalate monohydrate: use of turbidity measurements and computer-assisted simulations in characterizing early events in crystal formation. *Journal of Crystal Growth.* 108(3-4):455-464.

Chien, W., Tai, C.Y. & Hsu, J. 1999. The induction period of the $CaCl_2$-Na_2CO_3 system: Theory and experiment. *Journal of Chemical Physics.* 111(6):2657-2664.

Collier, A.P. & Hounslow, M.J. 1999. Growth and Aggregation Rates for Calcite and Calcium Oxalate Monohydrate. *American Institute of Chemical Engineers Journal.* 45(11):2298-2305.

Finlayson, B. 1978. Physicochemical aspects of urolithiasis. *Kidney International.* 13:344-360.

Gardner, G.L. & Nancollas, G.H. 1975. Kinetics of Dissolution of Calcium Oxalate Monohydrate. *The Journal of Physical Chemistry.* 79(24):2597-2600.

Garside, J., Brecevic, L. & Mullin, J.W. 1982. The Effect of Temperature on the Precipitation of Calcium Oxalate. *Journal of Crystal Growth.* 57(2):233-240.

Generalic, E. 2003. 22 March 2003-last update. *Solubility Product Constants.* Available: http://www.ktf-split.hr/periodni/en/abc/kpt.html [2010, 26 February].

Giulietti, M., Seckler, M.M., Derenzo, S., Re, M.I. & Cekinski, E. 2001. Industrial Crystallization and Precipitation from Solutions: State of the Technique. *Brazilian Journal of Chemical Engineering.* 18(4):423.

Houcine, I., Plasari, E., David, R. & Villermaux, J. 1997. Influence of Mixing Characteristics on the Quality and Size of Precipitated Calcium Oxalate in a Pilot Scale Reactor. *Institute of Chemical Engineers.* 75(A):252-256.

Hounslow, M.J., Mumtaz, H.S., Collier, A.P., Barrick, J.P. & Bramley, A.S. 2001. A micro-mechanical model for the rate of aggregation during precipitation from solution. *Chemical Engineering Science.* 56(7):2543-2552.

Hounslow, M.J., Ryall, R.L. & Marshall, V.R. 1988. A Discretized Population Balance for Nucleation, Growth, and Aggregation. *American Institute of Chemical Engineers Journal.* 34(11):1821-1832.

Hove, M., van Hille, R.P. & Lewis, A.E. 2008. Mechanisms of formation of iron precipitates from ferrous solutions at high and low pH. *Chemical Engineering Science.* 63(6):1626-1635.

Jones, A.G. 2002. *Crystallization Process Systems.* 1st ed.Oxford, UK: Butterworth-Heinemann.

Kashchiev, D. 2000. *Nucleation: Basic Theory with Applications.* 1st ed.Oxford, UK: Butterworth-Heinemann.

Kashchiev, D. & van Rosmalen, G.M. 2003. Review: Nucleation in solutions revisited. *Crystal Research and Technology.* 38(7-8):555-574.

Kuldipkumar, A., Kwon, G.S. & Zhang, G.G.Z. 2007. Determining the Growth Mechanism of Tolazamide by Induction Time Measurement. *Crystal Growth & Design.* 7(2):234-242.

Lancia, A., Musmarra, D. & Prisclandaro, M. 1999. Measuring Induction Period for Calcium Sulfate Dihydrate Precipitation. *American Institute of Chemical Engineers Journal.* 45(2):390-397.

Lewis, A.E. & van Rosmalen, G.M. 2010. *Understanding Industrial Crystallization Processes.*

Liew, T.L., Barrick, J.P. & Hounslow, M.J. 2003. A Micro-Mechanical Model for the Rate of Aggregation during Precipitation from Solution. *Chemical Engineering Technology.* 26(3):282-285.

Lindenberg, C., Scholl, J., Vicum, L., Mazzotti, M. & Brozio, J. 2008. L-Glutamic Acid Precipitation: Agglomeration Effects. *Crystal Growth & Design.* 8(1):224-237.

Liu, H. & Papangelakis, V.G. 2005. Chemical modeling of high temperature aqueous processes. *Hydrometallurgy.* 79(1-2):48-61.

Mahajan, A.J. & Kirwan, D.J. 1993. Rapid precipitation of biochemicals. *Journal of Physics D: Applied Physics.* 26:B176-B180.

Malvern Instruments Ltd. 2011. *Laser Diffraction Particle Sizing,* [Homepage of Spectris], [Online]. Available: http://www.malvern.com/LabEng/technology/laser_diffraction/particle_sizing.htm [2011, July, 24].

Mangere, M. , Nathoo, J. & Lewis, A.E. 2009. *Nucleation kinetics of selenium (+4) precipitation from an acidic copper sulphate solution.* Masters ed. Cape Town: University of Cape Town.

MathWorks, Inc. 2011. *MATLAB.* USA.

Mersmann, A. Ed. 2001. *Crystallization Technology Handbook*. 2nd ed. New York, USA: Marcel Dekker.

Millan, A., Sohnel, O. & Grases, F. 1997. The influence of crystal morphology on the kinetics of growth of calcium oxalate monohydrate. *Journal of Crystal Growth.* 179:231-239.

Mullin, J.W. 2001. *Crystallization.* 4th ed.Oxford, UK: Butterworth-Heinemann.

Mumtaz, H.S. & Hounslow, M.J. 2000. Aggregation during precipitation from solution: an experimental investigation using Poiseuille flow. *Chemical Engineering Science.* 55:5671-5681.

Mumtaz, H.S., Hounslow, M.J., Seaton, N.A. & Paterson, W.R. 1997. Orthokinetic Aggregation during Precipitation: A Computational Model for Calcium Oxalate Monohydrate. *Institute of Chemical Engineers.* 75(Part A):152-159.

Myerson, A.S. Ed. 2002. *Handbook of Industrial Crystallization*. 2nd ed. Boston, USA: Butterworth-Heinemann.

Nancollas, G.H. & Gardner, G.L. 1974. Kinetics of Crystal Growth of Calcium Oxalate Monohydrate. *Journal of Crystal Growth.* 21(2):267-276.

Nielsen, A.E. 1960. The Kinetics of Calcium Oxalate Precipitation. *Acta Chemica Scandinavica.* 14(7):1654-1659.

Nielsen, A.E. & Toft, J.M. 1984. Electrolyte Crystal Growth Kinetics. *Journal of Crystal Growth.* 67(2):278-288.

Nienow, A.W. 1997. On impeller circulation and mixing effectiveness in the turbulent flow regime. *Chemical Engineering Science.* 52(15):2557-2565.

Ntuli, F. & Lewis, A.E. 2009. Kinetic modelling of nickel powder precipitation by high-pressure hydrogen reduction. *Chemical Engineering Science.* 64(9):2202-2215.

OLI Systems, Inc. 2008. *OLI Stream Analyzer.* Morris Plains, New Jersey, USA.

Perry, R.H., Green, D.W. & O'Hara Maloney, J. 1997.Fluid Dynamics, Fluid Mixing, Stirred-Tank Agitation. In *Perry's Chemical Engineers' Handbook*. Eds. R.H. Perry, D.W. Green & J. O'Hara Maloney.7th ed.USA: McGraw-Hill. 6-34.

Randolph, A.D. & Larson, M.A. 1988. *Theory of Particulate Processes: Analysis and Techniques of Continuous Crystallization.* 2nd ed.San Diego, California: Academic Press, Inc.

Roelands, C.P.M., Roestenberg, R.R.W., ter Horst, J.H., Kramer, H.J.M. & Jansens, P.J. 2004. Development of an Experimental Method to Measure Nucleation Rates in Reactive Precipitation. *Crystal Growth & Design.* 4(5):921-928.

Roelands, C.P.M., ter Horst, J.H., Kramer, H.J.M. & Jansens, P.J. 2006. Analysis of Nucleation Rate Measurements in Precipitation Processes. *Crystal Growth & Design.* 6(6):1380-1392.

Ryall, R.L., Bagley, C.J. & Marshall, V.R. 1981. Independent Assessment of the Growth and Aggregation of Calcium Oxalate Crystals using the Coulter Counter. *Investigative Urology.* 18(5):401-405.

Salvatori, F., Muhr, H., Plasari, E. & Bossoutrot, J-M. 2002. Determination of nucleation and crystal growth kinetics of barium carbonate. *Powder Technology.* 128:114-123.

Scholl, J., Vicum, L., Muller, M. & Mazzotti, M. 2006. Precipitation of L-Glutamic Acid: Determination of Nucleation Kinetics. *Chemical Engineering Technology.* 29(2):257-264.

Sinnott, R.K., Coulson, J.M. & Richardson, J.F. 1999.Mixing Equipment, Liquid Mixing, Stirred Tanks. In *Coulson & Richardson's Chemical Engineering: Chemical Engineering Design*.4th ed. Butterworth-Heinemann Ltd. 470-475.

Sohnel, O. & Garside, J. 1992. *Precipitation: Basic Principles and Industrial Applications.* 1st ed.Oxford, UK: Butterworth-Heinemann.

Sohnel, O., Kroupa, M., Frankova, G. & Velich, V. 1997. Calcium oxalate crystallization kinetics from calorimetric measurements. *Thermochimica Acta.* 306:7-12.

Sohnel, O. & Mullin, J.W. 1978. A Method for the Determination of Precipitation Induction Periods. *Journal of Crystal Growth.* 44(4):377-382.

Sohnel, O. & Mullin, J.W. 1988. Interpretation of Crystallization Induction Periods. *Journal of Colloid and Interface Science.* 123(1):43-50.

Spanos, N. & Koutsoukos, P.G. 1998. Kinetics of Precipitation of Calcium Carbonate in Alkaline pH at Constant Supersaturation. Spontaneous and Seeded Growth. *Journal of Physical Chemistry B.* 102(34):6679-6684.

StatSoft. 2011. *STATISTICA 10.*

Stavek, J., Sipek, M., Hirasawa, I. & Toyokura, K. 1992. Controlled Double-Jet Precipitation of Sparingly Soluble Salts. A Method for the Preparation of High Added Value Materials. *Chemistry of Materials.* 4(3):545-555.

Tai, C.Y. & Chien, W. 2003. Interpreting the effects of operating variables on the induction period of $CaCl_2$-Na_2CO_3 system by a cluster coagulation model. *Chemical Engineering Science.* 58:3233-3241.

Thongboonkerd, V., Semangoen, T. & Chutipongtanate, S. 2006. Factors determining types and morphologies of calcium oxalate crystals: Molar concentrations, buffering, pH, stirring and temperature. *Clinica Chimica Acta.* 367:120-131.

Torbacke, M. & Rasmuson, A.C. 2001. Influence of different scales of mixing in reaction crystallization. *Chemical Engineering Science.* 56:2459-2473.

van der Leeden, M.C., Kashchiev, D. & van Rosmalen, G.M. 1992. Precipitation of Barium Sulfate: Induction Time and the Effect of an Additive on Nucleation and Growth. *Journal of Colloid and Interface Science.* 152(2):338-350.

van der Leeden, M.C., Kashchiev, D. & van Rosmalen, G.M. 1993. Effect of additives on nucleation rate, crystal growth rate and induction time in precipitation. *Journal of Crystal Growth.* 130(1-2):221-232.

Verdoes, D., Kashchiev, D. & van Rosmalen, G.M. 1992. Determination of nucleation and growth rates from induction times in seeded and unseeded precipitation of calcium carbonate. *Journal of Crystal Growth.* 118(3-4):401-413.

Zauner, R. & Jones, A.G. 2000. Determination of nucleation, growth, agglomeration and disruption kinetics from experimental precipitation data: the calcium oxalate system. *Chemical Engineering Science.* 55:4219-4232.

Appendix A: PSD and SEM Results from Seed Experiments

A.1 Seed Experiments with S_i = 10

A1.1 Single-Jet Method

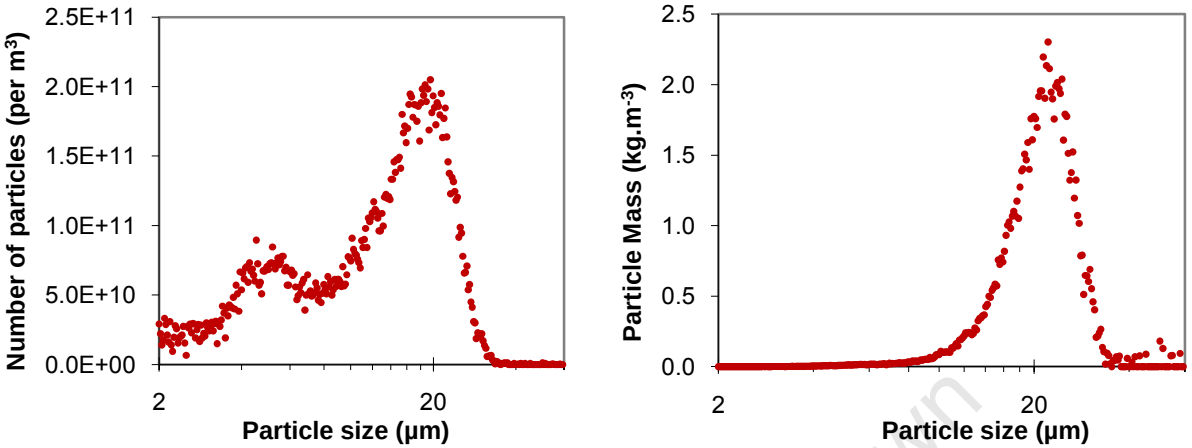

Figure 86: Number and volume distributions for seed sample A1.1.1

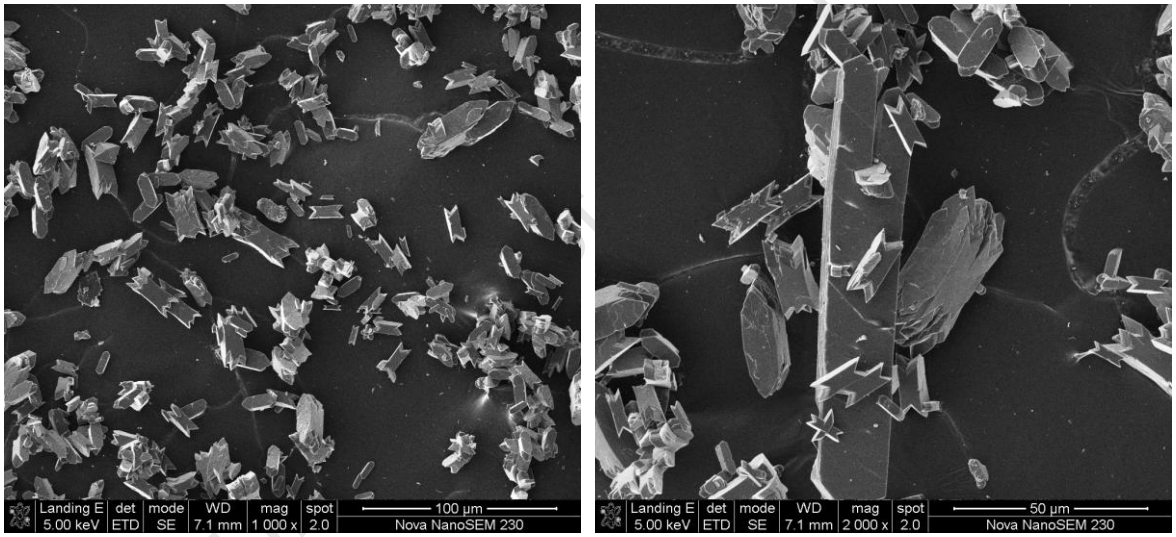

Figure 87: SEM images for seed sample A1.1.1

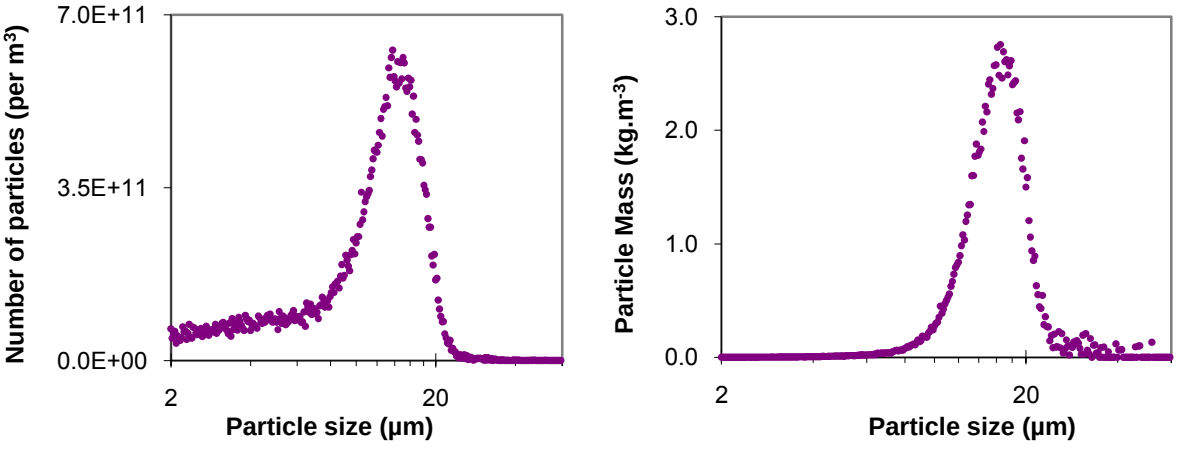

Figure 88: Number and volume distributions for seed sample A1.2.1

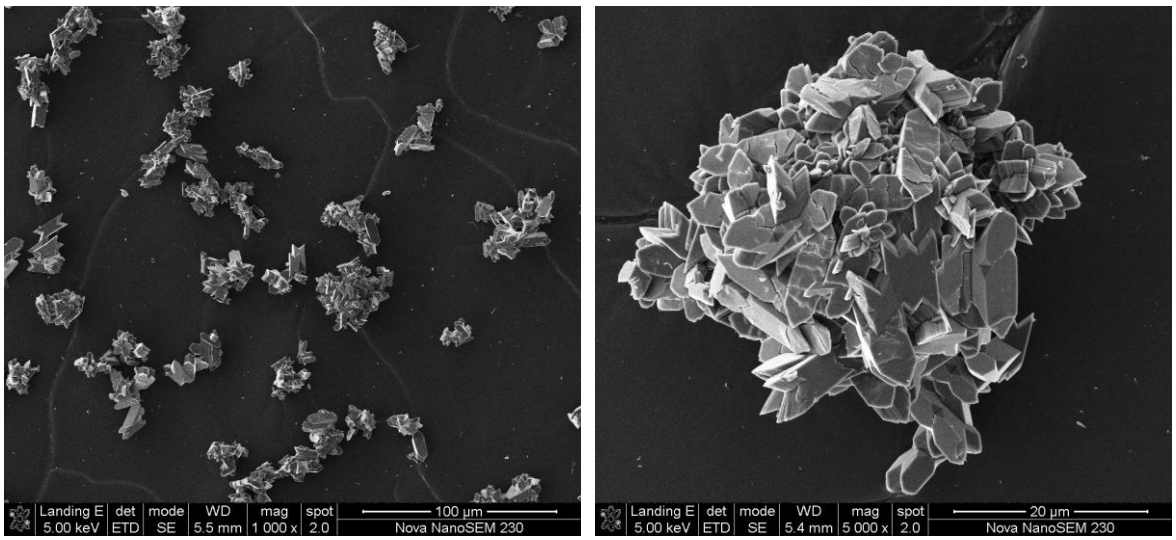

Figure 89: SEM images for seed sample A1.2.1

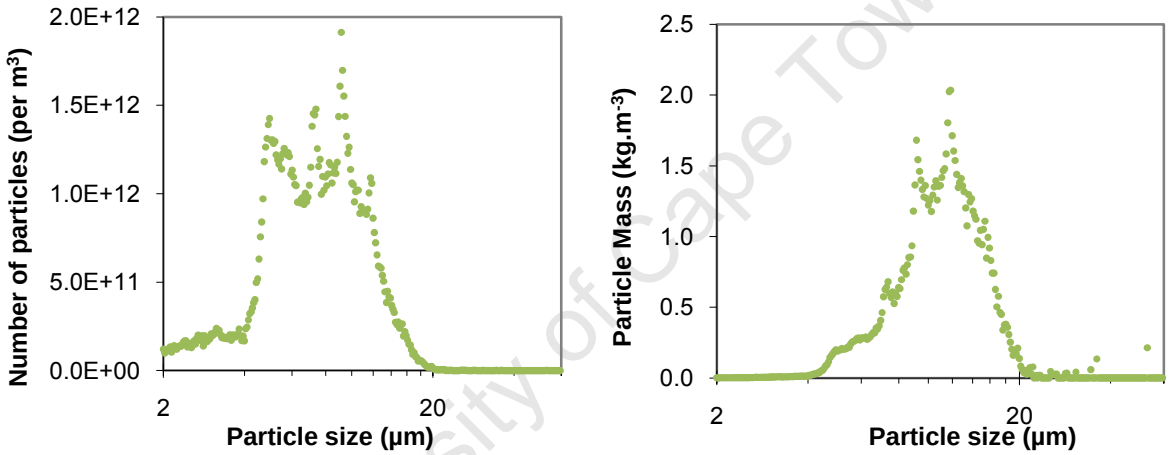

Figure 90: Number and volume distributions for seed sample A1.1.2

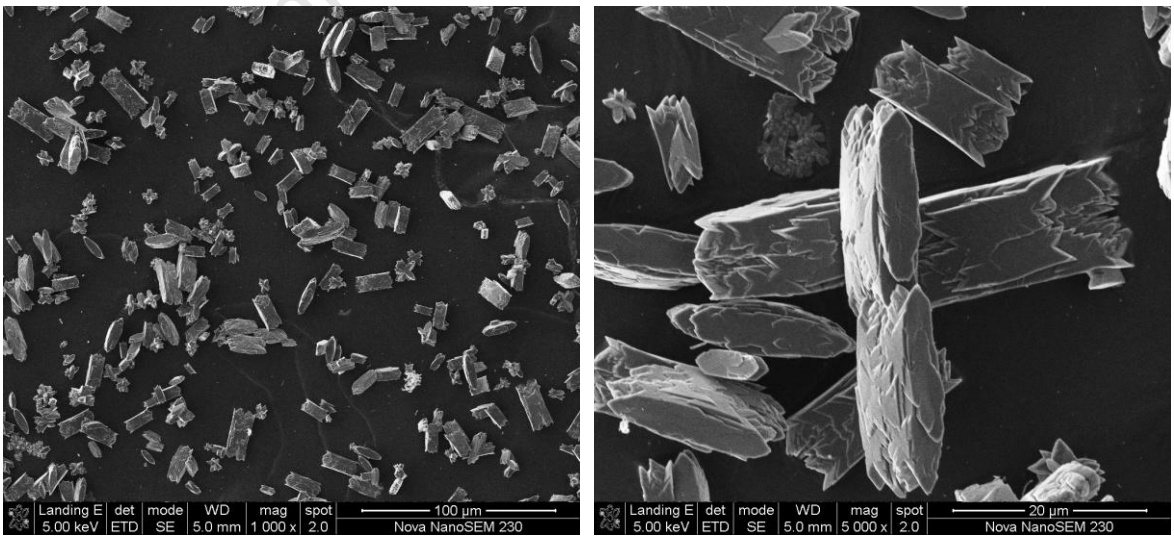

Figure 91: SEM images for seed sample A1.1.2

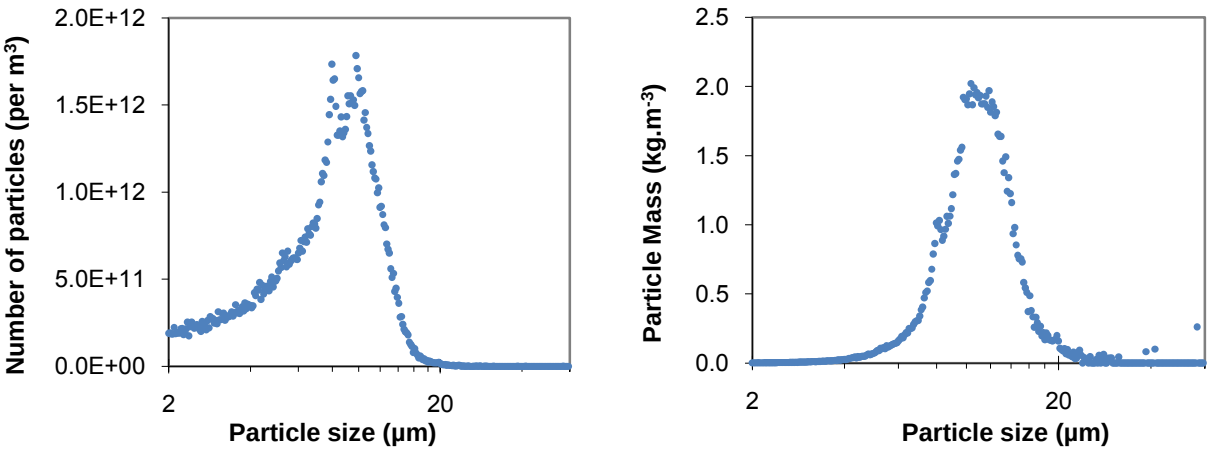

Figure 92: Number and volume distributions for seed sample A1.2.2

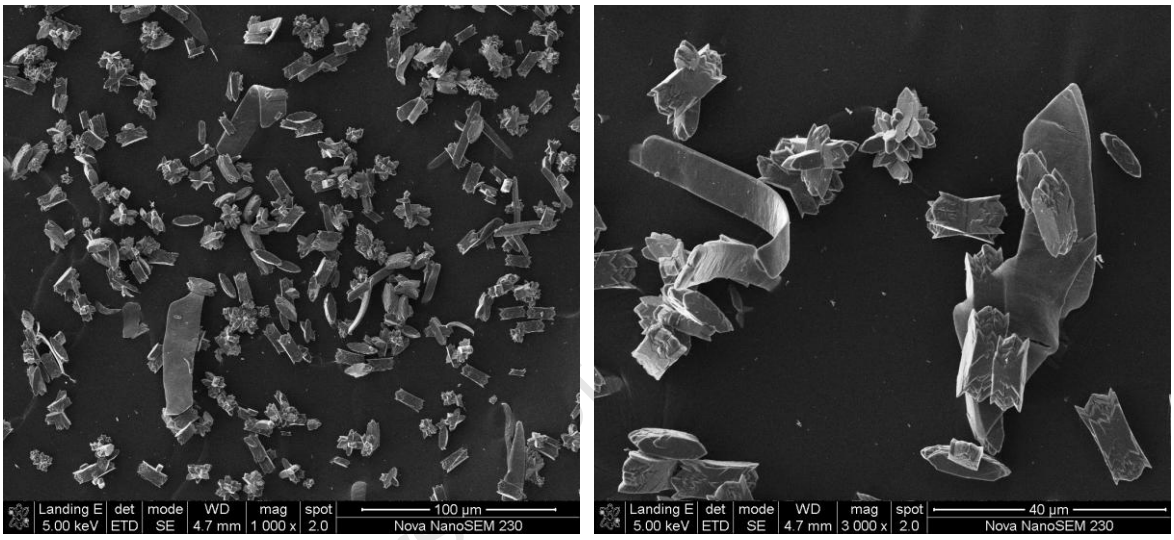

Figure 93: SEM images for seed sample A1.2.2

A1.2 Double-Jet Method

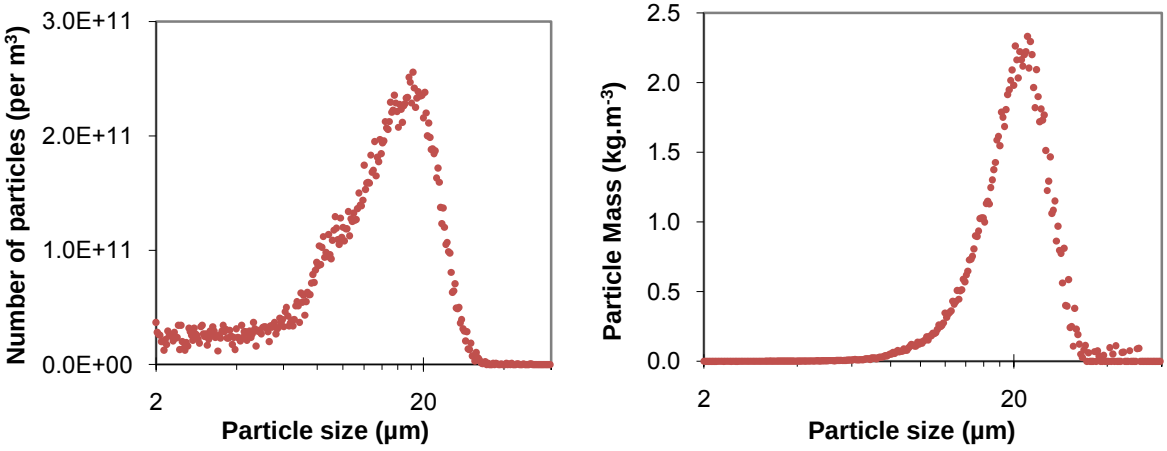

Figure 94: Number and volume distributions for seed sample B1.1.1

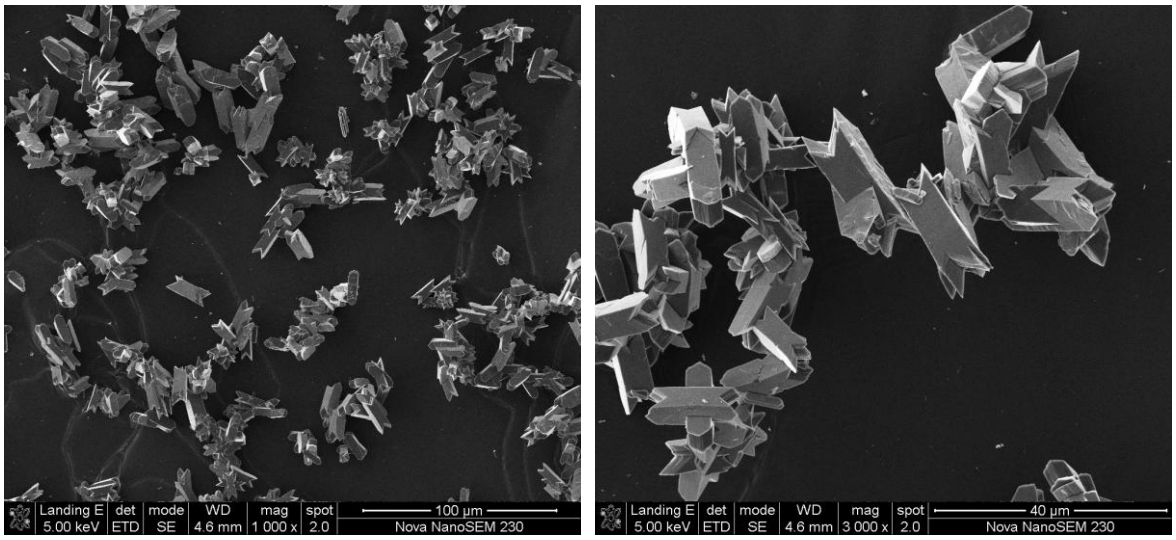

Figure 95: SEM images for seed sample B1.1.1

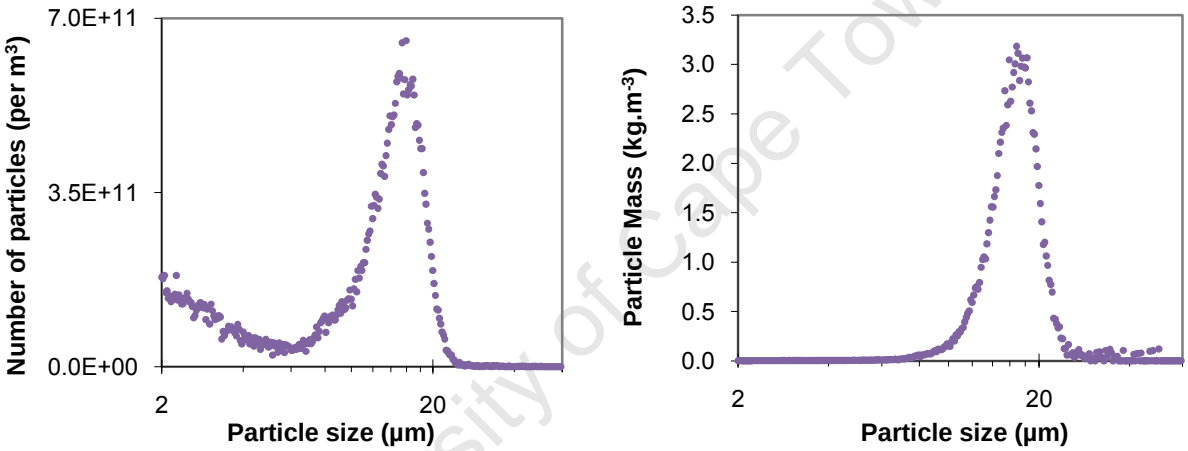

Figure 96: Number and volume distributions for seed sample B1.2.1

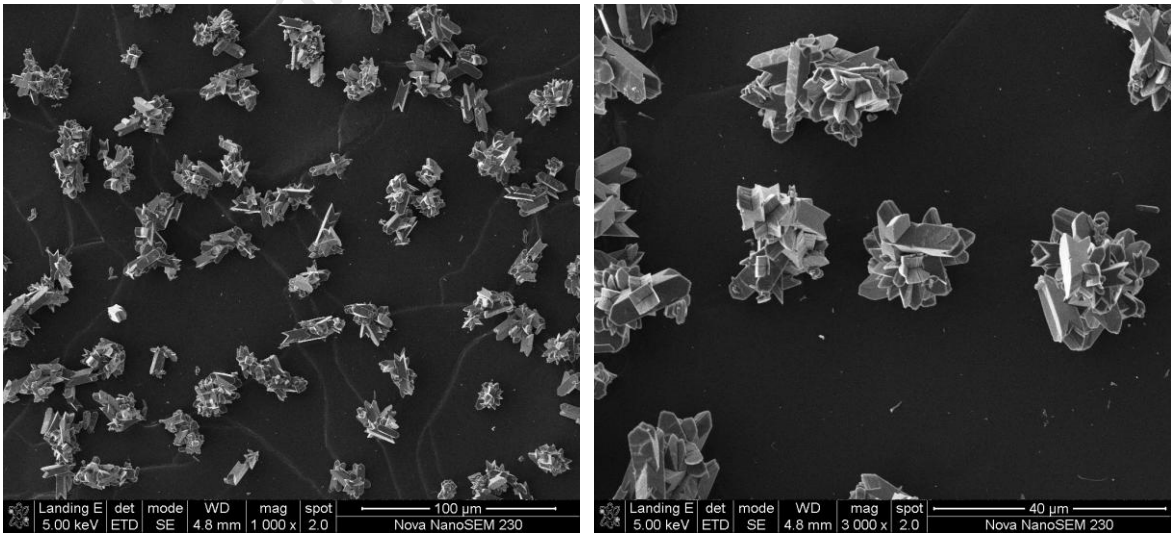

Figure 97: SEM images for seed sample B1.2.1

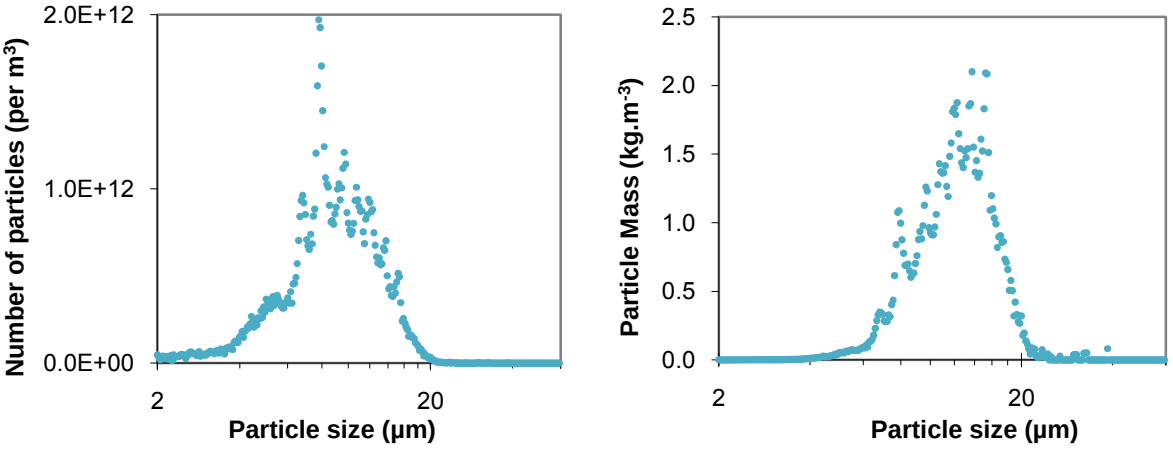

Figure 98: Number and volume distributions for seed sample B1.1.2

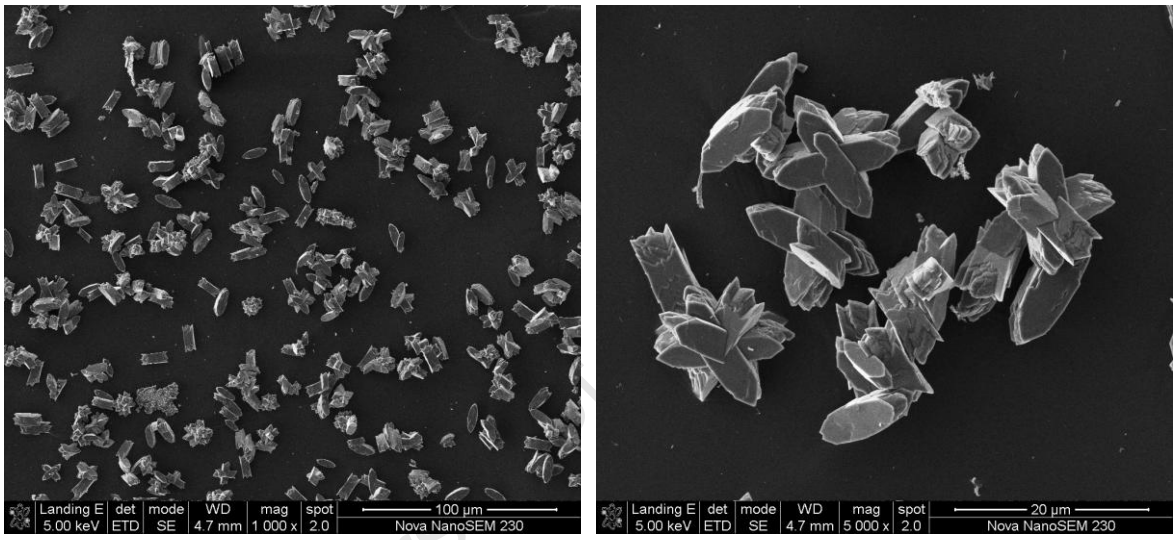

Figure 99: SEM images for seed sample B1.1.2

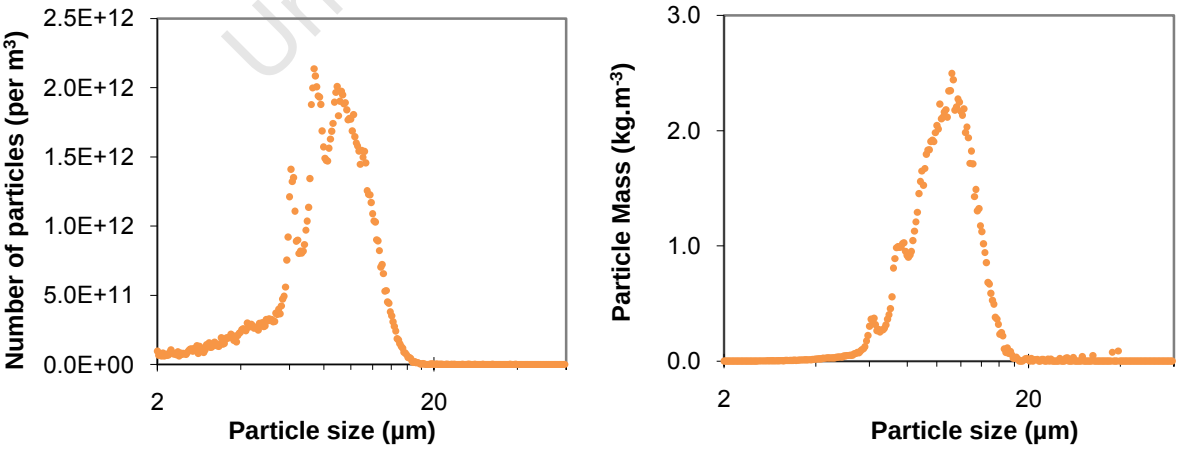

Figure 100: Number and volume distributions for seed sample B1.2.2

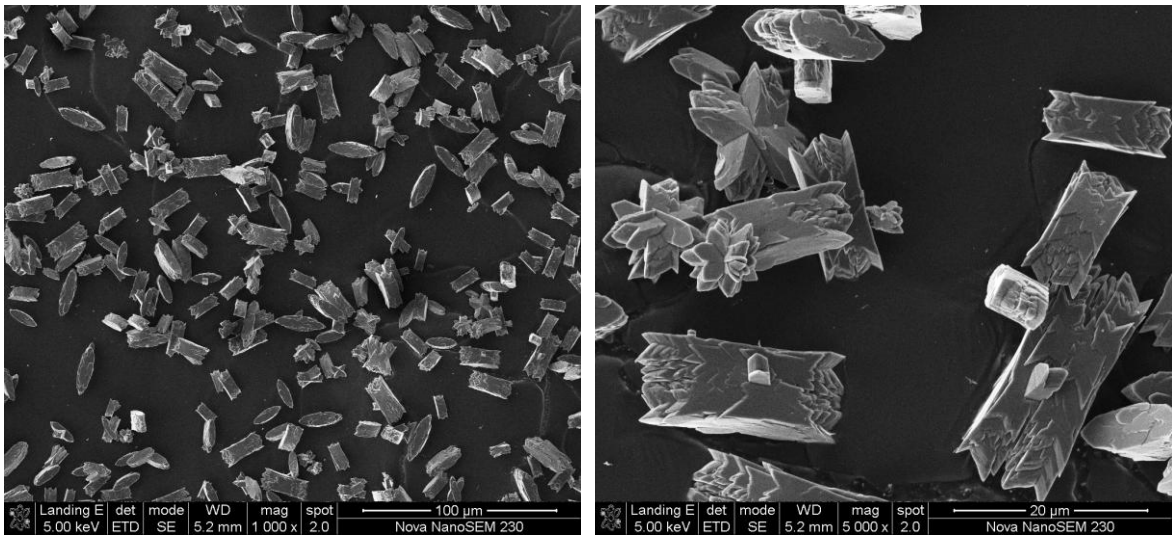

Figure 101: SEM images for seed sample B1.2.2

A.2 Seed Experiments with S_i = 17

A2.1 Single-Jet Method

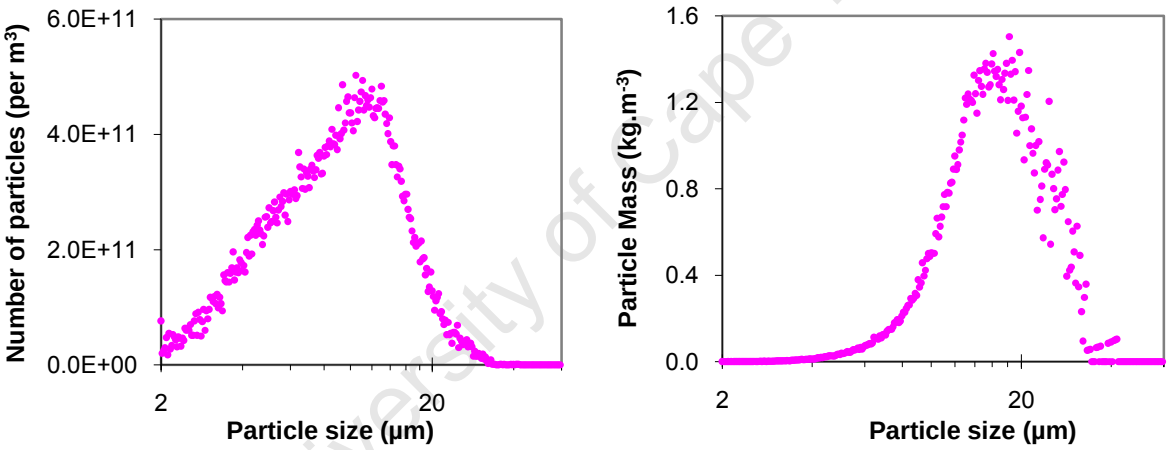

Figure 102: Number and volume distributions for seed sample A2.1.1

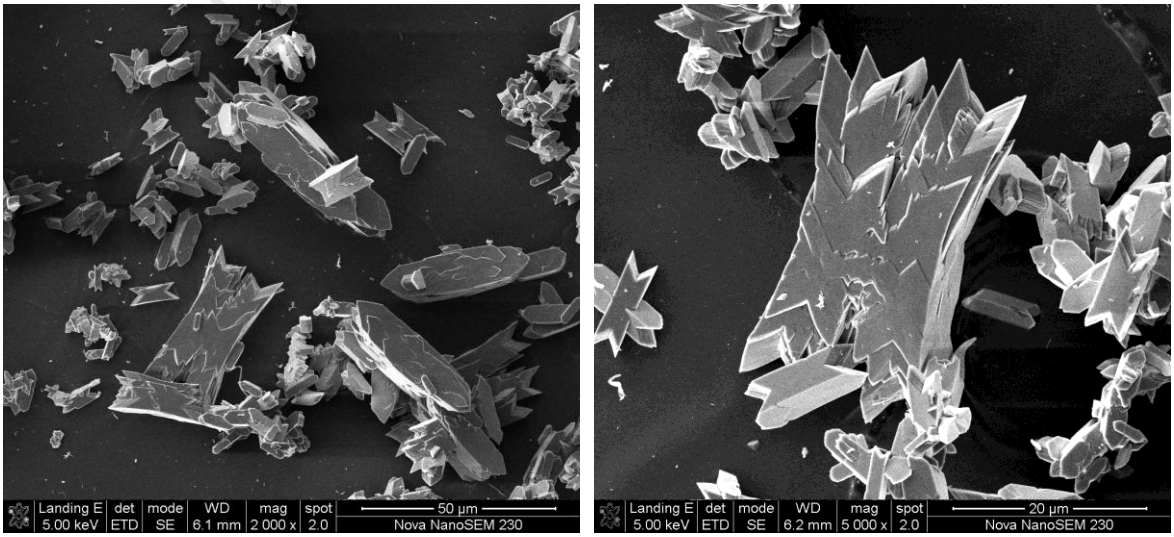

Figure 103: SEM images for seed sample A2.1.1

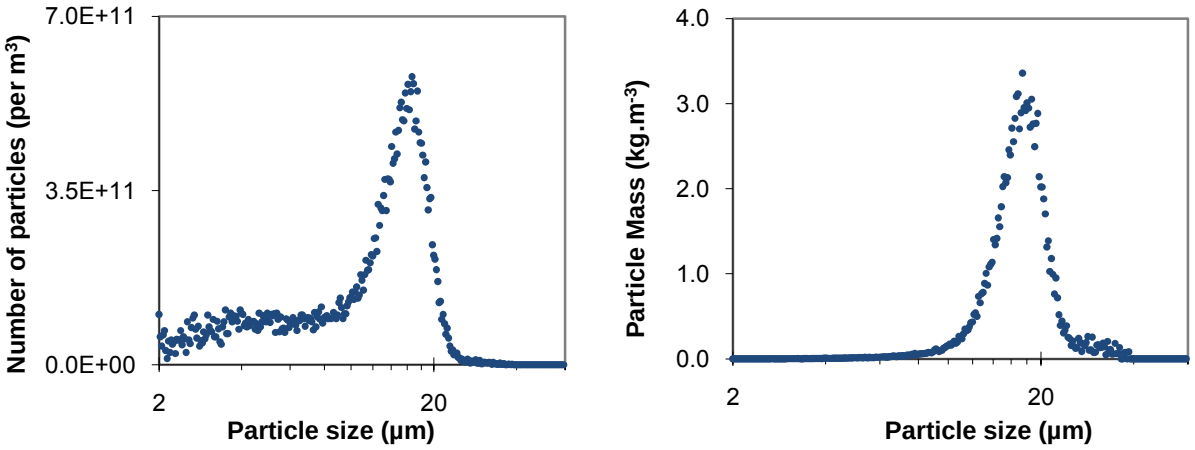

Figure 104: Number and volume distributions for seed sample A2.2.1

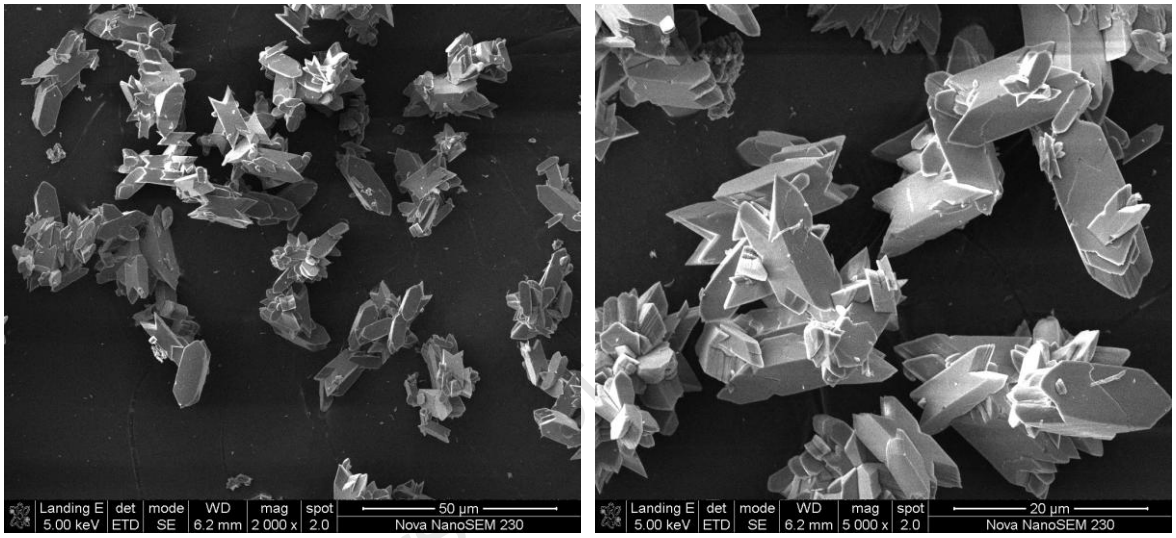

Figure 105: SEM images for seed sample A2.2.1

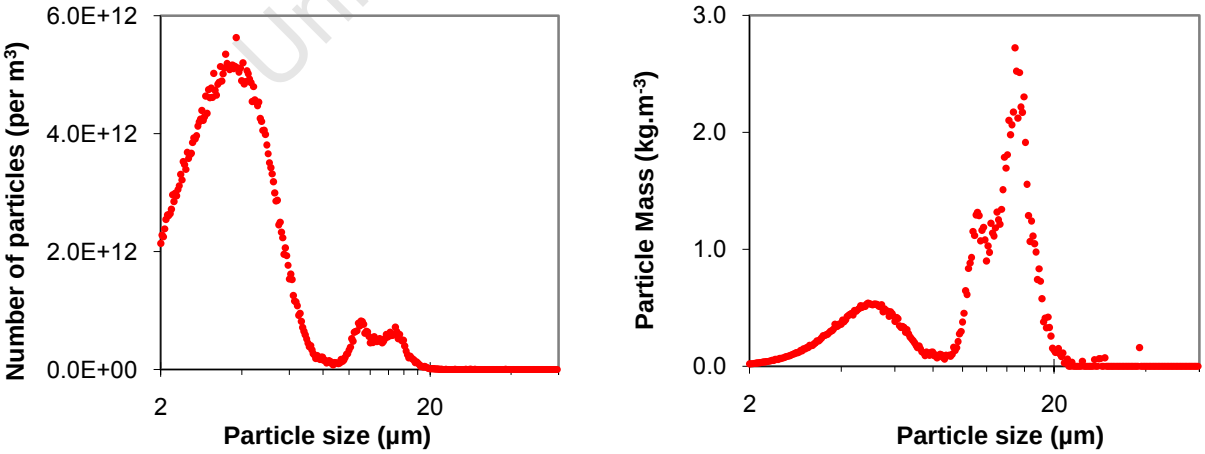

Figure 106: Number and volume distributions for seed sample A2.1.2

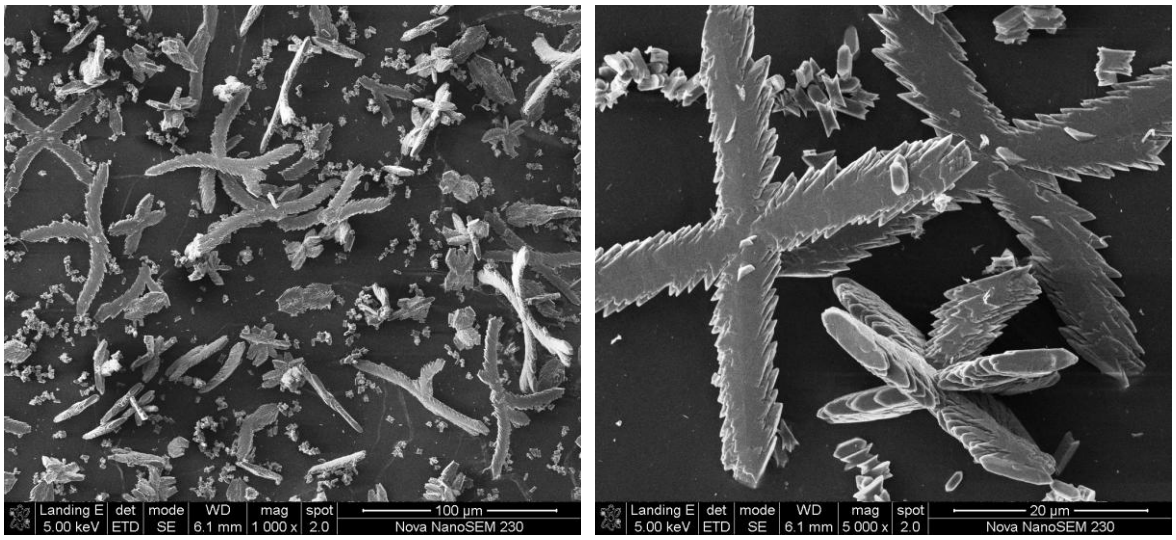

Figure 107: SEM images for seed sample A2.1.2

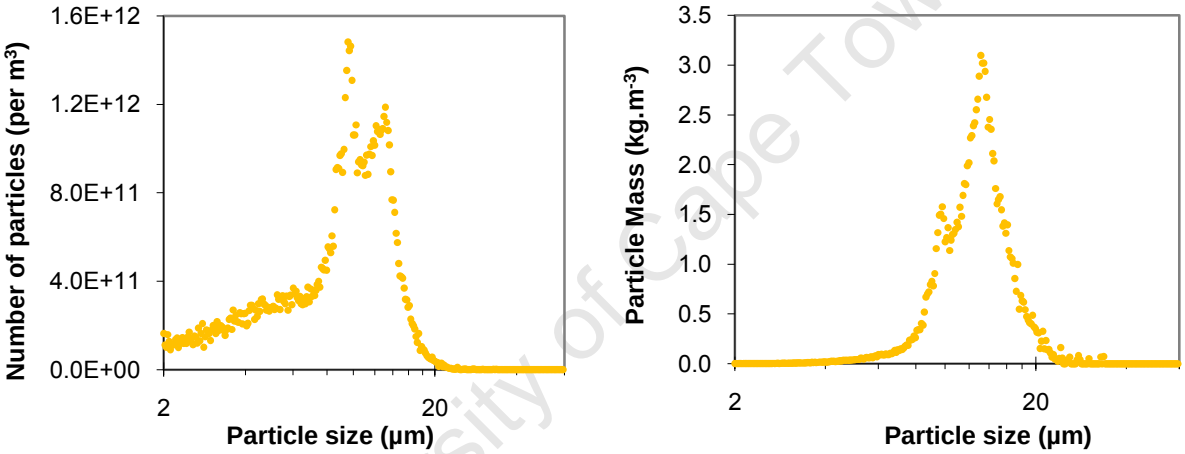

Figure 108: Number and volume distributions for seed sample A2.2.2

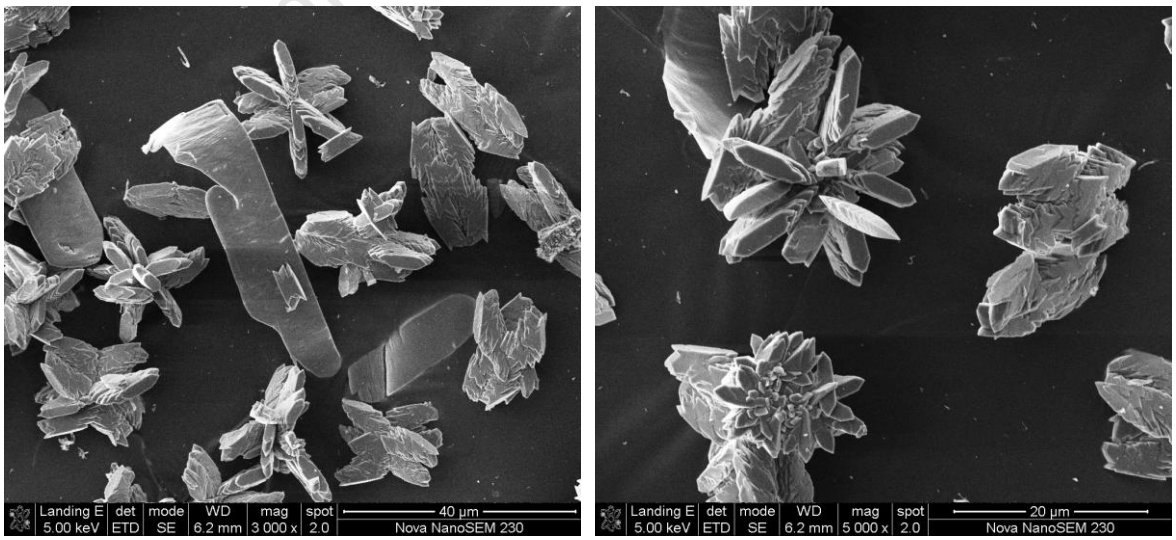

Figure 109: SEM images for seed sample A2.2.2

A2.2 Double-Jet Method

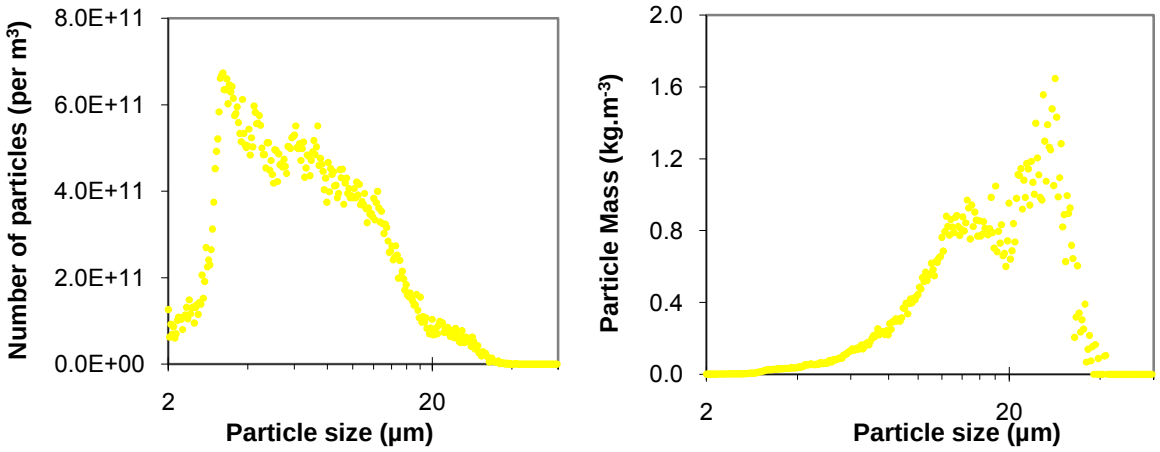

Figure 110: Number and volume distributions for seed sample B2.1.1

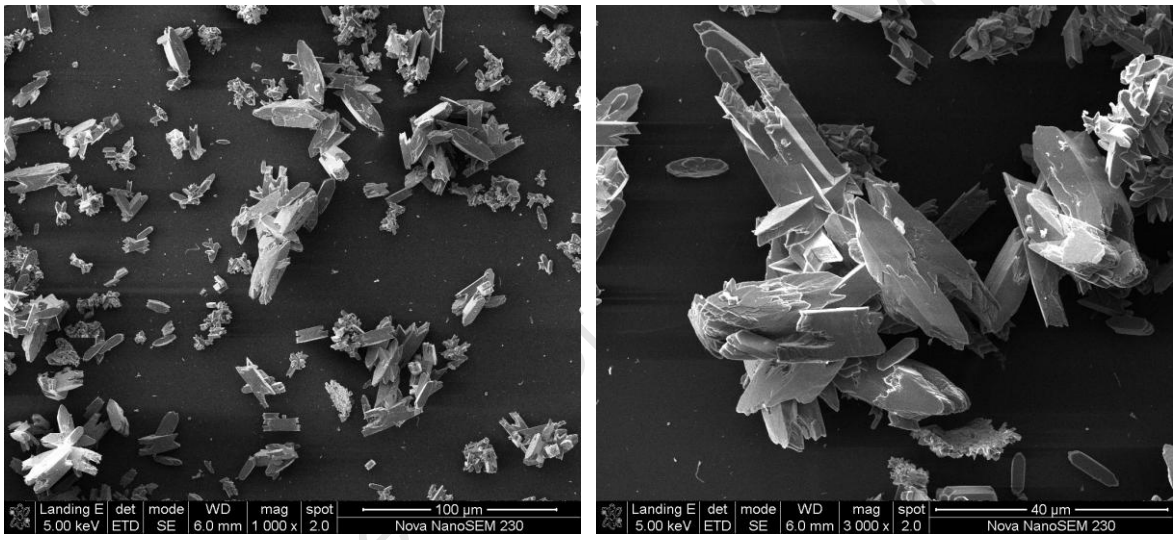

Figure 111: SEM images for seed sample B2.1.1

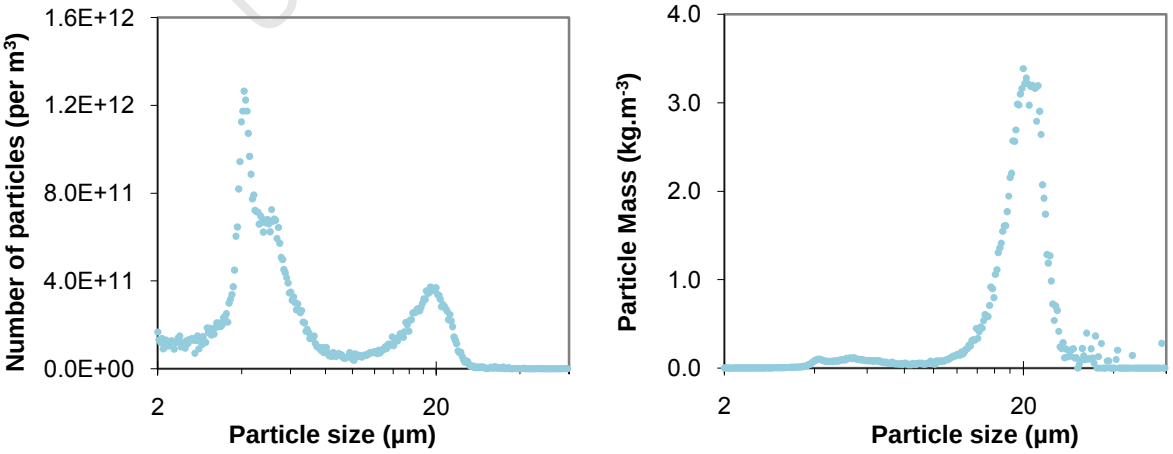

Figure 112: Number and volume distributions for seed sample B2.2.1

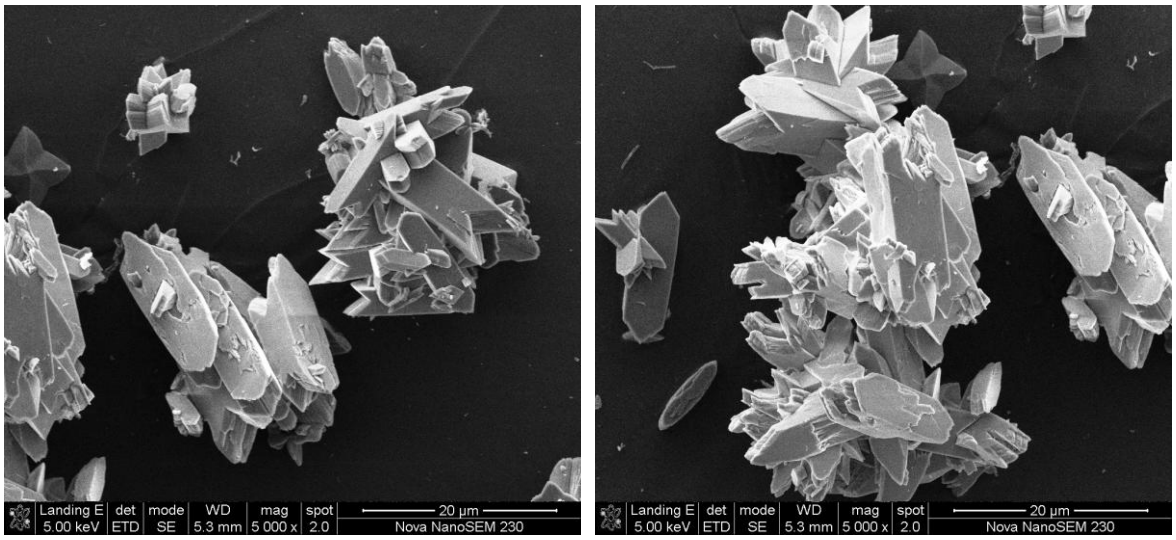

Figure 113: SEM images for seed sample B2.2.1

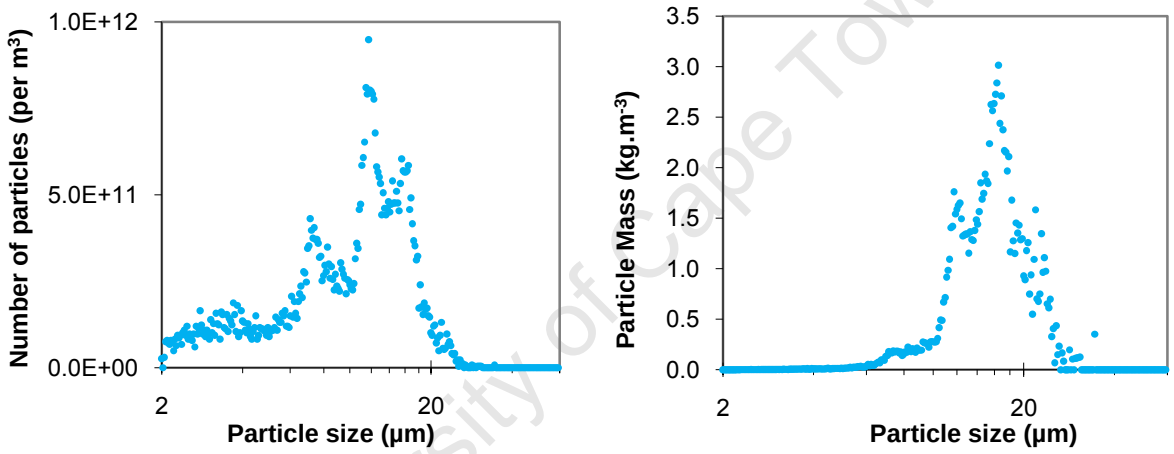

Figure 114: Number and volume distributions for seed sample B2.1.2

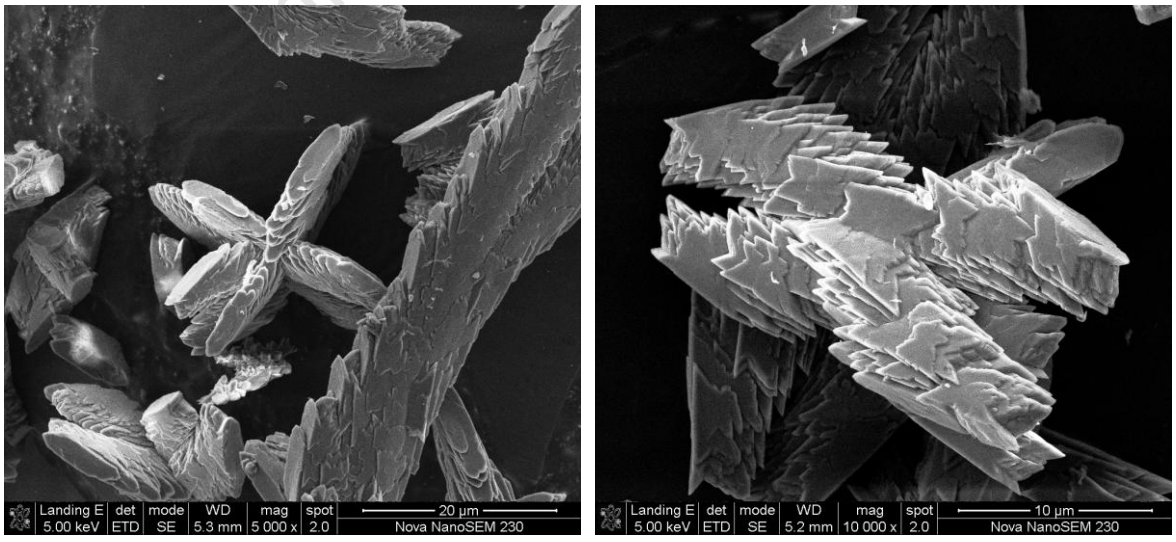

Figure 115: SEM images for seed sample B2.1.2

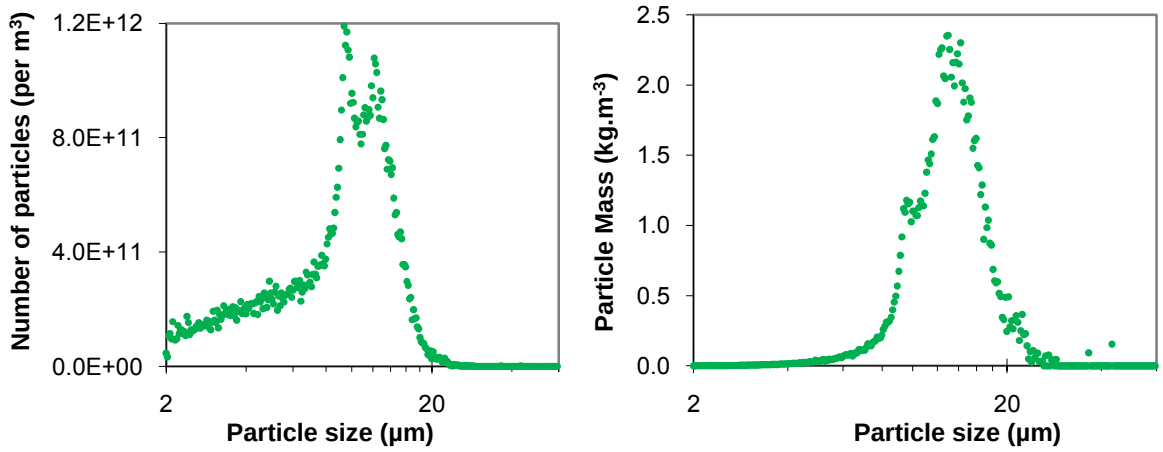

Figure 116: Number and volume distributions for seed sample B2.2.2

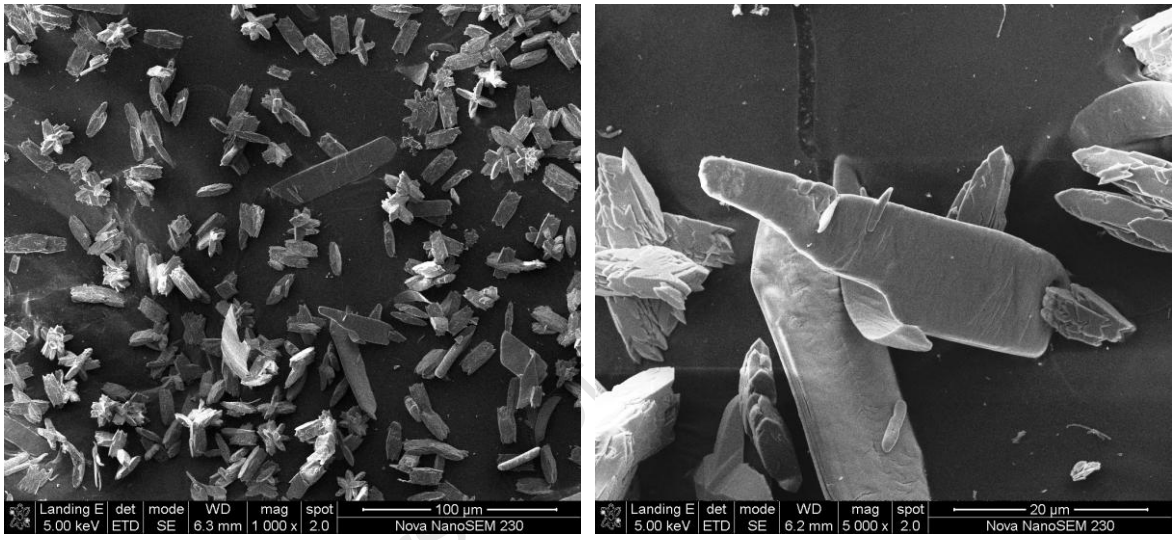

Figure 117: SEM images for seed sample B2.2.2

A.3 Seed Experiments with S_i = 30

A3.1 Single-Jet Method

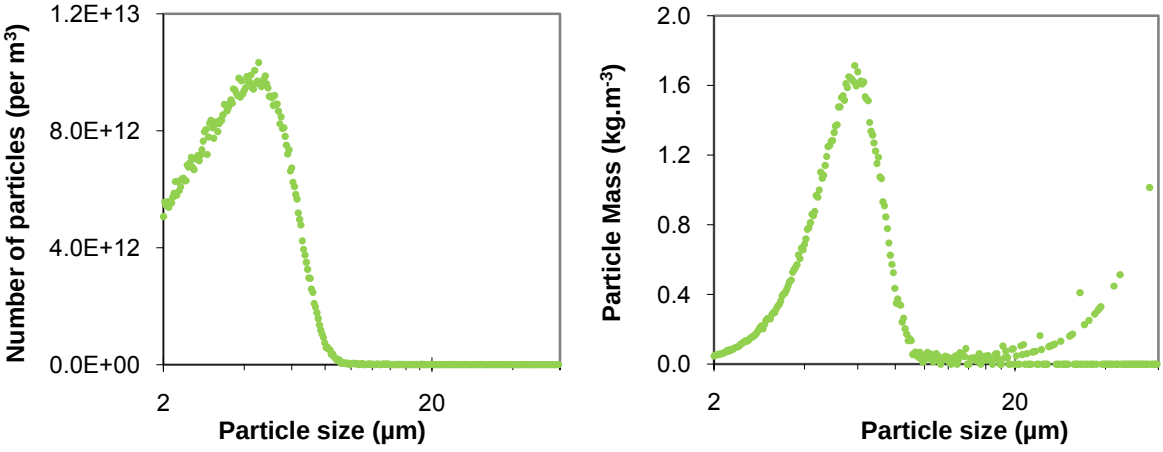

Figure 118: Number and volume distributions for seed sample A3.1.1

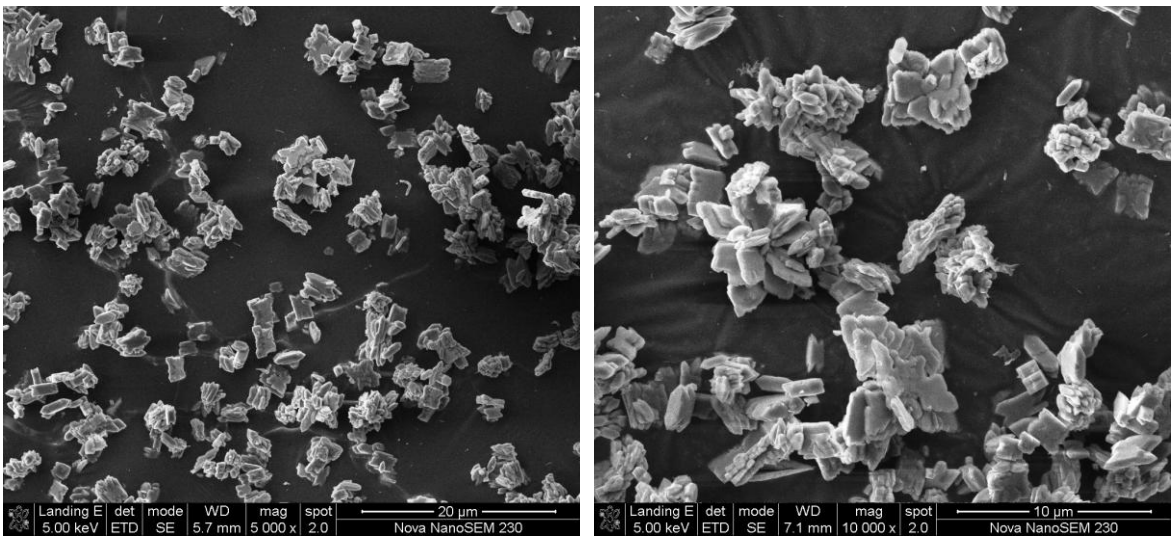

Figure 119: SEM images for seed sample A3.1.1

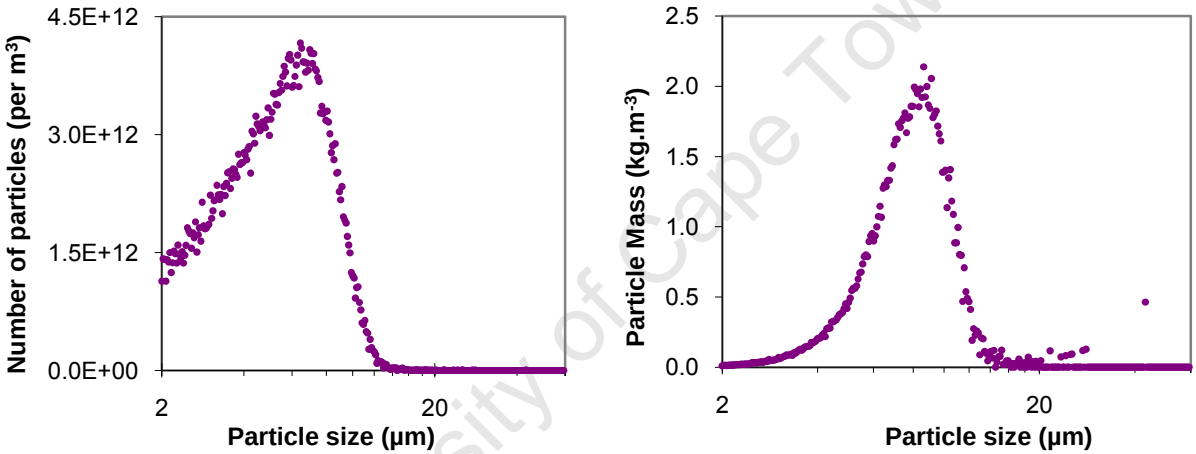

Figure 120: Number and volume distributions for seed sample A3.2.1

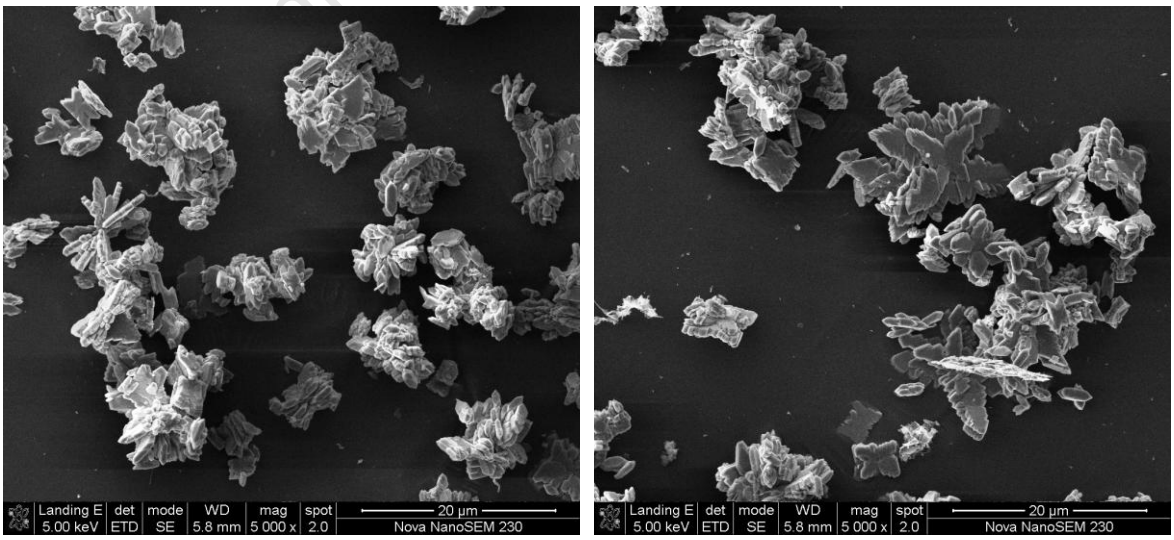

Figure 121: SEM images for seed sample A3.2.1

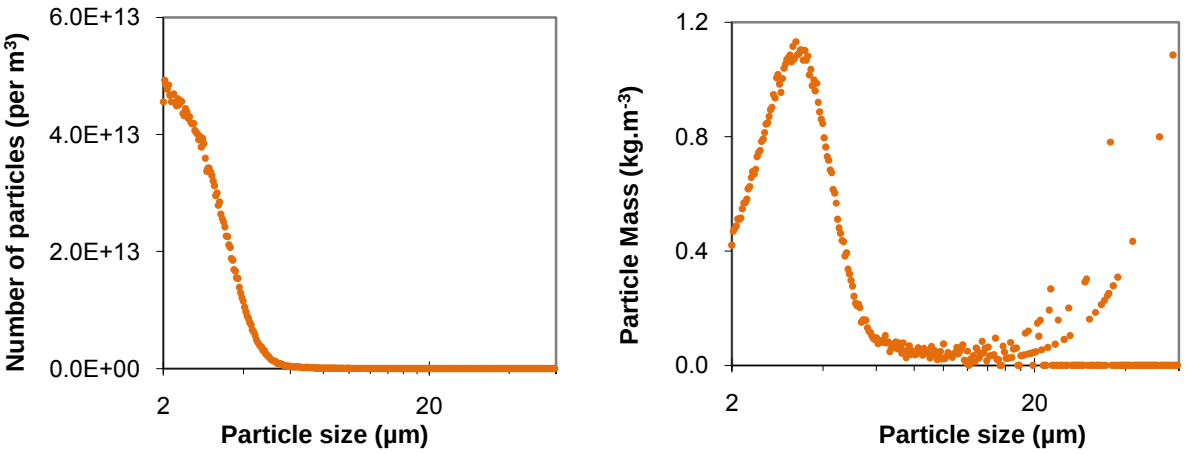

Figure 122: Number and volume distributions for seed sample A3.1.2

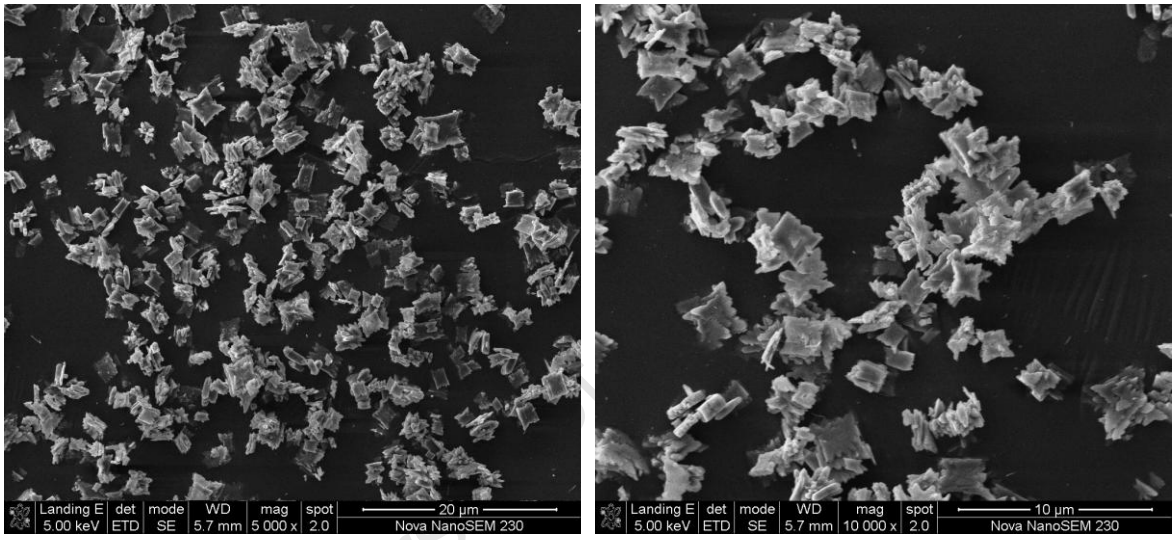

Figure 123: SEM images for seed sample A3.1.2

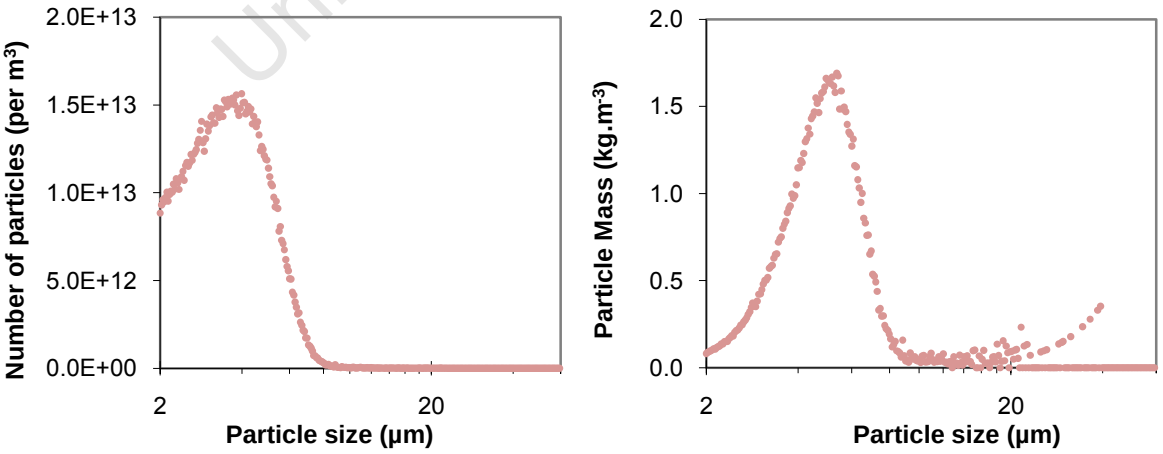

Figure 124: Number and volume distributions for seed sample A3.2.2

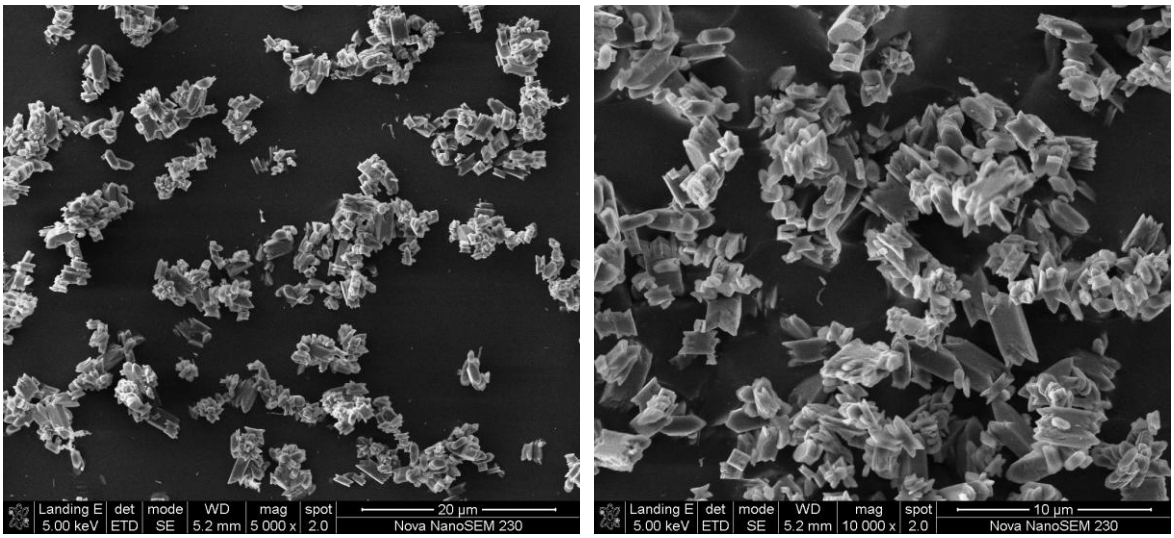

Figure 125: SEM images for seed sample A3.2.2

A3.2 Double-Jet Method

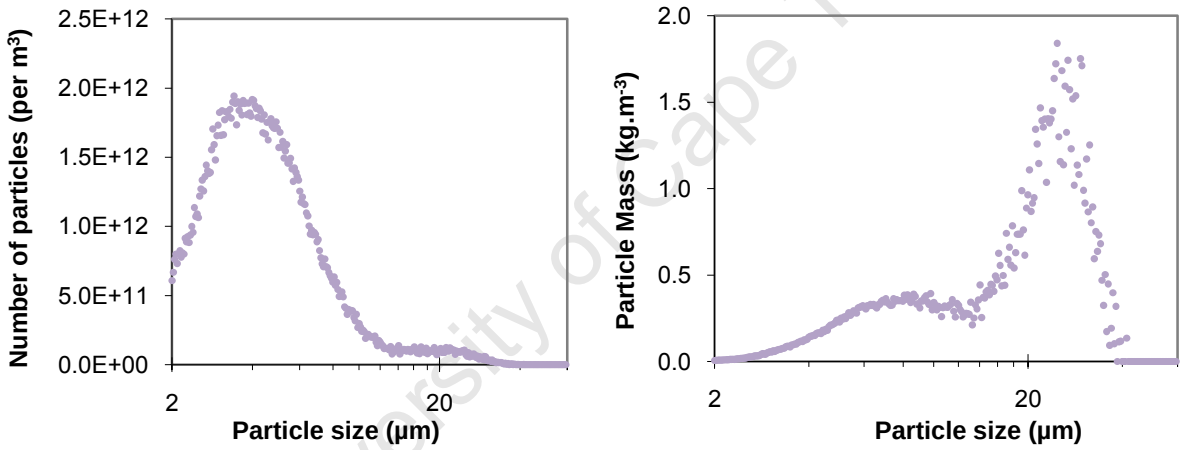

Figure 126: Number and volume distributions for seed sample B3.1.1

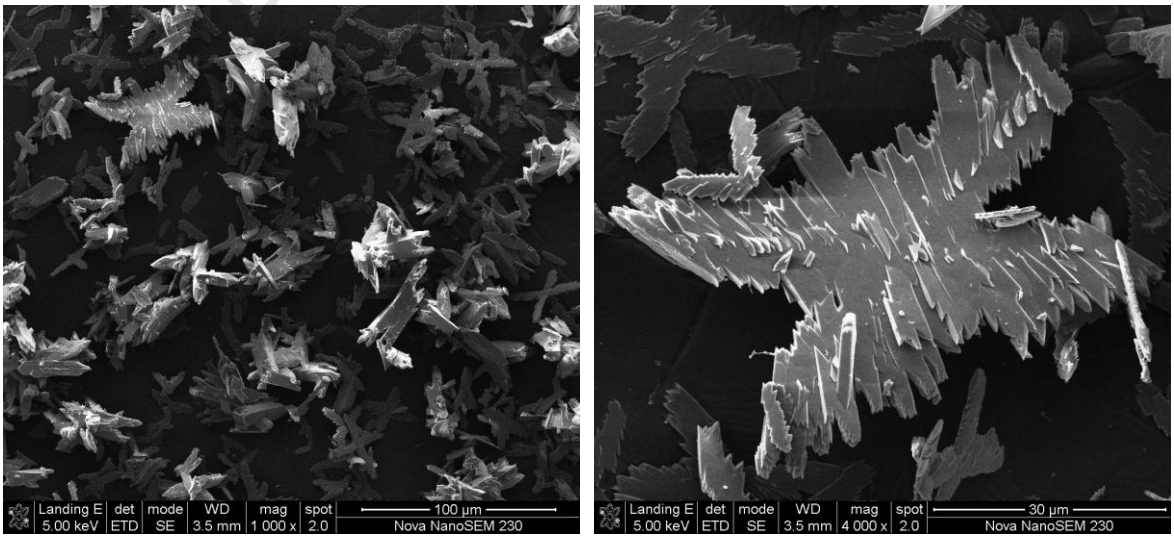

Figure 127: SEM images for seed sample B3.1.1

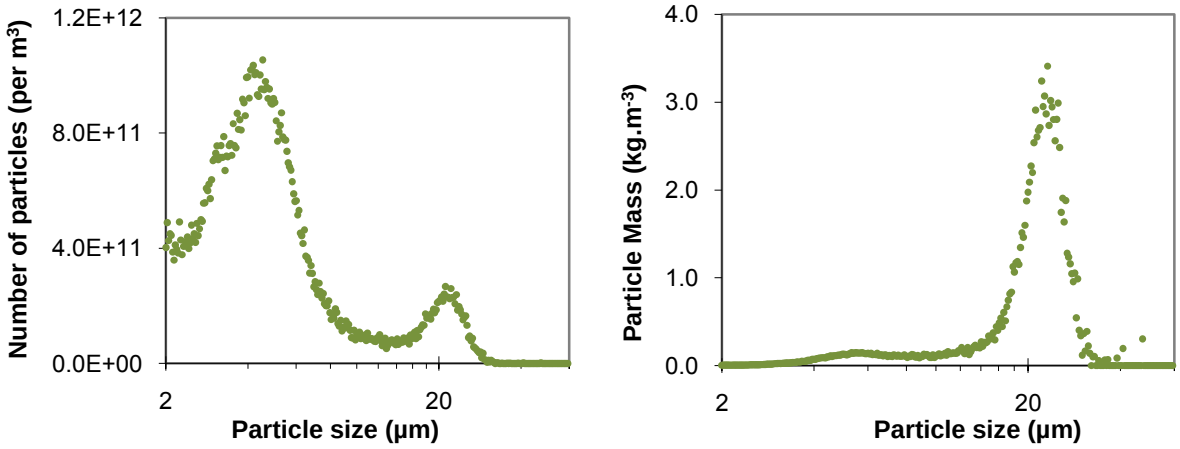

Figure 128: Number and volume distributions for seed sample B3.2.1

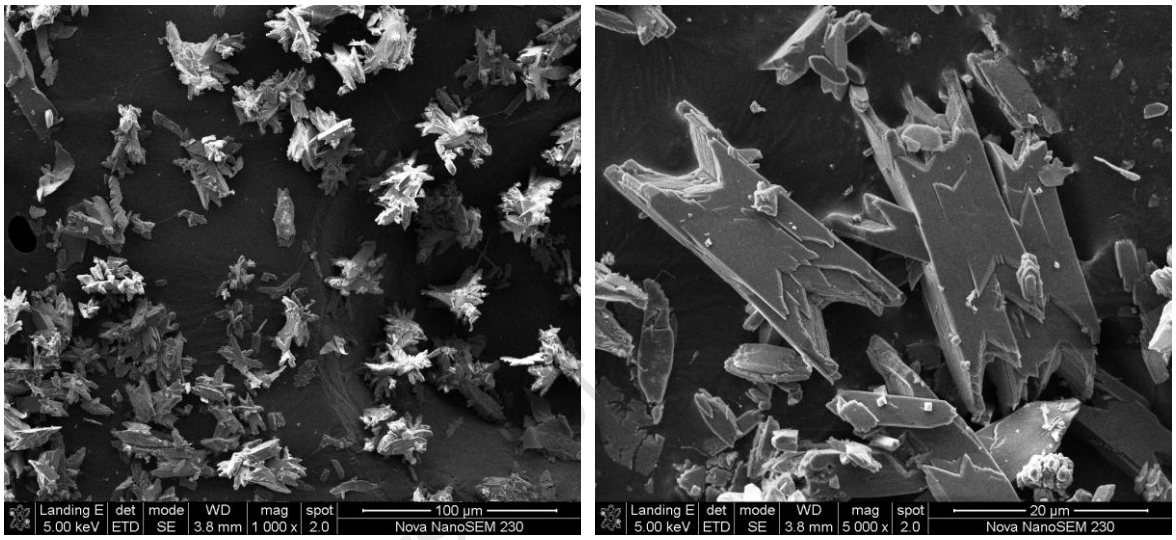

Figure 129: SEM images for seed sample B3.2.1

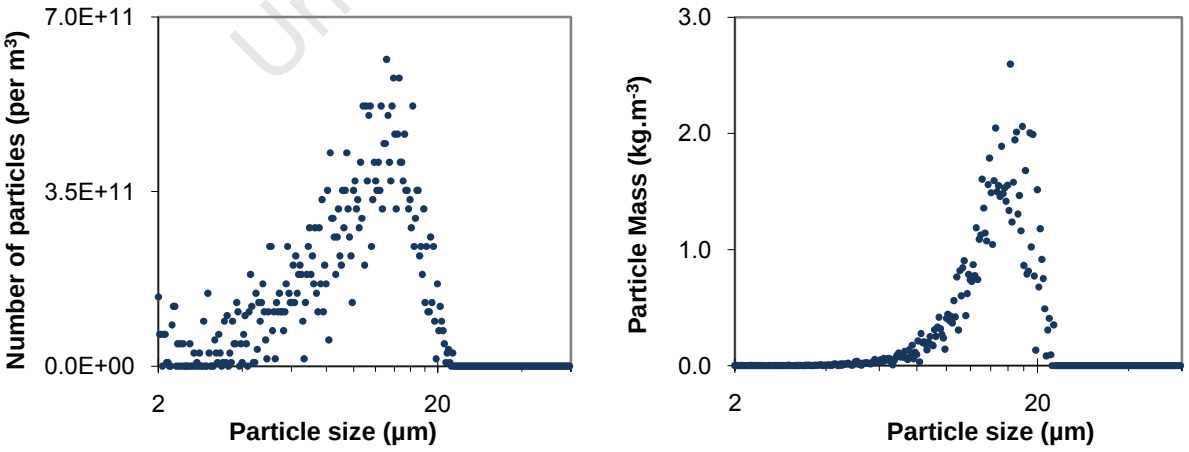

Figure 130: Number and volume distributions for seed sample B3.1.2

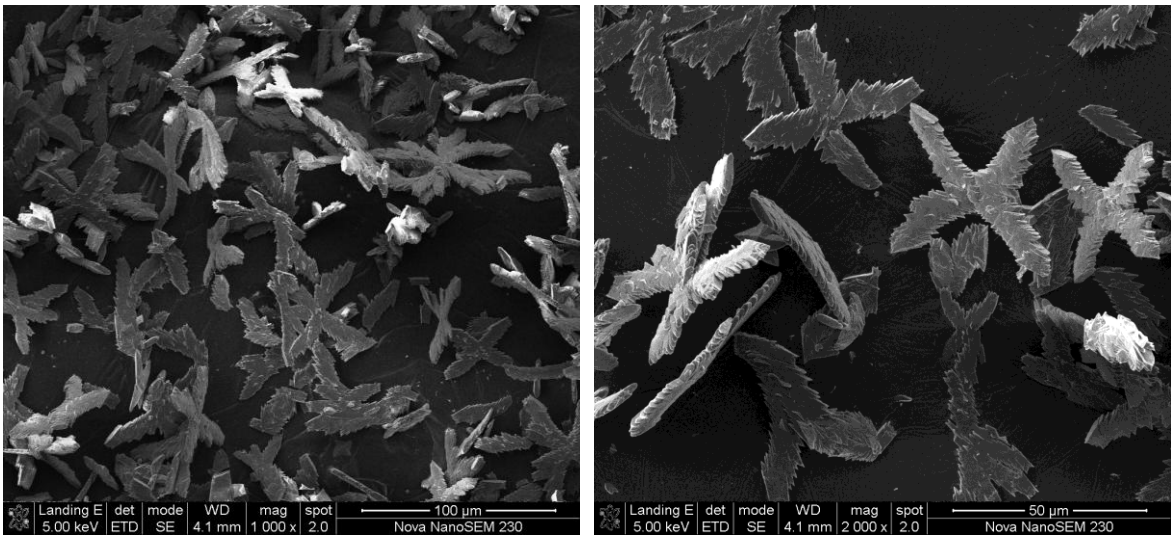

Figure 131: SEM images for seed sample B3.1.2

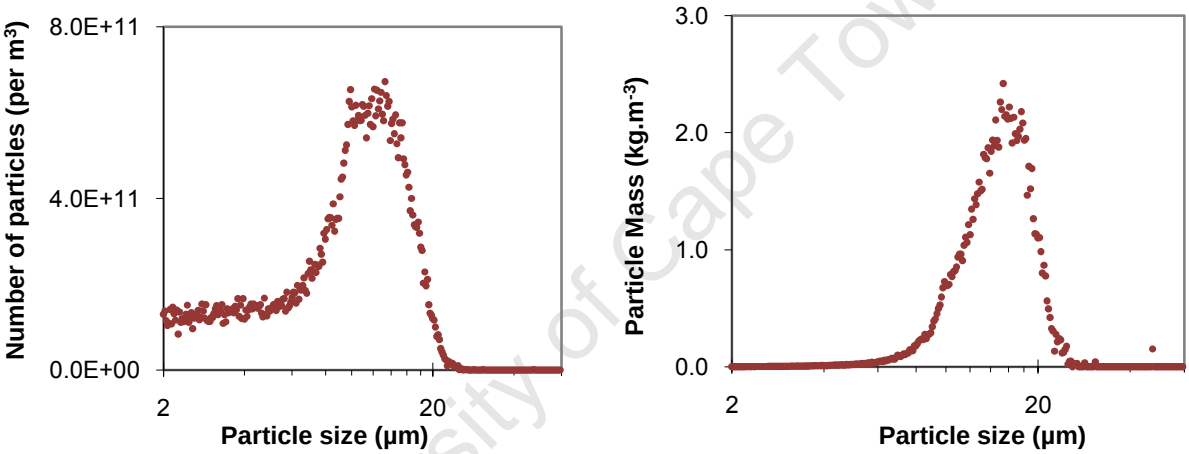

Figure 132: Number and volume distributions for seed sample B3.2.2

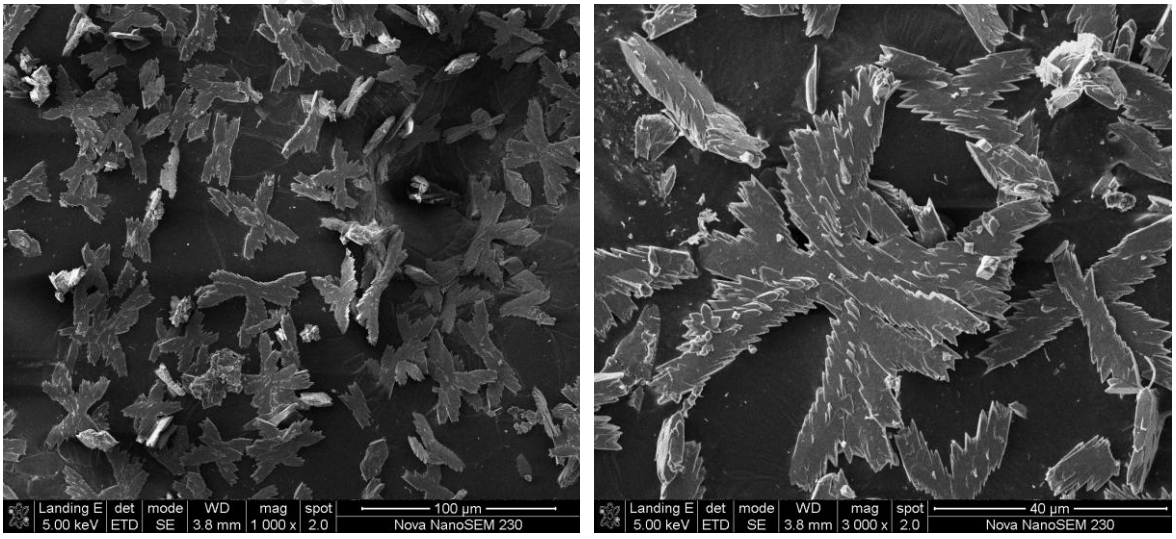

Figure 133: SEM images for seed sample B3.2.2

A.4 Purchased COM sample

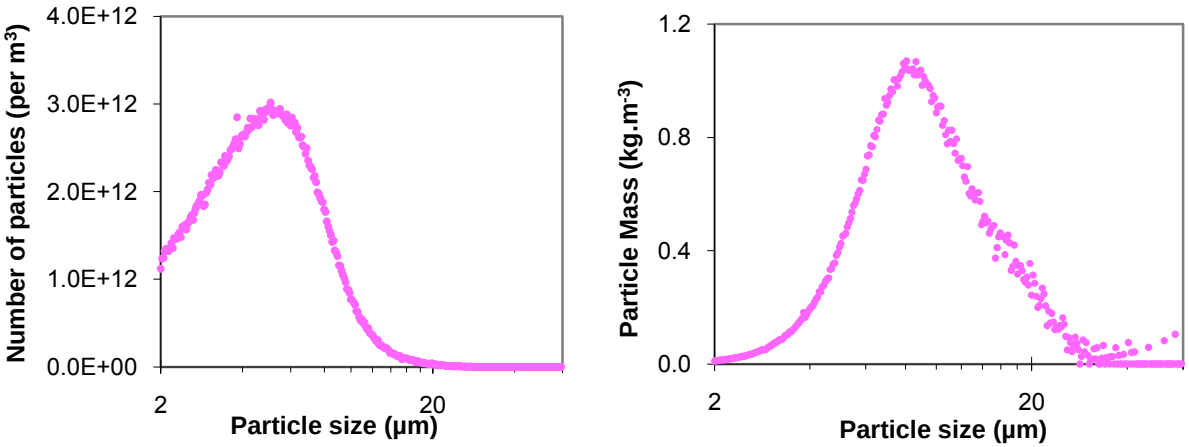

Figure 134: Number and volume distributions for purchased COM sample

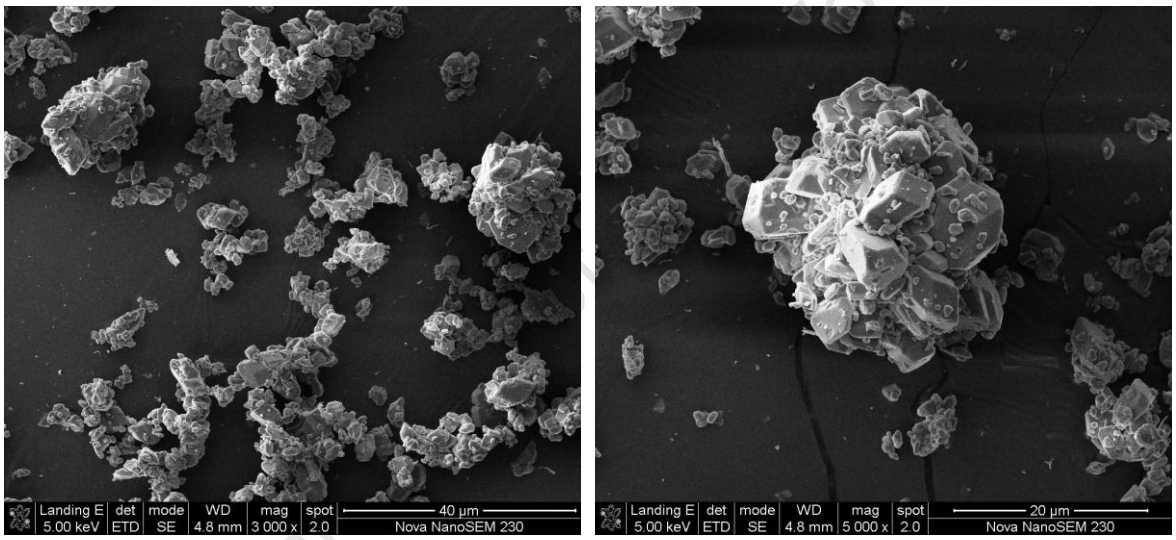

Figure 135: SEM images for purchased COM sample

Appendix B: Results from Kinetic Experiments

B.1 Evolution of m_0 and m_3

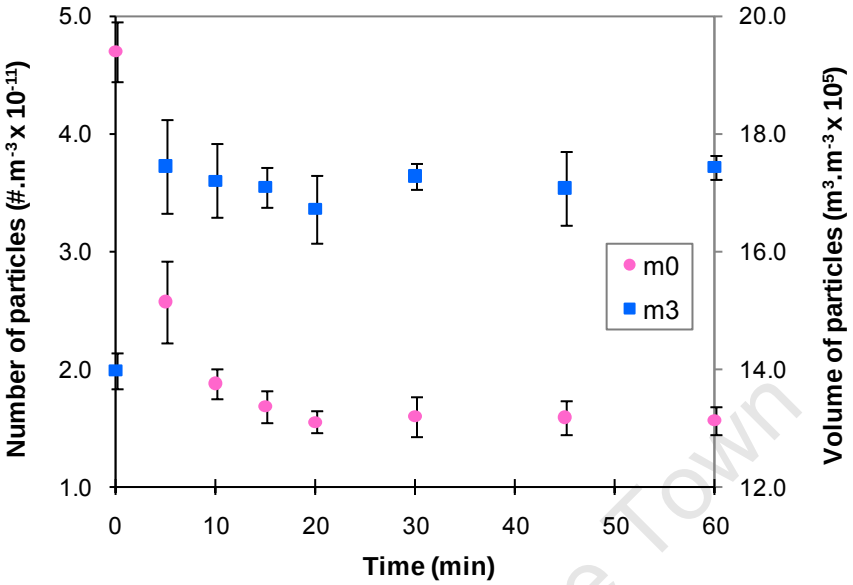

Figure 136: Evolution of m_0 and m_3 for S_i = 4.6 & C_{seeds} = 0.15g.dm^{-3}

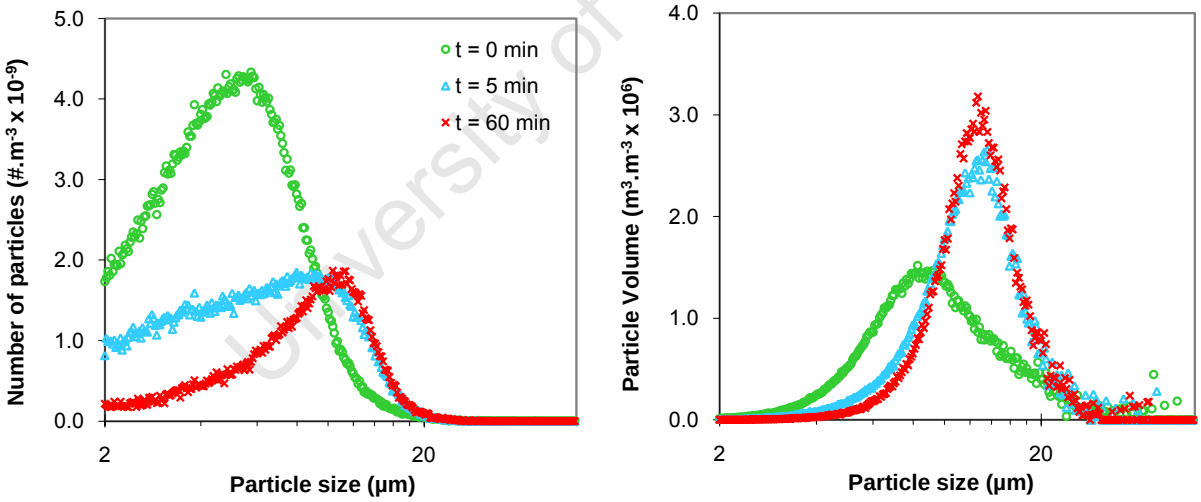

Figure 137: Number (left) and volume (right) size distributions for S_i = 4.6 & C_{seeds} = 0.15g.dm^{-3}

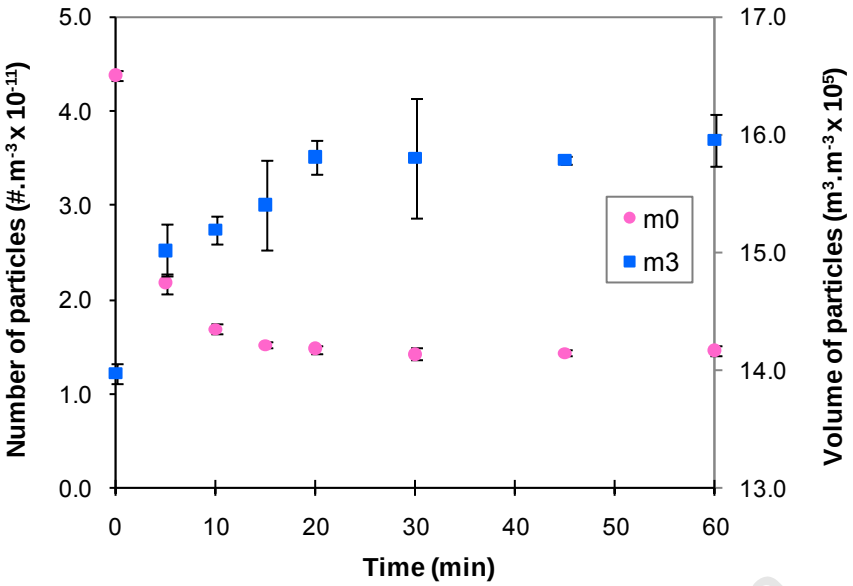

Figure 138: Evolution of m_0 and m_3 for S_i = 3.3 & C_{seeds} = 0.15g.dm^{-3}

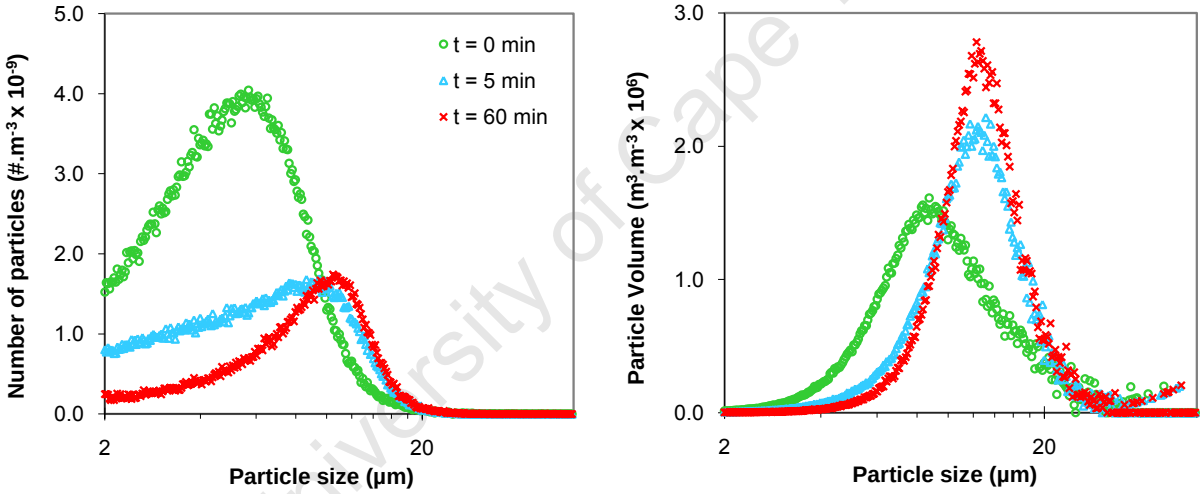

Figure 139: Number (left) and volume (right) size distributions for S_i = 3.3 & C_{seeds} = 0.15g.dm^{-3}

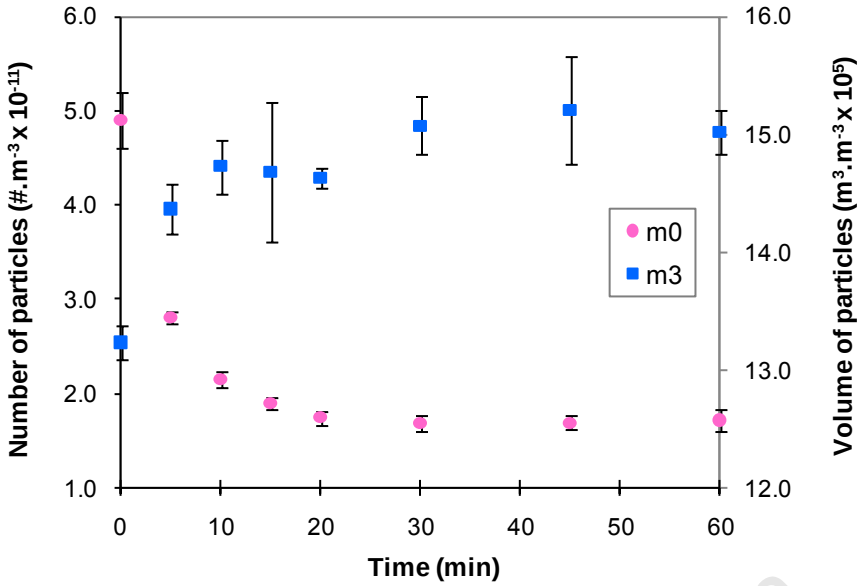

Figure 140: Evolution of m_0 and m_3 for S_i = 2.3 & C_{seeds} = 0.15g.dm^{-3}

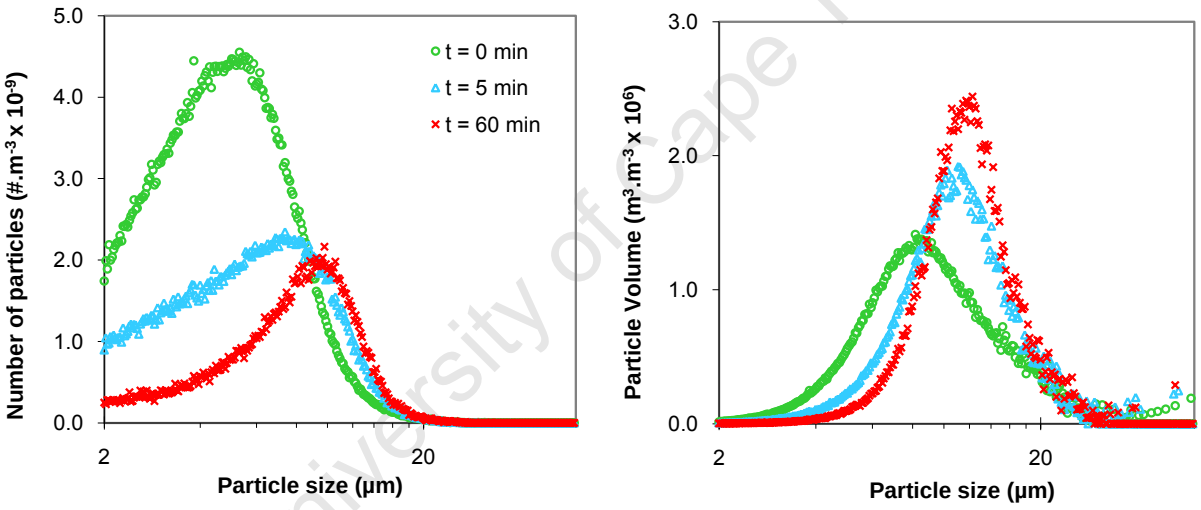

Figure 141: Number (left) and volume (right) size distributions for S_i = 2.3 & C_{seeds} = 0.15g.dm^{-3}

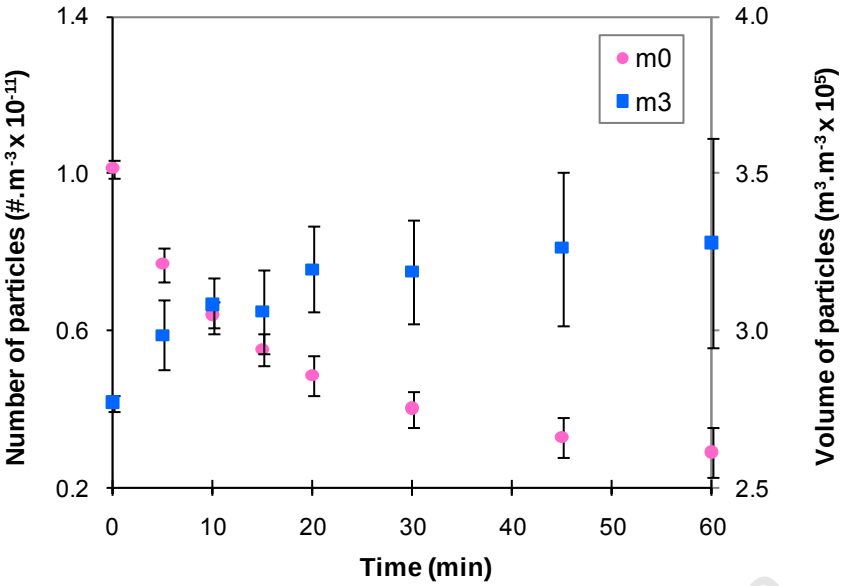

Figure 142: Evolution of m_0 and m_3 for S_i = 2.3 & C_{seeds} = 0.03g.dm^{-3}

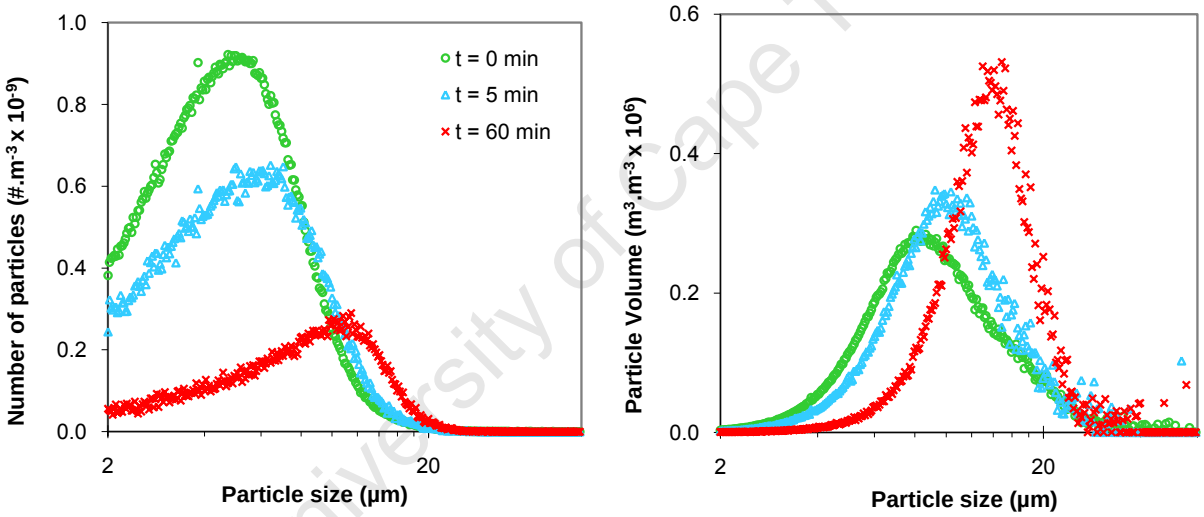

Figure 143: Number (left) and volume (right) size distributions for S_i = 2.3 & C_{seeds} = 0.03g.dm^{-3}

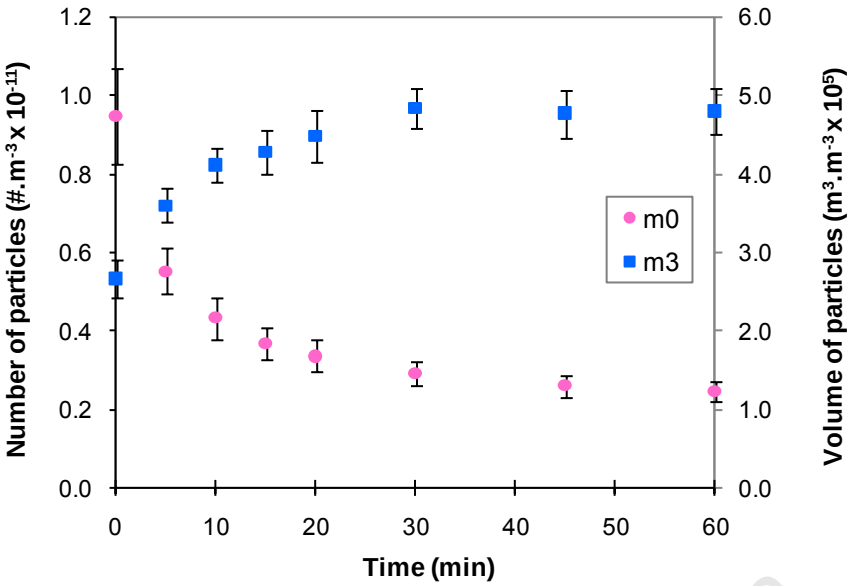

Figure 144: Evolution of m_0 and m_3 for S_i = 3.3, C_{seeds} = 0.03g.dm^{-3} & seed sample A3.2.1

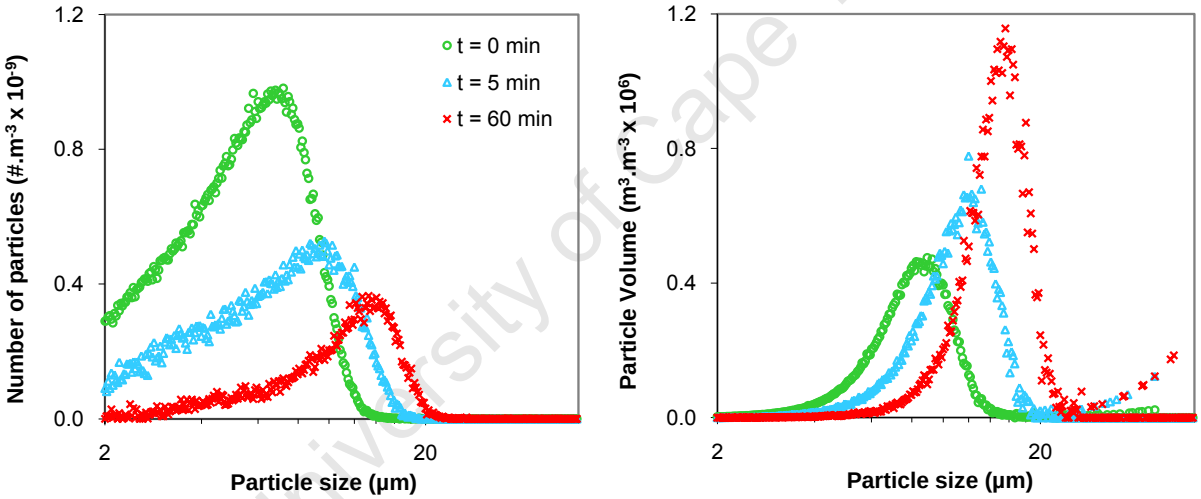

Figure 145: Number (left) and volume (right) size distributions for S_i = 3.3, C_{seeds} = 0.03g.dm^{-3} & seed sample A3.2.1

B.2 SEM Photographs

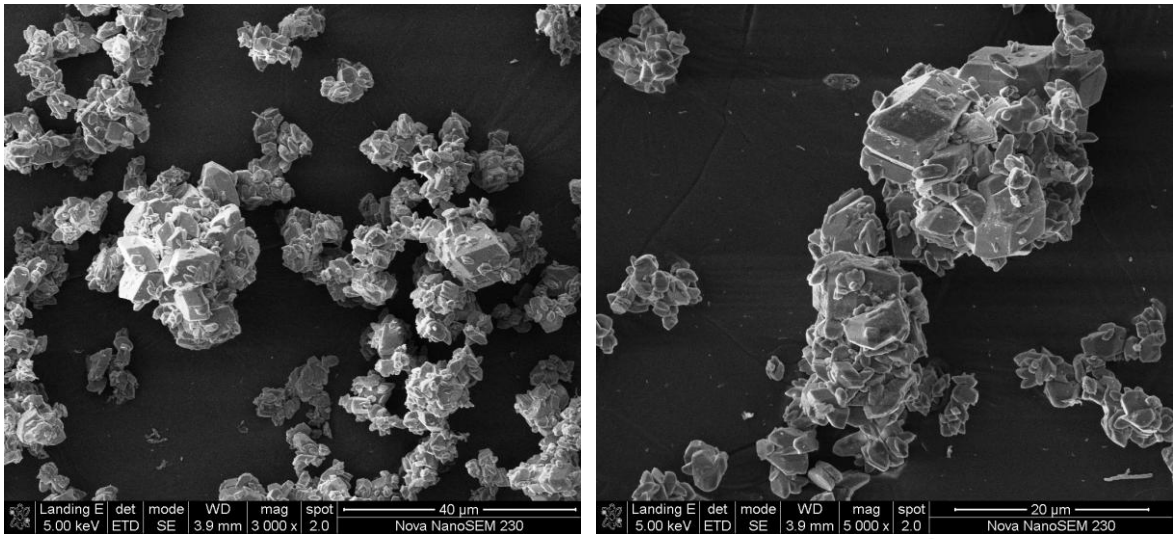

Figure 146: SEM images from kinetic experiment with S_i = 5.8 & C_{seeds} = 0.15g.dm^{-3}

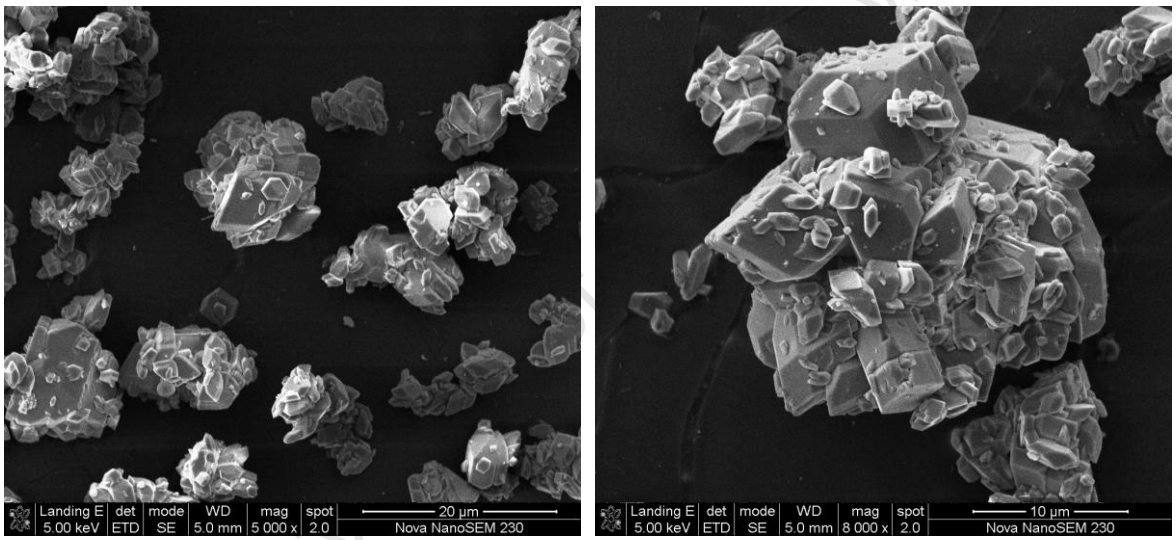

Figure 147: SEM images from kinetic experiment with S_i = 4.6 & C_{seeds} = 0.15g.dm^{-3}

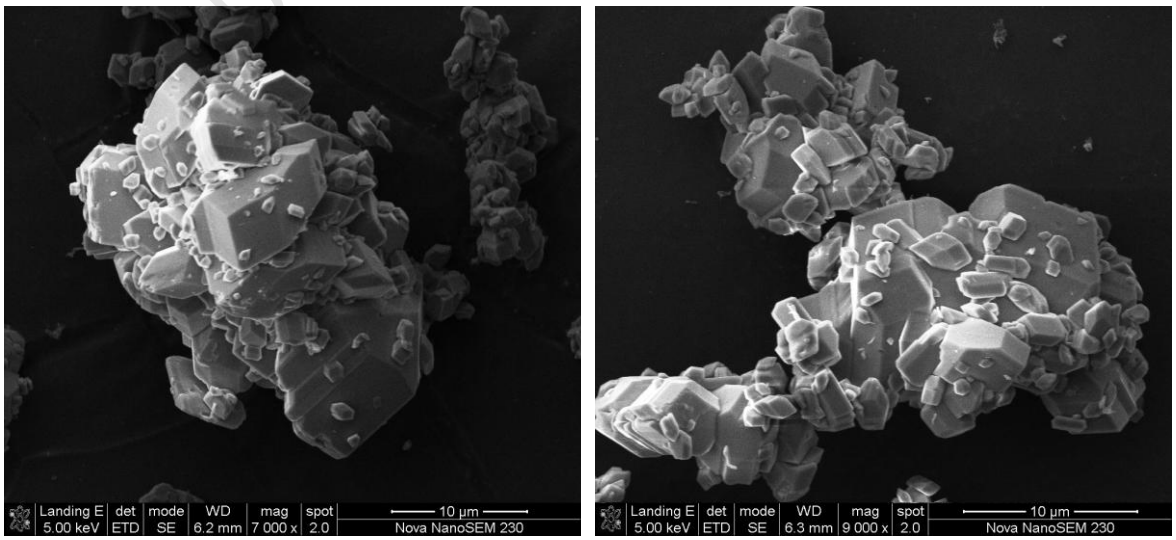

Figure 148: SEM images from kinetic experiment with S_i = 3.3 & C_{seeds} = 0.15g.dm^{-3}

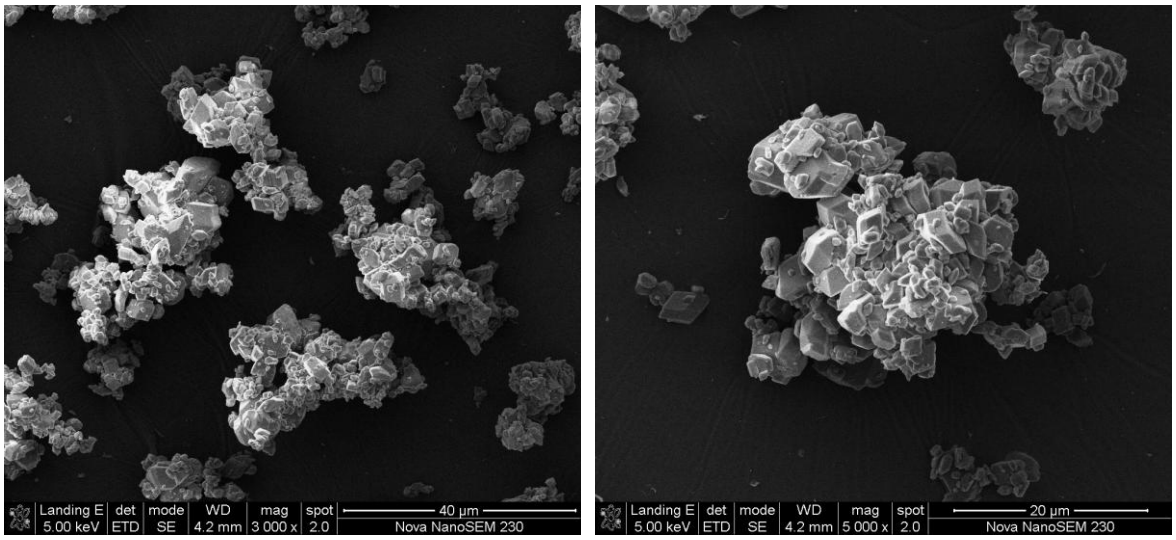

Figure 149: SEM images from kinetic experiment with S_i = 2.3 & C_{seeds} = 0.15g.dm^{-3}

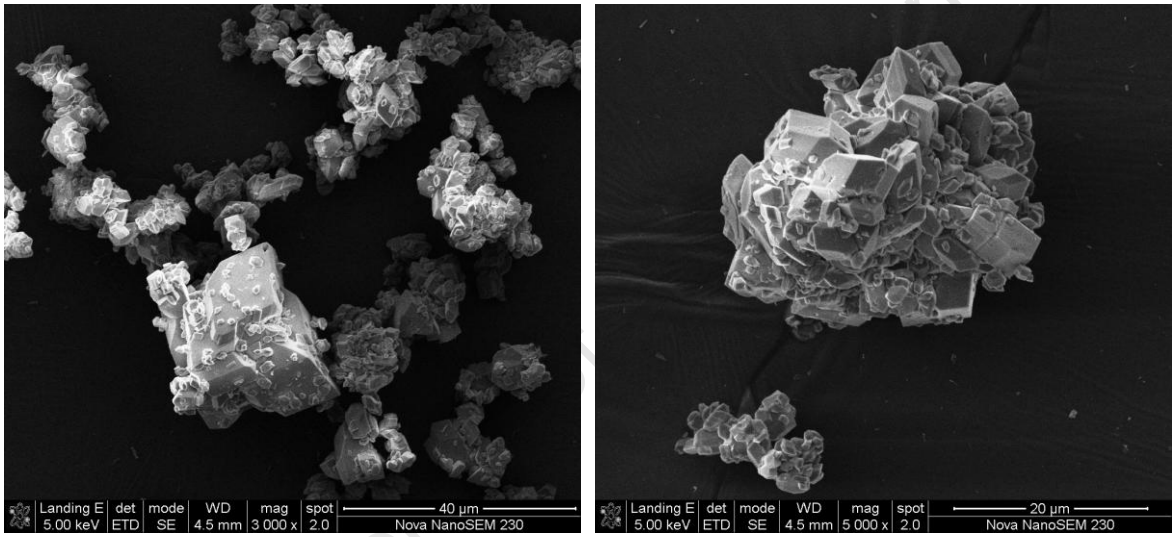

Figure 150: SEM images from kinetic experiment with S_i = 2.3 & C_{seeds} = 0.03g.dm^{-3}

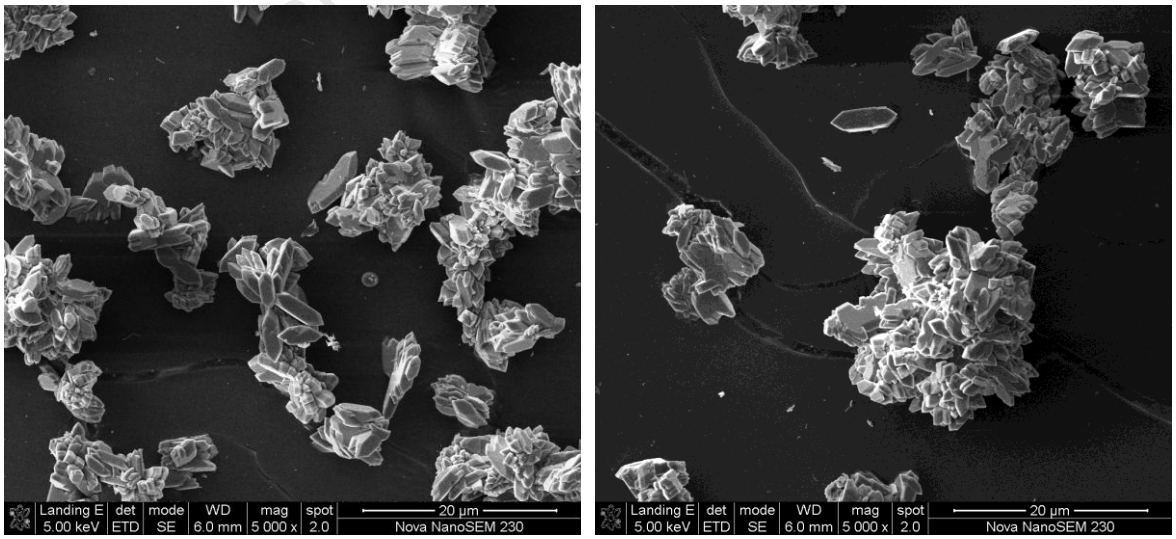

Figure 151: SEM images from kinetic experiment with S_i = 3.3, C_{seeds} = 0.03g.dm^{-3} & A3.2.1 seeds

B.3 Growth Kinetics Results

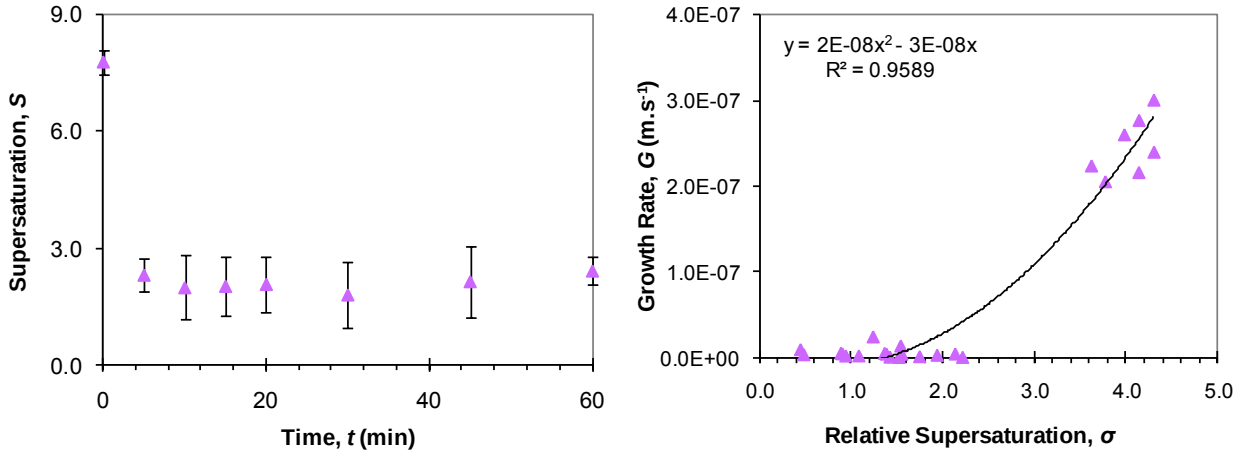

Figure 152: Growth results for kinetic experiment: S_i = 5.8 & C_{seeds} = 0.15g.dm^{-3}

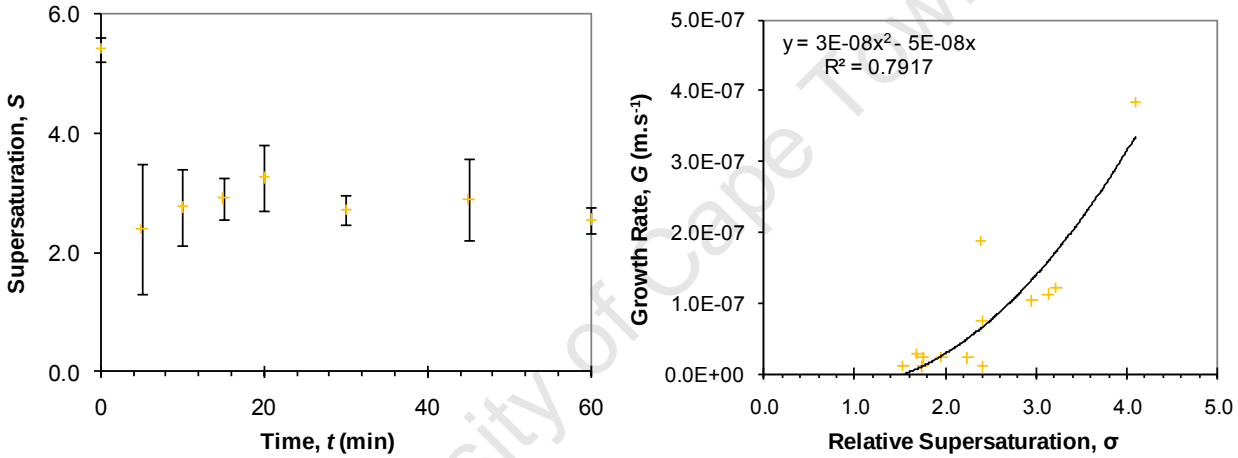

Figure 153: Growth results for kinetic experiment: S_i = 4.6 & C_{seeds} = 0.15g.dm^{-3}

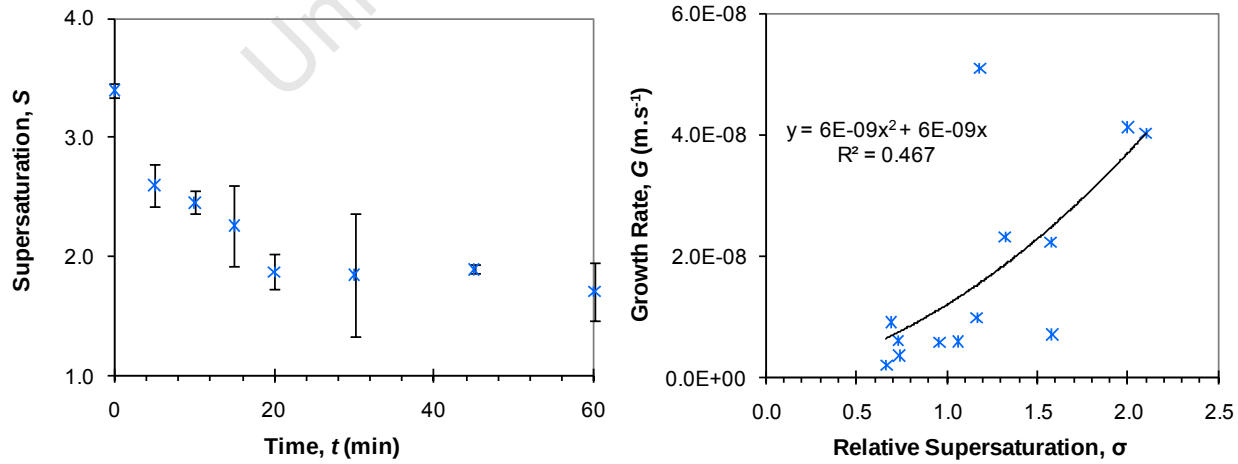

Figure 154: Growth results for kinetic experiment: S_i = 3.3 & C_{seeds} = 0.15g.dm^{-3}

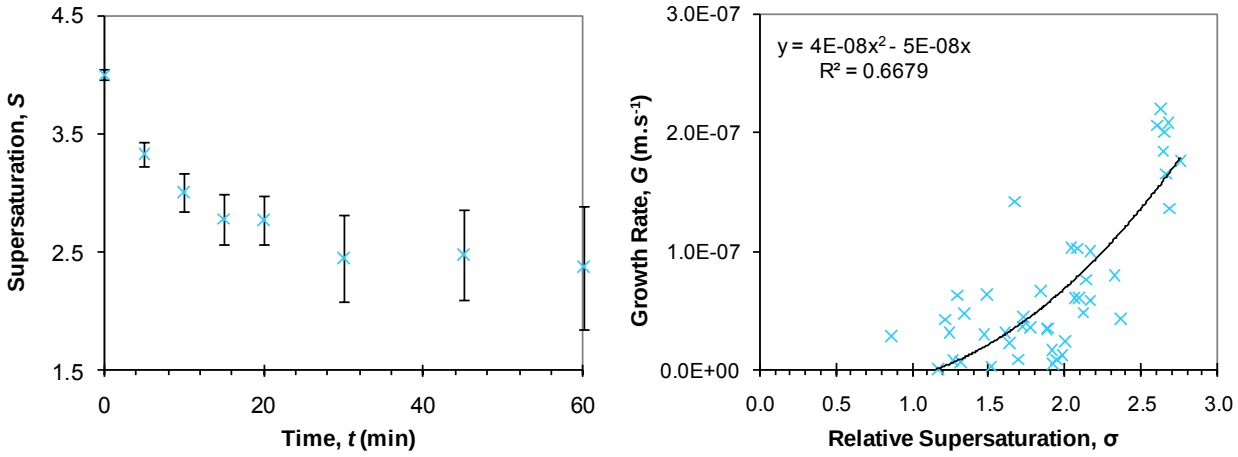

Figure 155: Growth results for kinetic experiment: S_i = 3.3 & C_{seeds} = 0.03g.dm^{-3}

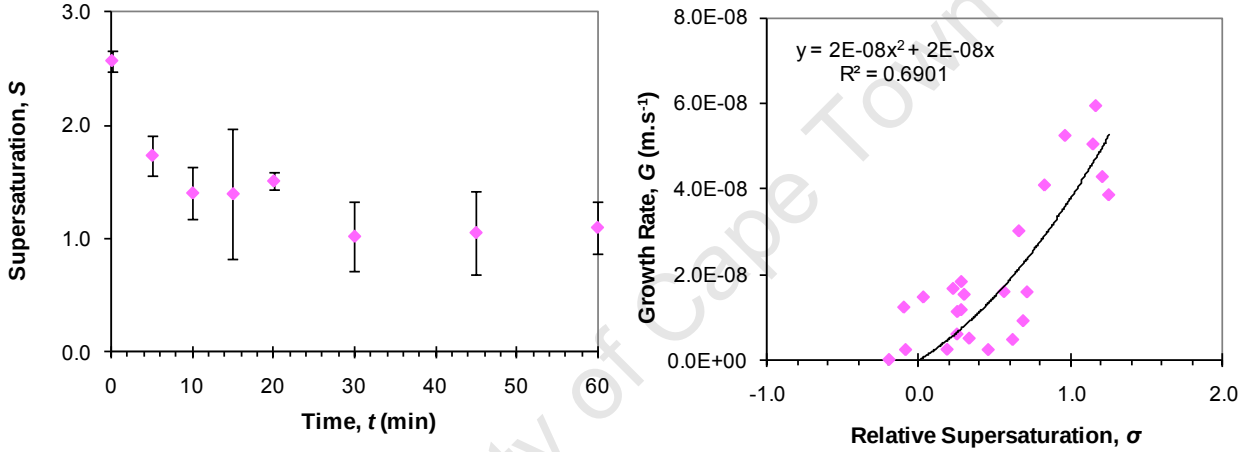

Figure 156: Growth results for kinetic experiment: S_i = 2.3 & C_{seeds} = 0.15g.dm^{-3}

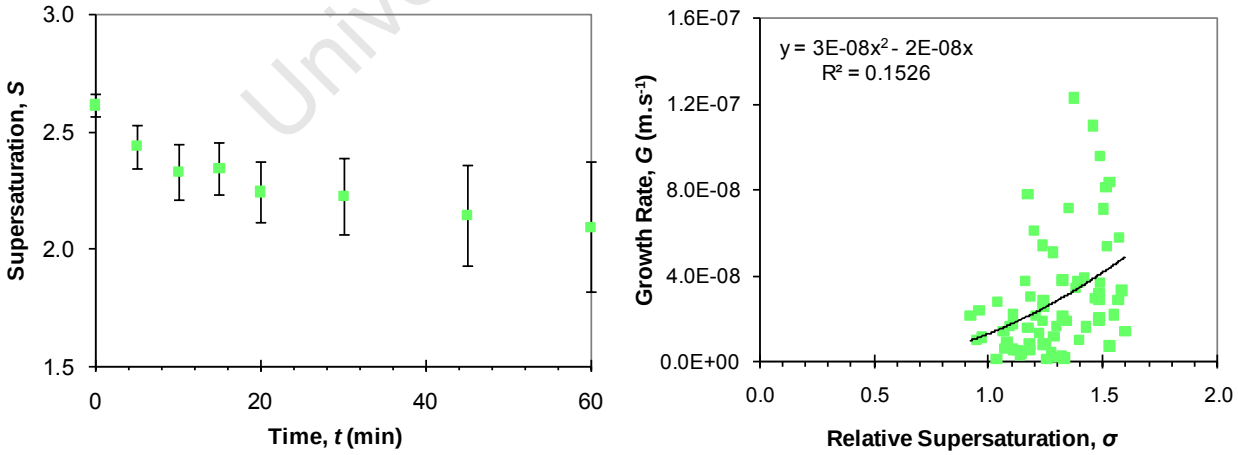

Figure 157: Growth results for kinetic experiment: S_i = 2.3 & C_{seeds} = 0.03g.dm^{-3}

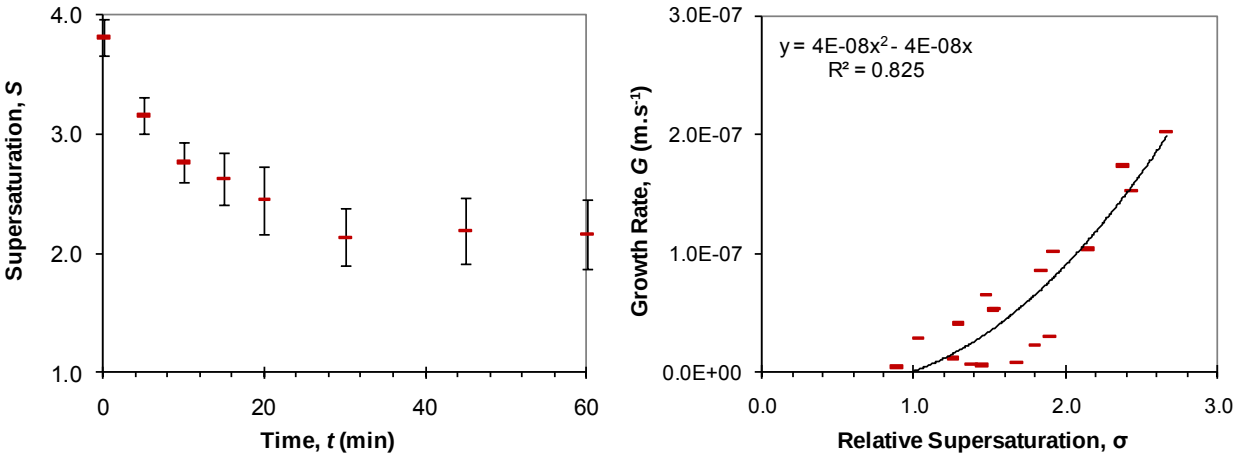

Figure 158: Growth results for kinetic experiment: S_i = 3.3 & C_{seeds} = 0.03g.dm^{-3} using seed sample A3.2.1

B.4 Aggregation Kinetics Results

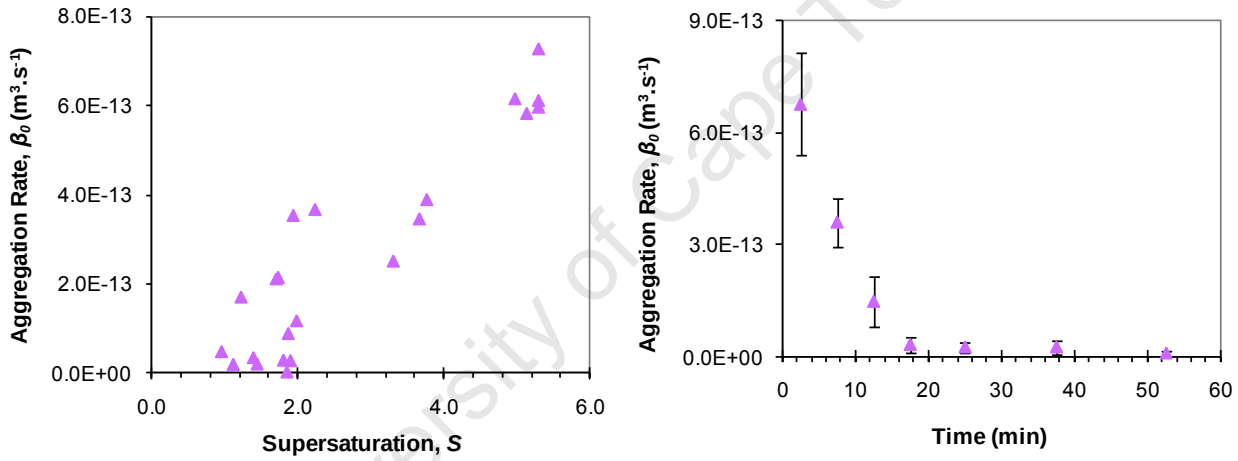

Figure 159: Aggregation results for kinetic experiment: S_i = 5.8 & C_{seeds} = 0.15g.dm^{-3}

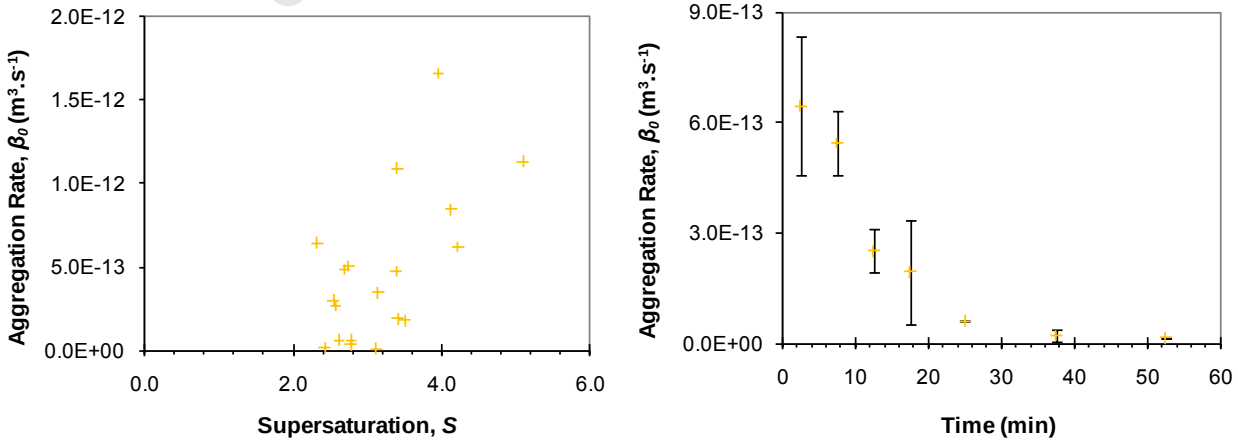

Figure 160: Aggregation results for kinetic experiment: S_i = 4.6 & C_{seeds} = 0.15g.dm^{-3}

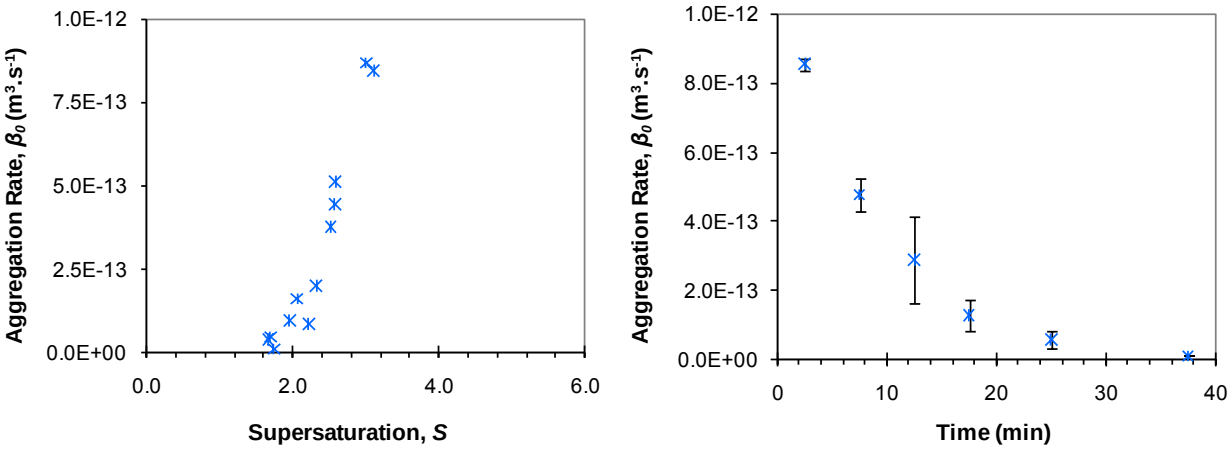

Figure 161: Aggregation results for kinetic experiment: S_i = 3.3 & C_{seeds} = 0.15g.dm^{-3}

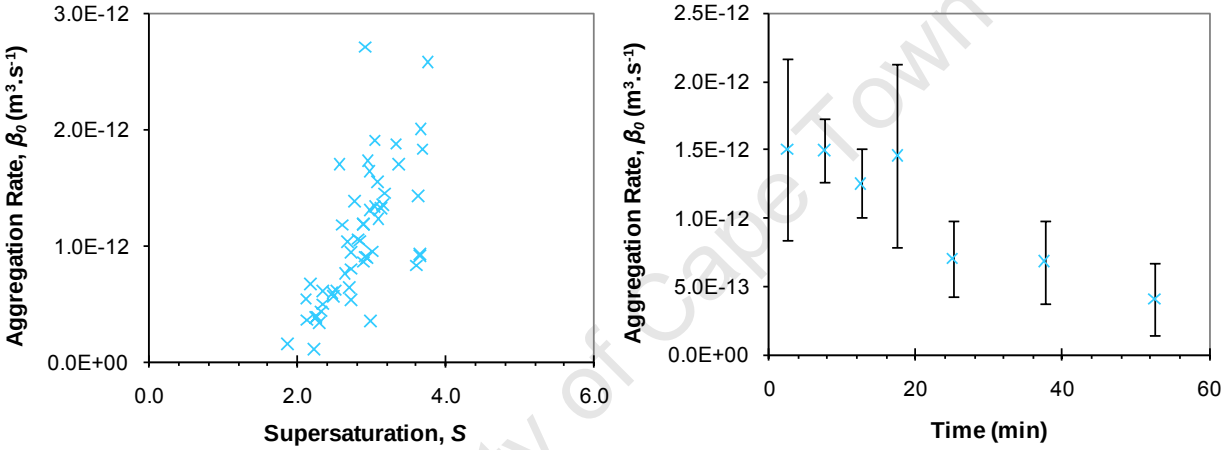

Figure 162: Aggregation results for kinetic experiment: S_i = 3.3 & C_{seeds} = 0.03g.dm^{-3}

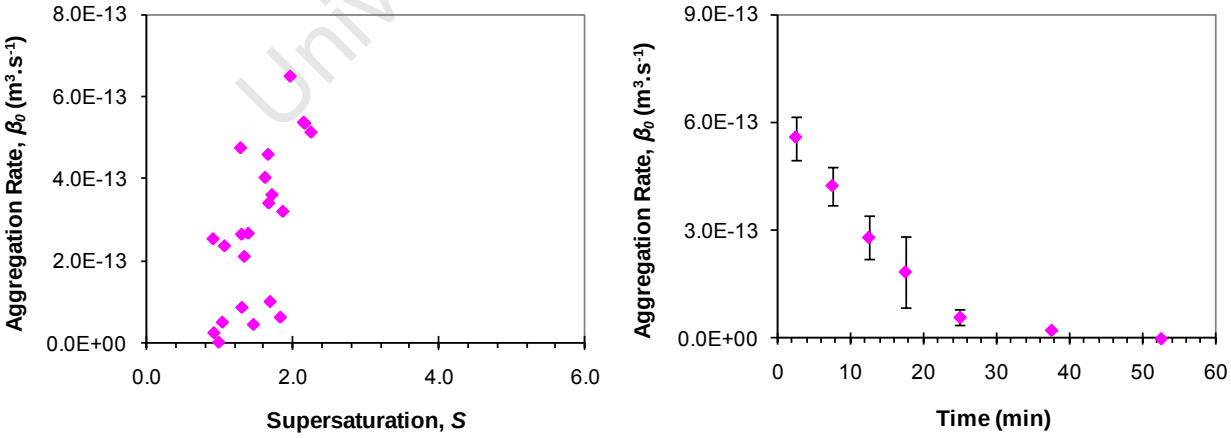

Figure 163: Aggregation results for kinetic experiment: S_i = 2.3 & C_{seeds} = 0.15g.dm^{-3}

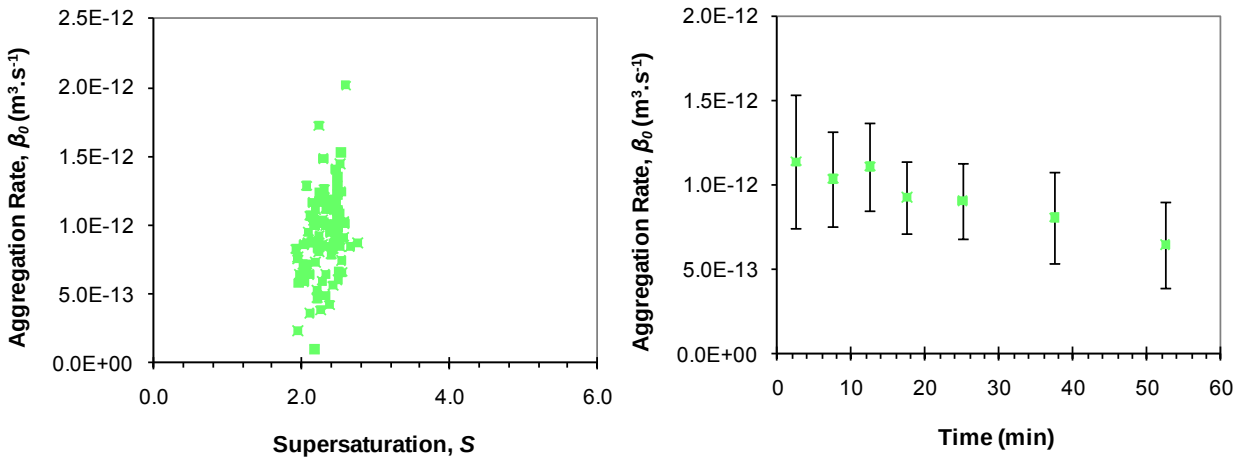

Figure 164: Aggregation results for kinetic experiment: S_i = 2.3 & C_{seeds} = 0.03g.dm^{-3}

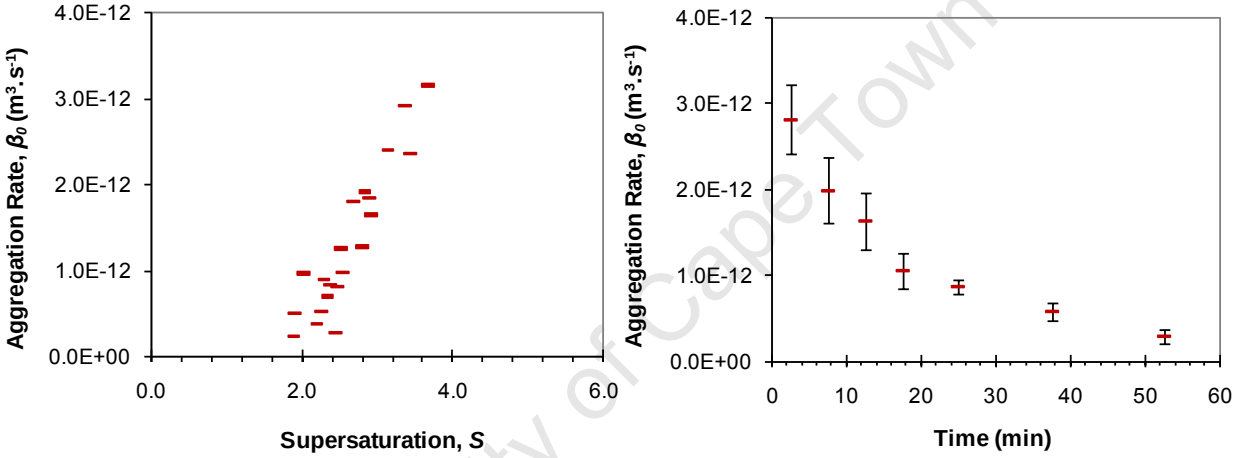

Figure 165: Aggregation results for kinetic experiment: S_i = 3.3 & C_{seeds} = 0.03g.dm^{-3} using seed sample A3.2.1

Appendix C: Raw Data & Sample Calculations

C.1 Chapter 3

Sample calculations for determining the macro, meso and micro mixing times as well as the Reynolds number and impeller power are shown below.

The following constants were used in the calculations:

$V_{reactor} = 0.001$ m^3 $\quad N_q = 0.73$

$d_{stir} = 0.05$ m $\quad a = 2$

$\Lambda = 2.0 \times 10^{-3}$ m $\quad A = 1.26 \times 10^{-5}$ m^2

$N_p = 1.5$ $\quad \nu = 6.98 \times 10^{-7}$ m^2.s^{-1}

$\rho_{soln} = 0.994$ kg.m^{-3} $\quad \mu = 6.94 \times 10^{-7}$ kg.m^{-1}.s^{-1}

$$q_C = N_q N d_{stir}^3 = 0.73 \times 0.83 s^{-1} \times (0.05\text{ m})^3 = 7.6 \times 10^{-5}\text{ m}^3.\text{s}^{-1}$$

$$t_c = \frac{V}{q_c} = \frac{0.001\ m^3}{7.6\times10^{-5}\ m^3.s^{-1}} = 13.2\text{ s}$$

$$t_{macro} = 4t_c = 4 \times 13.2 = 52.6\text{ s}$$

$$\varepsilon = a\frac{N_p N^3 d_{stir}^5}{V} = 2\frac{1.5\times(0.83s^{-1})^3\times(0.05m)^5}{0.001\ m^3} = 5.43 \times 10^{-4}\text{ W.kg}^{-1}$$

$$t_{meso} = a(\frac{\Lambda^2}{\varepsilon})^{\frac{1}{3}} = 2\left(\frac{(2.0\times10^{-3}m)^2}{5.43\times10^{-4}\ W.kg^{-1}}\right)^{\frac{1}{3}} = 0.389\text{ s}^{-1}$$

$$\bar{\varepsilon} = 0.25N^3 d_{stir}^2 = 0.25 \times (0.83s^{-1})^3 \times (0.05m)^2 = 3.6 \times 10^{-4}\text{ W.kg}^{-1}$$

$$t_{micro} = 12\left(\frac{\nu}{\bar{\varepsilon}}\right)^{0.5} = 12\left(\frac{6.98\times10^{-7}m^2.s^{-1}}{3.6\times10^{-4}W.kg^{-1}}\right)^{0.5} = 5.27 \times 10^{-1}\text{ s}$$

$$Re = \frac{\rho N d_{stir}^2}{\mu} = \frac{0.994\ kg.m^{-3}\times0.83s^{-1}\times(0.05m)^2}{6.94\times10^{-7}kg.m^{-1}.s^{-1}} = 2.98 \times 10^3$$

$$N_p = \frac{Pg}{\rho N^3 d_{stir}^5} \rightarrow P = \frac{N_p \rho N^3 d_{stir}^5}{g} = \frac{1.5\times(0.994\ kg.m^{-3})\times(0.83s^{-1})^3\times(0.05\ m)^5}{9.81\ m.s^{-1}} = 2.75 \times 10^{-8}\text{ W}$$

One set of raw data from the Coulter Counter has been included below for example purposes. The full set of raw data from Chapter 3 has not been included as it was too large to include in the Appendices.

Table 15: Raw data from seed experiment A1.2.1

Bin Number	Bin Diameter (Lower) (µm)	Differential Number (#/mL)			Average Diff. Number
		1	2	3	
1	2	18.00	28.00	31.00	25.67
2	2.0228	16.00	13.00	25.00	18.00
3	2.04587	27.00	18.00	18.00	21.00
4	2.06919	28.00	24.00	19.00	23.67
5	2.09279	14.00	16.00	12.00	14.00

6	2.11665	14.00	24.00	22.00	20.00
7	2.14078	27.00	15.00	14.00	18.67
8	2.16519	20.00	7.00	22.00	16.33
9	2.18988	11.00	20.00	24.00	18.33
10	2.21485	34.00	22.00	26.00	27.33
11	2.2401	21.00	20.00	29.00	23.33
12	2.26564	29.00	20.00	23.00	24.00
13	2.29147	15.00	20.00	16.00	17.00
14	2.3176	23.00	19.00	24.00	22.00
15	2.34403	30.00	26.00	32.00	29.33
16	2.37075	24.00	15.00	17.00	18.67
17	2.39778	15.00	22.00	17.00	18.00
18	2.42512	25.00	25.00	31.00	27.00
19	2.45277	24.00	34.00	21.00	26.33
20	2.48074	23.00	23.00	20.00	22.00
21	2.50902	20.00	19.00	24.00	21.00
22	2.53763	29.00	23.00	23.00	25.00
23	2.56656	22.00	14.00	30.00	22.00
24	2.59583	36.00	15.00	27.00	26.00
25	2.62543	15.00	26.00	17.00	19.33
26	2.65536	30.00	16.00	20.00	22.00
27	2.68564	15.00	23.00	27.00	21.67
28	2.71626	37.00	25.00	21.00	27.67
29	2.74723	25.00	25.00	20.00	23.33
30	2.77855	17.00	19.00	25.00	20.33
31	2.81023	29.00	26.00	14.00	23.00
32	2.84227	28.00	25.00	22.00	25.00
33	2.87468	22.00	22.00	31.00	25.00
34	2.90746	25.00	25.00	19.00	23.00
35	2.94061	33.00	26.00	29.00	29.33
36	2.97414	20.00	17.00	29.00	22.00
37	3.00805	32.00	24.00	20.00	25.33
38	3.04234	28.00	24.00	22.00	24.67
39	3.07703	33.00	22.00	28.00	27.67
40	3.11212	36.00	20.00	34.00	30.00
41	3.1476	33.00	23.00	37.00	31.00
42	3.18349	29.00	22.00	28.00	26.33
43	3.21979	38.00	25.00	25.00	29.33
44	3.2565	26.00	31.00	16.00	24.33
45	3.29363	30.00	20.00	15.00	21.67
46	3.33118	28.00	31.00	32.00	30.33
47	3.36916	24.00	21.00	14.00	19.67
48	3.40758	33.00	35.00	34.00	34.00
49	3.44643	29.00	25.00	21.00	25.00
50	3.48573	29.00	23.00	28.00	26.67
51	3.52547	27.00	30.00	34.00	30.33
52	3.56567	23.00	29.00	22.00	24.67
53	3.60632	39.00	27.00	39.00	35.00
54	3.64744	32.00	27.00	37.00	32.00
55	3.68903	30.00	28.00	28.00	28.67

56	3.73109	23.00	27.00	28.00	26.00
57	3.77363	22.00	20.00	31.00	24.33
58	3.81666	44.00	37.00	29.00	36.67
59	3.86017	36.00	39.00	27.00	34.00
60	3.90419	37.00	29.00	29.00	31.67
61	3.9487	24.00	34.00	40.00	32.67
62	3.99372	29.00	18.00	26.00	24.33
63	4.03926	26.00	27.00	35.00	29.33
64	4.08531	34.00	23.00	33.00	30.00
65	4.13189	24.00	24.00	37.00	28.33
66	4.17901	36.00	26.00	22.00	28.00
67	4.22665	33.00	25.00	20.00	26.00
68	4.27485	40.00	35.00	33.00	36.00
69	4.32359	39.00	22.00	43.00	34.67
70	4.37288	39.00	24.00	30.00	31.00
71	4.42274	32.00	25.00	33.00	30.00
72	4.47317	32.00	33.00	34.00	33.00
73	4.52417	35.00	22.00	36.00	31.00
74	4.57576	37.00	37.00	30.00	34.67
75	4.62793	42.00	30.00	38.00	36.67
76	4.68069	34.00	34.00	31.00	33.00
77	4.73406	39.00	31.00	43.00	37.67
78	4.78804	30.00	34.00	37.00	33.67
79	4.84263	33.00	24.00	36.00	31.00
80	4.89785	41.00	29.00	30.00	33.33
81	4.95369	43.00	29.00	29.00	33.67
82	5.01017	40.00	28.00	25.00	31.00
83	5.0673	27.00	24.00	24.00	25.00
84	5.12507	45.00	32.00	42.00	39.67
85	5.18351	42.00	33.00	28.00	34.33
86	5.24261	26.00	30.00	34.00	30.00
87	5.30239	40.00	34.00	34.00	36.00
88	5.36284	44.00	30.00	30.00	34.67
89	5.42399	32.00	27.00	28.00	29.00
90	5.48583	35.00	27.00	30.00	30.67
91	5.54838	41.00	25.00	28.00	31.33
92	5.61164	37.00	36.00	26.00	33.00
93	5.67563	38.00	34.00	37.00	36.33
94	5.74034	42.00	36.00	35.00	37.67
95	5.80579	54.00	36.00	31.00	40.33
96	5.87199	38.00	32.00	27.00	32.33
97	5.93894	43.00	32.00	32.00	35.67
98	6.00665	40.00	33.00	31.00	34.67
99	6.07514	36.00	31.00	31.00	32.67
100	6.14441	35.00	40.00	32.00	35.67
101	6.21447	32.00	24.00	36.00	30.67
102	6.28532	47.00	27.00	20.00	31.33
103	6.35699	49.00	38.00	31.00	39.33
104	6.42947	37.00	32.00	14.00	27.67
105	6.50277	53.00	41.00	46.00	46.67

106	6.57692	50.00	31.00	49.00	43.33
107	6.65191	39.00	24.00	54.00	39.00
108	6.72775	53.00	41.00	43.00	45.67
109	6.80446	41.00	38.00	33.00	37.33
110	6.88204	50.00	26.00	41.00	39.00
111	6.96051	56.00	40.00	30.00	42.00
112	7.03987	45.00	37.00	31.00	37.67
113	7.12014	40.00	44.00	33.00	39.00
114	7.20132	39.00	30.00	33.00	34.00
115	7.28343	54.00	46.00	33.00	44.33
116	7.36648	46.00	43.00	46.00	45.00
117	7.45047	50.00	55.00	49.00	51.33
118	7.53542	55.00	43.00	52.00	50.00
119	7.62133	50.00	41.00	39.00	43.33
120	7.70823	45.00	39.00	60.00	48.00
121	7.79612	53.00	42.00	50.00	48.33
122	7.88501	42.00	40.00	48.00	43.33
123	7.97491	52.00	66.00	37.00	51.67
124	8.06584	69.00	53.00	43.00	55.00
125	8.15781	67.00	57.00	55.00	59.67
126	8.25082	71.00	44.00	50.00	55.00
127	8.3449	56.00	60.00	70.00	62.00
128	8.44004	76.00	58.00	54.00	62.67
129	8.53627	68.00	62.00	63.00	64.33
130	8.6336	72.00	52.00	52.00	58.67
131	8.73204	69.00	68.00	68.00	68.33
132	8.8316	98.00	76.00	59.00	77.67
133	8.9323	83.00	60.00	57.00	66.67
134	9.03415	77.00	63.00	67.00	69.00
135	9.13715	84.00	86.00	86.00	85.33
136	9.24133	103.00	75.00	66.00	81.33
137	9.3467	90.00	76.00	63.00	76.33
138	9.45327	84.00	68.00	66.00	72.67
139	9.56105	93.00	89.00	75.00	85.67
140	9.67007	96.00	91.00	80.00	89.00
141	9.78032	97.00	103.00	94.00	98.00
142	9.89184	87.00	76.00	96.00	86.33
143	10.0046	103.00	103.00	80.00	95.33
144	10.1187	117.00	94.00	90.00	100.33
145	10.2341	117.00	98.00	86.00	100.33
146	10.3508	123.00	107.00	101.00	110.33
147	10.4688	144.00	146.00	119.00	136.33
148	10.5881	116.00	128.00	98.00	114.00
149	10.7089	141.00	114.00	106.00	120.33
150	10.831	135.00	121.00	130.00	128.67
151	10.9545	144.00	124.00	130.00	132.67
152	11.0794	132.00	140.00	133.00	135.00
153	11.2057	161.00	122.00	130.00	137.67
154	11.3334	164.00	133.00	150.00	149.00
155	11.4627	180.00	139.00	144.00	154.33

156	11.5934	182.00	163.00	145.00	163.33
157	11.7255	184.00	183.00	144.00	170.33
158	11.8592	174.00	174.00	160.00	169.33
159	11.9945	193.00	188.00	125.00	168.67
160	12.1312	179.00	180.00	164.00	174.33
161	12.2695	189.00	185.00	180.00	184.67
162	12.4094	195.00	188.00	205.00	196.00
163	12.5509	171.00	200.00	174.00	181.67
164	12.694	203.00	213.00	194.00	203.33
165	12.8388	182.00	214.00	221.00	205.67
166	12.9851	235.00	219.00	185.00	213.00
167	13.1332	208.00	208.00	203.00	206.33
168	13.2829	262.00	245.00	204.00	237.00
169	13.4344	234.00	238.00	216.00	229.33
170	13.5876	251.00	228.00	257.00	245.33
171	13.7425	261.00	259.00	234.00	251.33
172	13.8992	237.00	238.00	215.00	230.00
173	14.0577	222.00	255.00	202.00	226.33
174	14.2179	208.00	241.00	216.00	221.67
175	14.38	247.00	265.00	214.00	242.00
176	14.544	232.00	220.00	222.00	224.67
177	14.7098	252.00	223.00	249.00	241.33
178	14.8776	225.00	243.00	216.00	228.00
179	15.0472	262.00	243.00	231.00	245.33
180	15.2188	275.00	227.00	221.00	241.00
181	15.3923	226.00	206.00	230.00	220.67
182	15.5678	216.00	203.00	235.00	218.00
183	15.7453	199.00	263.00	224.00	228.67
184	15.9248	208.00	213.00	244.00	221.67
185	16.1064	229.00	223.00	229.00	227.00
186	16.29	204.00	181.00	214.00	199.67
187	16.4757	211.00	207.00	224.00	214.00
188	16.6636	195.00	168.00	191.00	184.67
189	16.8536	186.00	193.00	207.00	195.33
190	17.0458	162.00	167.00	219.00	182.67
191	17.2401	161.00	150.00	222.00	177.67
192	17.4367	164.00	162.00	163.00	163.00
193	17.6355	159.00	151.00	178.00	162.67
194	17.8366	147.00	162.00	171.00	160.00
195	18.0399	134.00	149.00	143.00	142.00
196	18.2456	123.00	123.00	169.00	138.33
197	18.4537	127.00	141.00	136.00	134.67
198	18.6641	108.00	127.00	110.00	115.00
199	18.8769	104.00	110.00	110.00	108.00
200	19.0921	94.00	115.00	115.00	108.00
201	19.3098	75.00	89.00	90.00	84.67
202	19.53	74.00	72.00	86.00	77.33
203	19.7526	71.00	92.00	95.00	86.00
204	19.9778	57.00	70.00	69.00	65.33
205	20.2056	61.00	66.00	73.00	66.67

206	20.436	44.00	50.00	53.00	49.00
207	20.669	34.00	47.00	44.00	41.67
208	20.9047	31.00	39.00	37.00	35.67
209	21.143	28.00	38.00	28.00	31.33
210	21.3841	25.00	33.00	37.00	31.67
211	21.6279	20.00	16.00	29.00	21.67
212	21.8745	17.00	19.00	19.00	18.33
213	22.1239	12.00	13.00	18.00	14.33
214	22.3762	13.00	14.00	13.00	13.33
215	22.6313	21.00	15.00	13.00	16.33
216	22.8894	8.00	7.00	10.00	8.33
217	23.1503	10.00	9.00	11.00	10.00
218	23.4143	5.00	10.00	7.00	7.33
219	23.6813	8.00	4.00	9.00	7.00
220	23.9513	3.00	4.00	4.00	3.67
221	24.2244	3.00	3.00	8.00	4.67
222	24.5006	2.00	1.00	3.00	2.00
223	24.7799	5.00	3.00	6.00	4.67
224	25.0624	3.00	1.00	2.00	2.00
225	25.3482	3.00	1.00	2.00	2.00
226	25.6372	3.00	5.00	6.00	4.67
227	25.9295	2.00	1.00	2.00	1.67
228	26.2252	4.00	4.00	4.00	4.00
229	26.5242	0.00	1.00	1.00	0.67
230	26.8266	1.00	1.00	2.00	1.33
231	27.1325	3.00	2.00	3.00	2.67
232	27.4418	2.00	1.00	2.00	1.67
233	27.7547	0.00	0.00	1.00	0.33
234	28.0712	0.00	0.00	5.00	1.67
235	28.3913	1.00	2.00	1.00	1.33
236	28.715	3.00	2.00	1.00	2.00
237	29.0424	4.00	0.00	1.00	1.67
238	29.3735	4.00	0.00	2.00	2.00
239	29.7084	1.00	1.00	3.00	1.67
240	30.0471	1.00	0.00	2.00	1.00
241	30.3897	1.00	0.00	0.00	0.33
242	30.7362	3.00	0.00	4.00	2.33
243	31.0867	0.00	1.00	0.00	0.33
244	31.4411	1.00	4.00	2.00	2.33
245	31.7996	0.00	1.00	1.00	0.67
246	32.1622	1.00	0.00	0.00	0.33
247	32.5289	2.00	1.00	2.00	1.67
248	32.8998	0.00	0.00	0.00	0.00
249	33.2749	2.00	1.00	0.00	1.00
250	33.6543	0.00	2.00	1.00	1.00
251	34.038	0.00	0.00	1.00	0.33
252	34.4261	1.00	0.00	0.00	0.33
253	34.8186	0.00	0.00	0.00	0.00
254	35.2156	1.00	1.00	0.00	0.67
255	35.6172	0.00	0.00	0.00	0.00

256	36.0233	1.00	0.00	1.00	0.67
257	36.434	0.00	0.00	0.00	0.00
258	36.8494	0.00	0.00	0.00	0.00
259	37.2696	0.00	1.00	0.00	0.33
260	37.6945	0.00	0.00	0.00	0.00
261	38.1243	0.00	0.00	0.00	0.00
262	38.559	0.00	0.00	0.00	0.00
263	38.9986	0.00	0.00	0.00	0.00
264	39.4433	0.00	1.00	1.00	0.67
265	39.893	0.00	0.00	0.00	0.00
266	40.3479	0.00	1.00	0.00	0.33
267	40.8079	1.00	0.00	0.00	0.33
268	41.2732	1.00	0.00	0.00	0.33
269	41.7438	0.00	0.00	0.00	0.00
270	42.2197	0.00	0.00	0.00	0.00
271	42.7011	0.00	0.00	0.00	0.00
272	43.188	0.00	0.00	0.00	0.00
273	43.6804	0.00	0.00	0.00	0.00
274	44.1784	0.00	0.00	0.00	0.00
275	44.6822	0.00	0.00	0.00	0.00
276	45.1916	0.00	0.00	0.00	0.00
277	45.7069	0.00	1.00	0.00	0.33
278	46.228	0.00	0.00	0.00	0.00
279	46.7551	1.00	0.00	0.00	0.33
280	47.2882	0.00	1.00	0.00	0.33
281	47.8274	0.00	0.00	0.00	0.00
282	48.3727	0.00	0.00	0.00	0.00
283	48.9242	0.00	0.00	0.00	0.00
284	49.4821	0.00	0.00	0.00	0.00
285	50.0462	0.00	0.00	0.00	0.00
286	50.6169	0.00	0.00	0.00	0.00
287	51.194	0.00	0.00	0.00	0.00
288	51.7777	0.00	0.00	1.00	0.33
289	52.368	0.00	0.00	0.00	0.00
290	52.9651	0.00	0.00	0.00	0.00
291	53.569	0.00	0.00	0.00	0.00
292	54.1798	0.00	0.00	0.00	0.00
293	54.7976	0.00	0.00	0.00	0.00
294	55.4224	0.00	0.00	0.00	0.00
295	56.0543	0.00	0.00	0.00	0.00
296	56.6934	0.00	0.00	0.00	0.00
297	57.3398	0.00	0.00	0.00	0.00
298	57.9936	0.00	0.00	0.00	0.00
299	58.6548	0.00	0.00	0.00	0.00
300	59.3236	0.00	0.00	0.00	0.00
	60	16932.00	15962.00	15976.00	16290.00

Calculations were performed on the raw data from the Coulter Counter in order to determine the total number of particles per m^3 (N_T), total mass/volume of particles per m^3 (M_T), and the moments ($m_0 - m_4$). An example of the sample calculations can be found below.

The average number of particles per mL was calculated for every bin as follows:

$\bar{N}_{T,1} = \left(\frac{N_{1,1}+N_{2,1}+N_{3,1}}{3}\right) = \left(\frac{18+28+31}{3}\right) = 25.67$ particles per mL in bin number 1.

The total number of particles per m^3 of solution was calculated by taking into account the numerous dilutions that took place when measuring the PSD of the seed sample. The total number of particles per m^3 was calculated for every bin as follows:

$$N_{T,1} = \left[\frac{(Avg.no.of\ particles\ in\ bin\ number\ 1)\times(Volume\ of\ electrolyte\ in\ Coulter\ beaker)\times(Volume\ of\ saturated\ solution)}{(Control\ volume\ used\ in\ Coulter\ Counter)\times(Volume\ of\ seed\ sample\ added\ to\ Coulter\ beaker)}\right]$$

$N_{T,1} = \left[\frac{(25.67/mL)\times(150mL)\times(10mL)}{(1mL)\times(0.6mL)}\right] \times \frac{10^6 mL}{1m^3} = 6.42 \times 10^{10}$ particles per m^3 in bin number 1.

The above calculation was repeated for each bin number. The sum of the total number of particles in all the bins yielded the zeroth moment i.e. $m_0 = \sum_{i=1}^{300} N_{T,i} = 4.01 \times 10^{13}$ particles per m^3.

The total mass of particles per m^3 was calculated for every bin as follows:

$M_1 = (Total\ no.of\ particles\ in\ bin\ number\ 1) \times (bin\ diameter)^3 \times \frac{\pi}{6} \times \rho_{COM}$

$M_1 = (6.42 \times 10^{10}\ particles/m^3) \times (2 \times 10^{-6} m)^3 \times \frac{\pi}{6} \times 2200 kg.m^{-3} = 5.91 \times 10^{-4}$ kg.m^{-3} in bin no. 1.

The moments $(m_1 - m_4)$ were calculated as follows:

$m_j = \sum_{i=1}^{300}\left[(Lbar_i)^j \times N_{T,i}\right]$

Thus, $m_1 = [(2 \times 10^{-6})^1 \times 6.42 \times 10^{10} + \cdots + (300 \times 10^{-6})^1 \times 0] = 4.85 \times 10^8$ m per m^3

The mean sizes of the particles were calculated by the following equations:

$d_{1,0} = \frac{m_1}{m_0} = \frac{4.85\times10^8}{4.07\times10^{13}} \times \frac{10^6 \mu m}{m} = 11.9$ µm

$d_{4,3} = \frac{m_4}{m_3} = \frac{1.70\times10^{-6}}{1.04\times10^{-1}} \times \frac{10^6 \mu m}{m} = 16.4$ µm

Table 16: Sample calculations for seed experiment A1.2.1

Bin Diameter (Lower) (µm)	Number (#.m^{-3})	Mass (kg.m^{-3})	Lbar*N	Lbar^2*N	Lbar^3*N	Lbar^4*N
2	6.42E+10	5.91E-04	1.28E+05	2.57E-01	5.13E-07	1.03E-12
2.0228	4.50E+10	4.29E-04	9.10E+04	1.84E-01	3.72E-07	7.53E-13
2.04587	5.25E+10	5.18E-04	1.07E+05	2.20E-01	4.50E-07	9.20E-13
2.06919	5.92E+10	6.04E-04	1.22E+05	2.53E-01	5.24E-07	1.08E-12
2.09279	3.50E+10	3.70E-04	7.32E+04	1.53E-01	3.21E-07	6.71E-13
2.11665	5.00E+10	5.46E-04	1.06E+05	2.24E-01	4.74E-07	1.00E-12
2.14078	4.67E+10	5.27E-04	9.99E+04	2.14E-01	4.58E-07	9.80E-13
2.16519	4.08E+10	4.77E-04	8.84E+04	1.91E-01	4.14E-07	8.97E-13
2.18988	4.58E+10	5.54E-04	1.00E+05	2.20E-01	4.81E-07	1.05E-12
2.21485	6.83E+10	8.55E-04	1.51E+05	3.35E-01	7.42E-07	1.64E-12
2.2401	5.83E+10	7.55E-04	1.31E+05	2.93E-01	6.56E-07	1.47E-12
2.26564	6.00E+10	8.04E-04	1.36E+05	3.08E-01	6.98E-07	1.58E-12
2.29147	4.25E+10	5.89E-04	9.74E+04	2.23E-01	5.11E-07	1.17E-12
2.3176	5.50E+10	7.89E-04	1.27E+05	2.95E-01	6.85E-07	1.59E-12
2.34403	7.33E+10	1.09E-03	1.72E+05	4.03E-01	9.44E-07	2.21E-12
2.37075	4.67E+10	7.16E-04	1.11E+05	2.62E-01	6.22E-07	1.47E-12
2.39778	4.50E+10	7.15E-04	1.08E+05	2.59E-01	6.20E-07	1.49E-12

2.42512	6.75E+10	1.11E-03	1.64E+05	3.97E-01	9.63E-07	2.33E-12
2.45277	6.58E+10	1.12E-03	1.61E+05	3.96E-01	9.71E-07	2.38E-12
2.48074	5.50E+10	9.67E-04	1.36E+05	3.38E-01	8.40E-07	2.08E-12
2.50902	5.25E+10	9.55E-04	1.32E+05	3.30E-01	8.29E-07	2.08E-12
2.53763	6.25E+10	1.18E-03	1.59E+05	4.02E-01	1.02E-06	2.59E-12
2.56656	5.50E+10	1.07E-03	1.41E+05	3.62E-01	9.30E-07	2.39E-12
2.59583	6.50E+10	1.31E-03	1.69E+05	4.38E-01	1.14E-06	2.95E-12
2.62543	4.83E+10	1.01E-03	1.27E+05	3.33E-01	8.75E-07	2.30E-12
2.65536	5.50E+10	1.19E-03	1.46E+05	3.88E-01	1.03E-06	2.73E-12
2.68564	5.42E+10	1.21E-03	1.45E+05	3.91E-01	1.05E-06	2.82E-12
2.71626	6.92E+10	1.60E-03	1.88E+05	5.10E-01	1.39E-06	3.77E-12
2.74723	5.83E+10	1.39E-03	1.60E+05	4.40E-01	1.21E-06	3.32E-12
2.77855	5.08E+10	1.26E-03	1.41E+05	3.92E-01	1.09E-06	3.03E-12
2.81023	5.75E+10	1.47E-03	1.62E+05	4.54E-01	1.28E-06	3.59E-12
2.84227	6.25E+10	1.65E-03	1.78E+05	5.05E-01	1.44E-06	4.08E-12
2.87468	6.25E+10	1.71E-03	1.80E+05	5.16E-01	1.48E-06	4.27E-12
2.90746	5.75E+10	1.63E-03	1.67E+05	4.86E-01	1.41E-06	4.11E-12
2.94061	7.33E+10	2.15E-03	2.16E+05	6.34E-01	1.86E-06	5.48E-12
2.97414	5.50E+10	1.67E-03	1.64E+05	4.87E-01	1.45E-06	4.30E-12
3.00805	6.33E+10	1.99E-03	1.91E+05	5.73E-01	1.72E-06	5.19E-12
3.04234	6.17E+10	2.00E-03	1.88E+05	5.71E-01	1.74E-06	5.28E-12
3.07703	6.92E+10	2.32E-03	2.13E+05	6.55E-01	2.02E-06	6.20E-12
3.11212	7.50E+10	2.60E-03	2.33E+05	7.26E-01	2.26E-06	7.04E-12
3.1476	7.75E+10	2.78E-03	2.44E+05	7.68E-01	2.42E-06	7.61E-12
3.18349	6.58E+10	2.45E-03	2.10E+05	6.67E-01	2.12E-06	6.76E-12
3.21979	7.33E+10	2.82E-03	2.36E+05	7.60E-01	2.45E-06	7.88E-12
3.2565	6.08E+10	2.42E-03	1.98E+05	6.45E-01	2.10E-06	6.84E-12
3.29363	5.42E+10	2.23E-03	1.78E+05	5.88E-01	1.94E-06	6.37E-12
3.33118	7.58E+10	3.23E-03	2.53E+05	8.42E-01	2.80E-06	9.34E-12
3.36916	4.92E+10	2.17E-03	1.66E+05	5.58E-01	1.88E-06	6.34E-12
3.40758	8.50E+10	3.87E-03	2.90E+05	9.87E-01	3.36E-06	1.15E-11
3.44643	6.25E+10	2.95E-03	2.15E+05	7.42E-01	2.56E-06	8.82E-12
3.48573	6.67E+10	3.25E-03	2.32E+05	8.10E-01	2.82E-06	9.84E-12
3.52547	7.58E+10	3.83E-03	2.67E+05	9.43E-01	3.32E-06	1.17E-11
3.56567	6.17E+10	3.22E-03	2.20E+05	7.84E-01	2.80E-06	9.97E-12
3.60632	8.75E+10	4.73E-03	3.16E+05	1.14E+00	4.10E-06	1.48E-11
3.64744	8.00E+10	4.47E-03	2.92E+05	1.06E+00	3.88E-06	1.42E-11
3.68903	7.17E+10	4.14E-03	2.64E+05	9.75E-01	3.60E-06	1.33E-11
3.73109	6.50E+10	3.89E-03	2.43E+05	9.05E-01	3.38E-06	1.26E-11
3.77363	6.08E+10	3.77E-03	2.30E+05	8.66E-01	3.27E-06	1.23E-11
3.81666	9.17E+10	5.87E-03	3.50E+05	1.34E+00	5.10E-06	1.95E-11
3.86017	8.50E+10	5.63E-03	3.28E+05	1.27E+00	4.89E-06	1.89E-11
3.90419	7.92E+10	5.43E-03	3.09E+05	1.21E+00	4.71E-06	1.84E-11
3.9487	8.17E+10	5.79E-03	3.22E+05	1.27E+00	5.03E-06	1.99E-11
3.99372	6.08E+10	4.46E-03	2.43E+05	9.70E-01	3.88E-06	1.55E-11
4.03926	7.33E+10	5.57E-03	2.96E+05	1.20E+00	4.83E-06	1.95E-11
4.08531	7.50E+10	5.89E-03	3.06E+05	1.25E+00	5.11E-06	2.09E-11
4.13189	7.08E+10	5.76E-03	2.93E+05	1.21E+00	5.00E-06	2.06E-11
4.17901	7.00E+10	5.88E-03	2.93E+05	1.22E+00	5.11E-06	2.13E-11
4.22665	6.50E+10	5.65E-03	2.75E+05	1.16E+00	4.91E-06	2.07E-11

4.27485	9.00E+10	8.10E-03	3.85E+05	1.64E+00	7.03E-06	3.01E-11
4.32359	8.67E+10	8.07E-03	3.75E+05	1.62E+00	7.00E-06	3.03E-11
4.37288	7.75E+10	7.46E-03	3.39E+05	1.48E+00	6.48E-06	2.83E-11
4.42274	7.50E+10	7.47E-03	3.32E+05	1.47E+00	6.49E-06	2.87E-11
4.47317	8.25E+10	8.51E-03	3.69E+05	1.65E+00	7.38E-06	3.30E-11
4.52417	7.75E+10	8.27E-03	3.51E+05	1.59E+00	7.18E-06	3.25E-11
4.57576	8.67E+10	9.56E-03	3.97E+05	1.81E+00	8.30E-06	3.80E-11
4.62793	9.17E+10	1.05E-02	4.24E+05	1.96E+00	9.09E-06	4.20E-11
4.68069	8.25E+10	9.75E-03	3.86E+05	1.81E+00	8.46E-06	3.96E-11
4.73406	9.42E+10	1.15E-02	4.46E+05	2.11E+00	9.99E-06	4.73E-11
4.78804	8.42E+10	1.06E-02	4.03E+05	1.93E+00	9.24E-06	4.42E-11
4.84263	7.75E+10	1.01E-02	3.75E+05	1.82E+00	8.80E-06	4.26E-11
4.89785	8.33E+10	1.13E-02	4.08E+05	2.00E+00	9.79E-06	4.80E-11
4.95369	8.42E+10	1.18E-02	4.17E+05	2.07E+00	1.02E-05	5.07E-11
5.01017	7.75E+10	1.12E-02	3.88E+05	1.95E+00	9.75E-06	4.88E-11
5.0673	6.25E+10	9.37E-03	3.17E+05	1.60E+00	8.13E-06	4.12E-11
5.12507	9.92E+10	1.54E-02	5.08E+05	2.60E+00	1.33E-05	6.84E-11
5.18351	8.58E+10	1.38E-02	4.45E+05	2.31E+00	1.20E-05	6.20E-11
5.24261	7.50E+10	1.24E-02	3.93E+05	2.06E+00	1.08E-05	5.67E-11
5.30239	9.00E+10	1.55E-02	4.77E+05	2.53E+00	1.34E-05	7.11E-11
5.36284	8.67E+10	1.54E-02	4.65E+05	2.49E+00	1.34E-05	7.17E-11
5.42399	7.25E+10	1.33E-02	3.93E+05	2.13E+00	1.16E-05	6.27E-11
5.48583	7.67E+10	1.46E-02	4.21E+05	2.31E+00	1.27E-05	6.94E-11
5.54838	7.83E+10	1.54E-02	4.35E+05	2.41E+00	1.34E-05	7.42E-11
5.61164	8.25E+10	1.68E-02	4.63E+05	2.60E+00	1.46E-05	8.18E-11
5.67563	9.08E+10	1.91E-02	5.16E+05	2.93E+00	1.66E-05	9.43E-11
5.74034	9.42E+10	2.05E-02	5.41E+05	3.10E+00	1.78E-05	1.02E-10
5.80579	1.01E+11	2.27E-02	5.85E+05	3.40E+00	1.97E-05	1.15E-10
5.87199	8.08E+10	1.89E-02	4.75E+05	2.79E+00	1.64E-05	9.61E-11
5.93894	8.92E+10	2.15E-02	5.30E+05	3.14E+00	1.87E-05	1.11E-10
6.00665	8.67E+10	2.16E-02	5.21E+05	3.13E+00	1.88E-05	1.13E-10
6.07514	8.17E+10	2.11E-02	4.96E+05	3.01E+00	1.83E-05	1.11E-10
6.14441	8.92E+10	2.38E-02	5.48E+05	3.37E+00	2.07E-05	1.27E-10
6.21447	7.67E+10	2.12E-02	4.76E+05	2.96E+00	1.84E-05	1.14E-10
6.28532	7.83E+10	2.24E-02	4.92E+05	3.09E+00	1.95E-05	1.22E-10
6.35699	9.83E+10	2.91E-02	6.25E+05	3.97E+00	2.53E-05	1.61E-10
6.42947	6.92E+10	2.12E-02	4.45E+05	2.86E+00	1.84E-05	1.18E-10
6.50277	1.17E+11	3.70E-02	7.59E+05	4.93E+00	3.21E-05	2.09E-10
6.57692	1.08E+11	3.55E-02	7.12E+05	4.69E+00	3.08E-05	2.03E-10
6.65191	9.75E+10	3.31E-02	6.49E+05	4.31E+00	2.87E-05	1.91E-10
6.72775	1.14E+11	4.00E-02	7.68E+05	5.17E+00	3.48E-05	2.34E-10
6.80446	9.33E+10	3.39E-02	6.35E+05	4.32E+00	2.94E-05	2.00E-10
6.88204	9.75E+10	3.66E-02	6.71E+05	4.62E+00	3.18E-05	2.19E-10
6.96051	1.05E+11	4.08E-02	7.31E+05	5.09E+00	3.54E-05	2.46E-10
7.03987	9.42E+10	3.78E-02	6.63E+05	4.67E+00	3.29E-05	2.31E-10
7.12014	9.75E+10	4.05E-02	6.94E+05	4.94E+00	3.52E-05	2.51E-10
7.20132	8.50E+10	3.66E-02	6.12E+05	4.41E+00	3.17E-05	2.29E-10
7.28343	1.11E+11	4.93E-02	8.07E+05	5.88E+00	4.28E-05	3.12E-10
7.36648	1.13E+11	5.18E-02	8.29E+05	6.10E+00	4.50E-05	3.31E-10
7.45047	1.28E+11	6.11E-02	9.56E+05	7.12E+00	5.31E-05	3.95E-10

7.53542	1.25E+11	6.16E-02	9.42E+05	7.10E+00	5.35E-05	4.03E-10
7.62133	1.08E+11	5.52E-02	8.26E+05	6.29E+00	4.80E-05	3.65E-10
7.70823	1.20E+11	6.33E-02	9.25E+05	7.13E+00	5.50E-05	4.24E-10
7.79612	1.21E+11	6.60E-02	9.42E+05	7.34E+00	5.73E-05	4.46E-10
7.88501	1.08E+11	6.12E-02	8.54E+05	6.74E+00	5.31E-05	4.19E-10
7.97491	1.29E+11	7.55E-02	1.03E+06	8.21E+00	6.55E-05	5.22E-10
8.06584	1.38E+11	8.31E-02	1.11E+06	8.95E+00	7.22E-05	5.82E-10
8.15781	1.49E+11	9.33E-02	1.22E+06	9.93E+00	8.10E-05	6.61E-10
8.25082	1.38E+11	8.90E-02	1.13E+06	9.36E+00	7.72E-05	6.37E-10
8.3449	1.55E+11	1.04E-01	1.29E+06	1.08E+01	9.01E-05	7.52E-10
8.44004	1.57E+11	1.09E-01	1.32E+06	1.12E+01	9.42E-05	7.95E-10
8.53627	1.61E+11	1.15E-01	1.37E+06	1.17E+01	1.00E-04	8.54E-10
8.6336	1.47E+11	1.09E-01	1.27E+06	1.09E+01	9.44E-05	8.15E-10
8.73204	1.71E+11	1.31E-01	1.49E+06	1.30E+01	1.14E-04	9.93E-10
8.8316	1.94E+11	1.54E-01	1.71E+06	1.51E+01	1.34E-04	1.18E-09
8.9323	1.67E+11	1.37E-01	1.49E+06	1.33E+01	1.19E-04	1.06E-09
9.03415	1.73E+11	1.47E-01	1.56E+06	1.41E+01	1.27E-04	1.15E-09
9.13715	2.13E+11	1.87E-01	1.95E+06	1.78E+01	1.63E-04	1.49E-09
9.24133	2.03E+11	1.85E-01	1.88E+06	1.74E+01	1.60E-04	1.48E-09
9.3467	1.91E+11	1.79E-01	1.78E+06	1.67E+01	1.56E-04	1.46E-09
9.45327	1.82E+11	1.77E-01	1.72E+06	1.62E+01	1.53E-04	1.45E-09
9.56105	2.14E+11	2.16E-01	2.05E+06	1.96E+01	1.87E-04	1.79E-09
9.67007	2.23E+11	2.32E-01	2.15E+06	2.08E+01	2.01E-04	1.95E-09
9.78032	2.45E+11	2.64E-01	2.40E+06	2.34E+01	2.29E-04	2.24E-09
9.89184	2.16E+11	2.41E-01	2.13E+06	2.11E+01	2.09E-04	2.07E-09
10.0046	2.38E+11	2.75E-01	2.38E+06	2.39E+01	2.39E-04	2.39E-09
10.1187	2.51E+11	2.99E-01	2.54E+06	2.57E+01	2.60E-04	2.63E-09
10.2341	2.51E+11	3.10E-01	2.57E+06	2.63E+01	2.69E-04	2.75E-09
10.3508	2.76E+11	3.52E-01	2.86E+06	2.96E+01	3.06E-04	3.17E-09
10.4688	3.41E+11	4.50E-01	3.57E+06	3.74E+01	3.91E-04	4.09E-09
10.5881	2.85E+11	3.90E-01	3.02E+06	3.20E+01	3.38E-04	3.58E-09
10.7089	3.01E+11	4.26E-01	3.22E+06	3.45E+01	3.69E-04	3.96E-09
10.831	3.22E+11	4.71E-01	3.48E+06	3.77E+01	4.09E-04	4.43E-09
10.9545	3.32E+11	5.02E-01	3.63E+06	3.98E+01	4.36E-04	4.78E-09
11.0794	3.38E+11	5.29E-01	3.74E+06	4.14E+01	4.59E-04	5.09E-09
11.2057	3.44E+11	5.58E-01	3.86E+06	4.32E+01	4.84E-04	5.43E-09
11.3334	3.73E+11	6.25E-01	4.22E+06	4.78E+01	5.42E-04	6.15E-09
11.4627	3.86E+11	6.69E-01	4.42E+06	5.07E+01	5.81E-04	6.66E-09
11.5934	4.08E+11	7.33E-01	4.73E+06	5.49E+01	6.36E-04	7.38E-09
11.7255	4.26E+11	7.91E-01	4.99E+06	5.85E+01	6.86E-04	8.05E-09
11.8592	4.23E+11	8.13E-01	5.02E+06	5.95E+01	7.06E-04	8.37E-09
11.9945	4.22E+11	8.38E-01	5.06E+06	6.07E+01	7.28E-04	8.73E-09
12.1312	4.36E+11	8.96E-01	5.29E+06	6.41E+01	7.78E-04	9.44E-09
12.2695	4.62E+11	9.82E-01	5.66E+06	6.95E+01	8.53E-04	1.05E-08
12.4094	4.90E+11	1.08E+00	6.08E+06	7.55E+01	9.36E-04	1.16E-08
12.5509	4.54E+11	1.03E+00	5.70E+06	7.15E+01	8.98E-04	1.13E-08
12.694	5.08E+11	1.20E+00	6.45E+06	8.19E+01	1.04E-03	1.32E-08
12.8388	5.14E+11	1.25E+00	6.60E+06	8.48E+01	1.09E-03	1.40E-08
12.9851	5.33E+11	1.34E+00	6.91E+06	8.98E+01	1.17E-03	1.51E-08
13.1332	5.16E+11	1.35E+00	6.77E+06	8.90E+01	1.17E-03	1.53E-08

13.2829	5.93E+11	1.60E+00	7.87E+06	1.05E+02	1.39E-03	1.84E-08
13.4344	5.73E+11	1.60E+00	7.70E+06	1.03E+02	1.39E-03	1.87E-08
13.5876	6.13E+11	1.77E+00	8.33E+06	1.13E+02	1.54E-03	2.09E-08
13.7425	6.28E+11	1.88E+00	8.63E+06	1.19E+02	1.63E-03	2.24E-08
13.8992	5.75E+11	1.78E+00	7.99E+06	1.11E+02	1.54E-03	2.15E-08
14.0577	5.66E+11	1.81E+00	7.95E+06	1.12E+02	1.57E-03	2.21E-08
14.2179	5.54E+11	1.83E+00	7.88E+06	1.12E+02	1.59E-03	2.26E-08
14.38	6.05E+11	2.07E+00	8.70E+06	1.25E+02	1.80E-03	2.59E-08
14.544	5.62E+11	1.99E+00	8.17E+06	1.19E+02	1.73E-03	2.51E-08
14.7098	6.03E+11	2.21E+00	8.87E+06	1.31E+02	1.92E-03	2.82E-08
14.8776	5.70E+11	2.16E+00	8.48E+06	1.26E+02	1.88E-03	2.79E-08
15.0472	6.13E+11	2.41E+00	9.23E+06	1.39E+02	2.09E-03	3.14E-08
15.2188	6.03E+11	2.45E+00	9.17E+06	1.40E+02	2.12E-03	3.23E-08
15.3923	5.52E+11	2.32E+00	8.49E+06	1.31E+02	2.01E-03	3.10E-08
15.5678	5.45E+11	2.37E+00	8.48E+06	1.32E+02	2.06E-03	3.20E-08
15.7453	5.72E+11	2.57E+00	9.00E+06	1.42E+02	2.23E-03	3.51E-08
15.9248	5.54E+11	2.58E+00	8.82E+06	1.41E+02	2.24E-03	3.56E-08
16.1064	5.68E+11	2.73E+00	9.14E+06	1.47E+02	2.37E-03	3.82E-08
16.29	4.99E+11	2.49E+00	8.13E+06	1.32E+02	2.16E-03	3.52E-08
16.4757	5.35E+11	2.76E+00	8.81E+06	1.45E+02	2.39E-03	3.94E-08
16.6636	4.62E+11	2.46E+00	7.69E+06	1.28E+02	2.14E-03	3.56E-08
16.8536	4.88E+11	2.69E+00	8.23E+06	1.39E+02	2.34E-03	3.94E-08
17.0458	4.57E+11	2.61E+00	7.78E+06	1.33E+02	2.26E-03	3.86E-08
17.2401	4.44E+11	2.62E+00	7.66E+06	1.32E+02	2.28E-03	3.92E-08
17.4367	4.08E+11	2.49E+00	7.11E+06	1.24E+02	2.16E-03	3.77E-08
17.6355	4.07E+11	2.57E+00	7.17E+06	1.26E+02	2.23E-03	3.93E-08
17.8366	4.00E+11	2.61E+00	7.13E+06	1.27E+02	2.27E-03	4.05E-08
18.0399	3.55E+11	2.40E+00	6.40E+06	1.16E+02	2.08E-03	3.76E-08
18.2456	3.46E+11	2.42E+00	6.31E+06	1.15E+02	2.10E-03	3.83E-08
18.4537	3.37E+11	2.44E+00	6.21E+06	1.15E+02	2.12E-03	3.90E-08
18.6641	2.88E+11	2.15E+00	5.37E+06	1.00E+02	1.87E-03	3.49E-08
18.8769	2.70E+11	2.09E+00	5.10E+06	9.62E+01	1.82E-03	3.43E-08
19.0921	2.70E+11	2.16E+00	5.15E+06	9.84E+01	1.88E-03	3.59E-08
19.3098	2.12E+11	1.76E+00	4.09E+06	7.89E+01	1.52E-03	2.94E-08
19.53	1.93E+11	1.66E+00	3.78E+06	7.37E+01	1.44E-03	2.81E-08
19.7526	2.15E+11	1.91E+00	4.25E+06	8.39E+01	1.66E-03	3.27E-08
19.9778	1.63E+11	1.50E+00	3.26E+06	6.52E+01	1.30E-03	2.60E-08
20.2056	1.67E+11	1.58E+00	3.37E+06	6.80E+01	1.37E-03	2.78E-08
20.436	1.23E+11	1.20E+00	2.50E+06	5.12E+01	1.05E-03	2.14E-08
20.669	1.04E+11	1.06E+00	2.15E+06	4.45E+01	9.20E-04	1.90E-08
20.9047	8.92E+10	9.38E-01	1.86E+06	3.90E+01	8.15E-04	1.70E-08
21.143	7.83E+10	8.53E-01	1.66E+06	3.50E+01	7.40E-04	1.57E-08
21.3841	7.92E+10	8.92E-01	1.69E+06	3.62E+01	7.74E-04	1.66E-08
21.6279	5.42E+10	6.31E-01	1.17E+06	2.53E+01	5.48E-04	1.19E-08
21.8745	4.58E+10	5.53E-01	1.00E+06	2.19E+01	4.80E-04	1.05E-08
22.1239	3.58E+10	4.47E-01	7.93E+05	1.75E+01	3.88E-04	8.58E-09
22.3762	3.33E+10	4.30E-01	7.46E+05	1.67E+01	3.73E-04	8.36E-09
22.6313	4.08E+10	5.45E-01	9.24E+05	2.09E+01	4.73E-04	1.07E-08
22.8894	2.08E+10	2.88E-01	4.77E+05	1.09E+01	2.50E-04	5.72E-09
23.1503	2.50E+10	3.57E-01	5.79E+05	1.34E+01	3.10E-04	7.18E-09

23.4143	1.83E+10	2.71E-01	4.29E+05	1.01E+01	2.35E-04	5.51E-09
23.6813	1.75E+10	2.68E-01	4.14E+05	9.81E+00	2.32E-04	5.50E-09
23.9513	9.17E+09	1.45E-01	2.20E+05	5.26E+00	1.26E-04	3.02E-09
24.2244	1.17E+10	1.91E-01	2.83E+05	6.85E+00	1.66E-04	4.02E-09
24.5006	5.00E+09	8.47E-02	1.23E+05	3.00E+00	7.35E-05	1.80E-09
24.7799	1.17E+10	2.04E-01	2.89E+05	7.16E+00	1.78E-04	4.40E-09
25.0624	5.00E+09	9.07E-02	1.25E+05	3.14E+00	7.87E-05	1.97E-09
25.3482	5.00E+09	9.38E-02	1.27E+05	3.21E+00	8.14E-05	2.06E-09
25.6372	1.17E+10	2.26E-01	2.99E+05	7.67E+00	1.97E-04	5.04E-09
25.9295	4.17E+09	8.37E-02	1.08E+05	2.80E+00	7.26E-05	1.88E-09
26.2252	1.00E+10	2.08E-01	2.62E+05	6.88E+00	1.80E-04	4.73E-09
26.5242	1.67E+09	3.58E-02	4.42E+04	1.17E+00	3.11E-05	8.25E-10
26.8266	3.33E+09	7.41E-02	8.94E+04	2.40E+00	6.44E-05	1.73E-09
27.1325	6.67E+09	1.53E-01	1.81E+05	4.91E+00	1.33E-04	3.61E-09
27.4418	4.17E+09	9.92E-02	1.14E+05	3.14E+00	8.61E-05	2.36E-09
27.7547	8.33E+08	2.05E-02	2.31E+04	6.42E-01	1.78E-05	4.94E-10
28.0712	4.17E+09	1.06E-01	1.17E+05	3.28E+00	9.22E-05	2.59E-09
28.3913	3.33E+09	8.79E-02	9.46E+04	2.69E+00	7.63E-05	2.17E-09
28.715	5.00E+09	1.36E-01	1.44E+05	4.12E+00	1.18E-04	3.40E-09
29.0424	4.17E+09	1.18E-01	1.21E+05	3.51E+00	1.02E-04	2.96E-09
29.3735	5.00E+09	1.46E-01	1.47E+05	4.31E+00	1.27E-04	3.72E-09
29.7084	4.17E+09	1.26E-01	1.24E+05	3.68E+00	1.09E-04	3.25E-09
30.0471	2.50E+09	7.81E-02	7.51E+04	2.26E+00	6.78E-05	2.04E-09
30.3897	8.33E+08	2.69E-02	2.53E+04	7.70E-01	2.34E-05	7.11E-10
30.7362	5.83E+09	1.95E-01	1.79E+05	5.51E+00	1.69E-04	5.21E-09
31.0867	8.33E+08	2.88E-02	2.59E+04	8.05E-01	2.50E-05	7.78E-10
31.4411	5.83E+09	2.09E-01	1.83E+05	5.77E+00	1.81E-04	5.70E-09
31.7996	1.67E+09	6.17E-02	5.30E+04	1.69E+00	5.36E-05	1.70E-09
32.1622	8.33E+08	3.19E-02	2.68E+04	8.62E-01	2.77E-05	8.92E-10
32.5289	4.17E+09	1.65E-01	1.36E+05	4.41E+00	1.43E-04	4.67E-09
32.8998	0.00E+00	0.00E+00	0.00E+00	0.00E+00	0.00E+00	0.00E+00
33.2749	2.50E+09	1.06E-01	8.32E+04	2.77E+00	9.21E-05	3.06E-09
33.6543	2.50E+09	1.10E-01	8.41E+04	2.83E+00	9.53E-05	3.21E-09
34.038	8.33E+08	3.79E-02	2.84E+04	9.65E-01	3.29E-05	1.12E-09
34.4261	8.33E+08	3.92E-02	2.87E+04	9.88E-01	3.40E-05	1.17E-09
34.8186	0.00E+00	0.00E+00	0.00E+00	0.00E+00	0.00E+00	0.00E+00
35.2156	1.67E+09	8.38E-02	5.87E+04	2.07E+00	7.28E-05	2.56E-09
35.6172	0.00E+00	0.00E+00	0.00E+00	0.00E+00	0.00E+00	0.00E+00
36.0233	1.67E+09	8.97E-02	6.00E+04	2.16E+00	7.79E-05	2.81E-09
36.434	0.00E+00	0.00E+00	0.00E+00	0.00E+00	0.00E+00	0.00E+00
36.8494	0.00E+00	0.00E+00	0.00E+00	0.00E+00	0.00E+00	0.00E+00
37.2696	8.33E+08	4.97E-02	3.11E+04	1.16E+00	4.31E-05	1.61E-09
37.6945	0.00E+00	0.00E+00	0.00E+00	0.00E+00	0.00E+00	0.00E+00
38.1243	0.00E+00	0.00E+00	0.00E+00	0.00E+00	0.00E+00	0.00E+00
38.559	0.00E+00	0.00E+00	0.00E+00	0.00E+00	0.00E+00	0.00E+00
38.9986	0.00E+00	0.00E+00	0.00E+00	0.00E+00	0.00E+00	0.00E+00
39.4433	1.67E+09	1.18E-01	6.57E+04	2.59E+00	1.02E-04	4.03E-09
39.893	0.00E+00	0.00E+00	0.00E+00	0.00E+00	0.00E+00	0.00E+00
40.3479	8.33E+08	6.31E-02	3.36E+04	1.36E+00	5.47E-05	2.21E-09
40.8079	8.33E+08	6.52E-02	3.40E+04	1.39E+00	5.66E-05	2.31E-09

41.2732	8.33E+08	6.75E-02	3.44E+04	1.42E+00	5.86E-05	2.42E-09
41.7438	0.00E+00	0.00E+00	0.00E+00	0.00E+00	0.00E+00	0.00E+00
42.2197	0.00E+00	0.00E+00	0.00E+00	0.00E+00	0.00E+00	0.00E+00
42.7011	0.00E+00	0.00E+00	0.00E+00	0.00E+00	0.00E+00	0.00E+00
43.188	0.00E+00	0.00E+00	0.00E+00	0.00E+00	0.00E+00	0.00E+00
43.6804	0.00E+00	0.00E+00	0.00E+00	0.00E+00	0.00E+00	0.00E+00
44.1784	0.00E+00	0.00E+00	0.00E+00	0.00E+00	0.00E+00	0.00E+00
44.6822	0.00E+00	0.00E+00	0.00E+00	0.00E+00	0.00E+00	0.00E+00
45.1916	0.00E+00	0.00E+00	0.00E+00	0.00E+00	0.00E+00	0.00E+00
45.7069	8.33E+08	9.17E-02	3.81E+04	1.74E+00	7.96E-05	3.64E-09
46.228	0.00E+00	0.00E+00	0.00E+00	0.00E+00	0.00E+00	0.00E+00
46.7551	8.33E+08	9.81E-02	3.90E+04	1.82E+00	8.52E-05	3.98E-09
47.2882	8.33E+08	1.02E-01	3.94E+04	1.86E+00	8.81E-05	4.17E-09
47.8274	0.00E+00	0.00E+00	0.00E+00	0.00E+00	0.00E+00	0.00E+00
48.3727	0.00E+00	0.00E+00	0.00E+00	0.00E+00	0.00E+00	0.00E+00
48.9242	0.00E+00	0.00E+00	0.00E+00	0.00E+00	0.00E+00	0.00E+00
49.4821	0.00E+00	0.00E+00	0.00E+00	0.00E+00	0.00E+00	0.00E+00
50.0462	0.00E+00	0.00E+00	0.00E+00	0.00E+00	0.00E+00	0.00E+00
50.6169	0.00E+00	0.00E+00	0.00E+00	0.00E+00	0.00E+00	0.00E+00
51.194	0.00E+00	0.00E+00	0.00E+00	0.00E+00	0.00E+00	0.00E+00
51.7777	8.33E+08	1.33E-01	4.31E+04	2.23E+00	1.16E-04	5.99E-09
52.368	0.00E+00	0.00E+00	0.00E+00	0.00E+00	0.00E+00	0.00E+00
52.9651	0.00E+00	0.00E+00	0.00E+00	0.00E+00	0.00E+00	0.00E+00
53.569	0.00E+00	0.00E+00	0.00E+00	0.00E+00	0.00E+00	0.00E+00
54.1798	0.00E+00	0.00E+00	0.00E+00	0.00E+00	0.00E+00	0.00E+00
54.7976	0.00E+00	0.00E+00	0.00E+00	0.00E+00	0.00E+00	0.00E+00
55.4224	0.00E+00	0.00E+00	0.00E+00	0.00E+00	0.00E+00	0.00E+00
56.0543	0.00E+00	0.00E+00	0.00E+00	0.00E+00	0.00E+00	0.00E+00
56.6934	0.00E+00	0.00E+00	0.00E+00	0.00E+00	0.00E+00	0.00E+00
57.3398	0.00E+00	0.00E+00	0.00E+00	0.00E+00	0.00E+00	0.00E+00
57.9936	0.00E+00	0.00E+00	0.00E+00	0.00E+00	0.00E+00	0.00E+00
58.6548	0.00E+00	0.00E+00	0.00E+00	0.00E+00	0.00E+00	0.00E+00
59.3236	0.00E+00	0.00E+00	0.00E+00	0.00E+00	0.00E+00	0.00E+00
60	4.07E+13	1.19E+02	4.85E+08	6.77E+03	1.04E-01	1.70E-06
	m_0		m_1	m_2	m_3	m_4

C.2 Chapter 4

The PSD data obtained from the Coulter Counter for all of the kinetic experiments is excessive and thus only one set of example data has been included in the Appendix.

The average number of particles, total number of particles per m^3, total mass/volume of particles per m^3, moments ($m_0 - m_4$) and mean particle sizes were all calculated using the same equations as shown in Section C.1 of the Appendix. The dilution factors were however different for all of the experiments.

Table 17: Raw data from kinetic experiments with S_i =3.3, C_{seeds} = 0.03g.dm^{-3} & A3.2.1

Bin Diameter	Average Diff. Number (#/2mL)							
(Lower) (µm)	t = 0	t = 5	t = 10	t = 15	t = 20	t = 30	t = 45	t = 60
2	386.33	22.67	6.33	5.67	3.67	1.67	2.67	0.00
2.0228	388.67	20.33	8.67	7.00	9.67	3.33	4.67	2.00
2.04587	403.33	28.00	16.67	9.33	11.33	5.00	4.67	1.67
2.06919	407.67	22.67	17.67	7.00	7.33	6.00	0.67	2.00
2.09279	394.00	34.00	18.00	16.33	9.33	9.33	8.67	7.00
2.11665	379.67	25.00	14.33	9.67	9.67	5.67	1.67	0.67
2.14078	417.33	32.67	18.67	10.67	10.00	4.67	4.33	3.33
2.16519	406.67	28.67	20.33	11.33	8.33	2.00	4.33	2.00
2.18988	449.00	27.00	13.00	12.00	12.67	6.00	1.00	0.00
2.21485	428.00	42.00	26.00	10.00	11.33	7.00	5.00	4.33
2.2401	457.33	29.33	18.33	14.00	14.67	6.00	6.33	2.00
2.26564	446.33	29.00	21.00	12.00	10.33	7.33	5.00	0.00
2.29147	459.33	33.67	20.67	14.67	13.33	4.33	2.00	0.67
2.3176	461.33	33.00	16.67	14.00	10.00	9.33	2.00	3.33
2.34403	482.33	41.00	27.00	20.33	10.33	0.67	2.00	1.33
2.37075	485.33	40.67	12.67	15.00	12.33	6.67	3.00	0.67
2.39778	498.67	41.33	26.67	23.33	18.00	13.33	9.00	11.00
2.42512	479.33	34.67	20.67	16.33	9.67	11.33	5.67	2.33
2.45277	519.33	42.33	23.33	12.33	13.33	10.33	3.67	8.00
2.48074	483.00	37.33	19.67	18.00	12.67	8.67	3.67	0.33
2.50902	512.00	42.33	25.67	18.67	16.00	8.33	10.67	7.00
2.53763	517.33	40.67	27.67	21.00	12.33	10.33	5.00	2.33
2.56656	522.33	35.00	19.00	12.00	8.33	3.33	1.33	0.00
2.59583	540.00	46.67	25.67	17.67	16.67	12.00	8.33	3.67
2.62543	544.67	36.00	22.67	13.67	10.33	5.00	0.00	0.00
2.65536	553.33	33.67	27.00	19.33	12.33	5.33	5.67	2.00
2.68564	552.00	48.00	36.67	22.00	12.67	11.67	6.00	4.67
2.71626	544.67	32.33	20.00	11.33	10.67	4.00	4.33	0.33
2.74723	575.00	48.33	34.67	18.00	21.33	13.67	8.67	3.00
2.77855	581.00	53.33	24.67	16.67	15.00	9.00	5.33	5.00
2.81023	550.67	46.00	28.00	22.33	20.33	9.00	10.00	5.33
2.84227	602.67	56.67	33.67	19.33	17.67	11.33	7.33	5.67
2.87468	590.67	43.00	22.67	20.67	13.00	11.00	9.33	3.67
2.90746	556.33	45.33	35.67	24.67	15.67	12.00	7.33	9.33
2.94061	588.67	46.67	30.33	18.00	18.67	9.67	4.00	4.33

2.97414	625.33	54.00	37.67	23.67	16.67	8.00	6.00	6.67
3.00805	627.33	41.67	36.00	25.67	17.67	9.67	4.00	2.00
3.04234	635.00	48.67	29.67	18.33	18.67	11.00	0.00	2.00
3.07703	639.33	57.00	28.67	25.67	24.67	17.67	9.67	9.00
3.11212	629.33	60.33	35.00	23.00	24.33	18.67	6.33	5.33
3.1476	628.67	59.67	36.00	22.33	17.33	11.00	5.33	3.33
3.18349	652.00	55.00	41.00	27.00	19.67	10.00	5.00	5.67
3.21979	673.33	59.33	45.00	29.33	26.00	18.00	10.67	9.00
3.2565	663.67	55.33	36.67	28.67	27.00	16.00	11.33	9.00
3.29363	671.33	62.00	36.67	27.33	22.00	12.67	10.00	8.00
3.33118	695.67	52.33	36.00	30.33	32.00	14.00	10.33	6.00
3.36916	686.67	62.00	38.00	34.00	22.67	13.67	13.33	6.67
3.40758	697.33	67.00	49.67	36.00	23.33	19.00	16.67	8.67
3.44643	704.33	63.00	39.00	34.67	24.67	20.67	13.33	14.33
3.48573	680.33	60.00	34.00	30.67	24.33	15.00	12.00	7.00
3.52547	736.33	60.67	44.00	34.67	31.00	17.67	13.00	10.33
3.56567	736.67	56.33	40.33	24.00	26.67	11.67	10.33	7.33
3.60632	742.33	51.67	39.67	26.33	20.33	18.33	11.00	14.33
3.64744	744.00	64.33	43.00	34.33	28.33	17.33	13.00	6.33
3.68903	731.67	64.33	40.00	32.67	24.67	22.33	13.33	12.00
3.73109	770.00	67.67	45.00	38.00	26.33	22.33	12.67	14.33
3.77363	768.67	58.67	42.33	30.00	29.00	17.67	13.67	11.33
3.81666	848.67	64.00	47.33	31.33	25.67	21.67	12.00	7.33
3.86017	805.33	69.00	48.33	37.67	27.00	17.33	15.33	13.67
3.90419	825.33	68.00	46.00	36.00	28.33	19.67	16.00	9.33
3.9487	798.67	69.33	51.00	33.00	35.67	28.67	18.00	10.00
3.99372	842.67	61.33	47.33	32.33	25.00	18.00	13.00	10.33
4.03926	845.33	68.00	42.00	35.33	24.67	17.33	10.33	13.00
4.08531	860.00	67.33	40.67	32.67	21.00	20.67	11.00	11.67
4.13189	874.33	59.67	47.67	31.33	25.33	14.67	12.33	10.00
4.17901	887.33	62.33	48.67	33.67	31.00	20.00	17.67	10.67
4.22665	863.67	57.33	44.00	33.00	26.00	16.67	15.67	14.67
4.27485	904.33	77.67	44.00	34.67	33.33	21.00	21.00	12.00
4.32359	909.00	69.00	43.00	40.33	28.33	24.67	18.00	15.00
4.37288	918.67	68.33	46.00	37.33	34.00	26.00	12.33	17.33
4.42274	894.00	70.00	42.33	36.00	32.00	30.00	18.00	16.00
4.47317	933.00	69.67	50.33	39.67	31.33	20.67	21.00	20.00
4.52417	951.33	71.00	42.00	36.00	24.67	20.67	14.33	12.67
4.57576	983.00	66.67	46.00	35.00	34.67	20.00	23.33	16.00
4.62793	952.00	74.67	49.00	36.00	29.00	26.00	23.00	18.00
4.68069	1000.33	81.33	49.67	39.00	35.67	32.33	16.67	17.00
4.73406	1011.67	81.67	51.67	34.33	31.33	21.00	19.33	10.33
4.78804	1037.33	70.33	48.33	33.67	26.33	18.67	17.33	10.67
4.84263	1001.33	72.67	51.00	36.00	34.00	27.33	16.67	11.33
4.89785	1006.33	73.33	43.33	37.67	24.67	23.33	17.33	13.67
4.95369	1027.33	84.33	46.00	33.00	29.67	26.00	18.67	15.67
5.01017	1064.00	80.00	46.33	41.67	26.33	22.33	16.33	13.67
5.0673	1109.00	76.67	48.33	38.00	35.00	20.67	17.67	14.67
5.12507	1091.33	72.00	51.00	44.00	36.67	24.67	18.33	18.00
5.18351	1082.33	72.67	53.33	44.33	34.33	20.00	20.00	15.00

5.24261	1112.00	88.00	44.00	39.33	33.67	29.00	22.67	18.00
5.30239	1110.00	87.33	61.67	38.33	33.33	27.67	23.00	23.33
5.36284	1104.67	80.00	53.00	47.67	34.00	27.33	17.00	15.67
5.42399	1136.00	83.33	55.67	43.00	34.67	24.67	17.67	21.00
5.48583	1134.00	94.00	56.33	39.33	41.33	27.00	18.67	24.33
5.54838	1162.67	87.33	52.67	34.33	29.33	22.00	24.00	16.33
5.61164	1229.00	77.00	56.33	41.33	32.33	20.00	20.00	16.67
5.67563	1171.67	85.00	51.00	48.00	32.33	27.67	19.33	18.33
5.74034	1183.67	88.00	59.33	46.33	33.67	26.67	22.33	18.33
5.80579	1288.00	85.33	60.33	38.67	39.00	28.00	20.00	14.67
5.87199	1216.00	97.00	51.33	45.33	41.00	27.67	19.67	21.33
5.93894	1189.33	85.67	68.67	48.00	37.00	29.00	20.67	23.33
6.00665	1254.67	91.00	56.33	43.33	35.33	28.33	18.33	20.00
6.07514	1228.00	91.67	57.67	44.67	34.00	33.00	25.00	18.00
6.14441	1230.33	92.67	64.33	41.67	40.33	27.33	22.67	14.67
6.21447	1241.00	94.00	55.00	45.00	35.00	33.33	28.67	21.33
6.28532	1255.00	101.67	61.33	48.33	34.67	27.00	15.00	16.67
6.35699	1248.67	102.00	59.67	53.00	44.33	30.33	19.33	18.33
6.42947	1285.67	93.00	63.00	50.67	39.67	32.67	29.00	16.33
6.50277	1262.67	103.33	71.33	51.00	40.67	27.00	23.33	26.00
6.57692	1296.67	100.67	61.00	49.67	42.33	36.00	26.00	21.67
6.65191	1278.33	100.33	66.00	50.00	42.33	35.00	25.33	19.67
6.72775	1290.00	96.33	77.67	49.67	47.67	33.33	26.33	27.67
6.80446	1299.67	107.00	64.00	54.67	37.33	33.67	28.00	25.33
6.88204	1265.00	97.67	70.00	52.67	47.00	28.67	27.00	25.33
6.96051	1291.33	103.00	67.67	51.67	47.00	33.67	32.00	28.00
7.03987	1280.67	98.33	79.00	54.33	46.00	31.33	30.00	20.00
7.12014	1266.33	104.33	67.00	53.67	39.00	35.67	23.33	28.33
7.20132	1308.67	114.33	68.33	48.33	47.00	38.33	24.67	30.00
7.28343	1251.33	102.33	75.67	56.00	44.33	38.00	33.33	25.67
7.36648	1214.00	107.00	80.00	59.67	48.67	36.00	33.33	24.33
7.45047	1274.67	103.33	64.67	54.00	46.00	32.33	28.67	27.00
7.53542	1255.00	114.67	67.67	57.67	56.00	32.00	25.67	29.33
7.62133	1205.00	109.00	90.00	57.33	59.33	44.00	35.67	30.00
7.70823	1229.67	120.00	75.00	59.67	51.00	30.00	31.00	30.33
7.79612	1184.00	112.67	74.33	61.00	49.00	35.67	35.33	31.33
7.88501	1165.00	125.00	81.67	56.00	50.33	44.33	33.00	35.33
7.97491	1166.67	112.67	73.33	67.00	56.00	39.33	33.33	33.00
8.06584	1150.00	122.33	81.67	63.67	47.00	50.33	34.00	37.33
8.15781	1074.00	111.33	83.00	62.33	50.67	46.67	41.33	34.67
8.25082	1099.33	125.33	84.00	69.00	52.67	46.00	42.67	33.67
8.3449	1053.67	120.33	88.00	66.33	57.00	43.67	40.00	36.33
8.44004	1024.67	119.00	96.67	74.67	62.00	40.00	40.33	40.00
8.53627	971.67	122.00	83.00	64.00	55.33	45.33	39.00	40.67
8.6336	951.00	117.67	94.00	72.33	52.33	48.33	41.67	43.00
8.73204	868.33	130.33	89.67	74.67	58.33	45.00	39.67	47.33
8.8316	871.67	129.00	78.33	76.67	68.00	54.00	41.33	44.33
8.9323	888.67	122.67	94.33	65.33	66.33	52.00	42.33	34.67
9.03415	811.33	126.67	85.00	78.33	59.33	56.67	44.33	38.33
9.13715	785.00	120.33	98.33	72.67	62.33	51.67	40.67	46.33

9.24133	795.67	124.33	92.00	63.67	68.67	61.33	48.67	45.33
9.3467	709.00	129.00	102.67	74.00	68.00	54.00	47.00	43.67
9.45327	698.67	122.00	94.67	77.67	71.00	54.33	48.00	52.00
9.56105	648.33	120.67	99.33	78.67	69.33	59.00	60.67	48.00
9.67007	579.00	132.00	99.00	85.67	73.67	56.33	51.67	43.67
9.78032	562.67	130.67	100.67	78.33	72.33	57.00	47.00	50.00
9.89184	549.67	124.67	96.67	92.00	74.00	59.67	52.67	46.33
10.0046	524.67	114.33	85.33	85.00	78.67	61.67	53.00	50.67
10.1187	471.33	119.33	97.00	83.67	78.33	67.67	62.67	50.67
10.2341	456.67	129.00	100.00	84.67	82.00	57.67	57.67	51.67
10.3508	399.67	110.33	96.67	91.00	80.67	64.67	63.00	61.67
10.4688	377.67	121.00	111.33	99.00	84.00	70.33	59.67	55.00
10.5881	356.33	121.67	108.33	89.00	81.00	79.67	62.00	54.00
10.7089	317.00	113.67	110.00	89.33	70.00	66.00	57.00	58.67
10.831	273.33	113.00	102.00	85.00	82.00	73.67	62.67	62.00
10.9545	255.33	113.33	101.33	96.00	81.33	78.00	59.33	64.00
11.0794	222.00	100.00	103.33	95.00	83.33	77.00	73.33	64.00
11.2057	213.00	103.00	97.00	93.67	85.67	69.00	69.67	71.67
11.3334	182.67	106.00	118.33	99.67	78.67	86.33	78.67	66.67
11.4627	157.33	101.67	98.67	81.33	82.67	82.00	71.33	67.67
11.5934	138.00	106.33	91.00	93.33	87.67	78.67	70.33	84.33
11.7255	128.67	101.33	97.00	93.33	87.00	88.67	68.33	73.33
11.8592	122.67	98.33	90.33	98.33	92.67	78.67	73.00	69.67
11.9945	98.00	112.67	101.33	84.33	88.67	77.67	79.00	73.67
12.1312	90.67	91.67	100.00	94.33	96.33	85.33	74.67	86.00
12.2695	71.33	90.00	103.33	85.00	91.33	88.67	82.67	82.33
12.4094	60.33	83.67	87.33	93.33	78.67	81.00	83.67	79.67
12.5509	45.67	82.33	94.00	82.67	86.33	99.00	84.33	74.00
12.694	43.33	68.67	95.67	99.67	84.33	91.67	82.67	90.67
12.8388	28.33	68.33	85.00	90.67	94.67	85.67	79.67	71.33
12.9851	33.00	67.67	97.33	89.33	92.67	86.67	85.67	82.33
13.1332	33.00	75.00	91.00	89.00	92.33	81.67	83.33	85.67
13.2829	23.33	62.00	77.33	73.33	87.67	91.67	88.00	91.33
13.4344	20.00	56.33	79.33	84.67	89.33	91.33	90.67	80.00
13.5876	19.67	55.00	74.00	81.33	73.33	86.67	81.67	88.33
13.7425	12.00	47.67	78.33	73.33	84.67	90.00	90.00	82.00
13.8992	14.33	48.67	79.67	68.67	79.33	87.33	82.00	83.00
14.0577	12.67	41.67	70.00	72.33	84.33	88.00	84.00	90.00
14.2179	6.67	39.33	61.00	80.33	79.00	83.00	84.33	82.00
14.38	6.67	37.33	65.00	70.33	75.33	82.33	86.00	87.00
14.544	7.67	32.33	69.33	65.33	70.33	92.33	85.67	83.33
14.7098	7.33	28.00	54.00	70.00	73.33	71.33	75.67	86.00
14.8776	4.33	29.00	50.67	59.33	77.33	78.00	79.33	78.33
15.0472	5.67	27.33	52.67	59.00	68.67	71.33	88.67	82.00
15.2188	2.67	23.67	42.33	57.67	68.33	70.00	75.33	72.67
15.3923	4.33	21.33	47.00	51.67	63.33	70.00	67.33	75.67
15.5678	3.33	17.33	35.33	46.00	61.00	60.67	63.67	76.67
15.7453	2.67	12.33	33.33	44.67	58.67	60.33	63.33	68.67
15.9248	2.67	14.00	29.67	53.00	46.33	58.33	69.67	67.67
16.1064	2.67	8.00	29.00	43.33	58.33	57.00	60.33	57.33

16.29	2.00	11.33	26.67	41.00	51.00	60.33	60.33	63.33
16.4757	1.67	10.33	19.67	32.67	42.67	51.33	60.67	58.67
16.6636	0.00	8.67	23.67	31.00	36.67	52.00	49.67	54.67
16.8536	3.33	3.33	19.67	29.67	32.00	42.67	45.00	42.33
17.0458	2.67	2.33	14.67	27.00	30.33	40.67	50.00	40.33
17.2401	0.67	4.33	14.67	21.67	30.67	34.00	48.00	39.67
17.4367	2.33	2.67	14.00	23.33	28.33	33.33	43.33	38.00
17.6355	0.33	1.33	9.67	23.00	22.67	37.33	33.00	30.33
17.8366	1.33	3.00	12.67	17.67	20.00	29.00	37.67	34.33
18.0399	0.33	2.67	9.67	13.00	14.00	25.00	26.33	37.33
18.2456	0.33	2.00	5.33	13.33	18.00	22.00	28.67	22.67
18.4537	1.00	2.00	5.67	10.00	15.00	21.67	24.33	26.67
18.6641	0.33	0.33	5.00	8.33	9.67	16.00	26.67	23.33
18.8769	1.00	0.67	2.00	7.67	6.33	15.67	19.67	20.33
19.0921	2.67	1.00	3.67	6.33	11.33	10.67	11.33	18.00
19.3098	1.33	0.00	5.00	5.00	11.00	12.33	14.33	12.67
19.53	0.67	0.00	2.67	3.67	10.33	10.00	13.67	12.00
19.7526	0.33	0.33	1.33	3.67	4.67	12.33	7.00	12.00
19.9778	0.33	0.67	1.33	2.00	4.67	7.00	9.33	7.67
20.2056	0.67	0.33	0.67	1.33	4.33	4.67	7.33	3.33
20.436	0.33	0.00	1.00	1.67	2.67	5.00	5.33	6.33
20.669	0.33	0.67	1.33	0.67	2.67	5.33	3.33	4.00
20.9047	0.33	0.33	1.00	1.33	1.67	3.00	3.00	3.67
21.143	0.67	0.00	0.00	1.00	2.00	2.00	2.00	4.67
21.3841	0.67	0.33	1.00	2.00	2.33	1.33	2.00	3.33
21.6279	0.33	0.67	0.67	1.67	0.67	2.67	3.00	2.67
21.8745	0.00	0.00	0.33	1.33	0.33	1.00	0.67	1.67
22.1239	0.67	0.00	0.33	0.00	0.67	1.67	1.33	1.67
22.3762	0.00	0.00	0.00	0.67	0.33	0.67	0.67	0.67
22.6313	0.00	0.00	0.00	0.00	0.00	0.33	0.00	1.67
22.8894	1.00	0.33	0.33	0.00	0.33	0.33	0.67	0.67
23.1503	0.33	0.00	0.00	1.00	0.00	0.67	0.33	0.33
23.4143	1.00	0.00	0.00	0.33	0.33	1.00	0.33	0.67
23.6813	0.67	0.00	0.00	0.00	0.00	0.00	0.67	1.00
23.9513	0.67	0.00	0.33	0.00	0.00	0.00	0.00	0.00
24.2244	0.67	0.00	0.00	0.00	0.00	0.00	0.00	0.00
24.5006	0.67	0.00	0.67	0.33	0.33	0.00	0.00	0.00
24.7799	0.33	0.33	0.33	0.00	0.00	0.00	0.00	0.33
25.0624	0.00	0.00	0.33	0.00	0.00	0.67	0.33	0.33
25.3482	0.00	0.00	0.00	0.00	0.33	0.33	0.00	0.67
25.6372	0.00	0.00	0.00	0.00	0.00	0.00	0.00	0.33
25.9295	0.67	0.00	0.67	0.00	0.00	0.00	0.33	0.33
26.2252	0.00	0.00	0.33	0.00	0.00	0.00	0.33	0.00
26.5242	0.33	0.33	0.00	0.33	0.00	0.00	0.33	0.00
26.8266	0.33	0.33	0.00	0.00	0.00	0.00	0.00	1.00
27.1325	0.00	0.00	0.33	0.00	0.33	0.00	0.00	0.00
27.4418	0.00	0.00	0.00	0.33	0.00	0.00	0.00	0.00
27.7547	0.00	0.00	0.00	0.33	0.67	0.00	0.00	0.00
28.0712	0.33	0.00	0.00	0.67	0.00	0.33	0.00	0.00
28.3913	0.33	0.00	0.00	0.00	0.33	0.00	0.00	0.00

28.715	0.00	0.00	0.00	0.00	0.00	0.33	0.00	0.33
29.0424	0.00	0.00	0.00	0.00	0.33	0.00	0.33	0.00
29.3735	0.00	0.33	0.00	0.00	0.00	0.00	0.00	0.33
29.7084	0.33	0.00	0.00	0.00	0.00	0.00	0.00	0.00
30.0471	0.67	0.00	0.00	0.00	0.00	0.00	0.33	0.00
30.3897	0.33	0.00	0.00	0.00	0.33	0.67	0.00	0.00
30.7362	0.00	0.00	0.00	0.00	0.33	0.00	0.00	0.00
31.0867	0.00	0.00	0.00	0.00	0.00	0.00	0.00	0.33
31.4411	0.00	0.00	0.00	0.00	0.33	0.00	0.00	0.00
31.7996	0.00	0.33	0.00	0.00	0.33	0.00	0.00	0.00
32.1622	0.33	0.00	0.00	0.00	0.00	0.00	0.00	0.00
32.5289	0.00	0.00	0.00	0.33	0.00	0.00	0.00	0.00
32.8998	0.00	0.33	0.33	0.00	0.00	0.33	0.00	0.00
33.2749	0.00	0.00	0.00	0.00	0.00	0.00	0.00	0.00
33.6543	0.33	0.00	0.00	0.00	0.00	0.00	0.00	0.00
34.038	0.00	0.00	0.00	0.00	0.00	0.00	0.33	0.00
34.4261	0.00	0.33	0.00	0.00	0.00	0.00	0.00	0.00
34.8186	0.00	0.00	0.33	0.00	0.00	0.67	0.00	0.00
35.2156	0.33	0.00	0.33	0.00	0.33	0.33	0.00	0.00
35.6172	0.00	0.00	0.00	0.00	0.00	0.00	0.33	0.00
36.0233	0.00	0.00	0.00	0.00	0.33	0.00	0.00	0.33
36.434	0.00	0.00	0.00	0.00	0.00	0.33	0.00	0.33
36.8494	0.00	0.00	0.00	0.33	0.00	0.33	0.00	0.00
37.2696	0.00	0.33	0.00	0.00	0.00	0.00	0.00	0.00
37.6945	0.33	0.00	0.00	0.00	0.00	0.00	0.00	0.00
38.1243	0.00	0.00	0.00	0.00	0.00	0.00	0.00	0.00
38.559	0.33	0.00	0.00	0.00	0.00	0.00	0.33	0.00
38.9986	0.00	0.00	0.00	0.00	0.00	0.00	0.00	0.00
39.4433	0.00	0.00	0.00	0.33	0.00	0.00	0.00	0.00
39.893	0.00	0.00	0.00	0.00	0.00	0.00	0.00	0.00
40.3479	0.33	0.00	0.00	0.33	0.00	0.00	0.00	0.00
40.8079	0.00	0.00	0.33	0.00	0.00	0.00	0.33	0.00
41.2732	0.33	0.00	0.00	0.00	0.00	0.00	0.00	0.33
41.7438	0.00	0.00	0.00	0.00	0.00	0.00	0.00	0.33
42.2197	0.00	0.00	0.00	0.00	0.00	0.00	0.33	0.00
42.7011	0.00	0.00	0.00	0.00	0.00	0.00	0.00	0.00
43.188	0.33	0.00	0.33	0.00	0.00	0.00	0.00	0.00
43.6804	0.00	0.00	0.00	0.00	0.00	0.00	0.00	0.00
44.1784	0.00	0.00	0.00	0.00	0.00	0.00	0.00	0.00
44.6822	0.00	0.00	0.00	0.00	0.00	0.00	0.00	0.00
45.1916	0.33	0.33	0.00	0.00	0.00	0.00	0.00	0.33
45.7069	0.00	0.00	0.00	0.00	0.00	0.00	0.00	0.00
46.228	0.00	0.00	0.00	0.00	0.00	0.00	0.00	0.00
46.7551	0.00	0.00	0.00	0.00	0.00	0.00	0.00	0.00
47.2882	0.00	0.00	0.00	0.00	0.00	0.00	0.00	0.00
47.8274	0.00	0.00	0.00	0.00	0.00	0.33	0.00	0.00
48.3727	0.00	0.00	0.00	0.00	0.00	0.00	0.00	0.00
48.9242	0.00	0.00	0.00	0.00	0.00	0.00	0.00	0.00
49.4821	0.00	0.00	0.00	0.00	0.00	0.00	0.00	0.00
50.0462	0.00	0.00	0.00	0.00	0.00	0.00	0.00	0.00

50.6169	0.00	0.00	0.00	0.00	0.00	0.33	0.00	0.33
51.194	0.00	0.00	0.00	0.00	0.00	0.00	0.00	0.00
51.7777	0.00	0.00	0.00	0.00	0.00	0.33	0.00	0.33
52.368	0.00	0.00	0.00	0.00	0.00	0.00	0.00	0.00
52.9651	0.00	0.00	0.00	0.00	0.00	0.33	0.00	0.00
53.569	0.00	0.00	0.00	0.00	0.00	0.00	0.00	0.00
54.1798	0.00	0.00	0.00	0.00	0.00	0.00	0.00	0.00
54.7976	0.00	0.00	0.00	0.00	0.00	0.00	0.00	0.00
55.4224	0.00	0.00	0.00	0.00	0.00	0.00	0.00	0.00
56.0543	0.00	0.00	0.00	0.00	0.00	0.00	0.00	0.00
56.6934	0.00	0.00	0.00	0.00	0.00	0.00	0.00	0.00
57.3398	0.00	0.00	0.00	0.00	0.00	0.00	0.00	0.00
57.9936	0.00	0.00	0.00	0.00	0.00	0.00	0.00	0.00
58.6548	0.00	0.00	0.00	0.00	0.00	0.33	0.00	0.00
59.3236	0.00	0.00	0.00	0.00	0.00	0.00	0.00	0.00
60	1.27E+05	1.38E+04	1.09E+04	9.21E+03	8.41E+03	7.32E+03	6.50E+03	6.15E+03

The table below shows the results from the sample calculations:

Table 18: Results from sample calculations for kinetic experiments with S_i = 3.3, C_{seeds} = 0.03g.dm^{-3} & A3.2.1

Time, *t* (min)	m_0 (#/m^3)	Mass (kg/m^3)	m^3 (m^3/m^3)	m_1/m_0 (µm)	m_4/m_3 (µm)
0	9.49E+10	3.08E-02	2.67E-05	5.66	8.40
5	5.53E+10	4.15E-02	3.60E-05	7.26	11.35
10	4.34E+10	4.75E-02	4.12E-05	8.24	12.69
15	3.68E+10	4.94E-02	4.28E-05	8.87	13.35
20	3.36E+10	5.18E-02	4.50E-05	9.35	13.76
30	2.93E+10	5.58E-02	4.84E-05	10.17	15.14
45	2.60E+10	5.51E-02	4.78E-05	10.76	14.70
60	2.46E+10	5.54E-02	4.81E-05	11.08	15.15

The growth and aggregation kinetics were calculated by using Equations (111) & (113) respectively. The supersaturation at each time interval was calculated using Equations (127) – (130) and Equation (132). Sample calculations are shown below for a single experiment where S_i = 3.3, C_{seeds} = 0.03g.dm^{-3} and using seed sample A3.2.1.

The growth rates were calculated from the second and third moments as follows:

$$\frac{dm_3}{dt} = 3Gm_2 \rightarrow G = \frac{dm_3/dt}{3m_2} = \frac{1.95\times10^{-6}}{3\times3.21} = 2.03 \times 10^{-7} \text{ m.s}^{-1}$$

Table 19: Sample calculations showing results for the determination of G

Time, t (min)	Time Interval (min)	m_3 (m^3/m^3)	Δm_3	dm_3/dt	$m_2 avg$	G (m/s)
0	-	2.39E-05	-	-	-	-
5	5	3.37E-05	9.76E-06	1.95E-06	3.21	2.03E-07
10	5	3.88E-05	5.11E-06	1.02E-06	3.28	1.04E-07
15	5	4.03E-05	1.47E-06	2.95E-07	3.26	3.01E-08
20	5	4.14E-05	1.11E-06	2.22E-07	3.21	2.30E-08
30	10	4.78E-05	6.40E-06	6.40E-07	3.29	6.48E-08
45	15	4.46E-05	-3.17E-06	-2.12E-07	3.28	-2.15E-08
60	15	4.55E-05	8.90E-07	5.93E-08	3.19	6.21E-09

In order to calculate the supersaturation at each sample point the following constants were used:

$W_0 = 0.027$ kg.m^{-3} $K_{sp} = 2.47 \times 10^{-9}$ (kmol.m^{-3})^2

$T^0_{Ca^{2+}} = 1.47 \times 10^{-3}$ kmol.m^{-3} $T^0_{Ox^{2-}} = 2.94 \times 10^{-4}$ kmol.m^{-3}

$M = 146$ kg.kmol^{-1} $\rho_s = 2200$ kg.m^{-3}

$\gamma_{Ca^{2+}} = 0.343$ $\gamma_{Ox^{2-}} = 0.274$

$a_{H_2 0} = 0.995$

Only K_{sp}, M & ρ_s stayed constant throughout the different kinetic experiments i.e. all of the other constants changed.

$W_t = \rho_s \frac{\pi}{6} m_3 = 2200 \times \frac{\pi}{6} \times (2.39 \times 10^{-5}) = 2.76 \times 10^{-2}$ kg.m^{-3}

$\Delta n = \frac{W_t - W_0}{M} = \frac{(2.76 \times 10^{-2} - 0.027)}{146} = 5.67 \times 10^{-6}$ kmol.m^{-3}

$T_{Ca^{2+}} = T^0_{Ca^{2+}} - \Delta n = (1.47 \times 10^{-3}) - (5.67 \times 10^{-6}) = 1.47 \times 10^{-3}$ kmol.m^{-3}

$T_{Ox^{2-}} = T^0_{Ox^{2-}} - \Delta n = (2.94 \times 10^{-4}) - (5.67 \times 10^{-6}) = 2.88 \times 10^{-4}$ kmol.m^{-3}

$S = \left[\frac{\gamma_{Ca^{2+}} \cdot T_{Ca^{2+}} \cdot \gamma_{Ox^{2-}} \cdot T_{Ox^{2-}} \cdot a_{H_2 O}}{K_{sp}}\right]^{\frac{1}{2}} = \left[\frac{0.343 \times 1.47 \times 10^{-3} \times 0.274 \times 2.88 \times 10^{-4} 0.995}{2.47 \times 10^{-9}}\right]^{\frac{1}{2}} = 4.0$

Table 20: Sample calculations showing results for the determination of S

W_t (kg/m^3)	Δn (kmol/m^3)	TCa^{2+} (kmol/m^3)	TOx^{2-} (kmol/m^3)	IAP	S	S_{avg}
2.76E-02	5.67E-06	1.47E-03	2.88E-04	3.95E-08	4.00	-
3.88E-02	8.26E-05	1.39E-03	2.11E-04	2.74E-08	3.33	3.66
4.47E-02	1.23E-04	1.35E-03	1.71E-04	2.15E-08	2.95	3.14
4.64E-02	1.35E-04	1.34E-03	1.59E-04	1.99E-08	2.84	2.90
4.77E-02	1.43E-04	1.33E-03	1.51E-04	1.87E-08	2.75	2.79
5.50E-02	1.94E-04	1.28E-03	1.00E-04	1.20E-08	2.20	2.48
5.14E-02	1.69E-04	1.30E-03	1.25E-04	1.52E-08	2.48	2.34
5.24E-02	1.76E-04	1.30E-03	1.18E-04	1.43E-08	2.41	2.44

The aggregation rate constants were calculated from the zeroth moment as follows:

$$\frac{dm_0}{dt} = -\frac{1}{2}\beta_0 m_0^2 \rightarrow \beta_0 = -2\frac{dm_0/dt}{m_0^2} = -2\frac{(-6.84\times10^9)}{(6.58\times10^{10})^2} = 3.16\times10^{-12}\ \text{m}^3.\text{s}^{-1}$$

Table 21: Sample calculations showing results for the determination of β_0

Time, *t* (min)	Time Interval (min)	m_0 (#/m^3)	Δm_0	dm_0/dt	β_0 (m^3/s)
0	-	8.29E+10	-	-	-
5	5	4.87E+10	-3.42E+10	-6.84E+09	3.16E-12
10	5	3.75E+10	-1.12E+10	-2.23E+09	2.41E-12
15	5	3.19E+10	-5.57E+09	-1.11E+09	1.85E-12
20	5	2.90E+10	-2.96E+09	-5.93E+08	1.28E-12
30	10	2.59E+10	-3.04E+09	-3.04E+08	8.07E-13
45	15	2.28E+10	-3.13E+09	-2.09E+08	7.03E-13
60	15	2.18E+10	-1.01E+09	-6.72E+07	2.70E-13

C.3 Chapter 5

The raw data below is an example of the conductivity-time data obtained during an induction time experiment. The data shows how the induction period was determined from the data i.e. see highlighted blocks in Table 22. Sample calculations are shown below.

$t_{ind} = (t_2 - t_1) = (184 - 168) = 16\ s$

The average t_{ind} was calculated from the four experiments for each S_i and the standard deviation was then calculated as follows:

$$\bar{t}_{ind@\ S_i=6.5} = \left(\frac{16+24+18+22}{4}\right) = 20\ s$$

$$STDEV_{S_i=6.5} = \sqrt{\frac{\sum(t_{ind,i}-\bar{t}_{ind})^2}{(n-1)}}$$

$$STDEV_{S_i=6.5} = \sqrt{\frac{(16-20)^2+(24-20)^2+(18-20)^2+(22-20)^2}{(4-1)}} = 3.7\ s$$

Table 22: Raw conductivity-time data from an induction time experiment with S_i = 6.5

	Time (s)	Cond (µS/cm)	Time (s)	Cond (µS/cm)	Time (s)	Cond (µS/cm)
	140	6.83	187	518	234	512
	141	7.2	188	518	235	511
	142	7.52	189	518	236	511
	143	7.35	190	518	237	511
	144	7.53	191	518	238	511
	145	7.3	192	518	239	511
	146	7.29	193	518	240	511
	147	17.19	194	518	241	511
	148	19.99	195	517	242	511
	149	100	196	517	243	510
	150	450	197	517	244	510
	151	478	198	517	245	510
	152	518	199	517	246	510
	153	511	200	517	247	510
	154	510	201	516	248	510
	155	512	202	516	249	509
	156	513	203	516	250	509
	157	513	204	516	251	509
	158	515	205	516	252	509
	159	515	206	516	253	508
	160	516	207	516	254	508
	161	517	208	516	255	508
	162	517	209	516	256	508
	163	518	210	516	257	508
	164	518	211	515	258	508
	165	518	212	515	259	508
	166	518	213	515	260	507
	167	518	214	515	261	508
t_1	168	519	215	515	262	507
	169	519	216	514	263	507
	170	519	217	514	264	507
	171	519	218	514	265	507
	172	519	219	514	266	506
	173	519	220	514	267	506
	174	519	221	513	268	506
	175	519	222	513	269	506
	176	519	223	513	270	506
	177	519	224	513	271	505
	178	519	225	513	272	506
	179	519	226	513	273	505
	180	519	227	513	274	505
	181	519	228	513	275	505
	182	519	229	512	276	505
	183	518	230	512	277	505
t_2	184	519	231	512	278	505
	185	518	232	512	279	505
	186	518	233	512	280	505

Appendix D: Ethics Form

20 APR 2010

EBE Faculty: Assessment of Ethics in Research Projects

Any person planning to undertake research in the Faculty of Engineering and the Built Environment at the University of Cape Town is required to complete this form before collecting or analysing data. When completed it should be submitted to the supervisor (where applicable) and from there to the Head of Department. If any of the questions below have been answered YES, and the applicant is NOT a fourth year student, the Head should forward this form for approval by the Faculty EIR committee: submit to Ms Zulpha Geyer (Zulpha.Geyer@uct.ac.za; Chem Eng Building, Ph 021 650 4791). Students must include a copy of the completed form with the thesis when it is submitted for examination.

Name of Principal Researcher/Student: Emily Musil (MSLEMI004) Department: Chemical Engineering

If a Student: Degree: Masters in Chemical Engineering Supervisor: Prof. A.E. Lewis

If a Research Contract indicate source of funding/sponsorship:

Research Project Title: Developing methods to measure the precipitation kinetics of sparingly soluble systems

Overview of ethics issues in your research project:

Question 1: Is there a possibility that your research could cause harm to a third party (i.e. a person not involved in your project)?	YES	NO ✓
Question 2: Is your research making use of human subjects as sources of data? If your answer is YES, please complete Addendum 2.	YES	NO ✓
Question 3: Does your research involve the participation of or provision of services to communities? If your answer is YES, please complete Addendum 3.	YES	NO ✓
Question 4: If your research is sponsored, is there any potential for conflicts of interest? If your answer is YES, please complete Addendum 4.	YES	NO ✓

If you have answered YES to any of the above questions, please append a copy of your research proposal, as well as any interview schedules or questionnaires (Addendum 1) and please complete further addenda as appropriate.

I hereby undertake to carry out my research in such a way that

- there is no apparent legal objection to the nature or the method of research; and
- the research will not compromise staff or students or the other responsibilities of the University;
- the stated objective will be achieved, and the findings will have a high degree of validity;
- limitations and alternative interpretations will be considered;
- the findings could be subject to peer review and publicly available; and
- I will comply with the conventions of copyright and avoid any practice that would constitute plagiarism.

Signed by:

	Full name and signature	Date
Principal Researcher/Student:	Emily Ann Musil Signed by candidate	21/04/2010

This application is approved by:

Supervisor (if applicable):	Signed by candidate	22/04/2010
HOD (or delegated nominee): Final authority for all assessments with NO to all questions and for all undergraduate research.	Signed by candidate	28 APRIL 2010
Chair : Faculty EIR Committee For applicants other than undergraduate students who have answered YES to any of the above questions.		